Radiolarian-based oceanic plate stratigraphy of the melanges and subduction-accretion processes in the western sector of the Yarlung–Tsangpo suture zone, southern Tibet

チベット南部ヤールンツァンポー縫合帯西域におけるメランジュの放散虫にもとづく海洋プレート層序の復元と沈み込み-付加過程

LI Xin

Doctoral Program in Environmental Science and Technology

Graduate School of Science and Technology

Niigata University

contents

Abstract

The southernmost Yarlung–Tsangpo suture zone (YTSZ) in the Tibet plateau is widely accepted as the youngest suture zone that separates the Indian continent to the south and the Lhasa terrane to the north. Early studies argued that the entire Tethyan oceanic crust was subducted along the southern margin of the Lhasa terrane through one subduction system. An alternate model proposes the existing of multiple subductions. The oceanic plate stratigraphy (OPS) and the subduction-accretion processes, which are required to reconcile these two models, are far poorly understood, especially in the western YTSZ.

Our research area is located in the western segment of the YTSZ, where the suture zone is divided by the Zhada–Zhongba terrane into the northern and the southern belts. The southern belt of the YTSZ contains ophiolitic melanges (Tanwa melange), volcanic-sedimentary melanges (Erba melange, Maquanhe melange, Tanong melange) and clastic dominated melange (Yisang melange). Detailed radiolarian analyses are conducted on melanges near Zhongba County. Macroscopic-, me soscopic- and microscopic observations are combined to elucidate the relationships of age, lithology and structure. New data are applied to reconstruct the oceanic plate stratigraphy and the subduction-accretion process.

The Tanwa melange, which is located south to the Zhada–Zhongba terrane, is characterized by a huge sequence of upper mantle peridotites and mafic rocks thrust north to a siliceous melange sequence. The Erba melange is characterized by highly sheared volcanoclastic or siliceous mudstone matrix including blocks of chert, claystone, basalt. Broken formations of tens-meters are observable in this melange.

In the Tanwa melange and the Erba melange, radiolarian assemblages from the highly sheared siliceous mudstone matrix of this melange are comparable with the *Arisaturnalis carinatus* (KR3) zone, the *Turbocapsula costata* Zone and the *Spoletoensis*

Zone, Aptian to Albian in age. Radiolarian assemblages from the chert blocks are comparable with the *Trillus elkhomensis* (JR2) Zone, the *Loopus primitivus* (JR8) zone, the *Pseudodictyomitra carpatica* (KR1) zone, and the *Cecrops septemporatus* (KR2) zone, Pliensbachian–Toarcian and Tithonian–Barremian in age.

The Maquanhe melange is located south of the Tanwa melange or the Erba melange. They are connected by faults. It consists of siliceous mudstone, chert, basalt, and limestone. This melange does not display the typical blocks-in-matrix fabric. Strata are grossly continuous. Radiolarian assemblages from the chert of the Maquanhe melange are comparable with the *Spoletoensis* Zone, late Albian in age.

The lowermost record of the OPS is thin Lower Jurassic bedded red chert with some layers of limestone. In the Late Jurassic, thin bedded green cherts interbedded with shales were deposited. Trace fossils were well developed. Above them, red cherts and claystones were accumulated from Late Jurassic to Early Cretaceous. During the Aptian to Albian, siliceous mudstones were accumulated in the northern part (the Tanwa melange and the Erba melange), while chert interbedded with limestone were dominant in the southern part (the Maquanhe melange).

Siliceous mudstones, which are Aptian to Albian in age, are always highly sheared. Isoclinally folds and pinch-and-swelled structure are well developed in the Tithonian to Barremian chert blocks. Well developed block-in-matrix fabric in the Late Jurassic to Early Cretaceous strata and rare preservation of strata older than Tithonian indicate a decollement fault formed in a siliceous claystone in the Late Jurassic near Tithonian. Type 2 brecciation developed in Tithonian to Barremian chert blocks and the Aptian to Albian siliceous mudstones indicates continuous tectonic shearing and fluid overpressure in the sediments above the decollement fault. Strata with different lithification and ratio of competent and incompetent materials displayed different deformations styles. No deformation in the radiolarian skeletons indicates that the subduction-accretion processes were in a shallow depth.

Because of the lack of terrrigenous trubidites in the Tanwa melange, the Erba melange, and the Maquanhe melange, the age of the youngest siliceous mudstones is the maximum constraint on the timing of accretion. The melanges become younger southward, which is consistent with the oceanic plate subducting northward under the Lhasa terrane during the Cretaceous. In the Albian, the presence of limestone interbedded with chert in the Maquanhe melange indicates sedimentation above or near the carbonate compensation depth (CCD). Compared with the coeval strata in the Tanwa melange and the Erba melange, the shallower water depth and the dominance of siliceous mudstone in the Maquanhe melange reflect the close proximity to the northernmost edge of the Indian continent.

Within the Tanwa melange, type 1 breccia is interpreted as proximal debris flow from the old accretionary complex. No clast of terrestrial material indicates the sources are only pelagic or hemipelagic. This breccia can be interpreted by the existing of an intra-oceanic subduction within the Neo-Tethys.

The lack of terrigenous turbidites in the melanges may caused by increasing distance from the continent, topographic barrier of intraoceanic island arcs and Zhada–Zhongba terrane, and the huge accomodation of the Xigaze forearc basin.

Chapter 1 Introduction

1.1 Background

The Tibetan plateau, with an elevated area nearly 3500 km by 1500 km in extent, is the highest and largest plateau on earth (Fielding, 1996). The Plateau is widely treated as a natural laboratory for the study of continental collision (Allègre et al., 1984; Molnar et al.,1993). The plateau affects the regional climate of Asia and Cenozoic global cooling, as well (An et al., 2001; Raymo and Ruddiman, 1992).

Sequential accretion of several blocks and island arcs onto the southern margin of the Eurasia continent since the early Paleozoic built up the Tibetan plateau (Chang and Zheng, 1973, Yin and Nie, 1996). The plateau consists of four blocks, Kunlun–Qaidam, Hoh Xil–Songpan Ganzi, Qiangtang, and Lhasa. They are separated by east-west trending sutures: Ayimaqin–Kunlun suture zone (AKSZ), the Jingsha suture zone (JSSZ), the Bangong–Nujiang suture zone (BNSZ), and the Yarlung–Tsangpo suture zone (YZSZ) (Yin and Harrison, 2000) (Fig. 1.1). These suture zones mark collision events of different blocks.

The southernmost YTSZ is widely accepted as the youngest suture zone that separates the Indian continent to the south and the Lhasa terrane to the north. The YZSZ contains remnants of the Neo-Tethys (Dai et al., 2011; Hébert et al., 2012). The evolution of the suture zone is complex as several lithotectonic units and events are encountered in a now very narrow zone.

1.2 Existing problems

Various scenarios for the evolution of the Neo-Tethys have been proposed. It is widely accepted that the entire Tethyan oceanic crust was subducted along the southern margin of the Lhasa terrane through one subduction system along the continental margin of Tethys (Allègre et al., 1984; Chang, 1984; Chang et al.,1986; Searle et al., 1987; Cai et al., 2012). The contrasted igneous, sedimentary, and metamorphic ages of the ophiolites, compositional diversity (Hébert et al., 1999; Aitchison et al., 2000, 2003; Aitchison and Davis, 2004; Davis et al., 2002, 2004; Guilmette et al., 2007, 2008, 2009), and multiple deformation structures (Xu et al., 2015) prove the existing of multiple subductions. The Yarlung–Tsangpo ophiolitic belt in southern Tibet is typically divided into eastern, central, and western segments. Previous studies of this ophiolitic belt are mainly focused on the eastern and the central segments (Hébert et al., 2003, 2012; Malpas et al., 2003; Robinson et al., 2004; Yang et al., 2007; Yamamoto et al., 2013)

Studies on the radiolarians along the YTSZ provide useful age constraints and important clues for elucidating the evolution of the Neo-Tethys (Figs. 1.1, 1.2). Some reports of radiolarian assemblages from the melange along the YTSZ are available. Late Jurassic and Early Cretaceous radiolarians from the melange near Zhongba are reported (Li et al., 2013, 2017; Zhong et al., 2016). Middle Triassic and Early Cretaceous radiolarians are reported from ophiolitic melange near Lhaze (Zhu et al., 2005). Upper Triassic to mid-Cretaceous radiolarian-bearing strata occupy the southern marginal part of the YTSZ near Xialu (Matsuoka et al., 2001, 2002, 2005; Wu, 2000; Ziabrev et al., 2004) and Ladakh (Kojima et al., 2001; Zyabrev et al., 2008). Late Albian to early Cenomanian radiolarian faunas have been reported from the Congdu Formation near Bainang (Wu, 1984; Li and Wu, 1985; Wu, 1986). Radiolarian faunas from the sedimentary succession (Congdu Formation) overlying the ophiolite near Bainang have been revised as Early Cretaceous (Ziabrev et al., 2003; Li et al., 2017). Early Cretaceous radiolarian assemblage from chert blocks near Zedong (Liu et al., 2016) has been reported. Middle to Late

Trassic radiolarians have been reported from a chert block in the melange near Zedong (Wang et al., 2002).

South to the YTSZ, Lower Cretaceous and Upper Paleocene strata of the Northern Tethys Himalaya contain well preserved radiolarians (Figs. 1.1, 1.2). Xu and Luo (2016) reported Late Jurassic to Early Cretaceous radiolarians from a cherty block in the Yamdrok melange near Gyangze. Li et al. (2017) conducted radiolarian biostratigraphic study and established zonation for Lower Cretaceous strata. Late Paleocene radiolarian assemblage has been reported from siliceous strata near Zhongba (Liang et al., 2012), Saga (Li et al., 2007; Ding, 2003, 2005; Wang et al., 2016), and Renbu (Liu and Aitchison, 2002).

However, several problems still exist due to the limited radiolarian biostratigraphic constriants on the YTSZ.

Firstly, rocks within the YTSZ are tectonically disrupted. Most of the reports on radiolarians are based on scattered samples from a vast area. This random data give us the mixed information from different accretionary complexes, which may come from different area of the Neo-Tethys.

Secondly, the radiolarian assemblages are obtained from chert blocks and the age is concentrated on the Late Jurassic to the Early Cretaceous. The chert blocks provide limited information of middle part of the oceanic plate, which was accumulated in mature pelagic paleoenvironment. Only few studies in the Bainang terrane (Matsuoka et al., 2001, 2002, 2005; Ziabrev et al., 2004) and the Dazhuqu terrane (Ziabrev et al., 2003) have provided the detailed radiolarian biostratigraphy, which include the hemipelagic or trench clastic sediments.

Thirdly, most of the results come from the central segment of the YTSZ. The information of the western segment is limited.

Finally, the melanges are dominant in the Yarlung–Tsangpo suture zone, however, studies on the melange fabric and the deformation processes are rare.

1.3 Objectives

Melanges in the YTSZ are characterized by highly sheared volcanoclastic or siliceous mudstone matrix including blocks of chert, claystone, basalt, and crystalline limestone. Pelagic or hemipelagic chert and siliceous mudstone are important constituents in the melange. Radiolarians are the only and significant fossils that can provide age constraint for chert and siliceous mudstone. Detailed radiolarian analyses are constructive for reconstruction of the onceanic plate stratigraphy of melanges.

Tectonic melanges are a common constituent of convergent margins. Despite their apparently chaotic nature, melanges often exhibit a high degree of internal organization and display a consistent suite of structures, which are indicative of the processes that formed the melange (Needham, 1995). Macroscopic-, mesoscopic- and microscopic observations on structure, lithology, and radiolarian assemblages are benificial for elucidating the fabric of melanges and the deformation styles of different lithology and ages. The subduction-accretion processes, which formed and affected on the mélanges, are inferred.

1.4 Methodology

1.4.1 Field work

Intensive sampling of siliceous rocks in the continuous sequences on the Indian passive margin is for geobiographic analyses. Six sections are conducted in this study. Intensive samples were collected from the matrix and blocks of the melange. Totally, 350 samples were collected, 117 of them contained well preserved radiolarians. The sections were detailed analyzed in chapters 4 and 5.

1.4.2 Radiolarian analyses

Radiolarians were extracted mainly from the red cherty siltstone and red chert. The method for extraction of radiolarians described by Pessagno and Newport (1972) was

followed. Light microscope, stereoscopic microscope, and scanning electron microscope were used for observation, picking up, and identification.

1.4.3 Observation on the fabric of melanges

Outcrop-, mesoscopic-, and microscopic- scales of observation features are conducted to highlight the fabric of melange.

To clarify the fabric of breccias without contamination, we treated the brecciated siliceous rocks as follows (Fig. 5.24). Firstly, soak all the samples in 5% hydrofluoric acid (HF) for one day at room temperature separately. After re-soaking in fresh water for one day, rocks are dried naturally. Then we check and select typical breccias. Secondly, the selected breccias are cut into several pieces with planar surfaces and these pieces are soaked in 10% chloric acid (HCl) for 5 hours to remove the calcite veins. Then remove the HCl and treat these pieces as the first step. Thirdly, the etched surface retaining the original fabric was observed under a stereoscopic microscope to clarify the lithology and mesoscopic structures. Finally, the surfaces of the pieces with gold coating are observed and photographed using a scanning electron microscope (SEM) to record the radiolarian assemblages in clasts and matrix.

Based on observation on mesoscopic-scale structures on the surface of slices, we clarified the crosscutting relations and the conditions under which they developed. The process is proposed for the sediments with different consolidation extent during progressive deformation of accreted sediments at shallow levels.

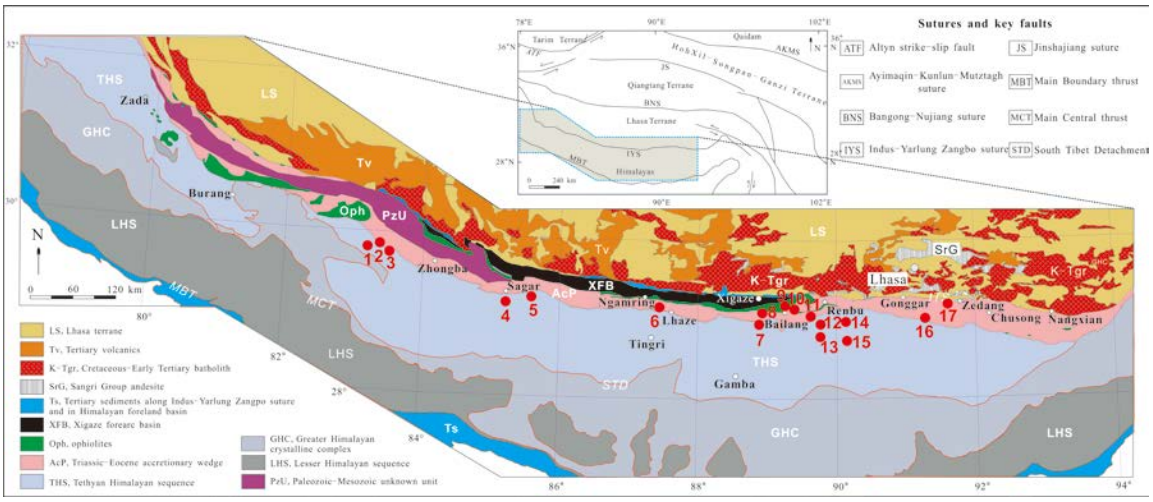

Fig. 1.1 Geological map of the Yarlung–Tsangpo suture zone

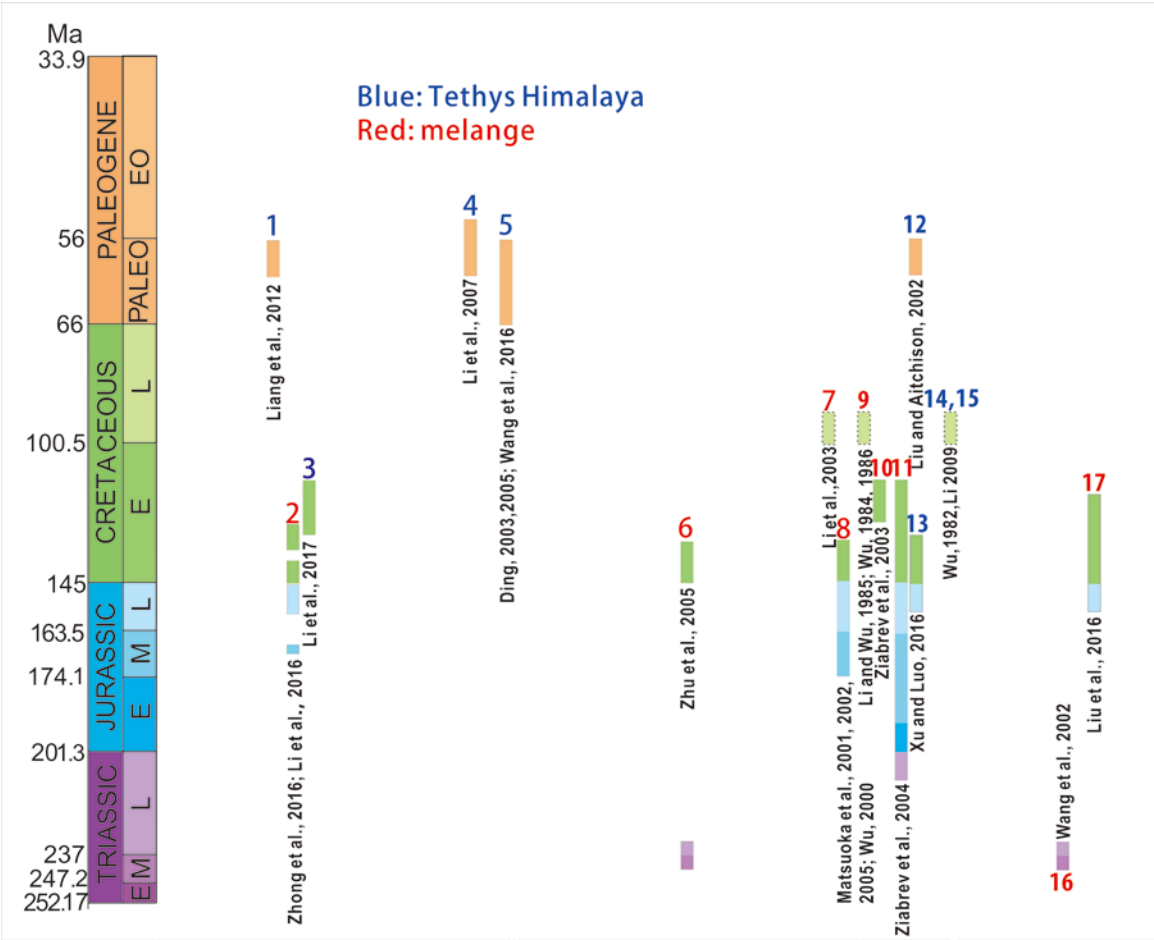

Fig. 1.2 Previous age-constraints of siliceous strata along the Yarlung–Tsangpo Suture Zone base on radiolarian assemblages. The numbers are corresponding to those in the fig. 1.1.

Chapter 2 Regional Geology

2.1 Tectonic units along the Yarlung–Tsangpo suture zone

Several terranes are exposed along the YTSZ. From north to south, important tectonic units include Lhasa terrane, Xigaze forearc basin, Yarlung–Tsangpo Suture Zone, and Tethys Himalaya.

2.1.1 Lhasa terrane

The Lhasa terrane, which rifted from Gondwana in the Triassic or the mid- to late Jurassic, drifted northward across the Tethyan ocean and collided with Eurasia along the Bangong–Nujiang suture zone, is regarded as the southernmost Eurasian continent (Audley-Charles, 1983; Yin and Harrison, 2000; Zhu et al., 2011). Based on different sedimentary cover rocks, the Lhasa terrane can be divided into three W–E trending subterranes by the Shiquan River–Nam Tso melange Zone and Luobadui–Milashan Fault, respectively (Pan et al., 2004; Zhu et al., 2011).

The southern Lhasa subterrane is characterized by widespread Cretaceous–early Paleogene Gangdese Batholiths and Linzizong volcanic succession. The central and northern subterranes are characterized by Mesozoic magmatic rocks.

Sedimentary cover in the southern subterrane is limited and mainly of Late Triassic to Cretaceous. Permo-Carboniferous metasedimentary rocks, Late Jurassic–Early Cretaceous volcano-sedimentary rocks, and Ordovician, Silurian, and Triassic limestones are distributed in the central subterrane. The sedimentary cover in the northern subterrane is mainly Jurassic–Cretaceous with minor Triassic in age.

2.1.2 Xigaze forearc basin

The Xigaze forearc basin sequence to the north of the YTSZ is located at the southern margin of the Lhasa terrane and trending east to west (Einsele et al., 1994; Wang et al., 1999, 2012). The forearc basin comprises of flysch-dominant Xigaze Group and shallow marine Cuojiangding Group, of the Albian–Coniacian and the Santonian–Ypresian respectively. The basement of the Xigaze forearc basin is regarded as the Xigaze ophiolite, which was formed before the Aptian. The basin was terminated during the middle Ypresian, when the Gyalaze Formation was deposited.

2.1.3 The Yarlung–Tsangpo Suture Zone

The YTSZ includes the ophiolite complexes, the ophiolitic melange, metamorphic and sedimentary sequences, and melanges reflecting the destruction of the Neo-Tethyan Ocean. The suture zone is located between the the Xigaze forearc basin and Luobusa conglomerate belt to the north and Tethyan Himalayan to the south. The ophiolites crop out discontinuously along the W–E-trending YTSZ and consist of disrupted ophiolitic massifs, which represent remnants of part of Neo-Tethyan ocean lithosphere. Melanges, which contain ophiolitic material, deep marine sedimentary rocks, and high-grade metamorphic rocks, are commonly underlain the ophiolites by faults (Hébert et al.,2012; Xu et al., 2015; Guilmette et al., 2008).

Spatially, the YZSZ ophiolitic belts can be divided into the eastern, central, and western segments. In the central and eastern segments, the ophiolites lie along a single lineament, whereas from the Saga ophiolite to the west (western segment), the ophiolitic belt is divided into the northern and southern belts (Pan et al., 1997; Lian et al., 2016).

2.1.3.1 The YTSZ in the eastern and the central segments

In the eastern and the central segments, important terranes according to a new nomenclature by Aitchison et al. (2000) include the Dazhuqu terrane, the Bainang terrane, and the Zedong terrane.

The Dazhuqu terrane consists of a series of serpentinized mantle peridotites, minor cumulates, gabbros, sheeted sills and dikes, pillow basalts, and marine sedimentary cover on mafic volcanic rocks. Near Zedong and Luobusa, ophiolitic rocks of Dazhuqu terrane are faulted against the Zedong terrane or thrust northwards over the Miocene conglomerates developed along the southern margin of the Lhasa terrane. In the Xigaze district, the Dazhuqu ophiolite is thrust northwards over the Xigaze forearc basin sediments. In the southern margin, the terrane is tectonically overlain by the Indian continental margin sediments of the Tethys Himalaya. They are bounded by the Miocene north-directed Renbu Zedong thrust system (Yin et al., 1999). In the Bainang district, where there is an S shaped sigmoidal bend in the Yarlung–Tsangpo suture zone, earlier contacts can be observed at south-directed thrusts that are locally truncated by strike-slip faults (Girardeau et al., 1985; Ratschbacher et al., 1994).

Zircon U–Pb age ranges from 110 to 132 Ma is attributed to the magmatic ophiolite crust (Malpas et al., 2003; Dai et al., 2013). Late Barremian–late Aptian radiolarian assemblages were reported from the marine sediments overlying the ophiolite (Ziabrev et al., 2003).

Aitchison et al. (2000) interpreted the ophiolites in the Dazhuqu terrane as having originated in a south-facing intra-oceanic subduction system and this is supported by detailed mineralogical and petrochemical studies in the Xigaze area (Hébert et al., 2000, 2001). Dai et al. (2013) proposed that ophiolites in the Dazhuqu terrane were formed in a forearc spreading setting through rapid slab rollback during subduction initiation between 130 and 120 Ma. Age and provenance of the lower Cretaceous units by U–Pb zircon geochronology, combined with the paleolatitudinal estimates, indicate that

spreading of the Xigaze ophiolite occurred in the Gangdese forearc, and formed the basement of the forearc strata (Huang et al., 2015).

Bainang terrane is bounded to the northwest by ophiolitic rocks of the Dazhuqu terrane and to the south by the Indian terrane by faults. The Bainang terrane composed of cherts, siliceous and tuffaceous mudstones, limestones, siliceous and calcareous shales. Good outcrops are located in the Donghla, Xialu, Bainang, and Zedong districts. Ziabrev et al. (2004) defined two “tracts” within the Bainang terrane. The southern tract is made of mudstone, limestone, and tuffs deposited during the Late Triassic to Bathonian time. The northern tract is made of chert deposited in an open ocean pelagic environment during Rhaetian to early Aptian and hemipelagic siliceous and tuffaceous mudstone during the late Aptian. They interpreted the northern tract of the Bainang terrane as an offscrape-related accretion after an intra-ocenic subduction which formed the ophiolite in the Dazhuqu terrane. The radiolarian biostratigraphic data indicate that the northern tract had been accreted by the end of the Aptian. While the southern tract of the Bainang terrane was accreted some time later by underplating.

2.1.3.2 The YTSZ in the western segment

In its western segment, the YTSZ is divided by the Zhada–Zhongba terrane into northern and southern branches. The northern belt, which is connected with the central (Saga, Sangsang, Jiding, and Xigaze) and eastern segment (Zedang and Luobusa), comprises highly deformed ophiolite bodies extending for more than 2000 km. The southern belt includes incomplete and mostly peridotitic massifs, which tectonically rest on Jurassic–Cretaceous accretionary prism of marine sediments (Xu et al., 2015; Lian et al., 2016; Dai et al., 2011; Li et al., 2013). The Zhada–Zhongba terrane, which lies between these two belts, is composed of Ordovician to Permian carbonate platform sediments, Triassic mixed continental shelf deposits, and Jurassic to Cretaceous passive continental margin slope sediments. As shown by detrital zircon and fossil evidence, the Zhada–Zhongba terrane has a Tethyan-Himalayan affinity (Sun and Hu, 2012).

Field geology, zircon U-Pb ages, whole-rock major and trace element compositions of mafic rocks from the Zhongba ophiolite in the western YTSZ reveal the existence of seamounts with Early Cretaceous age within the central-western segments of the YTSZ (Dai et al., 2012).

On the basis of the zircon U-Pb age of mafic intrusions, the geochemical characteristics of both mafic and ultramafic rocks, a detrital zircon study of the Zhongba terrane, and the klippen structure of ophiolitic massif in the southern belt, Lian et al. (2016) proposed that the northern and southern ophiolitic belts were developed in the same intraoceanic forearc-arc-back-arc system of the Neo-Tethyan ocean. Similar geochemical and Sr–Nd–Pb isotopic characteristics of doleritic rocks from the northern belt and the pillow basalts from the southern belt, and OIB-type rocks from other ophiolite massifs along the YZSZ suggest that their melt evolution might have been influenced by the same mantle plume within the Neo-Tethyan seaway. Zircon U–Pb dating of volcanic rocks from the northern belt of the western segment of the YZSZ in the Zhongba region reveals an igneous age of 160.5 ± 1.3 Ma, indicating a late Jurassic alkaline magmatic activity during the Neo-Tethyan evolution (He et al., 2016).

Middle Jurassic to Early Cretaceous radiolarian assemblages were reported from cherts in the melange near Zhongba (Li et al., 2013; Wei et al., 2015; Zhong et al., 2016) (Fig. 1.1).

2.1.4 Tethys Himalaya

The Tethyan Himalaya, which was accumulated on the Indian continent, consists of Mesozoic to lower Paleogene marine sequences deposited on the Indian passive continental margin. The strata have been roughly separated into two tectonic subzones by a line along the Gyirong-Kangmar Intracrustal Thrust, which was formed during the collision of the Indian and Eurasian continents.

The northern subzone of the Tethyan Himalaya (NTH) consists of sandstones, siltstones, and limestones (Liu and Einsele, 1994; Hu et al., 2008). Jurassic to lower

Paleogene strata of the northern subzone exposed in the Gyangze area are relatively well studied and divided into five formations (Liu and Einsele, 1994; Li et al., 1999; Wang et al., 2000; Liu and Aitchison, 2002; Hu et al., 2008): the Weimei Formation, Rilang Formation, Gyabula Formation, Chuangde Formation, and the overlying Zongzhuo Formation. The sedimentary strata consist of quartz sandstones, lithic sandstones, siliceous mudstones interbedded with claystones, and limestones. The strata trend NW–SE and dip to the north or south. These strata are comparable with the strata exposed in the Gyanze area and subdivided into the Weimei Formation, Rilang Formation, Duobeng Formation, Chuangde Formation, and Denggang Formation (Du et al., 2015). The latest Barremian to the Aptian radiolarian assemblage from the Duobeng Formation was reported near Zhongba County (Li et al., 2017).

The southern subzone of the Tethyan Himalaya (STH) is composed mainly of carbonate and clastic sediments (Wan et al., 2000). Well studied sections are located in the Gamba–Tingri area where the youngest shallow marine strata of the middle Eocene (Lutetian) have been reported (Wen, 1987; Willems et al., 1996; Xu, 2000).

2.2 Melanges in this study

The southern belt of the YTSZ near Zhongba is located in the south of the Yarlung–Tsangpo river. It includes incomplete and mostly peridotitic massifs and Jurassic–Cretaceous melanges of marine sediments (Xu et al., 2015; Lian et al., 2016; Dai et al., 2011; Li et al., 2013; Zhong et al., 2016). On the basis of various combinations of matrix and blocks and tectonic contacts, the melanges are divided into five units (Fig. 2.1). Units' names are given according to local toponym.

The Yisang melange consists of purple litharenite, polymictic conglomerate, and feldspar-quartz sandstone. Detrital zircons from sandstone of the Yisang melange display U–Pb age peaks at 60–80Ma, 120 Ma, 500–600Ma, 900–1200Ma, 1500Ma, and 1800Ma, similar to the Tethys Himalaya. The youngest zircon age peak is 60–80Ma. This provides a maximum age constraint for the accretion of the Yisang melange.

The Tanong melange is characterized by highly sheared siliceous mudstone matrix with blocks of chert, basalt, and limestone.

The Tanwa melange is characterized by a huge sequence of upper mantle peridotites and mafic rocks thrust north to a siliceous melange sequence. This melange is a typical ophiolitic melange.

The Erba melange is characterized by highly sheared volcanoclastic or siliceous mudstone matrix including blocks of chert, basalt, and crystalline limestone. Broken formations of tens-meters is observable in this melange.

The Maquanhe melange is located south of the Tanwa melange or the Maquanhe melange by fault. The Maquanhe melange is characterized by siliceous mudstone, chert, basalt, and limestone. This melange is characterized by grossly continuous bedding without typical matrix-in-blocks fabric.

We will introduce our research on the Tanwa melange in chapter 4. In chapter 5, studies on the Maquanhe melange and the Erba melange will be included.

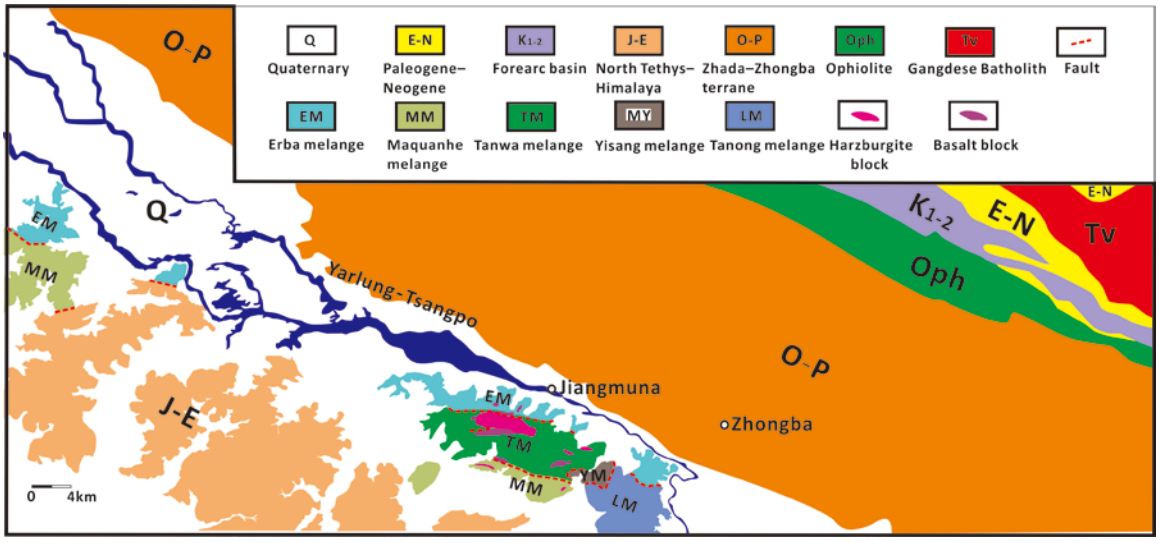

Fig. 2.1 Geological map of the southern branch of Yarlung–Tsangpo Suture Zone near Zhongba

Chapter 3 Radiolarian zonal schemes

The strata of the melanges in the YTSZ include pelagic sediments of Triassic to Cretaceous. The strata contain no other age-diagnostic fossils except radiolarians. Radiolarian biostratigraphy is applied as a key method to constrain ages of sedimentation and deformation. Identifications of species are based on recent taxomic studies of Jurassic to Early Cretaceous radiolarians (Jud, 1994; Baumgartner et al., 1995; Matsuoka, 1995; De Wever et al., 2001; O'Dogherty et al., 2009).

The zonation of Matsuoka (1995) is based primarily on radiolarian biostratigraphic data from both land sections in Japan and ocean sections in the western Pacific. This zonal scheme of Lower Jurassic to Lower Cretaceous is defined by bio-events such as evolutionary first appearance, first occurrence, and last occurrence biohorizons (Fig. 3.1).

The zonation of O'Dogherty (1994) was established based on the analyses of the vertical distribution of the taxa, which were recognized in the sections from northern Apennines (Italy) and the Betic Cordillera (Spain). The U.A. method is applied for the middle Cretaceous radiolarians and nine radiolarian biochronologic units (zones or subzones) are defined (Fig. 3.1). The biozones are tied to chronostratigraphy by means of other coexisting planktonic foraminifera or calcareous nannofossils that were studied previously by other authors.

Li et al. (2017) established zonal scheme for the Barremian to Aptain interval based on phyletic evolutions of the genus *Turbocapsula* and *Aurisaturnalis carinatus* (Foreman). The biostratigraphic data obtained from a continuous siliceous sequence on the Indian passive margin sediments in southern Tibet (Fig. 3.1).

Age assignments for the Lower Jurassic to Lower Cretaceous strata are mainly based on biostratigraphic zonation of Matsuoka (1995). Age assignments for the middle Cretaceous strata are referred to the zonal schemes of O'Dogherty (1994) and Li et al. (2017).

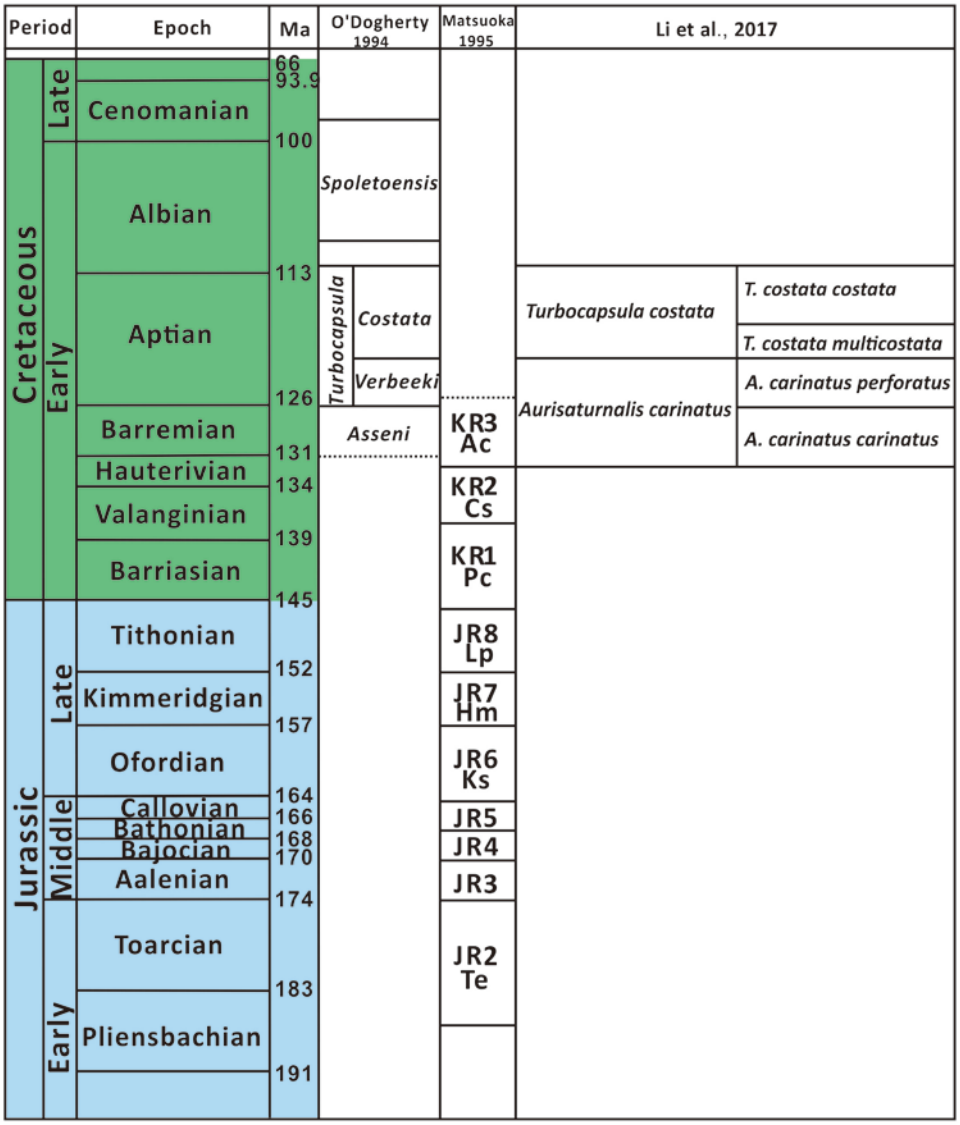

Fig. 3.1 Jurassic to Cretaceous radiolarian zonations of Matsuoka (1995), O'Dogherty (1994), and Li et al. (2017).

Chapter 4 The ophiolitic melange–Tanwa melange

4.1 Lithology and structure

The ophiolitic melange located south of the Yalung–Tsangpo river near Zhongba County. The melange includes blocks of upper mantle peridotites, mafic rocks, cherts, and limestones in a purplish-red or grayish-green siliceous shale matrix. Blocks range in size from a few centimeters to several kilometers and are commonly sheared along their boundaries against the matrix. The peridotites are relatively fresh and composed mainly of harzburgites with a small amount of dunites. The harzburgites display a well-developed, high-temperature mantle foliation. Mafic rocks comprise basaltic and andesitic pillow to massive lavas, intruded by gabbroic dikes. Pillow basalts are fine grained and commonly aphyric. Purplish-red and greenish-gray siliceous shales including blocks of radiolarian chert, limestone, and basalt commonly are overlain to the north by the pillow basalts (Figs. 4.1, 4.2). Dai et al. (2011, 2012) interpreted that the OIB-type mafic rocks suggest the existence of a series of seamounts and originated from a late-stage magmatic activity above an intra-oceanic supra-subduction zone within the Neo-Tethys during the Early Cretaceous (Ca. 126 Ma). He et al. (2016) interpreted the OIB-type mafic rocks represent the Neo-tethyan oceanic lithosphere, which were formed along a plume-proximal seafloor-spreading system. We conducted one section (Section 0804) and collected radiolarian bearing samples including siliceous mudstone, chert, and shales in the southern part of this melange (Fig. 4.2D).

4.2 Section 0804

The section is about 600 m in thickness. Foliations of the melange globally strike W–E and dip mostly toward the north. The matrix connects with blocks tectonically.

Based on the lithologies of matrix and blocks, we divided this section into 13 units. Units are connected with each other by faults (Fig. 4.3).

Unit 1 is composed of purple and green, scaly siliceous mudstone matrix with blocks of red and green chert. The siliceous mudstone matrix is overwhelming and highly sheared (Fig. 4.4A).

Unit 2 is characterized by basalt with small tens-meters blocks of chert, siliceous mudstone, and limestone. Basalt is predominant in this unit, while chert and siliceous mudstone are commonly small pieces inserted in the basalt (Fig. 4.4B).

Unit 3 is characterized by scaly siliceous mudstone matrix red or green in color. Blocks of chert, siliceous mudstone, and basalt are enveloped in the seriously sheared matrix. Meter-sized basalt blocks are concentrated in the lower part of this unit. Quartz veins perpendicular to the bedding are developed in the chert blocks. Siliceous mudstone in this unit is sheared. Isoclinally folds are recognizable in the siliceous mudstone block (0804-057), the chert block (0804-045), and the basalt block (Fig. 4.4C).

Unit 4 consists of scaly siliceous mudstone matrix which may contain volcanic clasts. Blocks of red chert or siliceous mudstone are involved in the matrix (Fig. 4.4D). One basalt layer about two meters thick (above 0804-063) is in the upper part of this unit (Fig. 4.4E).

Unit 5 is characterized by type 1 breccias. In the lower part of this unit, the breccias are tens-centimeters in thickness. In the upper part of this unit, the breccias are serious sheared with typical scaly fabric (Fig. 4.5A).

Unit 6 In the lower part of this unit, blocks of siliceous mudstone and chert are involved in the highly sheared matrix (Fig. 4.5B). In the upper part of this unit the blocks are characterized by type 1 breccias. The breccias commonly include red or green chert clasts. One isoclinally fold is recognizable in a red chert block (0804-088). Quartz veins perpendicular to the bedding are developed in this chert blocks.

Unit 7 is composed of siliceous mudstone matrix. In the lower part of this unit, blocks of siliceous mudstone and chert are involved in the matrix. In the upper part of this unit the blocks are characterized by type 1 breccias (Figs. 4.5C, D). The breccias commonly include red chert clasts.

Unit 8 is composed of green siliceous mudstone matrix. The lower part of this unit consists of type 1 breccias (Fig. 4.5E). The breccias are characterized by green clastic matrix with chert clasts. The upper part of this unit consists of siliceous mudstone matrix with blocks of chert, siliceous mudstone, and basalt. Isoclinally folds are recognizable in a red chert block (0804-112).

Unit 9 is composed of purple and green, scaly siliceous mudstone matrix with blocks of red chert and siliceous mudstone. The matrix is highly sheared. Isoclinally folds are well developed in the chert blocks (Fig. 4.5F).

Unit 10 consists of volcanic clasts and blocks of chert and siliceous mudstone. One basalt layer about five meters thick (above 0804-145) is in the upper part of this unit (Fig. 4.6A).

Unit 11 is composed of purple scaly siliceous mudstone matrix with blocks of red chert and siliceous mudstone. The matrix is highly sheared. Isoclinally folds are well developed in the chert blocks (Fig. 4.6B).

Unit 12 is characterized by the dominant of pillow basalt. Below the basalt, the limestone and chert are about 5 meters totally (Fig. 4.6C, D).

Unit 13 is composed of purple scaly siliceous mudstone matrix with blocks of chert, siliceous mudstone, basalt, limestone, and sedimentary breccias (Fig. 4.6E, F). The matrix is highly sheared.

Within this section, two different kinds of breccias are recognizable.

Type 1 breccia is clast-supported and quartz-cemented (Fig. 4.7). No jigsaw puzzle geometry can be observed. The sizes of the clasts range from 2 mm to 5 mm. The breccia includes clasts of different lithologies: red chert and green chert is predominant, a few mafic rocks are also present. They display angular to sub-angular shapes. The clasts underwent significant rotations. Clasts of different lithology, size, and extend of rounding and sphericity are gathered together randomly. The thickness of the cement zone separating two neighbour clasts is comprised between 1 and 5 mm. The average cement-to-clast ratio is 1:9.

Type 2 breccia consists of chert and claystone (Fig. 4.8G, H). The differences between the chert and claystone parts are commonly undistinguishable in hand sample. After etching by the HF, laminate formed by radiolarian skeletons and boundary between chert and claystone become obvious. The ratio of chert to claystone varies in different samples. Lightly brecciated rocks are characterized by discrete or a few millimeters dislocation by fault or shear in chert and claystone layers (Figs. 4.8C–F, 4.9). Seriously brecciated rocks are characterized by chert clasts with angular shapes scattered in the claystone (Fig. 4.8A, B). Type 2 breccia is observable in siliceous mudstone matrix only under the light microscope. Sheared siliceous-mudstone parts disrupted the radiolarian-abundant parts into boudins (Figs. 4.10–4.13).

Totally, 170 samples including chert and siliceous mudstone were collected from this section for radiolarian analyses. Lithology, preservation and age assignments are listed in Fig. 4.3.

4.3 Radiolarians and age assignments

Six different radiolarian assemblages, which is comparable with the *Loopus primitivus* (JR8) zone, the *Pseudodictyomitra carpatica* (KR1) zone, the *Cecrops septemporatus* (KR2) zone, the *Aurisaturnalis carinatus* (KR3) zone (Matsuoka, 1995; Li et al., 2017), the *Turbocapsula costata* Zone (Li et al., 2017), and the *Spoletoensis* Zone (O'Dogherty, 1994) can be obtained from this section.

Samples 0804-068, 0804-069, 0804-082, 0804-119, 0804-129, 0804-153 contains radiolarian assemblage which is comparable to the *Loopus primitivus* (JR8) zone. Samples 0804-068, 0804-069, and 0804-082 are type 1 breccias. Samples 0804-119, 0804-129, and 0804-153 are chert with high abundance of radiolarians.

Samples contain radiolarian assemblages, which can be compared with the *Pseudodictyomitra carpatica* (KR1) zone or the *Cecrops septemporatus* (KR2) zone are mainly chert blocks showing different extent of type 2 brecciation. Some chert blocks are involved in isoclinally folds.

Siliceous mudstones, which are commonly highly sheared, obtain radiolarian assemblages which are comparable with the upper part of the *Arisaturnalis carinatus* (KR3) zone (Fig. 4.15) and the *Spoletoensis* Zone (Figs. 4.16, 4.17). Type 2 brecciation is observable under light microscope (Figs. 4.11– 4.13). The felsic tuff sample (0804-025) yielded the radiolarian assemblage which is comparable to the *Spoletoensis* Zone (Fig. 4.14). Radiolarian assemblages assigned to the *Spoletoensis* Zone is characterized by the occurrence of *Pseudodictyomitra nakasekoi* Taketani, *Xitus elegans* (Squinabol), *Archaeodictyomitra chalilovi* (Aliev), *Thanarla brouweri* (Tan), *Xitus spicularius* (Aliev), *Sticomitra communis* (Squinabol), and *Rhopalosyringium mosquense* (Smirnova & Aliev) (Figs. 4.18–23).

4.4 Interpretations

4.4.1 The formation of two different types of breccias

Type 1 breccia contains a variety of clast types derived both from chert sediments and mafic rocks. The angular to sub angular clasts are randomly oriented. These indicate the breccia was formed through sedimentary process and the clasts were deposited in a proximal debris flow. No clast of terrestrial material indicates the sources are only pelagic or hemipelagic. They are interpreted to record deposition on slope-aprons that developed between a platform and the basin floor (Stow et al., 1996).

Type 2 breccia was formed in chert blocks of the Tithonian to the early Barremian and in siliceous mudstone in the Aptian to the Albian. From the clasts and matrix, we know the original strata must be abundant radiolarian bearing chert layers interbedded with rare radiolarian bearing claystone layers or mudstone layers. The breccias are interpreted to be formed by shearing and fluid overpressure during the subduction.

4.4.2 Reconstruction of the OPS

Only one type 1 breccias recorded the chert deposited in the Neo-Tethys during Middle Jurassic. The Kimmeridgian to the Barremian radiolarian bearing cherts are domiant. Chert contains radiolarian skeletons without detrital grains from a continental provenance indicating pelagic sediment environment from Middle Jurassic to Early Cretaceous. Increasing proximity to a subduction zone during plate convergence is indicated by the appearance of the siliceous mudstone. The Aptian to the Albian siliceous mudstones contain fine-grained detritus and radiolarian skeletons. They typically overlie chert sequences and represent sediments in a hemipelagic environment close to convergent margin (Matsuoka and Yao 1990; Matsuda and Isozaki 1991). Fine grained mustone and felsic tuff were deposited. The tuff is green and contains corroded quartz. The felsic tuff samples yielded the radiolarian fossils of the Aptian to the Albian age. The Aptian to the Albian tuff is interpreted that it was sourced from the Ghangdese Batholith or island arcs formed in the intraoceanic island arcs (discussed in 6.3). The change from pelagic chert to hemipelagic siliceous mudstone and felsic tuff accumulation records the initial influence of subduction zone-related sedimentation from Aptian.

4.4.3 The formation of the Tanwa melange

In our section 0804, chert blocks commonly contain abundant radiolarian skeletons. The age range of the chert in this section is from the Kimmeridgian to the Early Barremian. The size of the chert blocks ranges from several centimeters to tens meters. Type 1 and type2 brecciations are well developes in these chert blocks. Hydroplastic

shear fractures were formed when the claystone parts were still unlithified. Shear fractures are always developed near the boundary between the chert part and the claystone part (Figs. 4.8, 4.9).

Within the Kimmeridgian to Early Barremian chert blocks, isoclinally folds are well developed. Layer thickness is constant or limbs are thinner than hinges, belonging to class 1B or 1C folds according to Ramsay's classification. The extension and shortening, in the outer and inner arcs of the folds, respectively, were accommodated by the grain movement. Certain layers show slightly brecciation (Fig. 4.9). It is interpreted that the isoclinally folds were conducted when the strata were semilithified.

During the subduction of Tanwa melange, Kimmeridgian to Early Barremian and Aptian to Albian strata was deformed by dewatering, N–S compaction, and layer parallel shearing when the strata were not completely lithified.

The age of the siliceous mudstones in the Tanwa melange ranges from late Aptian to Albian. They are highly sheared matrix or thick siliceous sequence. During the subduction and accretion the siliceous mudstone worked out as a weak material. This may be caused by the low competence and unlithified condition of the siliceous mudstone. The chert blocks dispersed within the shale. The accretion of the Tanwa melange should be conducted after Albian, during the Late Cretaceous possibly.

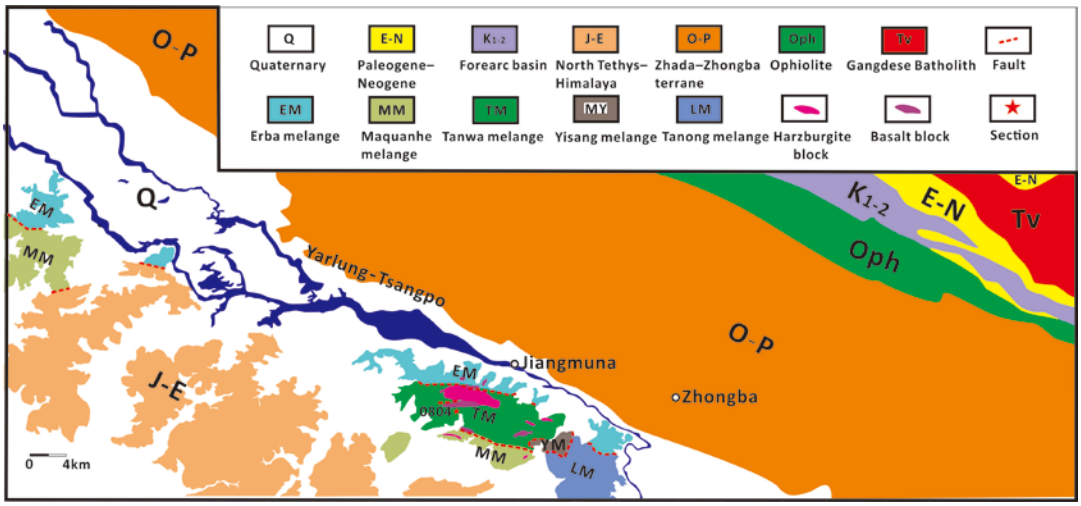

Fig. 4.1 Geological map of the Yarlung–Tsangpo Suture Zone near Zhongba and section position

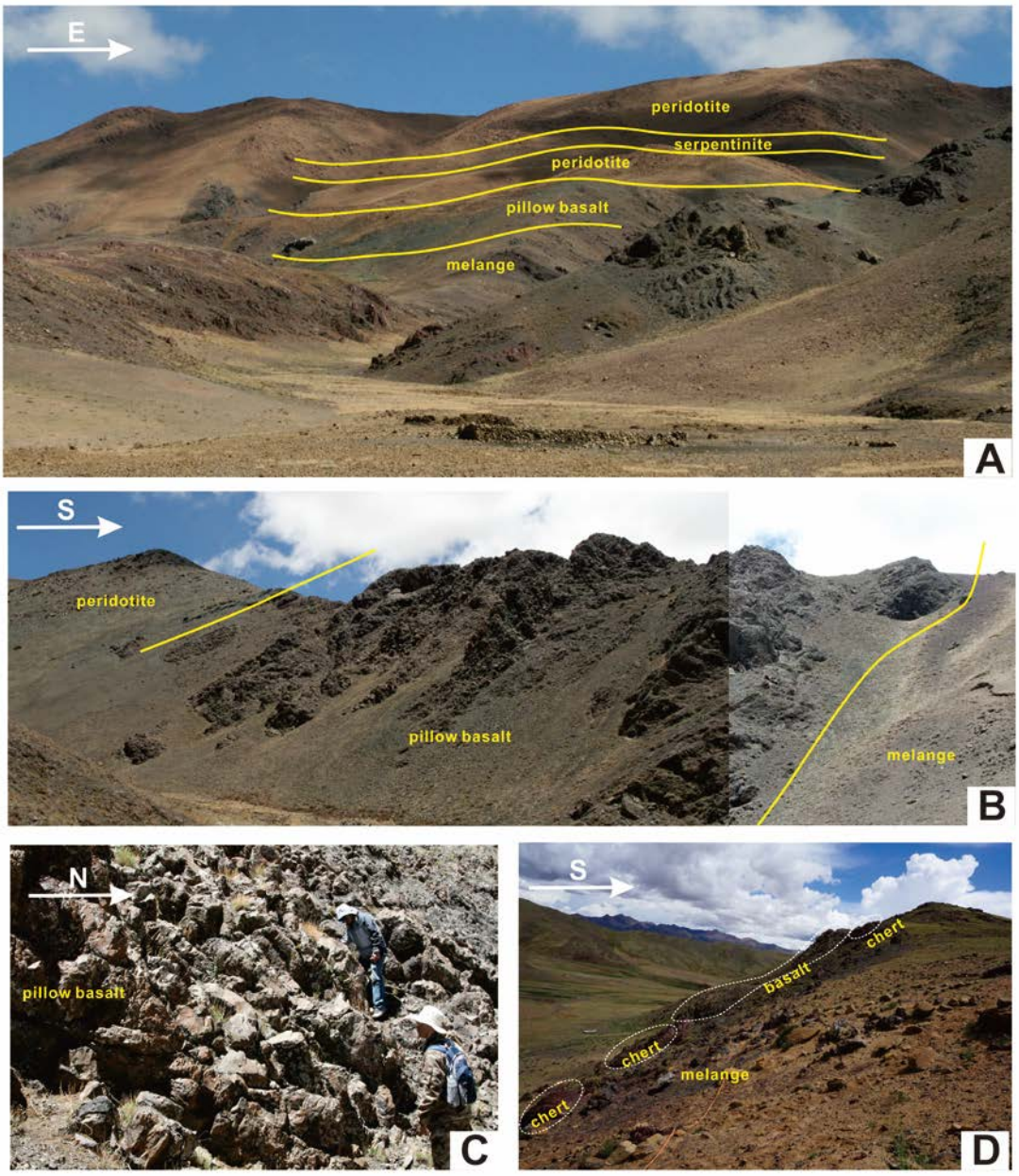

Fig. 4.2 Photographs showing outcrops of the Tanwa melange. **A:** Outcrop of Tanwa melange; **B:** Peridotites, mafic rocks, and siliceous melange and their connections; **C:** Pillow basalt north to the siliceous melange (section 0804); **D:** Melange consists of chert and basalt blocks in the highly sheared siliceous mudstone matrix.

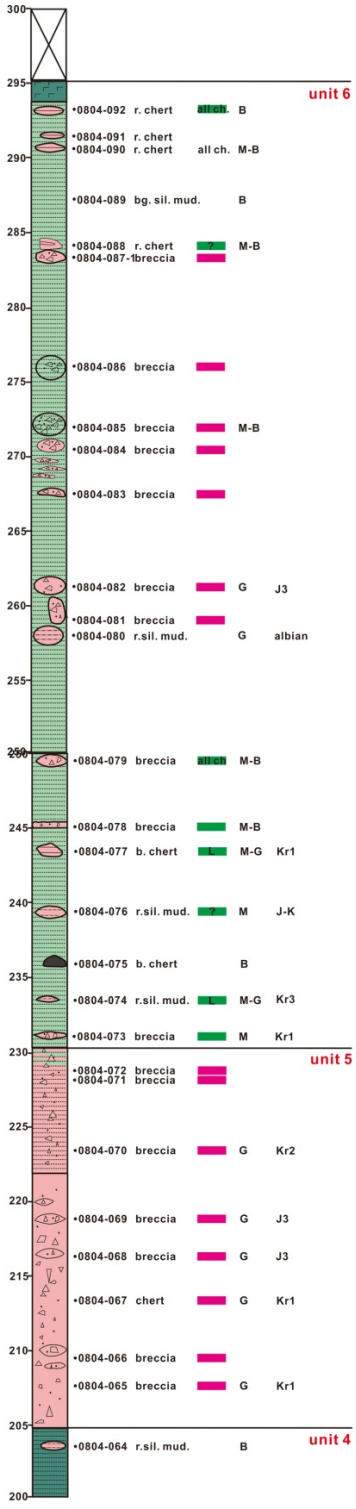
unit 6
•0804-092 r. chert all ch. B
•0804-091 r. chert
•0804-090 r. chert all ch. M-B
•0804-089 bg. sil. mud. B
•0804-088 r. chert ? M-B
•0804-087-1 breccia
•0804-086 breccia
•0804-085 breccia M-B
•0804-084 breccia
•0804-083 breccia
•0804-082 breccia G J3
•0804-081 breccia
•0804-080 r.sil. mud. G albian
•0804-079 breccia all ch M-B
•0804-078 breccia M-B
•0804-077 b. chert L M-G Kr1
•0804-076 r.sil. mud. ? M J-K
•0804-075 b. chert B
•0804-074 r.sil. mud. L M-G Kr3
•0804-073 breccia M Kr1
unit 5
•0804-072 breccia
•0804-071 breccia
•0804-070 breccia G Kr2
•0804-069 breccia G J3
•0804-068 breccia G J3
•0804-067 chert G Kr1
•0804-066 breccia
•0804-065 breccia G Kr1
unit 4
•0804-064 r.sil. mud. B
300
295
290
285
280
275
270
265
260
255
250
245
240
235
230
225
220
215
210
205
200

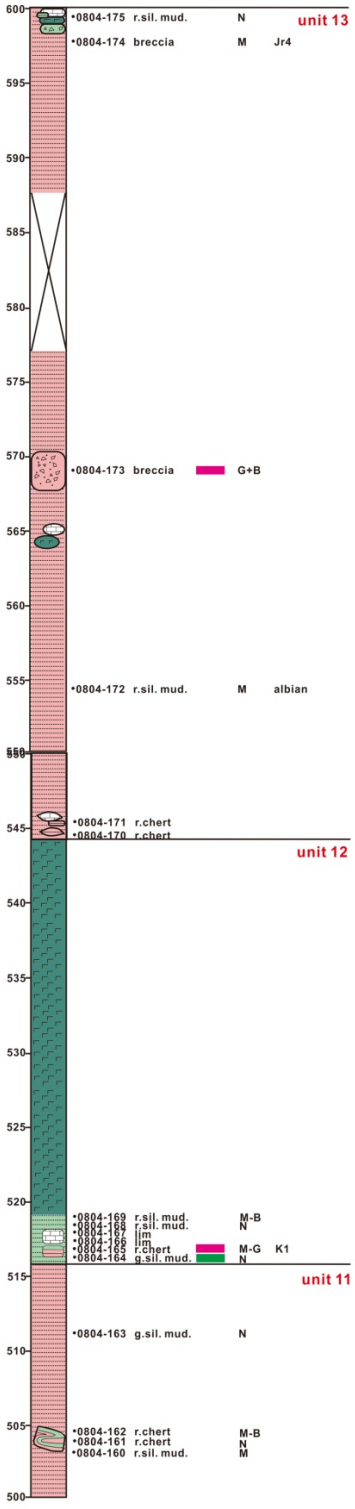
•0804-175 r.sil. mud. N unit 13
•0804-174 breccia M Jr4
•0804-173 breccia G+B
•0804-172 r.sil. mud. M albian
•0804-171 r.chert
•0804-170 r.chert
unit 12
•0804-169 r.sil. mud. M-B
•0804-168 r.sil. mud. N
•0804-167 ||m
•0804-166 ||m
•0804-165 r.chert M-G K1
•0804-164 g.sil. mud. N
unit 11
•0804-163 g.sil. mud. N
•0804-162 r.chert M-B
•0804-161 r.chert N
•0804-160 r.sil. mud. M
600
595
590
585
580
575
570
565
560
555
550
545
540
535
530
525
520
515
510
505
500

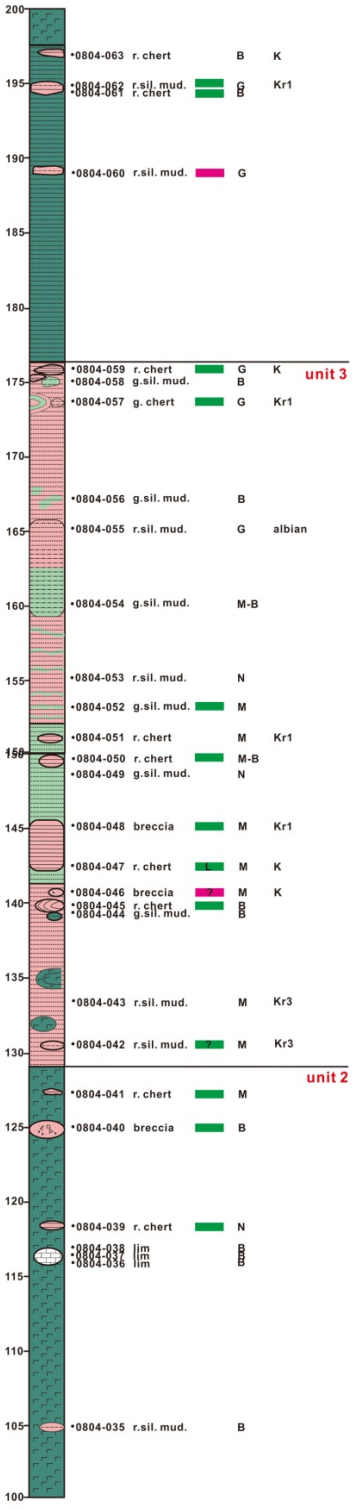
200
195
190
185
180
175
170
165
160
155
150
145
140
135
130
125
120
115
110
105
100
•0804-063 r. chert B K
•0804-062 r.sil. mud. G Kr1
•0804-061 r. chert B
•0804-060 r.sil. mud. G
•0804-059 r. chert G K
unit 3
•0804-058 g.sil. mud. B
•0804-057 g. chert G Kr1
•0804-056 g.sil. mud. B
•0804-055 r.sil. mud. G albian
•0804-054 g.sil. mud. M-B
•0804-053 r.sil. mud. N
•0804-052 g.sil. mud. M
•0804-051 r. chert M Kr1
•0804-050 r. chert M-B
•0804-049 g.sil. mud. N
•0804-048 breccia M Kr1
•0804-047 r. chert M K
•0804-046 breccia M K
•0804-045 r. chert B
•0804-044 g.sil. mud. B
•0804-043 r.sil. mud. M Kr3
•0804-042 r.sil. mud. M Kr3
unit 2
•0804-041 r. chert M
•0804-040 breccia B
•0804-039 r. chert N
•0804-038 lim B
•0804-037 lim B
•0804-036 lim B
•0804-035 r.sil. mud. B

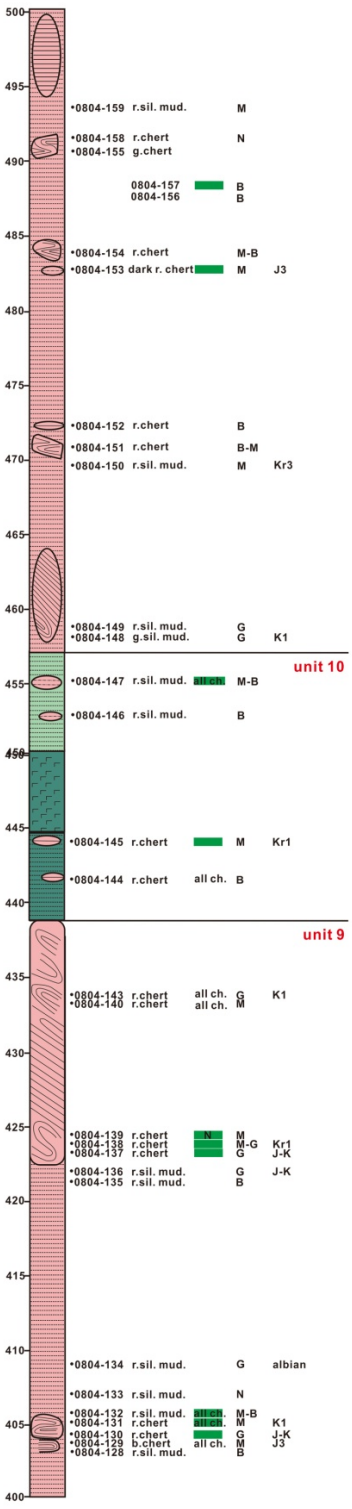
500
495
490
485
480
475
470
465
460
455
450
445
440
435
430
425
420
415
410
405
400
•0804-159 r.sil. mud. M
•0804-158 r.chert N
•0804-155 g.chert
0804-157 B
0804-156 B
•0804-154 r.chert M-B
•0804-153 dark r. chert M J3
•0804-152 r.chert B
•0804-151 r.chert B-M
•0804-150 r.sil. mud. M Kr3
•0804-149 r.sil. mud. G
•0804-148 g.sil. mud. G K1
unit 10
•0804-147 r.sil. mud. all ch. M-B
•0804-146 r.sil. mud. B
•0804-145 r.chert M Kr1
•0804-144 r.chert all ch. B
unit 9
•0804-143 r.chert all ch. G K1
•0804-140 r.chert all ch. M
•0804-139 r.chert N M
•0804-138 r.chert M-G Kr1
•0804-137 r.chert G J-K
•0804-136 r.sil. mud. G J-K
•0804-135 r.sil. mud. B
•0804-134 r.sil. mud. G albian
•0804-133 r.sil. mud. N
•0804-132 r.sil. mud. all ch. M-B
•0804-131 r.chert all ch. M K1
•0804-130 r.chert G J-K
•0804-129 b.chert all ch. M J3
•0804-128 r.sil. mud. B

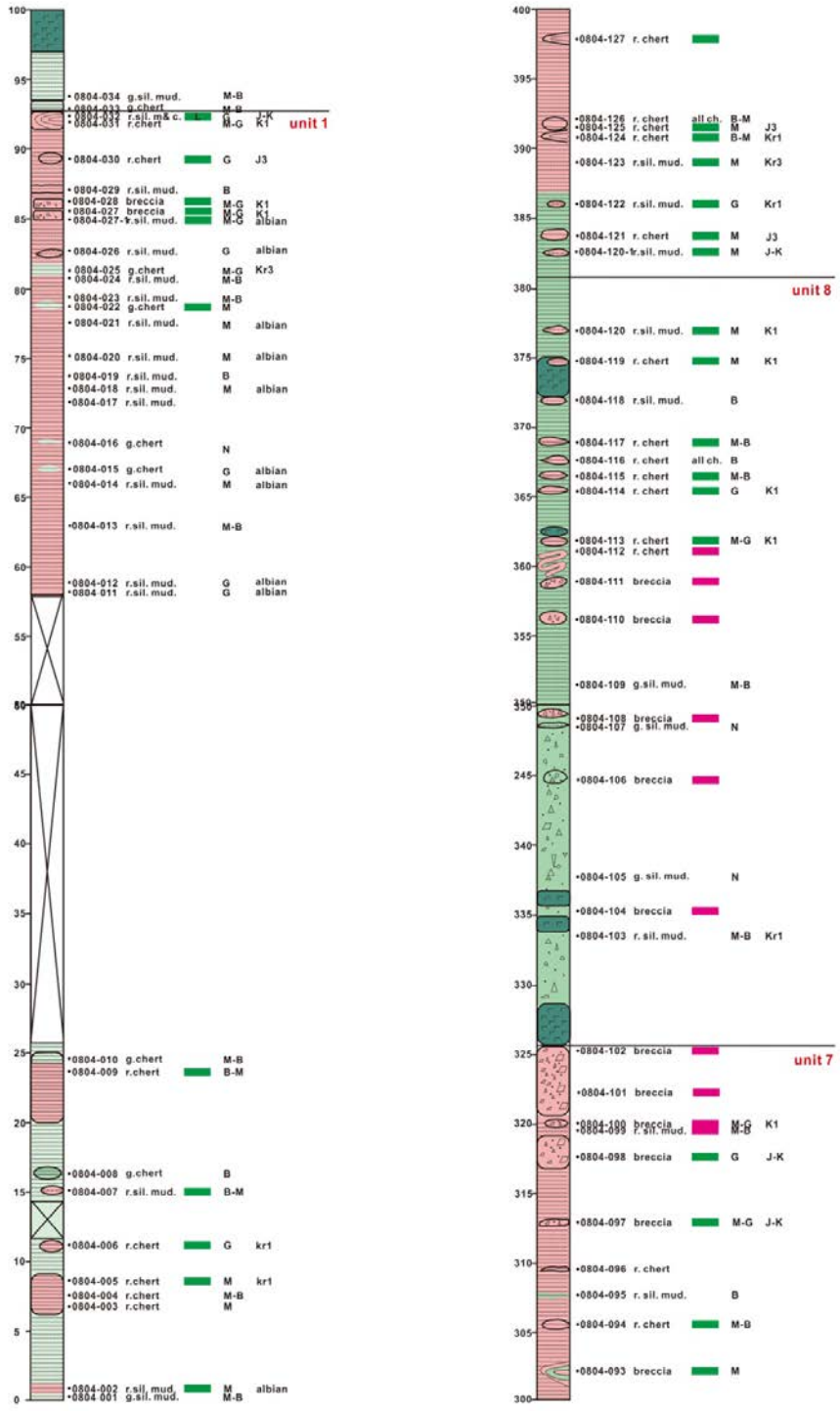

Fig. 4.3 Columar section of 0804 indicating sampling horizons, lithology, brecciation (Red bar indicates type 1 breccia. Green bar indicates type 2 breccia), preservation, and zonations of radiolarian assemblages.

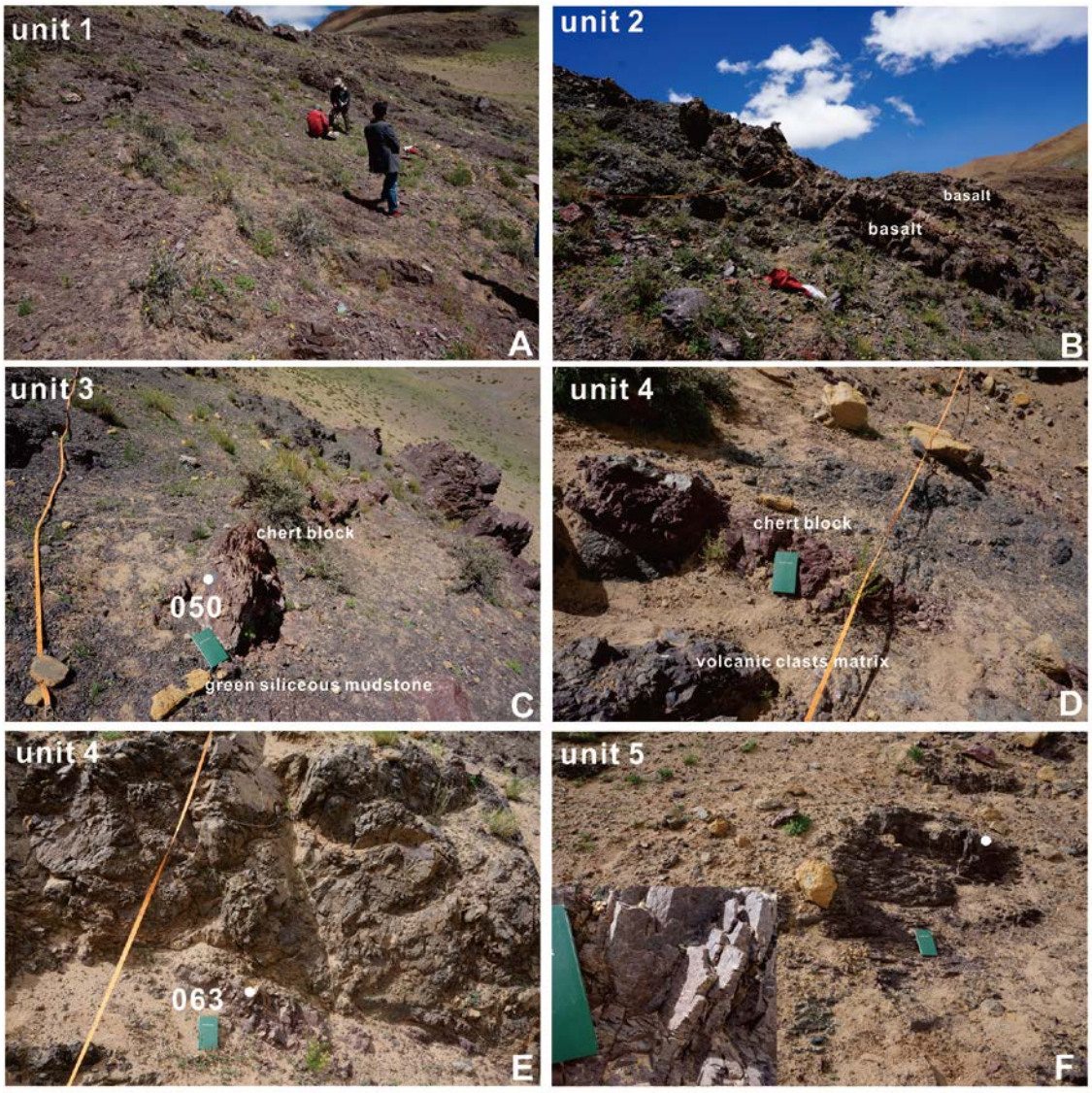

Fig. 4.4 Photographs of outcrops of section 0804. **A:** Siliceous mudstone dominant in unit 1; **B:** Basalt dominant in in unit 2; **C:** Siliceous mudstone matrix with chert blocks in unit 3; **D:** Volcanic clasts matrix with chert block in unit 4; **E:** Thick basalt in the upper part of unit 4; **F:** Type 1 breccia in the lower part of unit 5.

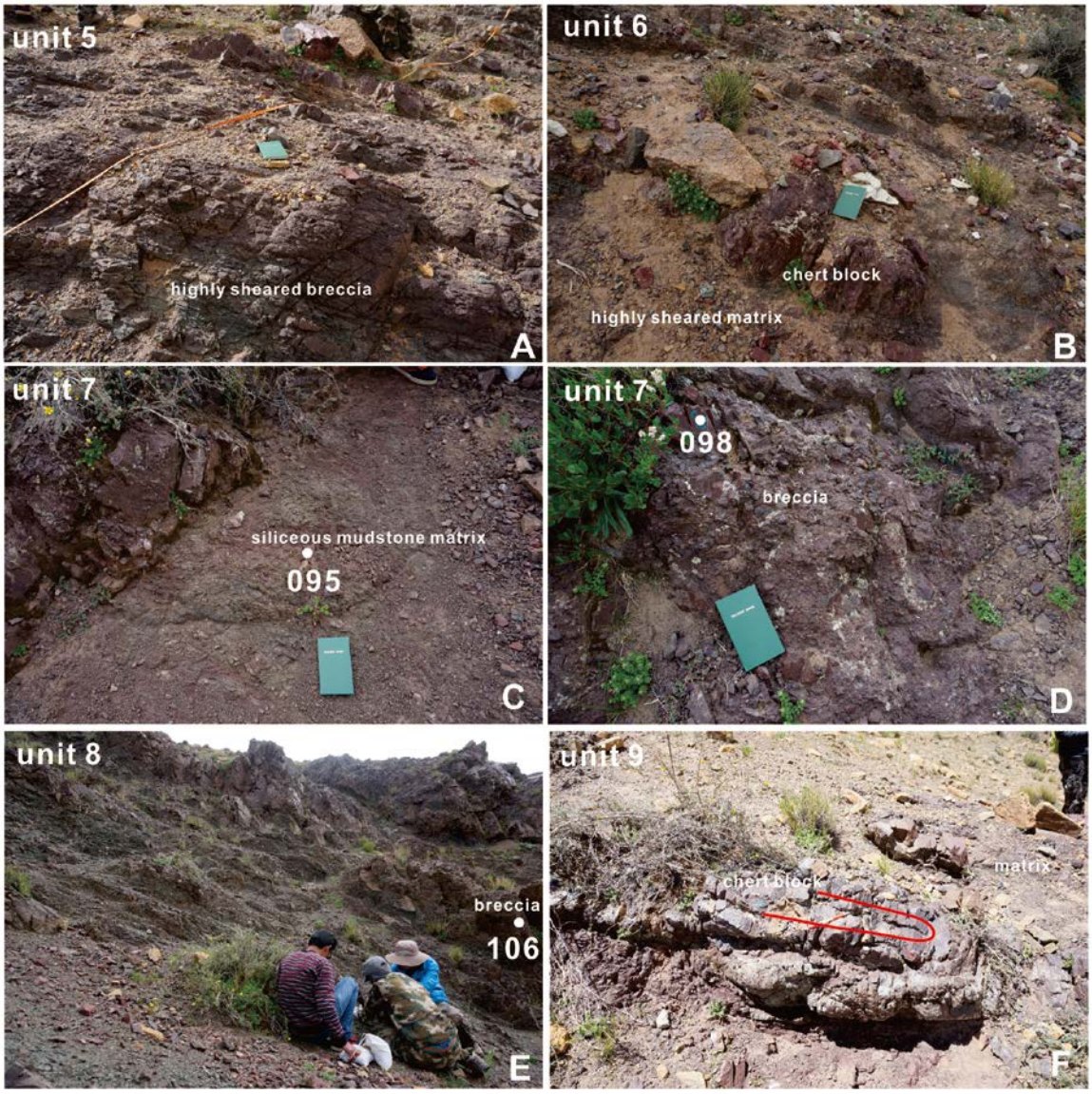

Fig. 4.5 Photographs of outcrops of section 0804. **A:** Highly sheared breccias in upper part of unit 5; **B:** Blocks of chert involved in the highly sheared matrix in unit 6; **C:** Green siliceous mudstone matrix with breccia block in unit 7; **D:** Type 1 breccia in unit 7; **E:** Highly sheared green siliceous mudstone matrix with blocks of type 1 breccias in unit 8; **F:** Scaly siliceous mudstone matrix with blocks of red chert, chert developing isoclinally folds in unit 9.

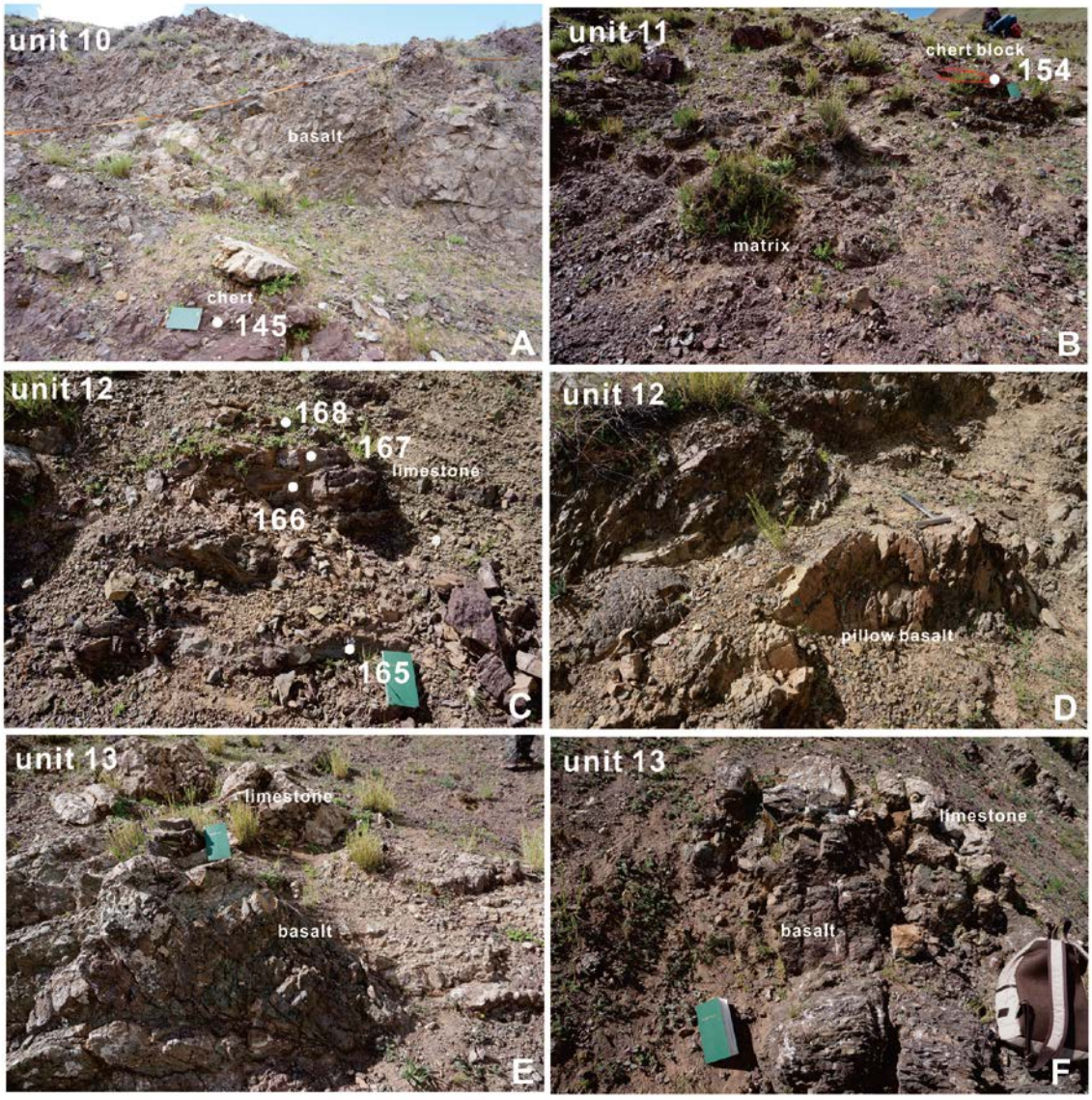

Fig. 4.6 Photographs of outcrops of section 0804. **A:** Thick basalt in the upper part of unit 10; **B:** Scaly siliceous mudstone matrix with blocks of red chert; **C:** Limestone and chert in the lower part of unit 12; **D:** Pillow basalt in the upper part of unit 12; **E:** Limestone and basalt blocks in unit 13; **F:** Limestone and basalt blocks in unit 13.

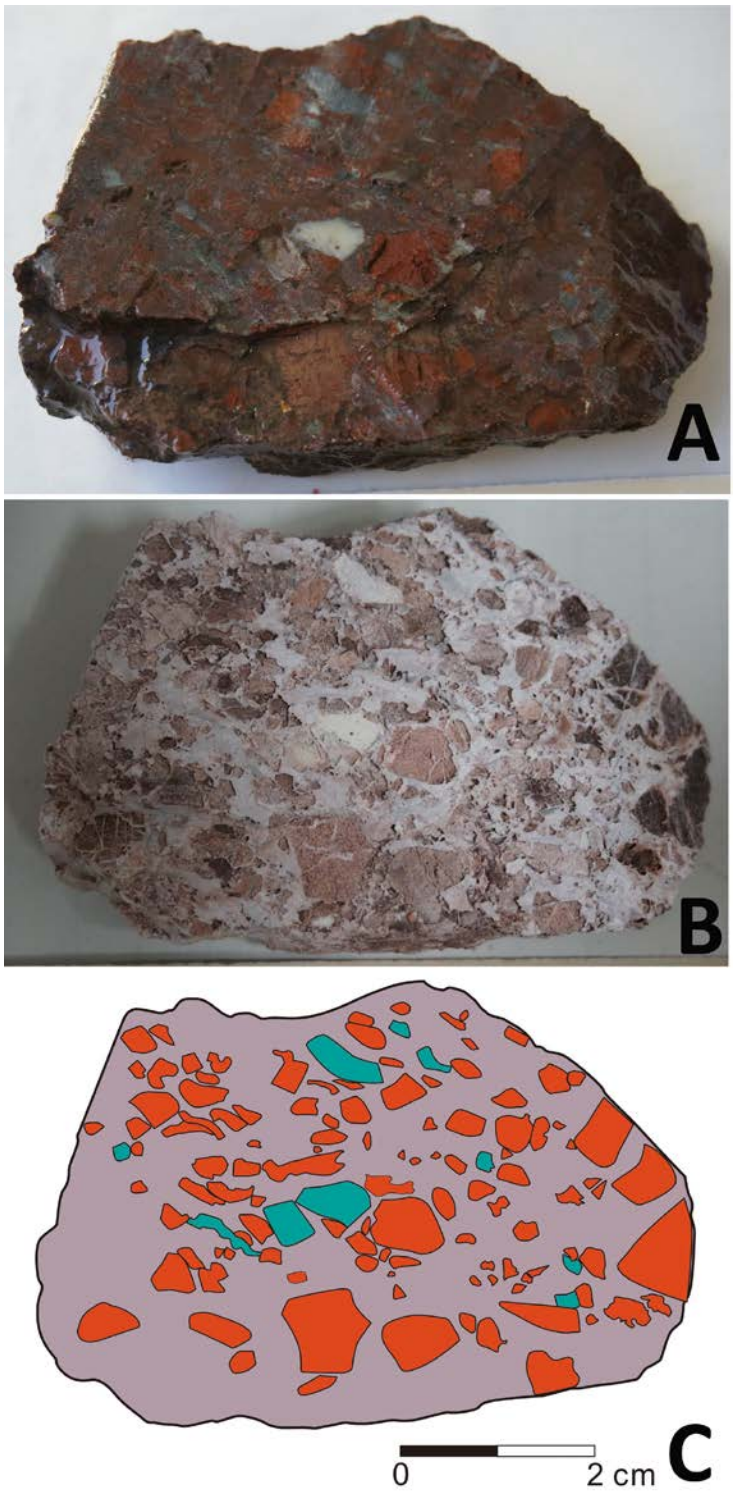

Fig. 4.7 Photographs of sample 0804-087-1 showing the type 1 breccia. **A:** The surface of the breccia; **B:** Etched surface of the breccia; **C:** Draft showing the clasts and the matrix.

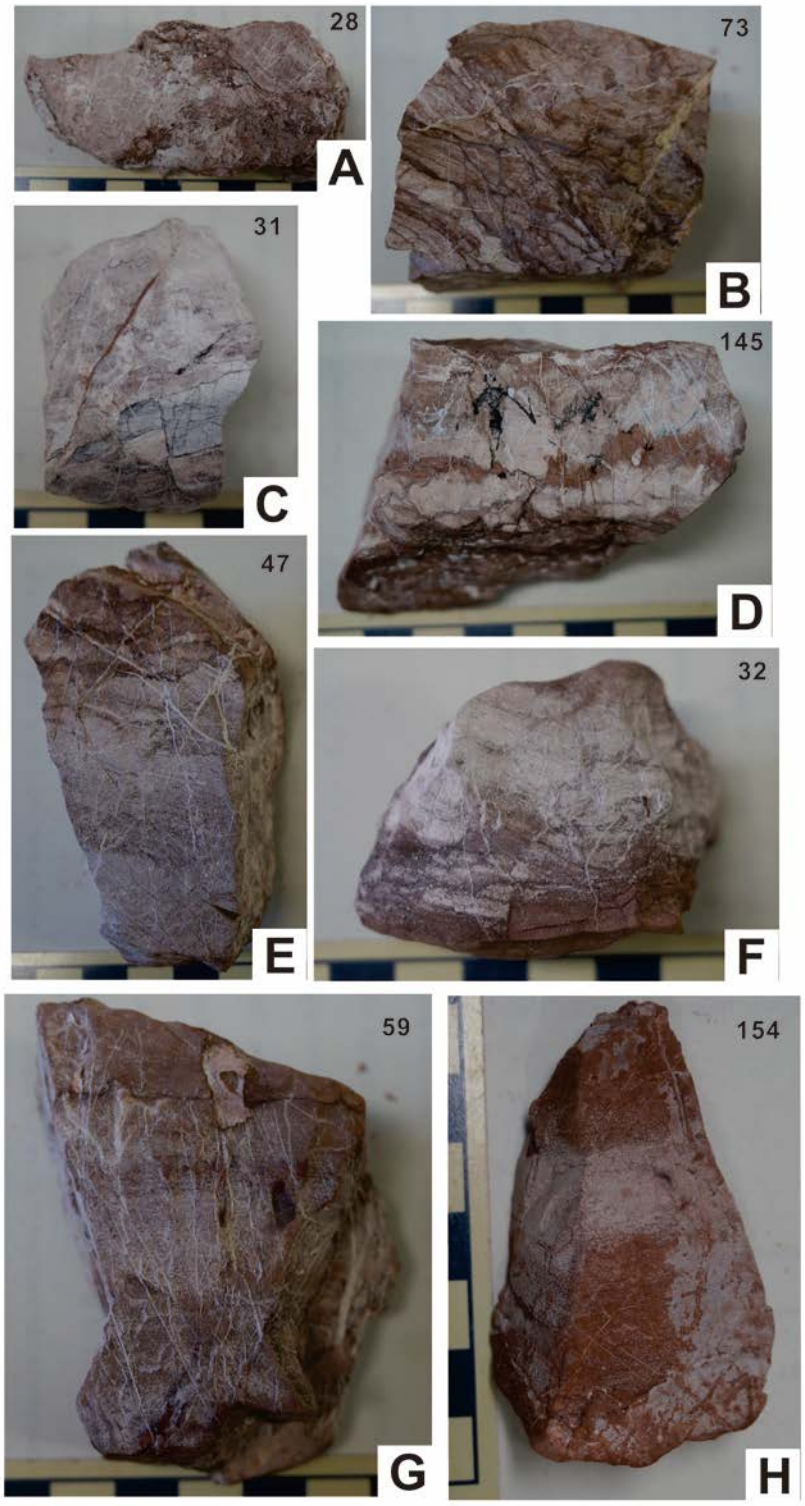

Fig. 4.8 Photographs of the etched surface of chert blocks in section 0804 showing different extents of type 2 brecciation.

Fig. 4.9 Photographs showing chert with slightly type 2 brecciation in a big chert block in section 0804.

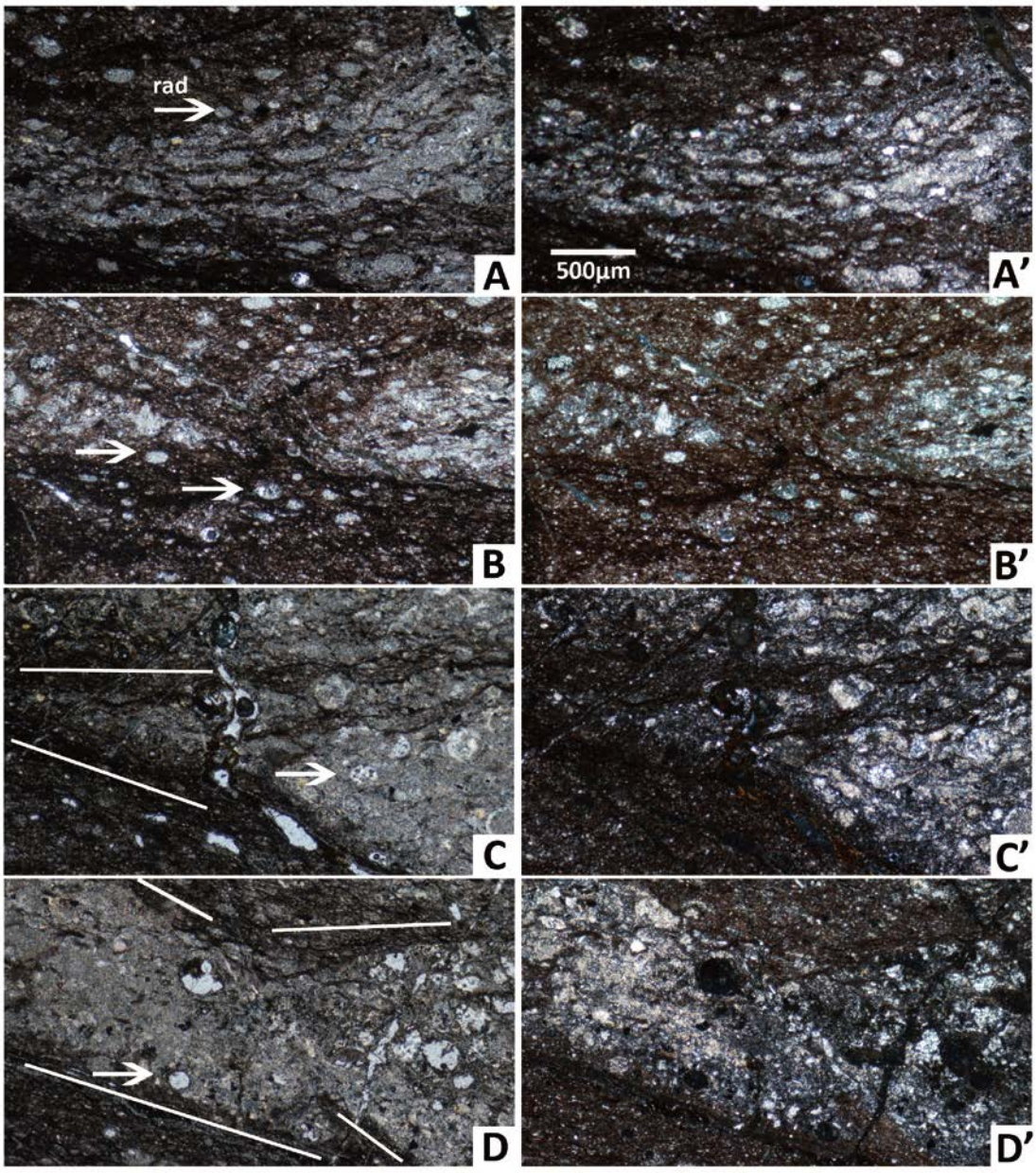

Fig. 4.10 Photographs showing microscopic texture of siliceous mudstone with type 2 brecciation in sample 0804-021-1. A, B, C, D are in plane polarized light. A', B', C', D' are in perpendicular polarized light. **A, B:** Deformed radiolarians and shear gouge between the radiolarian dominant part and the siliceous mudstone. The long axis of ellipsoidal radiolarian is parallel to shear planes. **C, D:** Rhombic chert domains surrounded by two oriented foliations which merged into each other.

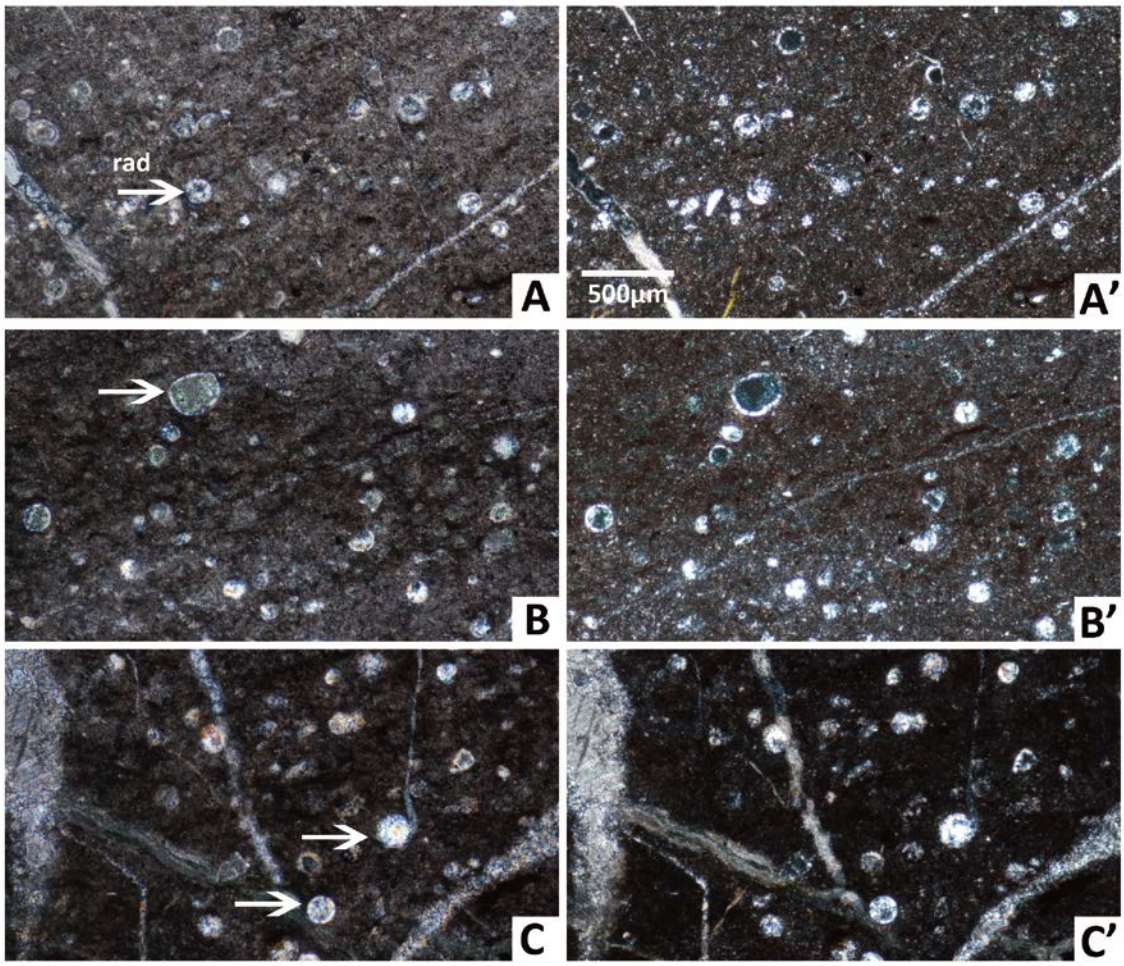

Fig. 4.11 Photographs showing siliceous mudstone (sample 0804-026). A, B, C are in plane polarized light. A', B', C' are in perpendicular polarized light.

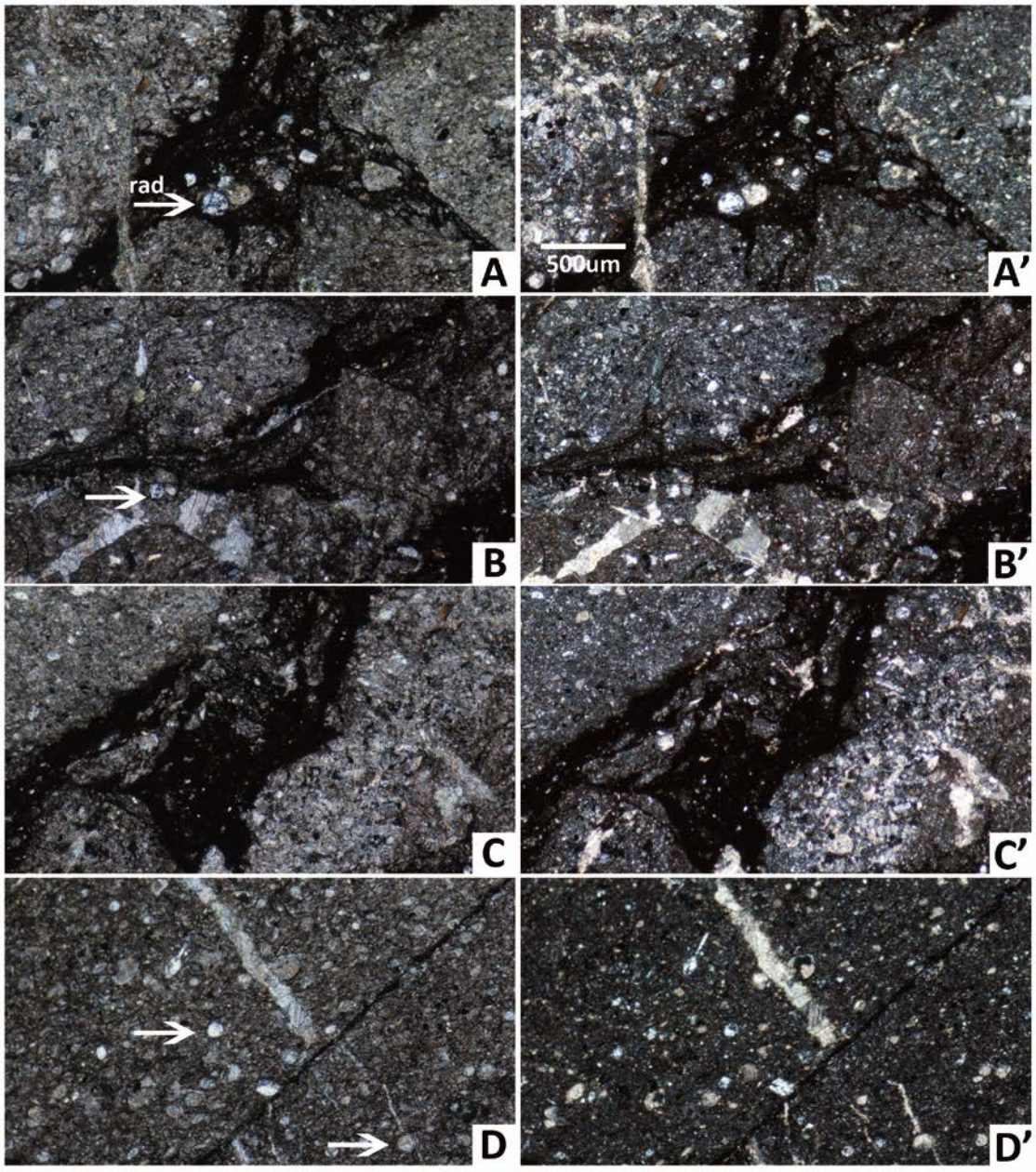

Fig. 4.12 Photographs showing siliceous mudstone with type 2 brecciation (sample 0804-055). A, B, C, D are in plane polarized light. A', B', C', D' are in perpendicular polarized light. Black shear gouges disrupted the siliceous mudstone.

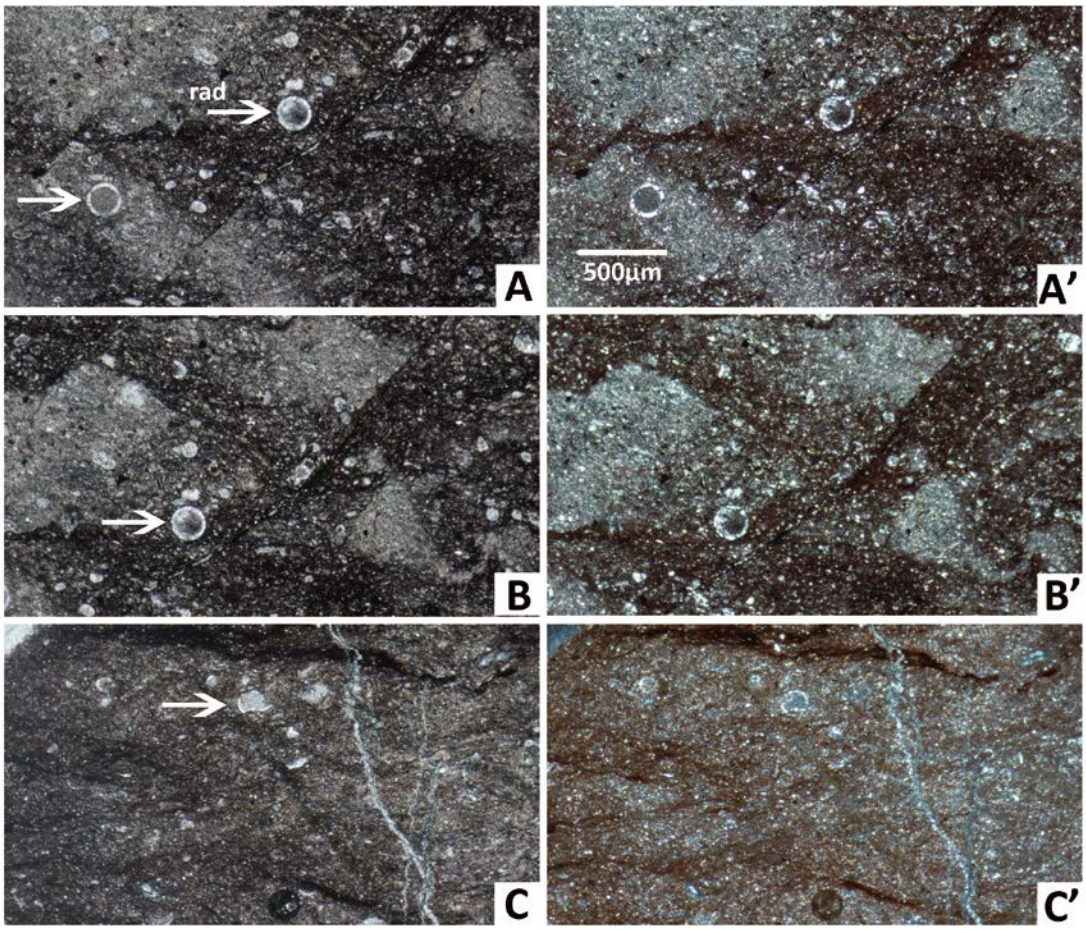

Fig. 4.13 Photographs showing siliceous mudstone with type 2 brecciation (sample 0804-080) and siliceous mudstone (Sample 0804-172). A, B, C are in plane polarized light. A', B', C' are in perpendicular polarized light. A and B are from sample 0804-080; C is from sample 0804-172.

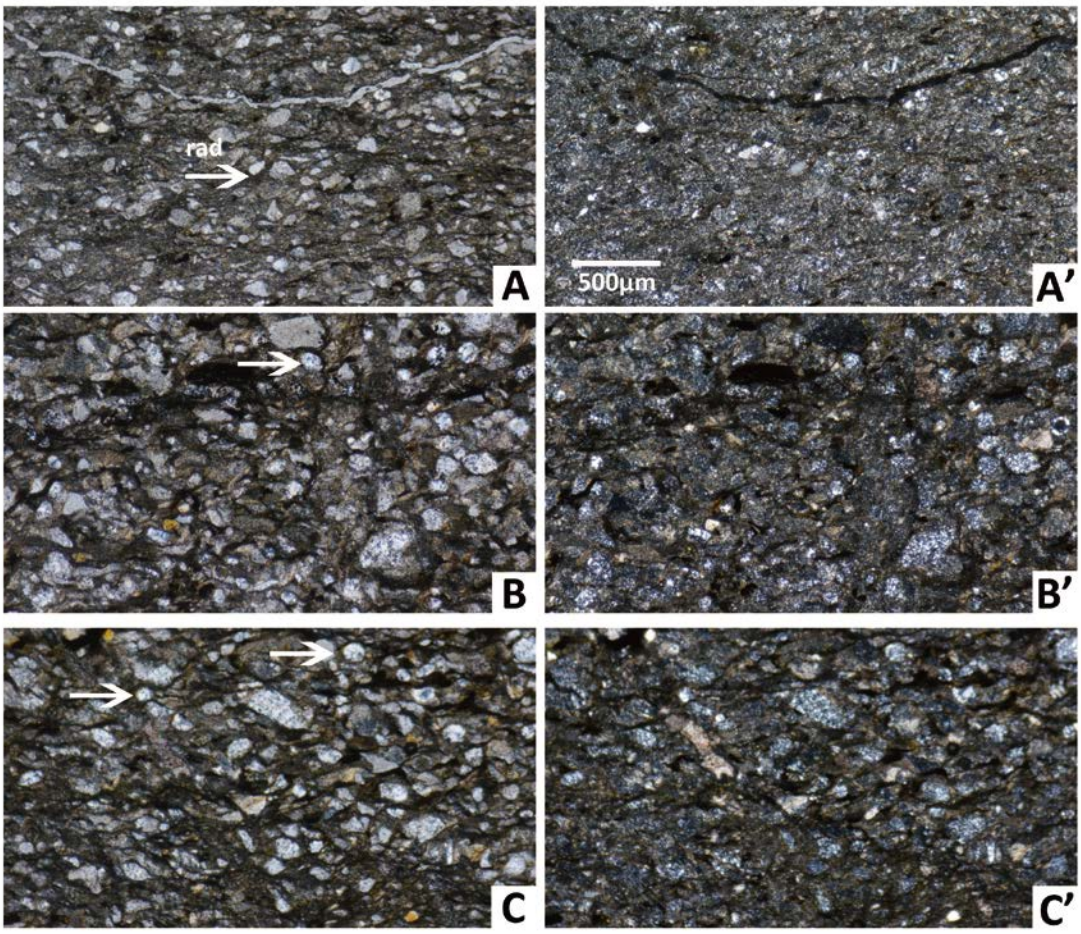

Fig. 4.14 Photographs showing tuffaceous mudstone (sample 0804-025). A, B, C are in plane polarized light. A', B', C' are in perpendicular polarized light.

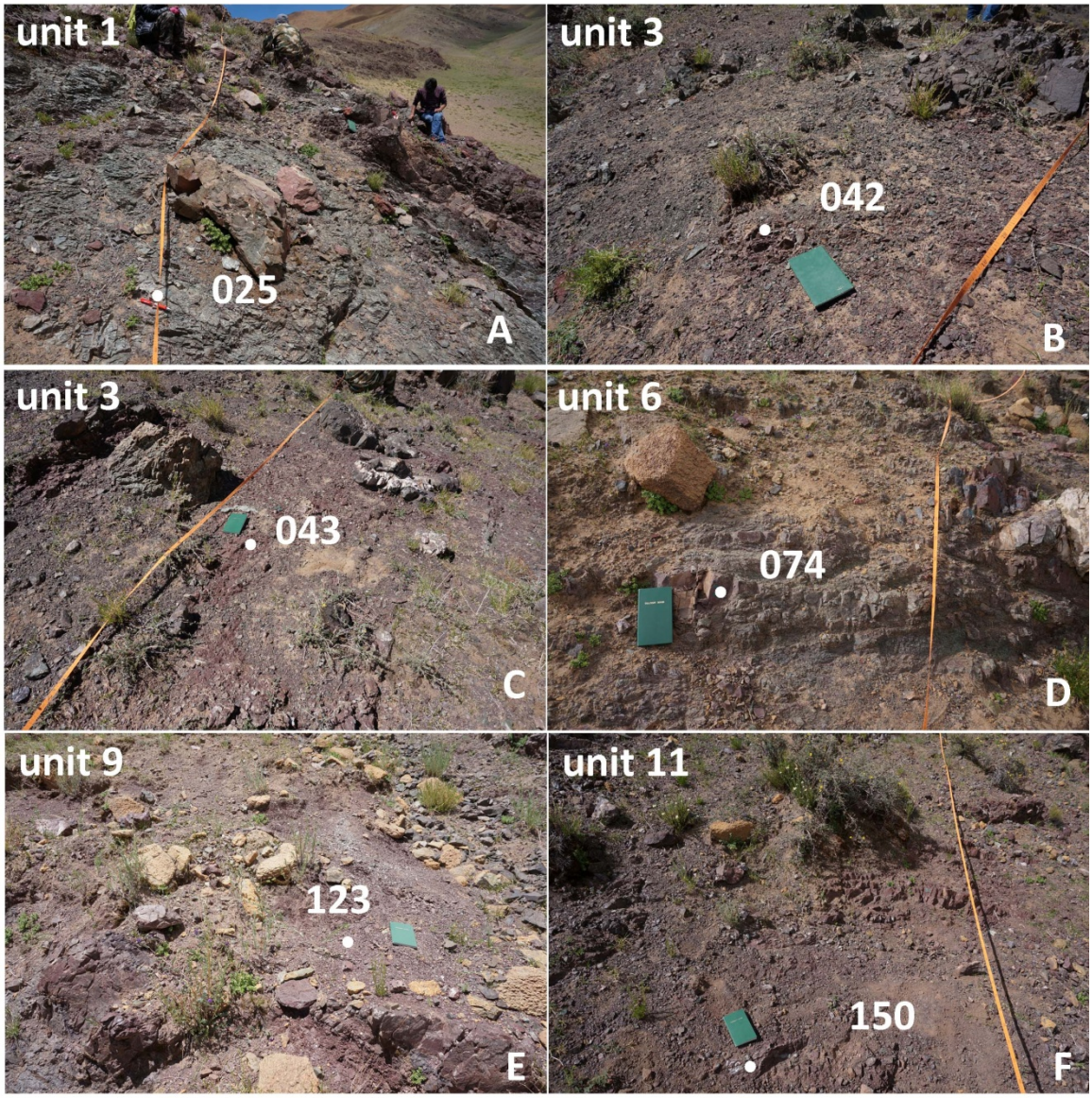

Fig. 4.15 Photographs of samples containing radiolarian assemblages that are comparable to the *Arisaturnalis carinatus* (KR3) zone (Aptian in age).

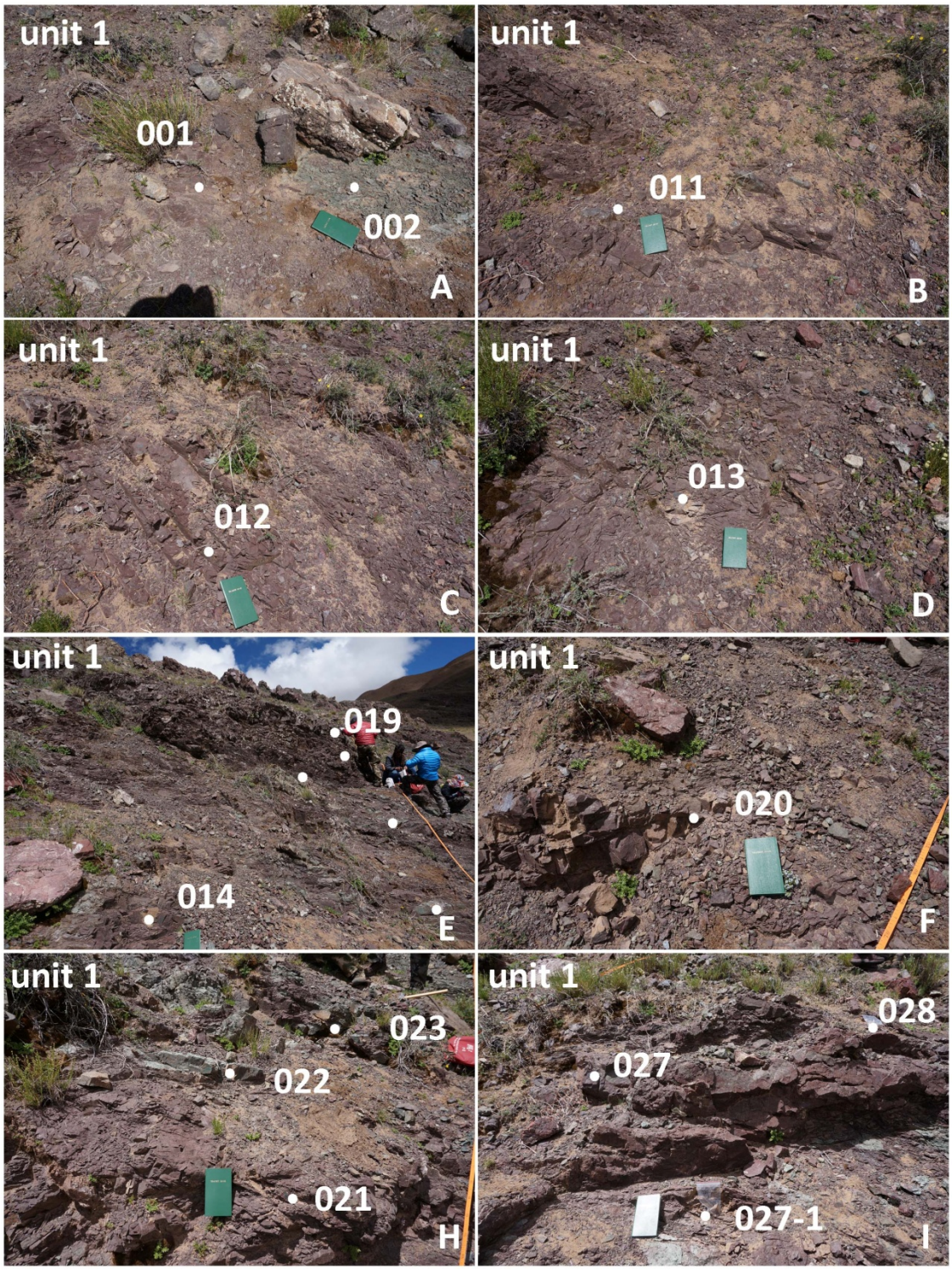

Fig. 4.16 Photographs of samples containing radiolarian assemblages that are comparable to the *Spoletoensis* Zone (Albian in age).

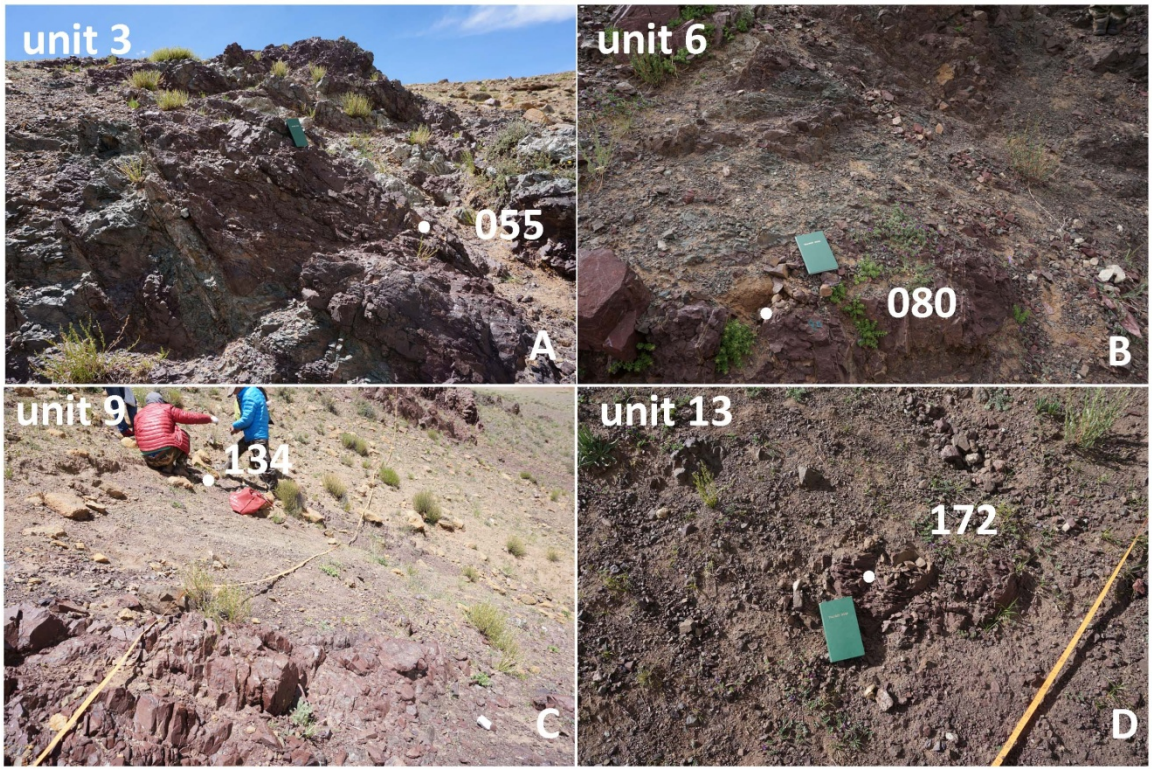

Fig. 4.17 Photographs of samples containing radiolarian assemblages that are comparable to the *Spoletoensis* Zone (Albian in age).

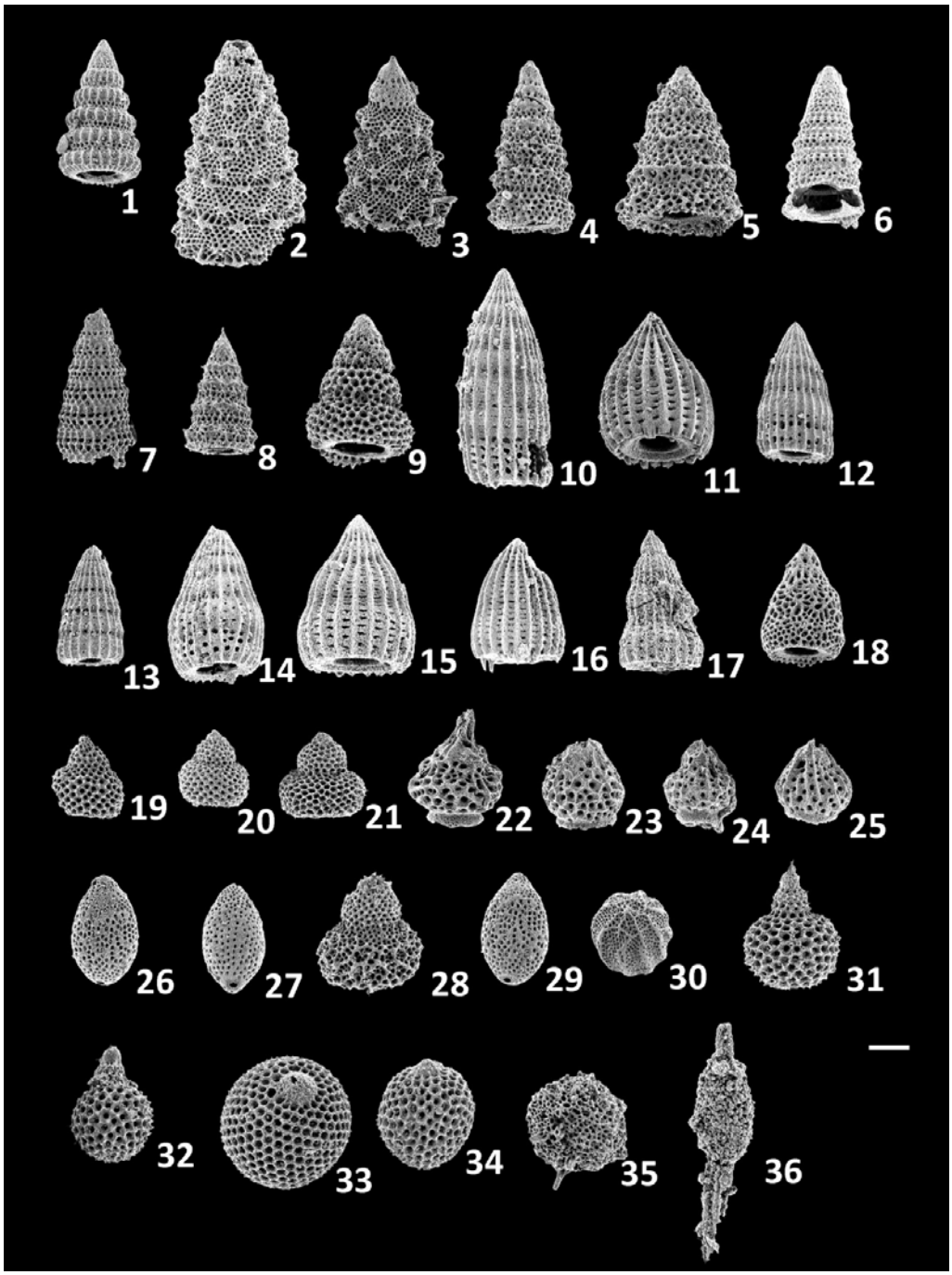

Fig. 4.18 Scanning electron micrographs of radiolarians from sample 0804-015. **1.** *Pseudodictyomitra hornatissima* (Squinabol); **2, 3.** *Xitus spicularius* (Aliev); **9.** *Sticomitra communis* (Squinabol); **10, 12, 13.** *Thanarla* sp. 11, **14–17.** *Thanarla brouweri* (Tan); **19–21.** *Rhopalosyringium*(?) sp. C in Musavu & Danelian (2006); **22–24.** *Rhopalosyringium mosquense* (Smirnova & Aliev); **25.** *Rhopalosyringium perforaculum* O'Dogherty; **26, 27, 29.** *Turbocapsula* sp. **30.** *Turbocapsula costata* (Wu); **31, 32.** *Squinabollum asseni* (Tan); **33, 34.** *Cryptamphorella conara* (Foreman); **36.** *Archaeospongoprunum cortinaensis* Pessagno

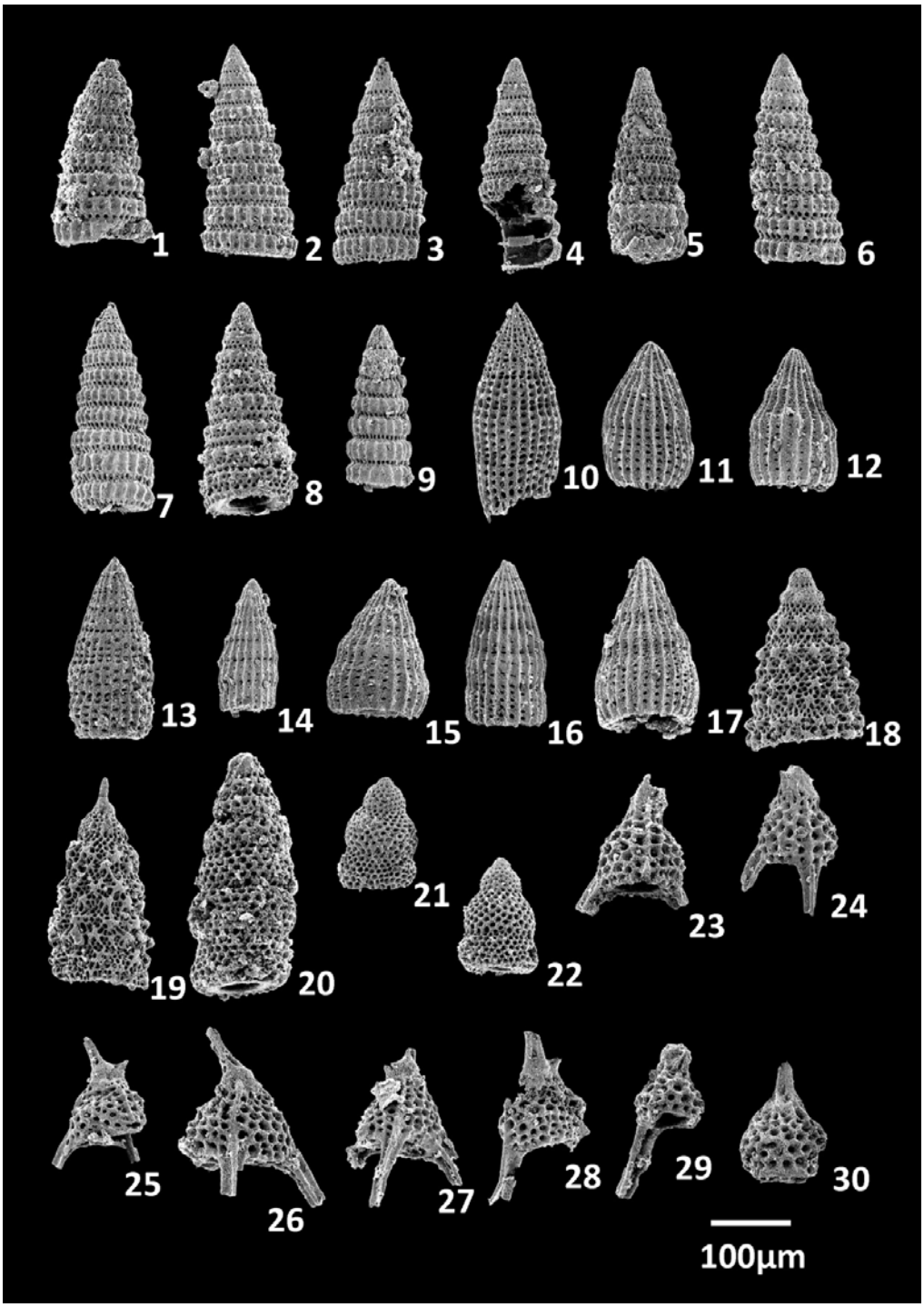

Fig. 4.19 Scanning electron micrographs of radiolarians from sample 0804-055. **1–7.** *Pseudodictyomitra nakasekoi* Taketani; **8.** *Xitus elegans* (Squinabol); **9.** *Pseudodictyomitra* sp. **10, 13.** *Archaeodictyomitra chalilovi* (Aliev); **11, 12, 15, 17.** *Thanarla brouweri* (Tan); **14, 16.** *Dictyomitra* sp. **18, 19.** *Xitus spicularius* (Aliev); **20.** *Sticomitra communis* (Squinabol); **21, 22.** *Sticomitra* sp. **23–29.** *Ultranapora* sp. **30.** *Rhopalosyringium mosquense* (Smirnova & Aliev)

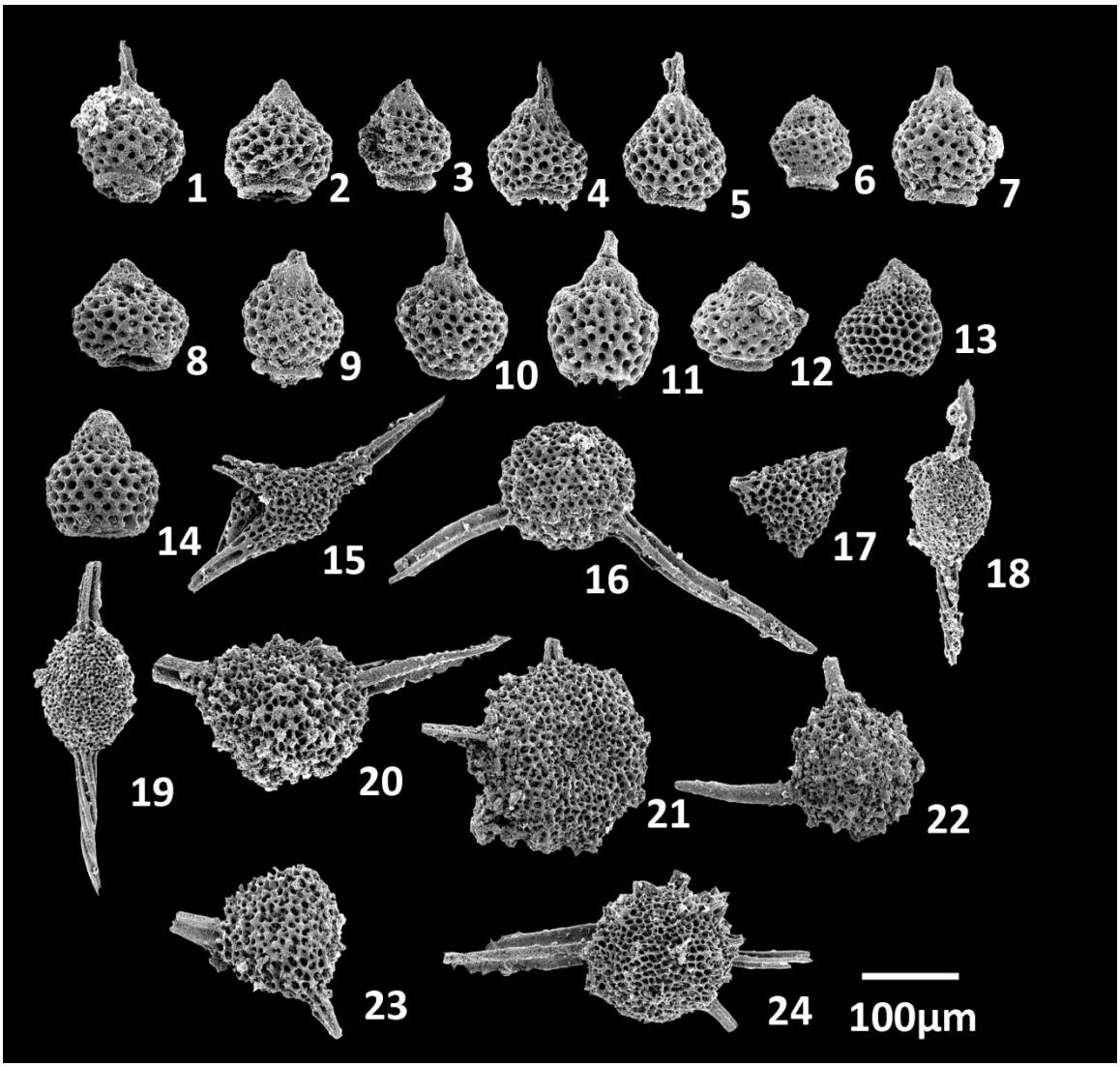

Fig. 4.20 Scanning electron micrographs of radiolarians from sample 0804-055. **1–12.** *Rhopalosyringium mosquense* (Smirnova & Aliev); **13, 14.** *Rhopalosyringium*(?) sp. C in Musavu & Danelian (2006); **15.** *Crucella* sp. **16.** *Triactoma* sp. **17, 20, 23.** *Alievium* sp. **18, 19.** *Archaeospongoprunum cortinaensis* Pessagno; **21.** *Patellula* sp. **22, 24.** *Dactyliodiscus* sp.

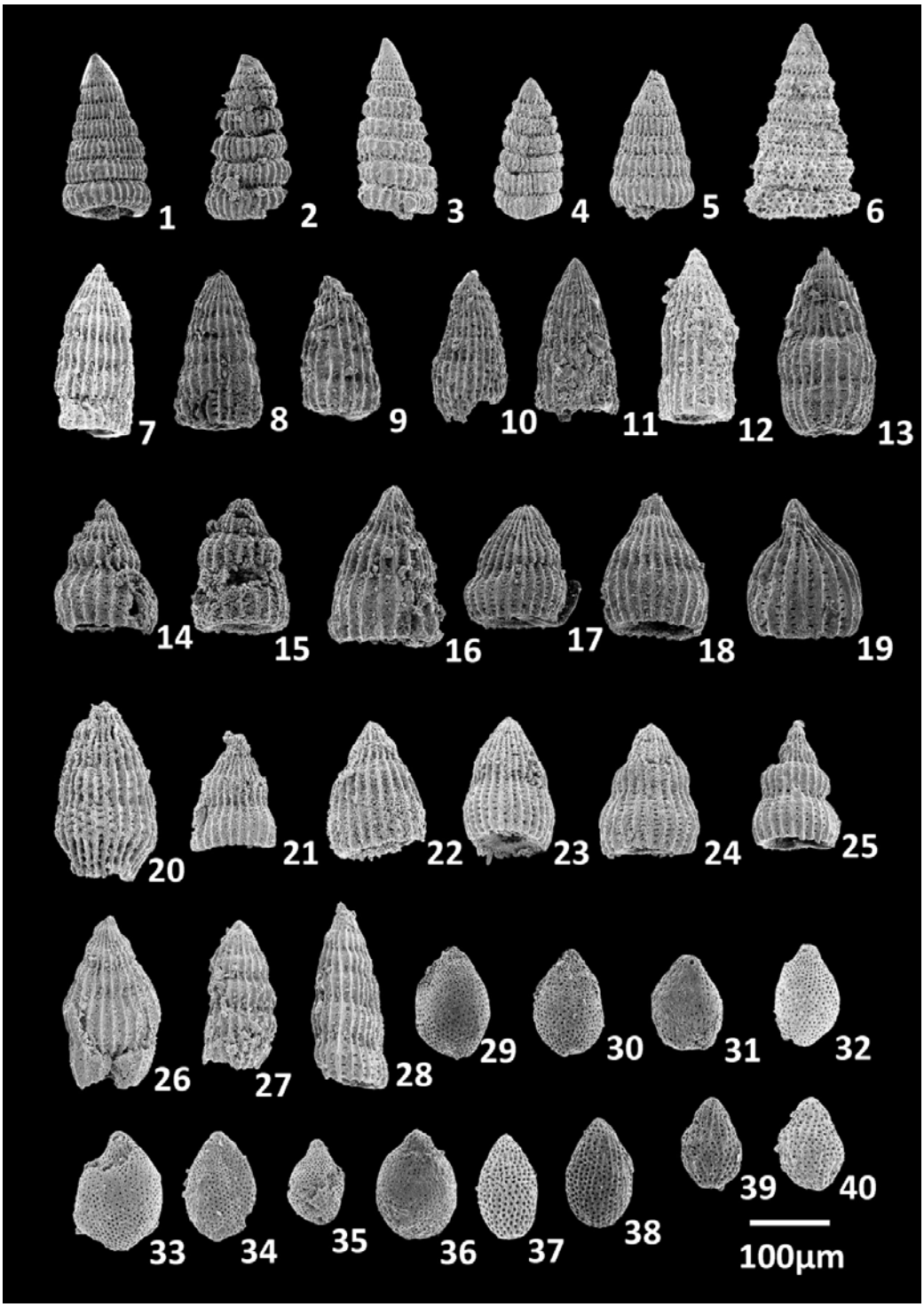

Fig. 4.21 Scanning electron micrographs of radiolarians from sample 0804-080. **1–5.** *Pseudodictyomitra lodogaensis* Pessagno; **6.** *Xitus elegans* (Squinabol); **7–13, 27, 28.** *Dictyomitra communis* (Squinabol); **14–23.** *Thanarla brouweri* (Tan); **24–26.** *Thanarla* sp. **29–37.** *Turbocapsula fugitiva* O'Dogherty; **38–40.** *Turbocapsula* sp.

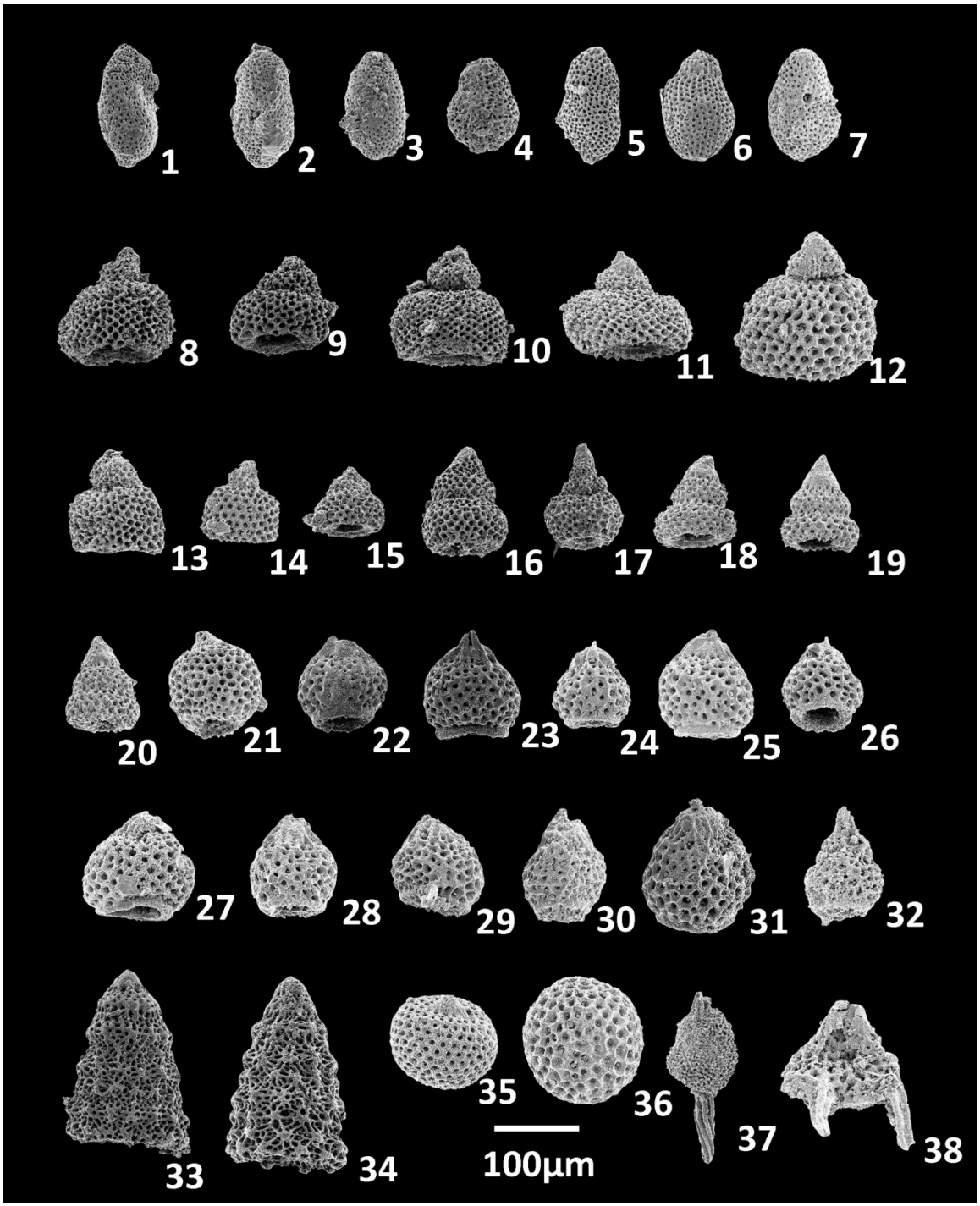

Fig. 4.22 Scanning electron micrographs of radiolarians from sample 0804-080. **1–6.** *Diacanthocapsa* sp. **7.** *Diacanthocapsa betica* O'Dogherty; **8–15.** *Rhopalosyringium*(?) sp. C in Musavu & Danelian (2006); **16–20.** *Stichomitra* sp. **21.** *Rhopalosyringium perforaculum* O'Dogherty; **22–32.** *Rhopalosyringium mosquense* (Smirnova & Aliev); **33, 34.** *Xitus* sp. **35, 36; 37.** *Archaeospongoprunum* sp. **38.** *Ultranapora* sp.

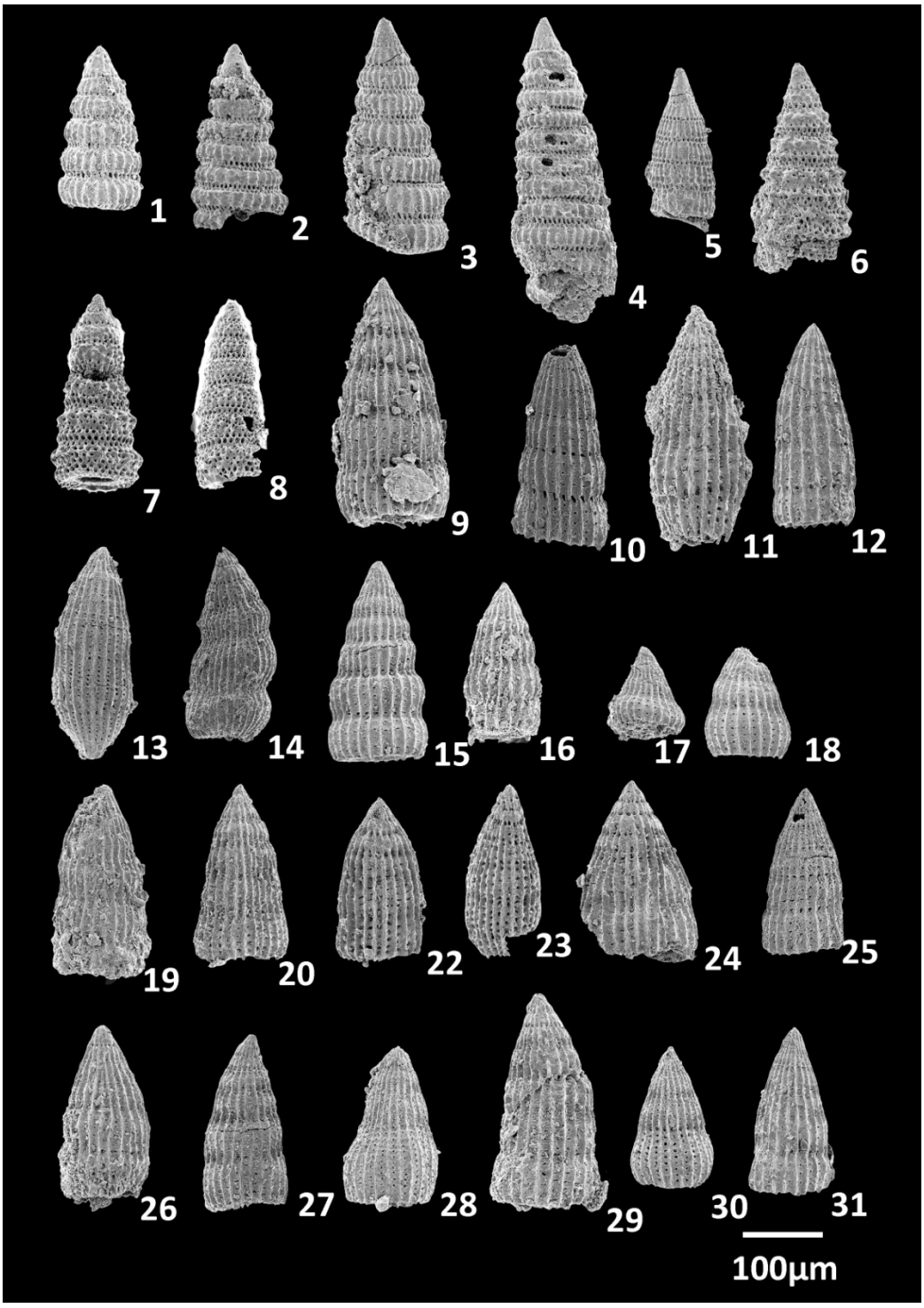

Fig. 4.23 Scanning electron micrographs of radiolarians from sample 0804-134. **1–4.** *Pseudodictyomitra paronai* (Aliev); **5.** *Pseudodictyomitra* sp. **6.** *Xitus elegans* (Squinabol); **7, 8.** *Xitus* sp. **9–12.** *Dictyomitra montisserei* (Squinabol); **13–31.** *Thanarla* sp.

Chapter 5 The volcanic-sedimentary melanges

The volcanic-sedimentary strata near Najiu County are located to the south of Yarlung–Tsangpo River. The melanges can be divided into two WN–ES trending units: the northern unit (Erba melange) and southern unit (Maquanhe melange). There is a big fault between these two units (Figs. 5.1, 5.2A).

The Erba melange is characterized by highly sheared siliceous mudstone including blocks of chert, siliceous mudstone, and basalt (Fig. 5.2B). Broken formations of chert sequences tens-meters in thickness are observable. We conducted three sections in this melange: section 0808-1, section 0808-2, and section SB (from north to south).

The Maquanhe melange comprises thrust-imbricated successions of basic extrusive igneous rocks, pillow basalt intercalated with radiolarian cherts and minor pelagic carbonates (Fig. 5.2C).

5.1 Erba melange

5.1.1 Section 0808-1

This section is a chert sequence of 40 m thick, which is disrupted by faults. Isoclinally folds and Chevron (planar limbs meet at discrete hinge point) are well developed. The bedding extends W–E and dips to the north. Totally, 20 samples were collected from this section. Cherts contain abundant radiolarians. The radiolarian fossils in this section are usually moderately to bad preserved (Fig. 5.3). Radiolarian assemblages from samples 0808-005, 0808-015, and 0808-016 can be compared with the *Pseudodictyomitra carpatica* (KR1) zone, Tithonian to Berriasian in age.

Radiolarian assemblage from sample 0808-016 is characterized by the occurrence of *Pseudodictyomitra carpatica* (Loziniyak), *Pseudodictyomitra nuda* (Schaaf), *Svinitzium depressum* (Baumgartner), *Svinitzium pseudopuga* Dumitrica, *Xitus* sp., *Tethysetta*

boessi (Parona), *Cinguloturris cylindra* Kemkin et Rudenko, *Archaeodictyomitra apiarium* Rüst, *Archaeodictyomitra* sp., *Mictyoditra lacrimula* (Foreman), *Hiscocapsa* sp. aff. *H. kaminogoensis* (Aita), *Sethocapsa* sp., *Cryptamphorella conara* (Foreman), *Neorelumbra kiesslingi* Dumitrica, *Pantanellium squinaboli* (Tan), *Alievium* sp (Fig. 5.4).

5.1.2 Section 0808-2

5.1.2.1 Lithology

This section consists of highly sheared red siliceous mudstone matrix with blocks of chert, claystone, and type 2 breccias (Fig. 5.5). The foliations of the siliceous mudstone extend W–E and dip to the north. Blocks are thin (3 cm) to thick (50 cm) bedded siliceous sequences of 1 m extend tens meters long. The extending direction is parallel to the foliation. Small blocks, less than 1 m in thickness and length, are also observable. The top of this section is composed of fine-grained tuffaceous siltstone.

5.1.2.2 Radiolarian assemblages and age assignments

Sample 0808-027 consists of chert and claystone, the ratio of chert to claystone is 1:9. After HF, the laminations in the chert are obvious. The boundary between the chert and claystone is slightly brecciated. Radiolarians from this sample are abundant and well preserved. Radiolarian assemblage (Fig. 5.6) from this sample is characterized by the occurrence of *Pseudodictyomitra carpatica* (Loziniyak), *Pseudodictyomitra nuda* (Schaaf), *Svinitzium pseudopuga* Dumitrica, *Praeparvicingula cosmoconica* (Foreman), *Archaeodictyomitra excellens* (Tan), *Archaeodictyomitra apiarium* (Rüst), *Archaeodictyomitra* sp., *Mirifusus dianae minor* Baumgartner, *Stichomitra* sp. aff. *S. euganea* (Squinabol), *Sethocapsa* sp., *Pantanellium squinaboli* (Tan), *Acanthocircus trizonalis dicranacanthos* (Squinabol), *Alievium* sp., and *Emiluvia* sp. The radiolarian assemblage is assigned to the *Pseudodictyomitra carpatica* (KR1) zone, Tithonian to Berriasian in age.

Sample 0808-038 is characterized by claystone dominant with chert. Radiolarians from this sample are abundant and well preserved. Radiolarian assemblage (Fig. 5.7) from this sample is characterized by the occurrence of *Pseudodictyomitra carpatica* (Loziniyak), *Loopus nuda* (Schaaf), *Cinguloturris cylindra* Kemkin et Rudenko, *Svinitzium depressum* (Baumgartner), *Svinitzium pseudopuga* Dumitrica, *Archaeodictyomitra tumandae* Dumitrica, *Neorelumbra kiesslingi* Dumitrica, *Hiscocapsa* sp. aff. *H. kaminogoensis* (Aita), and *Archaeodictyomitra* sp. The radiolarian assemblage is assigned to the *Pseudodictyomitra carpatica* (KR1) zone, Tithonian to Berriasian in age.

Sample 0808-045 is a red siliceous mudstone, which is highly sheared. Scaly fabric is well developed in this sample. Radiolarians from this sample are well preserved and show low abundance and diversity. Radiolarian assemblage (Fig. 5.8) from this sample is characterized by the occurrence of *Pseudodictyomitra hornatissima* (Squinabol), *Dictyomitr* sp., *Turbocapsula fugitiva* O'Dogherty, *Turbocapsula costata* (Wu), *Holocryptocanium* sp., and *Holocryptocanium barbui* Dumitrica. The radiolarian assemblage is comparable to the *Turbocapsula costata* zone, Aptian to Albian in age.

Sample 0808-048 collected from a red claystone block, which is 2 m in thickness and extends 10 m. The claystone is slightly sheared. Radiolarians from this sample are well preserved and show low abundance and diversity. Radiolarian assemblage (Fig. 5.9) from this sample is characterized by the occurrence of *Pseudodictyomitra carpatica* (Loziniyak), *Svinitzium depressum* (Baumgartner), *Cinguloturris cylindra* Kemkin et Rudenko, *Archaeodictyomitra minoensis* (Mizutani), *Loopus nuda* (Schaaf), *Svinitzium pseudopuga* Dumitrica, *Archaeodictyomitra excellens* (Tan), *Archaeodictyomitra apiarium* Rüst, *Neorelumbra kiesslingi* Dumitrica, *Tethysetta boessi* (Parona), *Eucyrtidiellum pyramis* (Aita), *Hiscocapsa zweilii* (Jud), *Sethocapsa kitoi* (Jud), *Hiscocapsa* sp., and *Alievium* sp. The radiolarian assemblage is comparable to the *Loopus primitivus* zone (JR8), Tithonian in age.

Sample 0808-049 collected from a chert layer of claystone, which is 10 m in thickness. The chert layer extends 3 m. Radiolarians from this sample are abundant and

well preserved. Radiolarian assemblage (Fig. 5.10) from this sample is characterized by the occurrence of *Pseudodictyomitra carpatica* (Loziniyak), *Svinitzium depressum* (Baumgartner), *Cinguloturris cylindra* Kemkin et Rudenko, *Archaeodictyomitra excellens* (Tan), *Archaeodictyomitra apiarium* Rüst, *Dictyomitra pseudoscalaris* Tan sensu Schaaf, *Xitus* sp., *Tethysetta boessi* (Parona), *Svinitzium pseudopuga* Dumitrica, *Neorelumbra kiesslingi* Dumitrica, *Archaeodictyomitra* sp., *Sticomitra* sp., *Hiscocapsa uterculus* (Parona), *Podobursa* sp., and *Acanthocircus trizonalis dicranacanthos* (Squinabol). The radiolarian assemblage is assigned to the *Pseudodictyomitra carpatica* (KR1) zone, Tithonian to Berriasian in age.

Sample 0808-051 collected from the scaly siliceous mudstone matrix. Radiolarians from this sample are well preserved. Radiolarian assemblage (Fig. 5.11) from this sample is characterized by the occurrence of *Pseudodictyomitra hornatissima* (Squinabol), *Pseudodictyomitra paronai* (Aliev), *Pseudodictyomitra pentacolaensis* Pessagno, *Pseudodictyomitra* sp., *Dictyomitra communis* (Squinabol), *Thanarla brouweri* (Tan), *Xitus spicularius* (Aliev), *Sticomitra communis* (Squinabol), *Hiscocapsa* sp., *Cryptamphorella* sp., and *Godia* sp. The radiolarian assemblage is assigned to the *Turbocapsula costata* zone, Aptian to Albian in age.

Sample 0808-062 collected from the purple siliceous mudstone which is slightly sheared. Radiolarian assemblage (Fig. 5.12) from this sample is characterized by the occurrence of *Pseudodictyomitra lodogaensis* Pessagno, *Pseudodictyomitra paronai* (Aliev), *Pseudodictyomitra pentacolaensis* Pessagno, *Tugurium pagoda* (Squinabol), *Dictyomitra* sp., *Dictyomitra communis* (Squinabol), *Xitus spicularius* (Aliev), *Thanarla* sp., *Rhopalosyringium mosquense* (Smirnova & Aliev), *Diacantthocapsa* sp., *Hiscocapsa* sp., and *Turbocapsula costata* (Wu). The radiolarian assemblage is Albian in age.

5.1.2.3 Brecciation

Type 2 breccia in this section is well developed and observable in the field. The breccia is matrix supported (Fig. 5.13). Clasts are chert with angular or subangular

shapes. The size of the clasts ranges from 2 mm to 5 cm. The clasts are chert with abundant radiolarians and the matrix is claystone with a few radiolarians. Clasts are randomly arranged. Radiolarians in the matrix are good preserved. Radiolarians in the chert clasts are moderately to bad preserved (Fig. 5.13). Chert clasts and claystone matrix of sample 0808-033, which shows typical type 2 brecciation, contain good to moderately preserved radiolarians. Radiolarian assemblages (Figs. 5.14–23, Table 5.1) are comparable with the *Pseudodictyomitra carpatica* (KR1) zone and the the *Cecrops septemporatus* (KR2) zone.

5.1.3 Section SB

5.1.3.1 Lithology and structures

The section consists of four thrust slices in ascending order (Fig. 5.25). Boundaries between units are marked by zones of shearing or faults. The siliceous sequence is cut into slices by numerous thrust faults. These outcrop-scale fault zones are characterized by intense shearing (Fig. 5.26). Faults dip to the north or northwest, trending SW–NE. Big basalt and chert blocks, tens of meters sized, are connected with this sequence by faults (Figs. 5.27A, B). The thickness of the units ranges from 15 to 30 m. Foliations of the melange and beddings of the coherent sequence globally strike SW–NE and dip mostly toward the northwest.

Unit 4 is composed of m-sized blocks of basalts and red chert, in a scaly matrix of mudstone (Figs. 5.26A, B). The matrix is highly sheared. Deformed structures in basalts and cherts are pinch-and-swelled structure or pinched-out boudins with various wavelengths. Extension fractures perpendicular or parallel to the bedding are recognizable in chert blocks. A network of cleavages is recognizable in the basalt. The millimeter-sized quartz veins perpendicular to the bedding are well-developed in red cherts. The blocks are necked or cut perpendicular to the bedding. Detailed observations on the mesoscopic structures highlight the presents of brecciations in

some chert blocks. Ubiquitous boudinage and pinch and swell structures are well developed in unit 4.

Unit 3 is characterized by broken formation of cherts bounded by scaly shales. The cherts are grossly layered in spite of obvious strata disruption (Fig. 5.26C). Cherts sequences are divided by scaly shales. The foliation surfaces parallel bedding on outcrop scale. Cleavages perpendicular to the bedding are recognizable.

Unit 2 consists of coherent sequence of thin-bedded chert interbedded with shale. The chert/shale ratio ranges from 1 in the upper part (Fig. 5.26D) to 3 in the lower part (Fig. 5.26E). Symmetrical gentle folds are recognizable in units 2 and 3. Axial surfaces of these folds are perpendicular to the bedding (Fig. 5.27C, D). In some chert layers, trace fossils without tectonic interruption are recognizable (Fig. 5.28A, B). Laminations are clearly visible in many layers. Cleavages perpendicular to the bedding are recognizable.

Unit 1 is represented by coherent sequence of thin-bedded red chert with few layers of limestone (Fig. 5.26F). Cleavages perpendicular to the bedding are recognizable.

High angle thin veins, ranging from sub-millimeter to some millimeters in thickness, are recognizable in chert layers (Fig. 5.28). Veins are filled in quartz or calcite. Veins have sharp, planar or curviplanar interfaces with wall rocks. These veins are generally arranged in two conjugate systems making an angle of 40° to 90° to bedding mean strike. Fractures, which are some millimeters in thickness and perpendicular to bedding, are abundant in chert layers.

5.1.3.2 Radiolarian age assignment

Totally 60 siliceous samples were collected continuously from this section for radiolarian biostratigraphic research. The general preservation in units 1–3 is moderate to bad, but better in unit 4.

Ten samples were collected from unit 4, six of which contain moderately to well-preserved radiolarians.

Radiolarian assemblage (Fig. 5.29) from sample SB002 is characterized by the occurrence of *Pseudodictyomitra carpatica* (Loziniyak), *Svinitzium depressum* (Baumgartner), *Dictyomitra pseudoscalaris* Tan sensu Schaaf, *Tethysetta boessi* (Parona), *Tethysetta usotanensis* (Tumanda), *Hiscocapsa uterculus* (Parona), *Williriedellum carpathicum* Dumitrica, *Cecrops septemporatus* (Parona), *Acanthocircus trizonalis dicranacanthos* (Squinabol), *Crucella remanei* Jud, *Crucella bossoensis* Jud, *Suna echiodes* (Foreman), and *Acastea diaphorognona* (Foreman).

Radiolarian assemblage (Fig. 5.30) from sample SB007 is characterized by the occurrence of *Pseudodictyomitra carpatica* (Loziniyak), *Cinguloturris cylindra* Kemkin et Rudenko, *Loopus nuda* (Schaaf), *Svinitzium depressum* (Baumgartner), *Archaeodictyomitra pseudoscalaris* (Tan sin Hok), *Archaeodictyomitra apiarium* Rüst, *Tethysetta usotanensis* (Tumanda), *Eucyrtidiellum pyramis* (Aita), *Hemicryptocapsa capita* Tan, *Cryptamphorella conara* (Foreman), *Cecrops septemporatus* (Parona). *Eucyrtidiellum pyramis* (Aita) are reported in older strata than *Cecrops septemporatus* (Parona). The co-occurrence of these two species indicates a mixture of different aged strata.

Nine samples were collected from unit 3. No age diagnostic assemblage is obtained because of the bad preservations in this unit.

Twelve samples were collected from unit 2, two of which contain moderately preserved radiolarians.

Sample SB027 is characterized by the occurrence of (Fig. 5.31) *Tethysetta dhimeniaensis* (Baumgartner), *Amphipyndax tsunoensis* Aita, *Sethocapsa aculeata* Cortese, *Crucella* sp., and *Emiluvia* sp. The radiolarian assemblage is assigned to the *Loopus primitiva* (JR8) Zone (Matsuoka, 1995).

Sample SB041 is characterized by the occurrence of (Fig. 5.32) *Amphipyndax tsunoensis* Aita, *Eucyrtidiellum ptyctum* (Reidel and Sanfilippo), *Sethocapsa trachyostraca* Foreman, *Sethocapsa aculeata* Cortese, *Gongylothorax sakawaensis*

Matsuoka, *Pantanellium* sp., *Pseudoeucyrtis* sp., *Archaeospongoprunum* sp., *Triactoma* sp., and *Crucella* sp. The radiolarian assemblage is correlative to the *Kilinora spiralis* (JR6) Zone or the *Hsuum maxwelli* (JR7) Zone.

Nineteen samples were collected from unit 1, two of which contains moderately preserved radiolarian.

Sample SB047 yield *Parahsuum simplum* Yao, *Parahsuum* sp., *Canoptsum anulatum* Passagno & Poisson, *Bagotum* sp., *Pseudoristola* sp., *Stichocapsa plicata* Matsuoka, *Holocryptocanium tuberculatum* Dumitrica (Fig. 5.33). The radiolarian assemblage is assigned to the *Trillus elkhomensis* (JR2) Zone.

5.1.3.3 Brecciation

Even with careful observation, the brecciation in chert blocks in Unit 4 is difficult to discover in the field. Only after HF treatment, the clast-in-matrix fabric and the distribution of veins can be recognized. This fabric is observed and described based on two samples. Because type 2 brecciation can be observed in samples SB002 and SB007, original strata containing different aged radiolarian assemblages might be mixed togher throught the brecciation. The radiolarian assemblages obtained from the residule may provide a bias age assignment. To avoid this bias, radiolarian assemblages of different parts on the etched surface were directly observed under the SEM (Figs. 5.34, 5. 35). Sample SB002 was cut into 3 pieces. Sample SB007 was cut into 4 pieces. Siliceous clasts were numbered for each pieces (Figs. 5.34, 5.35). Abundance, preservation, and zonal assignment for each clast of samples SB007 and SB002 are listed in Tables 5.2, 5.3.

(1) Variation of clasts based on radiolarian fossils

In sample SB002, the boundaries between the chert clasts and claystone matrix are obscure. The original boundaries and lithologies are serious interrupted by the well-developed veins (Fig. 5.34). Different parts that are characterized by different abundance and preservation of radiolarian shells are distinguishable (Figs. 5.34, 36–42,

Table 5.3). The chert parts (SB002-1-4, SB002-1-5, SB002-1-6) contain abundant, moderate preserved radiolarians. The claystone parts (SB002-1-2, SB002-1-3) contain abundant, well preserved radiolarians. Some claystone parts (SB002-1-1, SB002-1-7) do not contain radiolarian fossils (Fig. 5.36). Radiolarian assemblages from chert parts (SB002-1-4, SB002-1-6) are comparable with the *Cecrops septemporatus* (KR2) zone. Radiolarian assemblages from the claystone parts are comparable with the *Pseudodictyomitra carpatica* (KR1) zone or the *Cecrops septemporatus* (KR2) zone (Figs. 5.38–5.40). The claystone part in SB002-3-1 contians abundant, well preserved radiolarians. Radiolarian assemblage from this part is comparable with the *Cecrops septemporatus* (KR2) zone.

In sample SB007, the clasts are chert or claystone, angular and subangular in shape, millimeters to centimeters long (Fig. 5.35, Table 5.1). The clasts are floated with a random distribution in the claystone matrix. Chert clasts with abundant and moderately preserved radiolarians, chert clasts with abundant but bad preserved radiolarians, and siliceous mudstone clasts with conman and moderately preserved radiolarians can be distinguished (Figs. 5.35, 5.43–5.42, Table 5.2). Radiolarian fossils in the clasts are not deformed, but cutted by veins. In matrix parts in sample SB007, no radiolarians or isolated, well to moderately preserved radiolarians can be found.

(2) Veins in the breccias

In sample SB007, there are three types of veins in the brecciated chert: quartz veins, calcite veins, and siliceous veins (Fig. 5.35).

There are two sets of quartz veins: veins developed internally in the clasts and veins cut both the clasts and matrix (Fig. 5.35A-1, C-1, C-4). Quartz veins have sharp, straight interfaces with chert clasts and mudstone matrix. Within the clasts, one set of submillimeter-sized quartz veins characterized by mutual crosscutting relationship and large interfacial angle is recognizable. Clast-internal veins are well developed in the large chert clast (1 cm in size). Another set of millimeter-sized quartz veins, which is parallel to one of the clast-internal veins, cuts both the clasts and matrix.

Calcite veins are also well-developed in the breccias. These veins are always irregular in shape and cut both the matrix and clasts (Fig. 5.35A-1, B-4, C-2). Vein thickness is typically some millimeters. White siliceous veins, which are only developed in matrix, with asymmetric plastic flow structures are recognizable.

In sample SB002, veins are predominant filled in quartz (Fig. 5.34A–C). Quartz veins are more abundant and thicker than those in sample SB007. Quartz veins have sharp, straight interfaces with wall rocks. Most veins cut both the chert and siliceous mudstone parts. Quartz veins are better developed in the siliceous mudstone parts.

(3) The structures of the matrix

In sample SB007, irregular swirling asymmetric feature of the matrix is clear around clasts. Siliceous mudstone injections along fractures in the chert clasts are recognized (Fig. 5.35A-1, C-3). Mudstone matrix with irregular and asymmetrical shapes is recognizable in SB007-3(Fig. 5.35C). In sample SB002, the boundaries of the siliceous mudstone and the chert parts are irregularly curviplanar. Siliceous mudstone with irregular shape injects into the chert clasts (Fig. 5.34).

5.1.3.4 Reconstruct the oceanic plate stratigraphy

We reconstruct the ocean plate stratigraphy (OPS) based on radiolarian biostratigraphy from section SB. The chert represents radiolarian ooze in a pelagic environment. The siliceous shale is a mixture of radiolarian tests and very fine terrigenous clayey grains. It is obscure whether the basalts blocks in unit 4 in-situ which erupted along with sedimentation of cherts or exotic.

The lowermost unit (unit 1) of the OPS of this sequence is thin bedded red chert with some layers of limestone. The accumulation of the limestone within the chert sequence suggests the marine depth was near the carbonate compensation depth (CCD). Lower Jurassic radiolarians are found from this unit.

The Late Jurassic unit (unit 2) is characterized by thin bedded green chert interbedded with shale. Trace fossils are well developed in this unit. The rhythmical bedding is formed by the cyclic deposition of a slow, but continuous accumulation of siliceous claystone, and the fast, episodic blooming of radiolarian (Hori et al., 1993).

The radiolarian chert passes into siliceous shale with chert (units 3, 4). The siliceous shale becomes overwhelming upward. Chert contains Early Cretaceous radiolarian assemblages. No terrigenous clastic materials are retained in this sequence.

This sequence represents the middle parts of the ocean plate stratigraphy. Or the reconstructed stratigraphy in our less disrupted sequence testifies to the sediment-starved nature of the oceanic lithosphere when involved in subduction.

5.2 Maquanhe melange

The Maquanhe melange comprises thrust-imbricated successions of basic extrusive igneous rocks, pillow basalt intercalated with radiolarian cherts and minor pelagic carbonates (Fig. 5.2C). This melange does not display the typical matrix-in-blocks fabric. Strata are grossly continous. Compared with the Tanwa melange and the Erba melange, the ratio of siliceous mudstone and limestone are higher.

Two sections are conducted in this melange. Totally, 55 samples were collected. Four of them (0807-014, 0807-031, 0807-031-1, 0807-032) contain moderate to well preserved radiolarians. The radiolarian assemblage can be compared with those in the the *Spoletoensis* Zone, late Albian in age.

Sample 0807-032 collected from thin chert layer (Fig. 5.50) 1 m above the limestone. Radiolarian assemblage (Fig. 5.51) from this sample is characterized by the occurrence of *Pseudodictyomitra lodogaensis* Pessagno, *Pseudodictyomitra paronai* (Aliev), *Pseudodictyomitra pentacolaensis* Pessagno, and *Rhopalosyringium mosquense* (Smirnova & Aliev). The radiolarian assemblage is Albian in age.

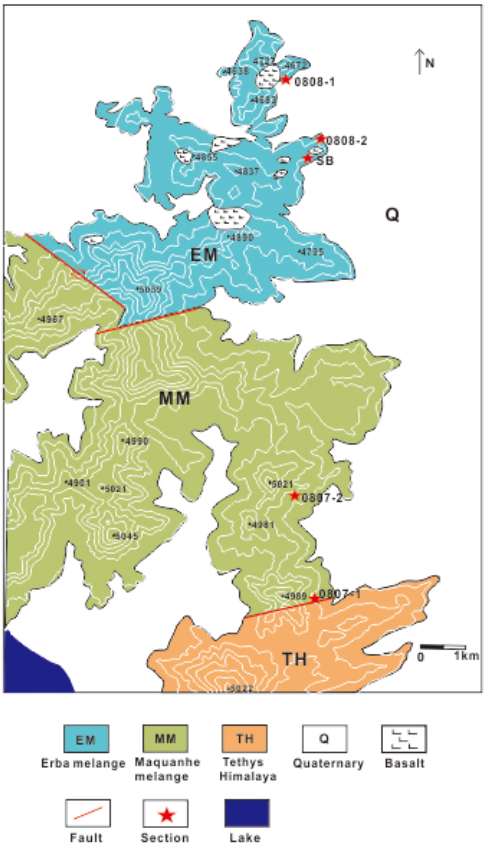

Fig. 5.1 Geological map of the volcanic-sedimentary melanges near Najiu County and section positions

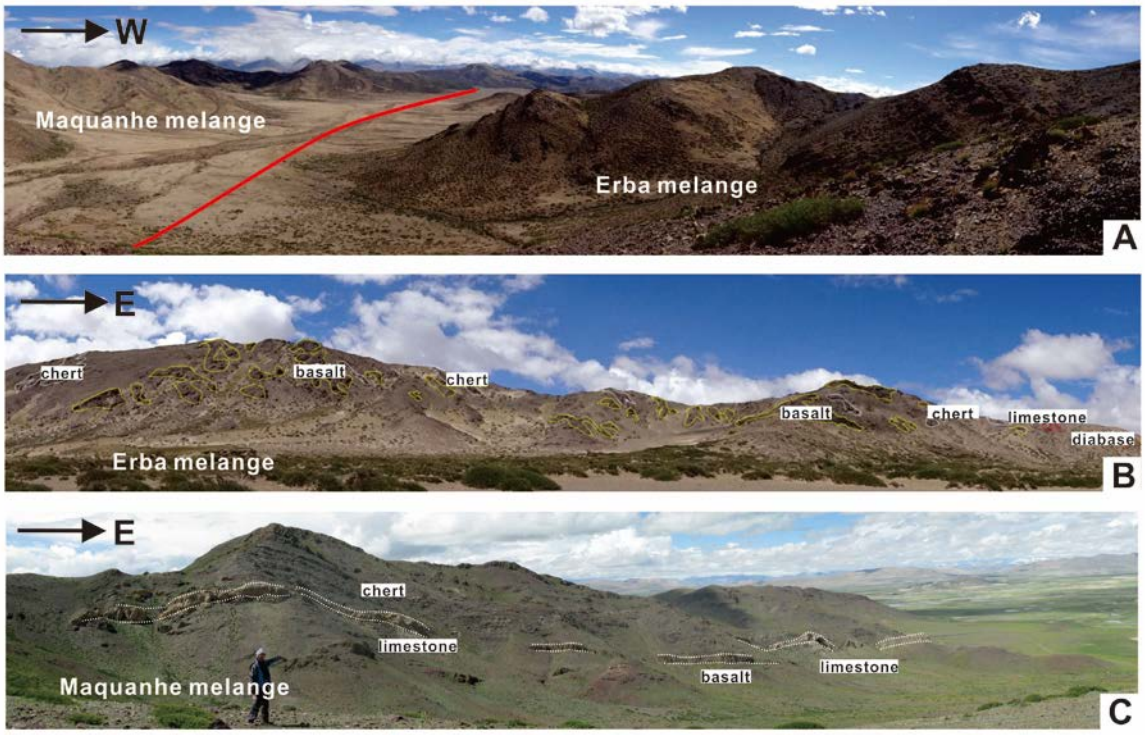

Fig. 5.2 Photographs of outcrops of the volcanic-sedimentarymelanges. **A:** Erba melange in the north, Maquanhe melange in the south, and the fault between them. **B:** Earba melange with blocks-in-matrix fabric, blocks including chert, basalt, limestone, and diabase. **C:** Successions of basalt intercalated with radiolarian cherts and limestones in Maquanhe melange.

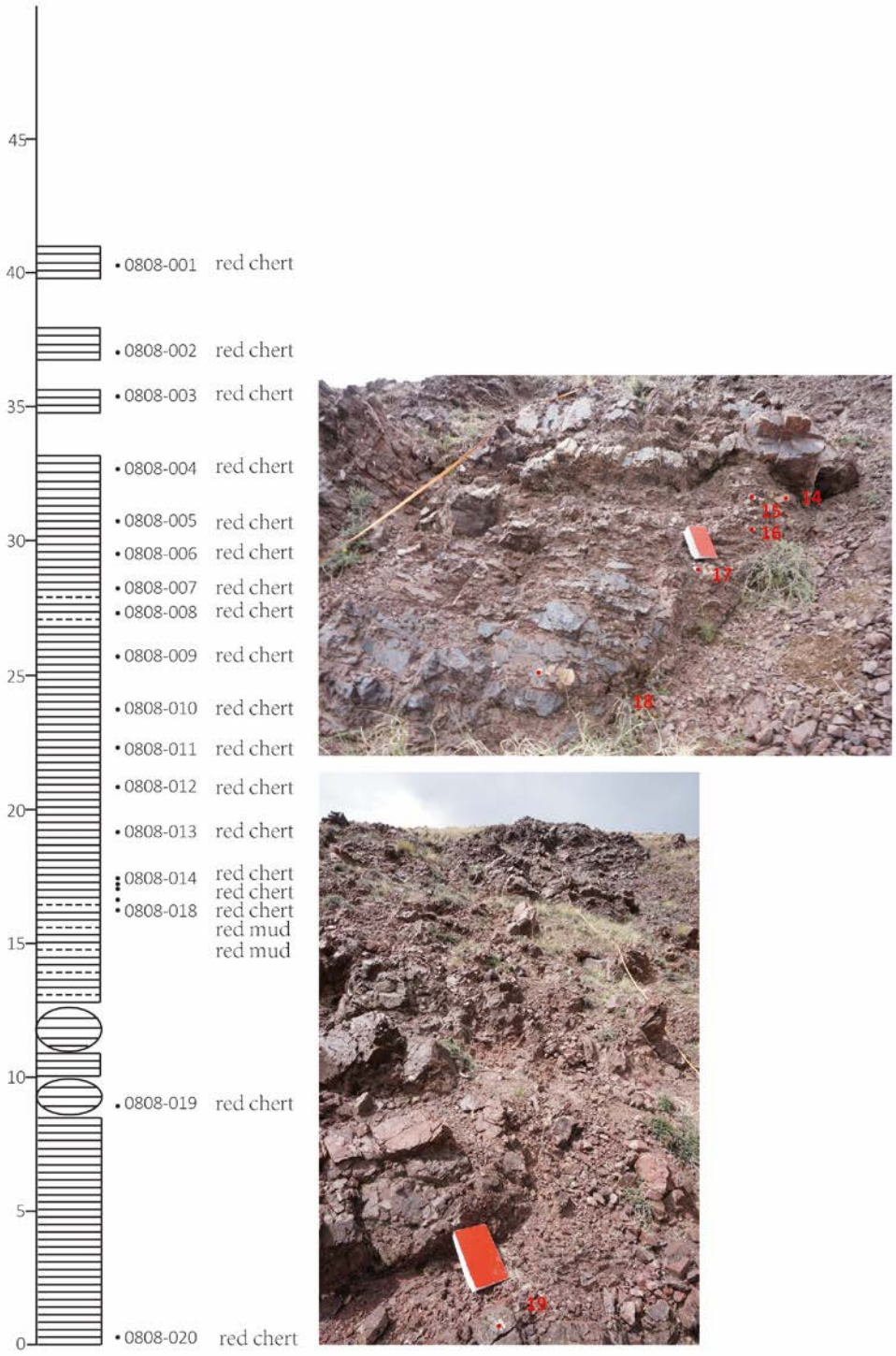

Fig. 5.3 Columar section and outcrops of section 0808-1 (in Erba melange)

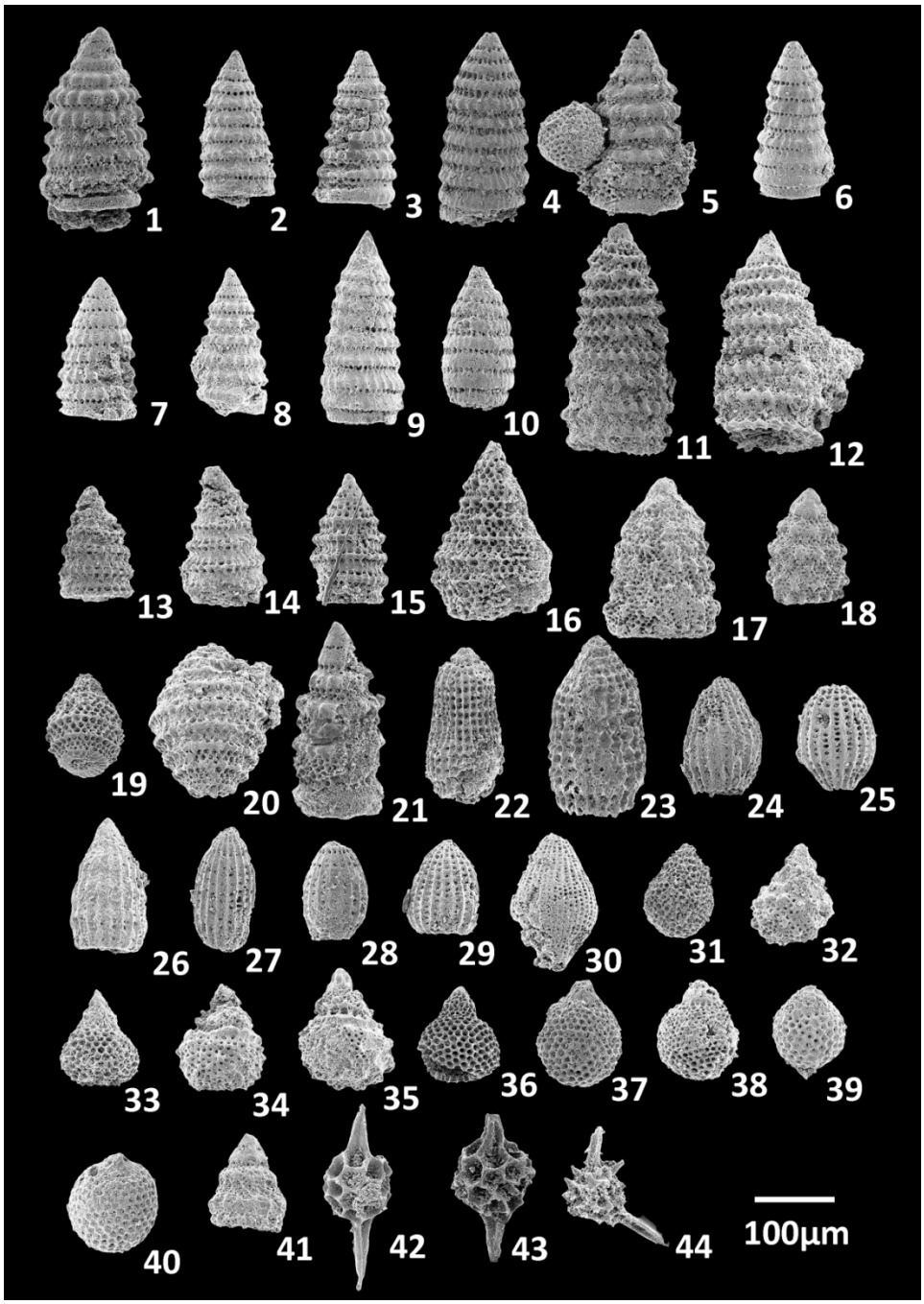

Fig. 5.4 Scanning electron micrographs of radiolarian assemblage from a red siliceous mudstone (sample 0808-016). **1–9.** *Pseudodictyomitra carpatica* (Loziniyak); **10.** *Loopus nuda* (Schaaf); **11, 12.** *Svinitzium depressum* (Baumgartner); **13–15.** *Svinitzium pseudopuga* Dumitrica; **16.** *Tethysetta* sp. **17, 18.** *Xitus* sp. **19, 20.** *Tethysetta boessi* (Parona); **21.** *Cinguloturris cylindra* Kemkin et Rudenko; **22, 23.** *Archaeodictyomitra apiarium* Rüst; **24–29.** *Archaeodictyomitra* sp. **30.** *Mictyoditra lacrimula* (Foreman); **31, 33, 36.** *Sethocapsa* sp. **32, 34, 35.** *Hiscocapsa kaminogoensis* (Aita); **37, 39.** *Cryptamphorella* sp. **38.** *Zhamoidellum ovum* Dumitrica; **40.** *Cryptamphorella conara* (Foreman); **41.** *Neorelumbra kiesslingi* Dumitrica; **42, 43.** *Pantanellium squinaboli* (Tan); **44.** *Alievium* sp.

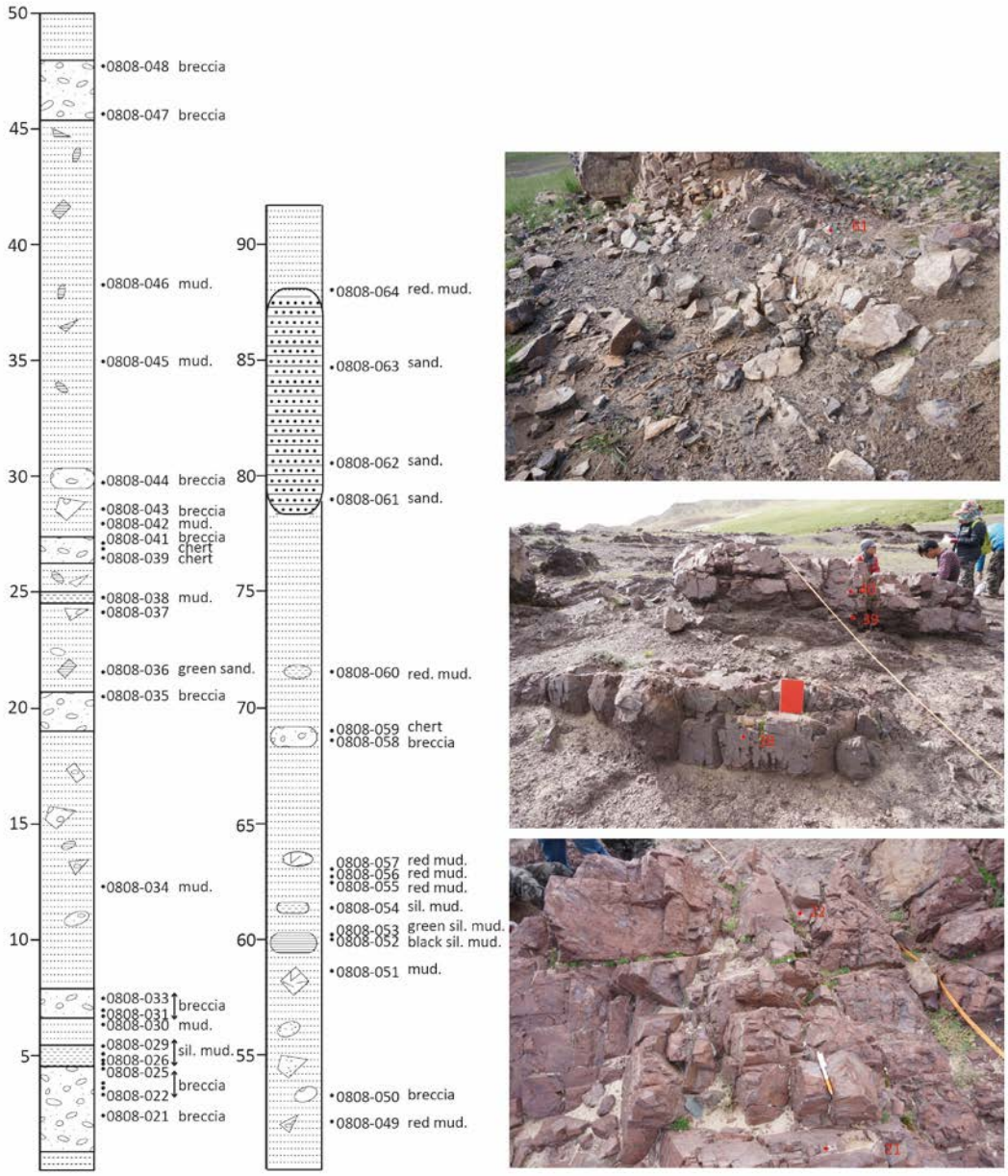

Fig. 5.5 Columar section and outcrops of section 0808-2 (in Erba melange)

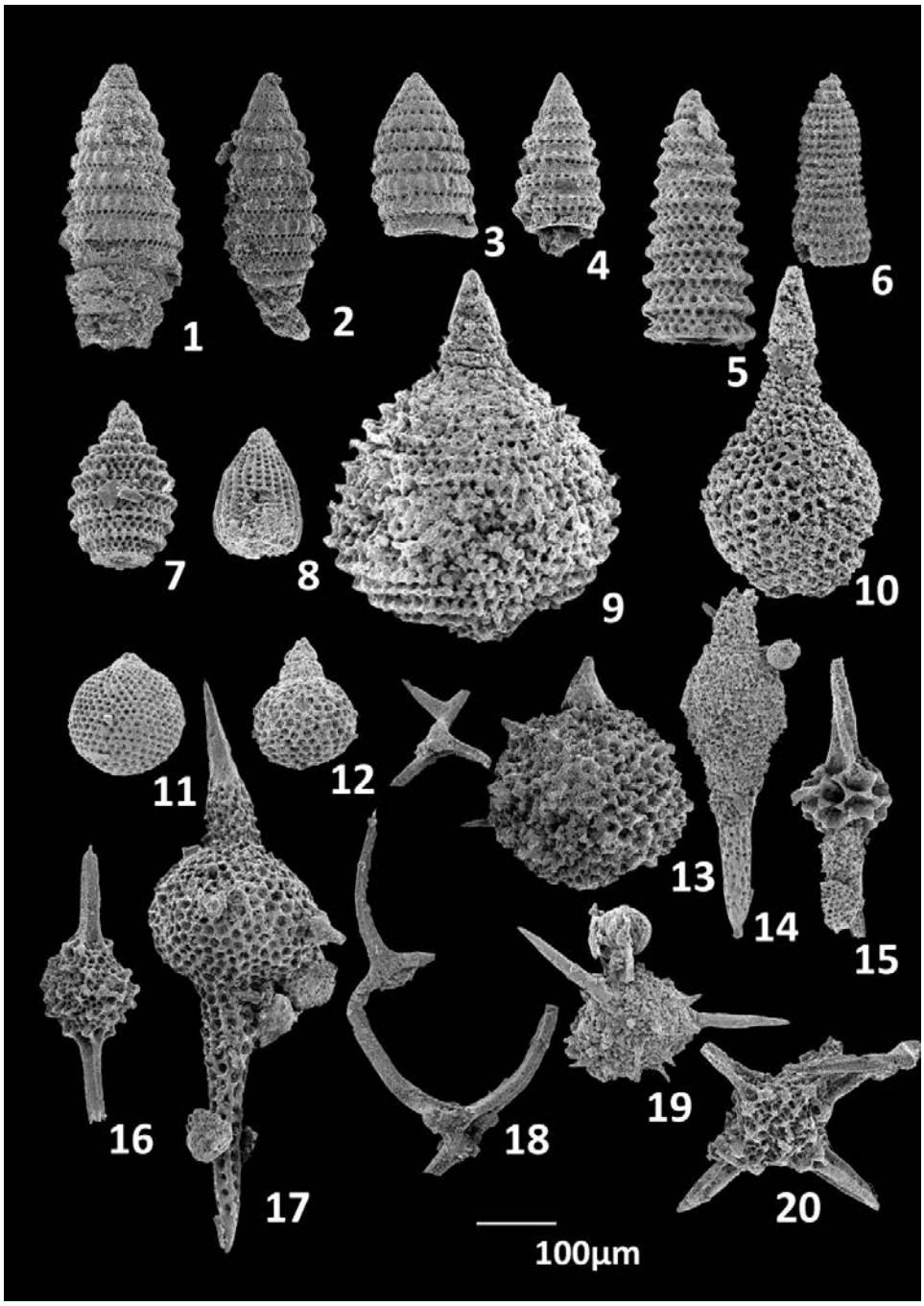

Fig. 5.6 Scanning electron micrographs of radiolarian assemblage from a red chert (sample 0808-027). **1, 2.** *Pseudodictyomitra carpatica* (Loziniyak); **3.** *Loopus nuda* (Schaaf); **4.** *Svinitzium pseudopuga* Dumitrica; **5.** *Praeparvicingula cosmoconica* (Foreman); **6.** *Archaeodictyomitra excellens* (Tan); **7.** *Tethysetta boessi* (Parona); **8.** *Archaeodictyomitra* sp. **9.** *Mirifusus dianae minor* Baumgartner; **10.** *Stichomitra* sp. aff. *S. euganea* (Squinabol); **11.** *Cryptamphorella* sp. **12.** *Hiscocapsa* sp. **13.** *Sethocapsa* sp. **14.** *Eucyrtis* sp. **15.** *Pantanellium squinaboli* (Tan); **18.** *Acanthocircus trizonalis dicranacanthos* (Squinabol); **19.** *Alievium* sp. **20.** *Emiluvia* sp.

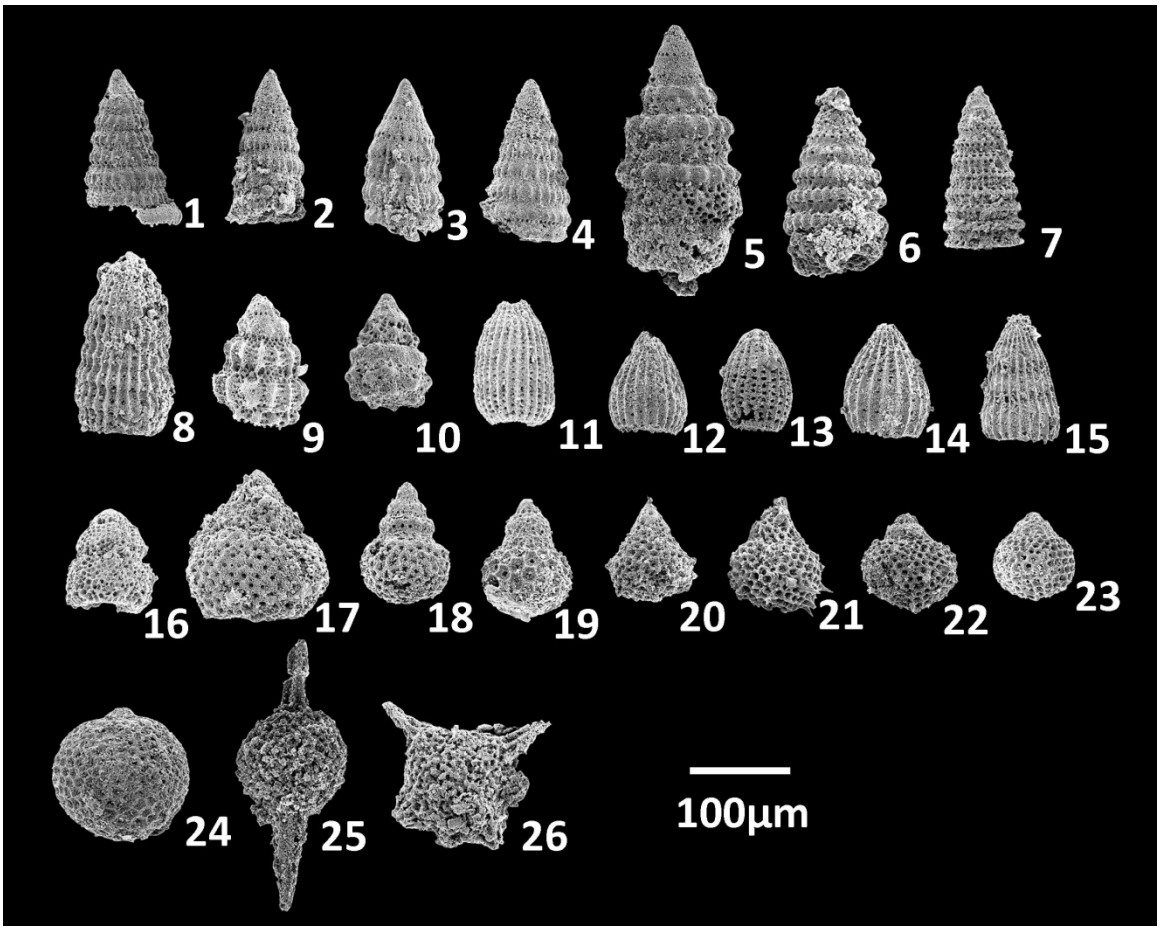

Fig. 5.7 Scanning electron micrographs of radiolarian assemblage from a red claystone (sample 0808-038). **1, 2, 4.** *Pseudodictyomitra carpatica* (Loziniyak); **3.** *Loopus nuda* (Schaaf); **5.** *Cinguloturris cylindra* Kemkin et Rudenko; **6.** *Svinitzium depressum* (Baumgartner); **7.** *Svinitzium pseudopuga* Dumitrica; **8.** *Archaeodictyomitra pseudoscalaris* (Tan sin Hok); **9.** *Neorelumbra buwaydahensis* Kiessling; **10.** *Hiscocapsa* sp. aff. *H. kaminogoensis* (Aita); **11–15.** *Archaeodictyomitra* sp. **18–20.** *Hiscocapsa* sp. **21.** *Sethocapsa* sp. **22, 23.** *Zhamoidellum* sp. **24.** *Cryptamphorella conara* (Foreman); **25.** *Archaeospongoprunum* sp. **26.** *Haliodictya* sp.

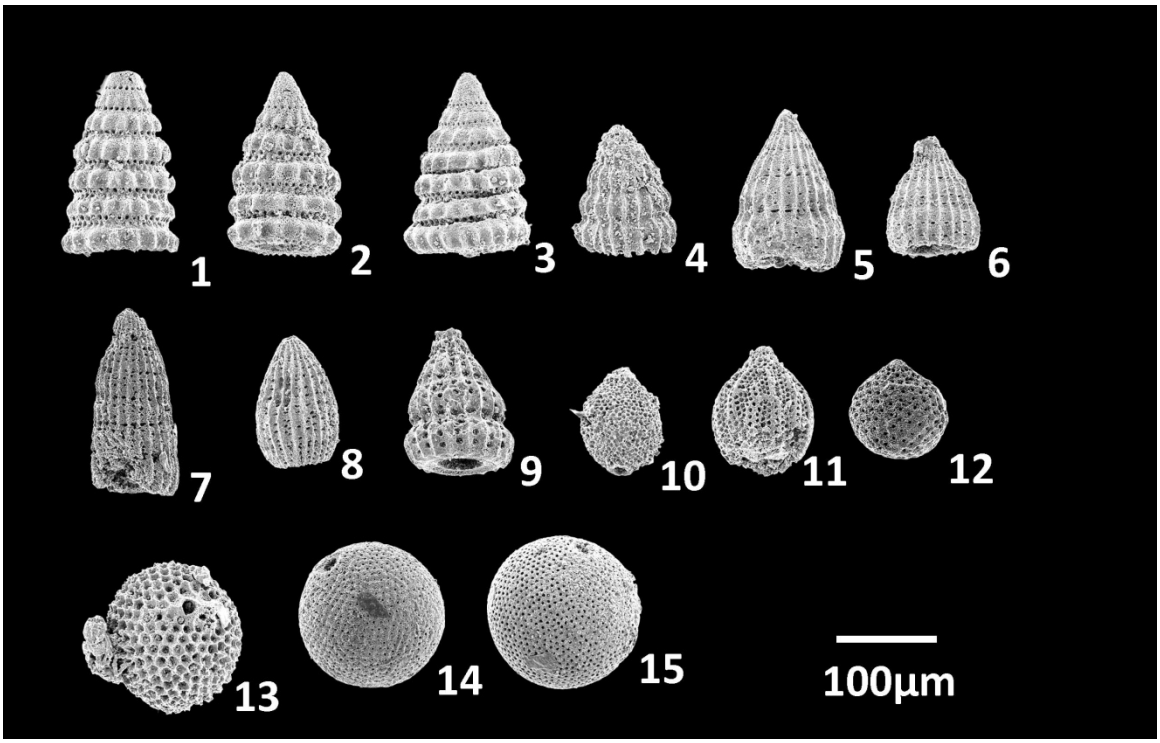

Fig. 5.8 Scanning electron micrographs of radiolarian assemblage from a red siliceous mudstone (sample 0808-045). **1–3.** *Pseudodictyomitra homatissima* (Squinabol); **4–9.** *Dictyomitr* sp. **10.** *Turbocapsula fugitiva* O'Dogherty; **11.** *Turbocapsula costata* (Wu); **12.** *Zhamoidellum* sp. **13.** *Holocryptocanium* sp. **14, 15.** *Holocryptocanium barbui* Dumitrica

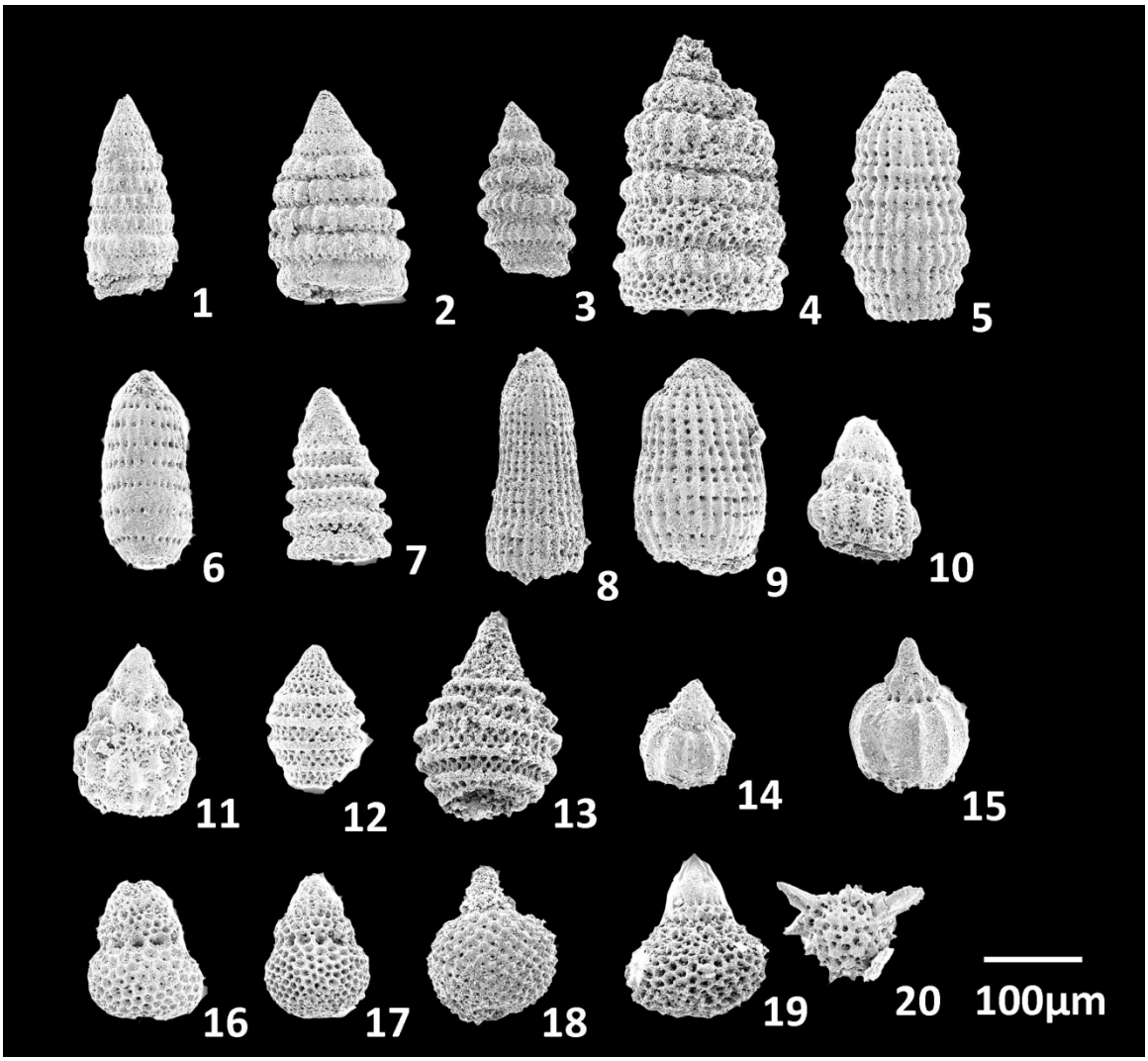

Fig. 5.9 Scanning electron micrographs of radiolarian assemblage from a red claystone block (sample 0808-048). **1, 2.** *Pseudodictyomitra carpatica* (Loziniyak); **3.** *Svinitzium depressum* (Baumgartner); **4.** *Cinguloturris cylindra* Kemkin et Rudenko; **5.** *Archaeodictyomitra minoensis* (Mizutani); **6.** *Loopus nuda* (Schaaf); **7.** *Svinitzium pseudopuga* Dumitrica; **8.** *Archaeodictyomitra excellens* (Tan); **9.** *Archaeodictyomitra apiarium* Rüst; **10.** *Neorelumbra kiesslingi* Dumitrica; **11.** *Xitus* sp. **12, 13.** *Tethysetta boessi* (Parona); **14, 15.** *Eucyrtidiellum pyramis* (Aita); **16, 17.** *Hiscocapsa zweilii* (Jud); **18.** *Hiscocapsa pseudouterculus* (Aita); **19.** *Hiscocapsa* sp. **20.** *Alievium* sp.

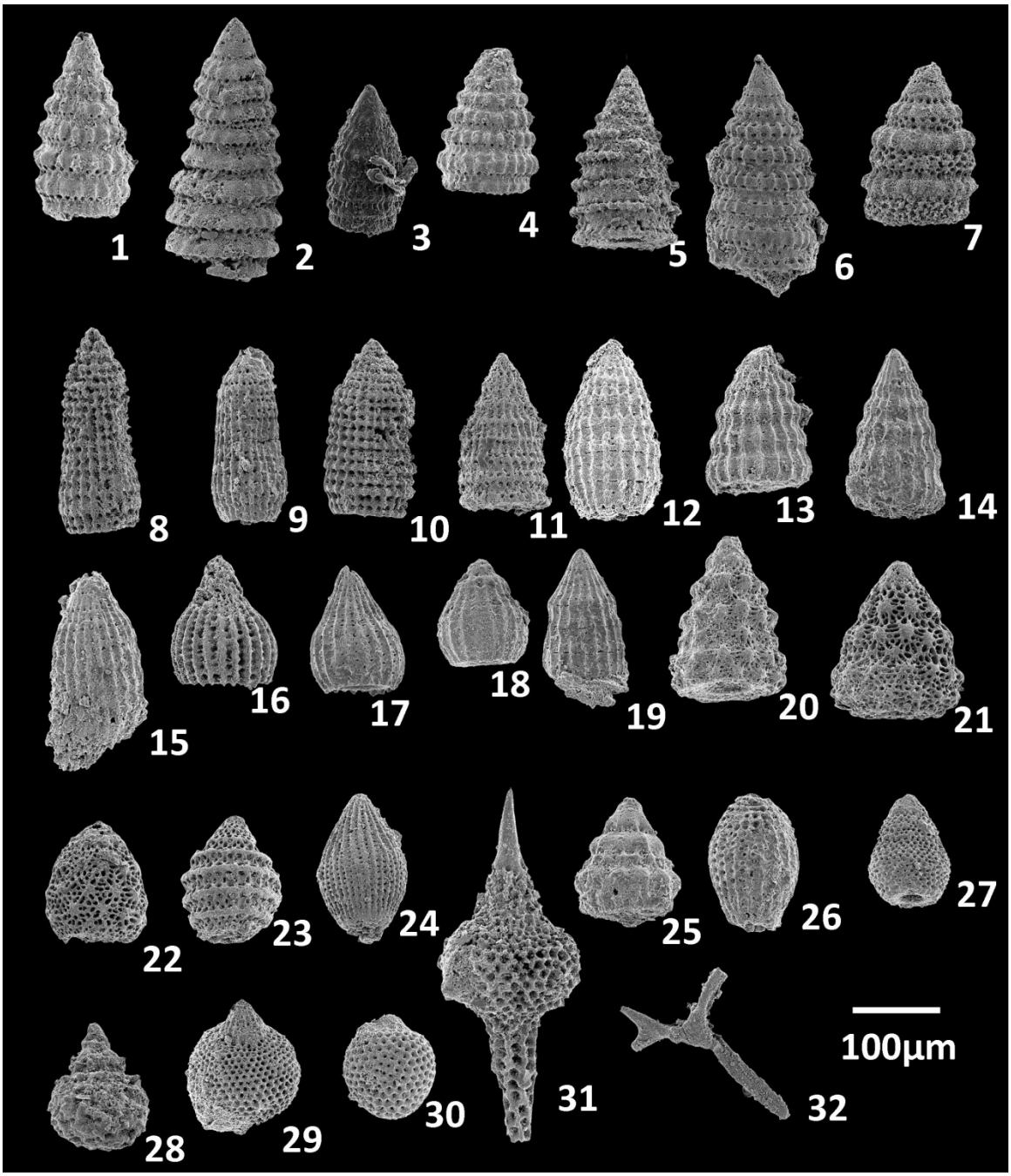

Fig. 5.10 Scanning electron micrographs of radiolarian assemblage from a red claystone (sample 0808-049). **1–4.** *Pseudodictyomitra carpatica* (Loziniyak); **5, 11.** *Svinitzium pseudopuga* Dumitrica; **6.** *Svinitzium depressum* (Baumgartner); **7.** *Cinguloturris cylindra* Kemkin et Rudenko; **8, 9.** *Archaeodictyomitra excellens* (Tan); **10.** *Archaeodictyomitra apiarium* Rüst; **12–14, 19.** *Archaeodictyomitra pseudoscalaris* (Tan sin Hok); **15–18.** *Archaeodictyomitra* sp. **20–22.** *Xitus* sp. **23.** *Tethysetta boessi* (Parona); **24, 26.** *Archaeodictyomitra* sp. **25.** *Neorelumbra kiesslingi* Dumitrica; **27.** *Sticomitra* sp. **28.** *Hiscocapsa uterculus* (Parona); **29.** *Zhamoidellum* sp. **30.** *Zhamoidellum ovum* Dumitrica; **31.** *Podobursa* sp. **32.** *Acanthocircus trizonalis dicranacanthos* (Squinabol).

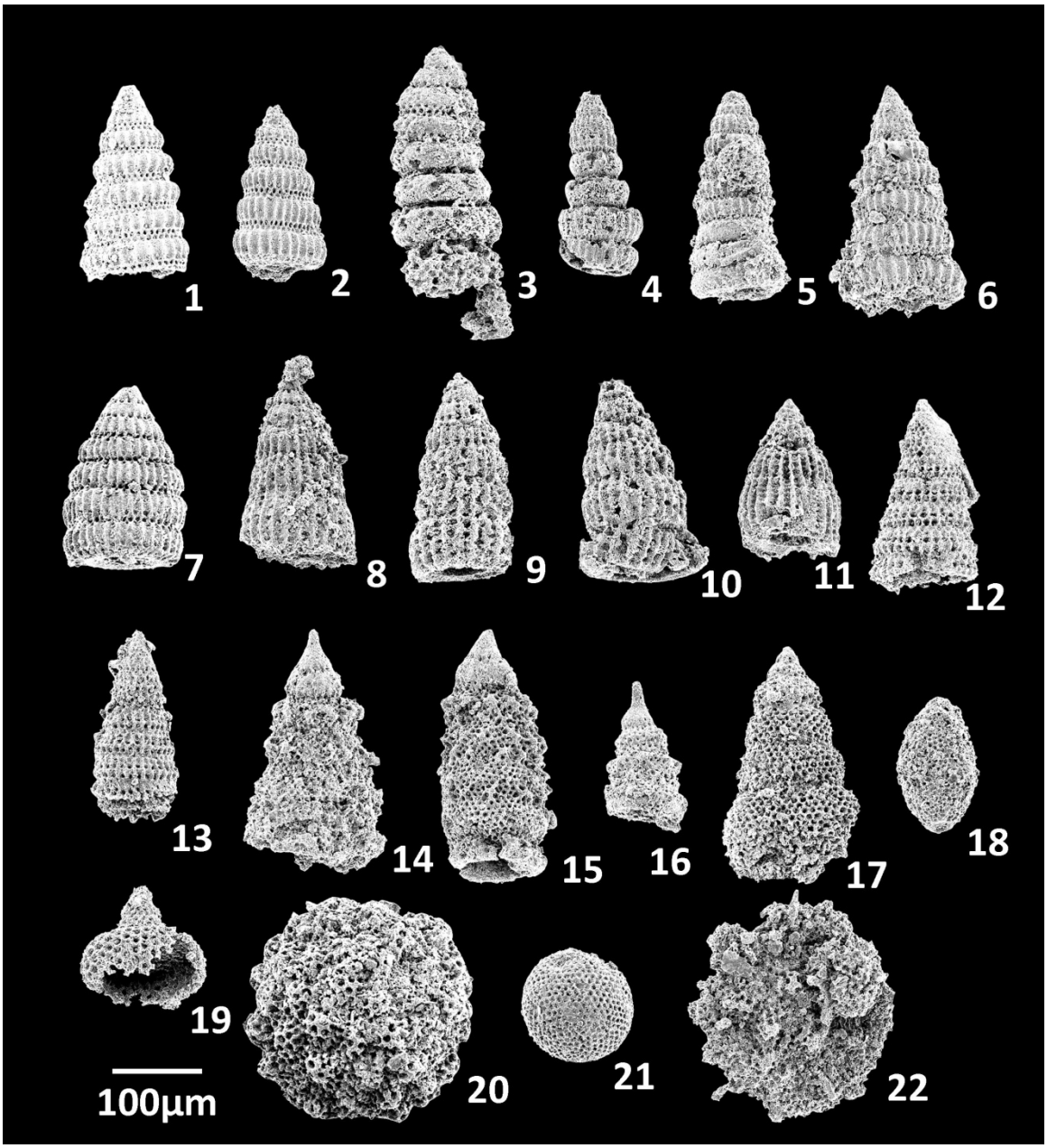

Fig. 5.11 Scanning electron micrographs of radiolarian assemblage from a siliceous mudstone (sample 0808-051). **1.** *Pseudodictyomitra hornatissima* (Squinabol); **2, 6.** *Pseudodictyomitra paronai* (Aliev); **3–5.** *Pseudodictyomitra pentacolaensis* Pessagno; **7.** *Pseudodictyomitra* sp. **8–10.** *Dictyomitra communis* (Squinabol); **11.** *Thanarla brouweri* (Tan); **12, 13.** *Archaeodictyomitra* sp. **14–16.** *Xitus spicularius* (Aliev); **17.** *Sticomitra communis* (Squinabol); **18.** *Turbocapsula* sp. **19.** *Hiscocapsa* sp. **20.** *Cryptamphorella* sp. **21.** *Holocryptocanium barbui* Dumitrica; **22.** *Godia* sp.

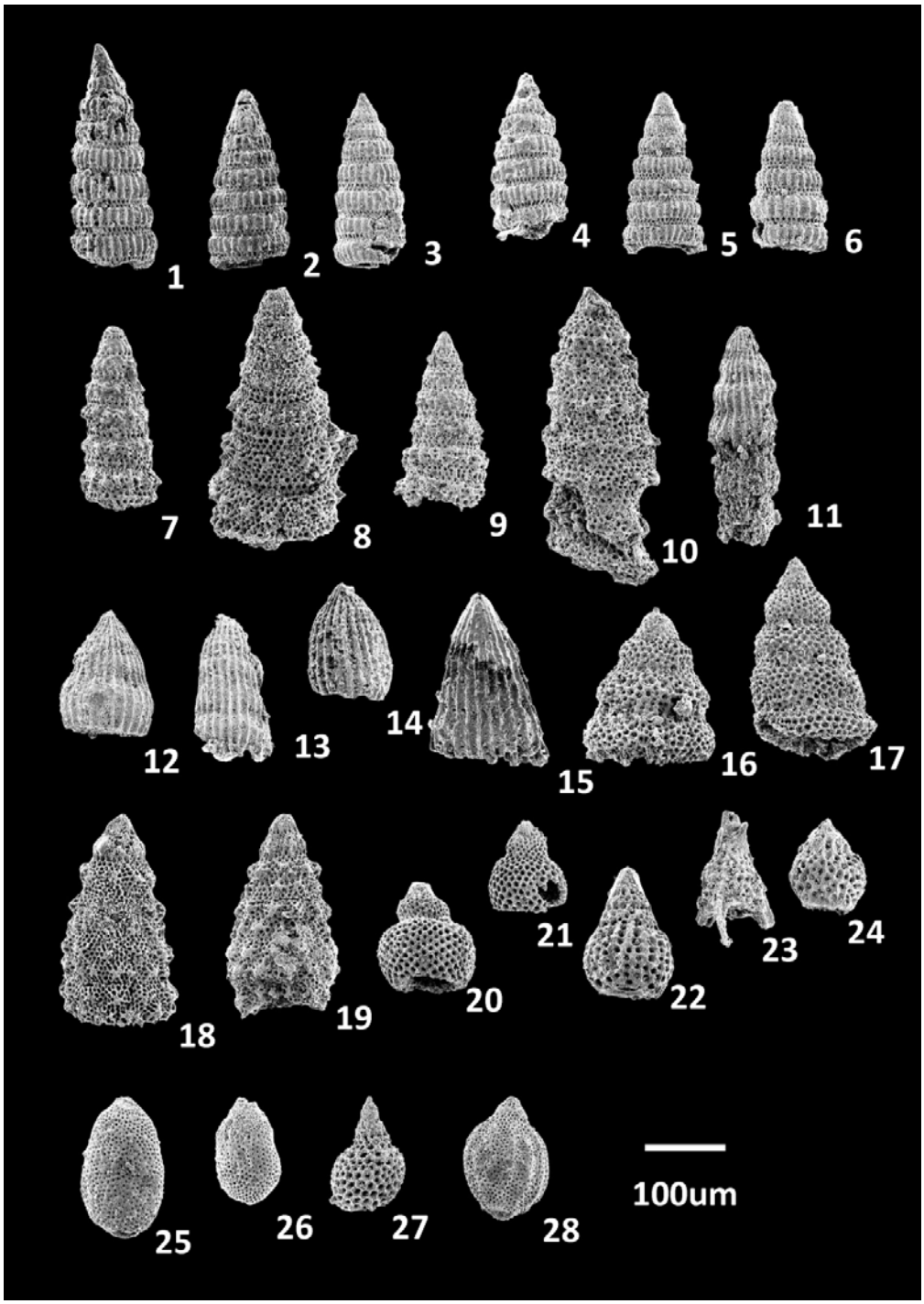

Fig. 5.12 Scanning electron micrographs of radiolarian assemblage from a siliceous mudstone (sample 0808-062). **1, 3, 4.** *Pseudodictyomitra lodogaensis* Pessagno; **2.** *Pseudodictyomitra paronai* (Aliev); **5, 6.** *Pseudodictyomitra pentacolaensis* Pessagno; **7–10.** *Tugurium pagoda* (Squinabol); **11–15.** *Dictyomitra* sp. **16, 17.** *Dictyomitra communis* (Squinabol); **18, 19.** *Xitus spicularius* (Aliev); **20, 21.** *Rhopalosyringium*(?) sp. C in Musavu & Danelian (2006); **22.** *Thanarla* sp. **23.** *Ultranapora* sp. **24.** *Rhopalosyringium mosquense* (Smirnova & Aliev); **25, 26.** *Diacantthocapsa* sp. **27.** *Hiscocapsa* sp. **28.** *Turbocapsula costata* (Wu).

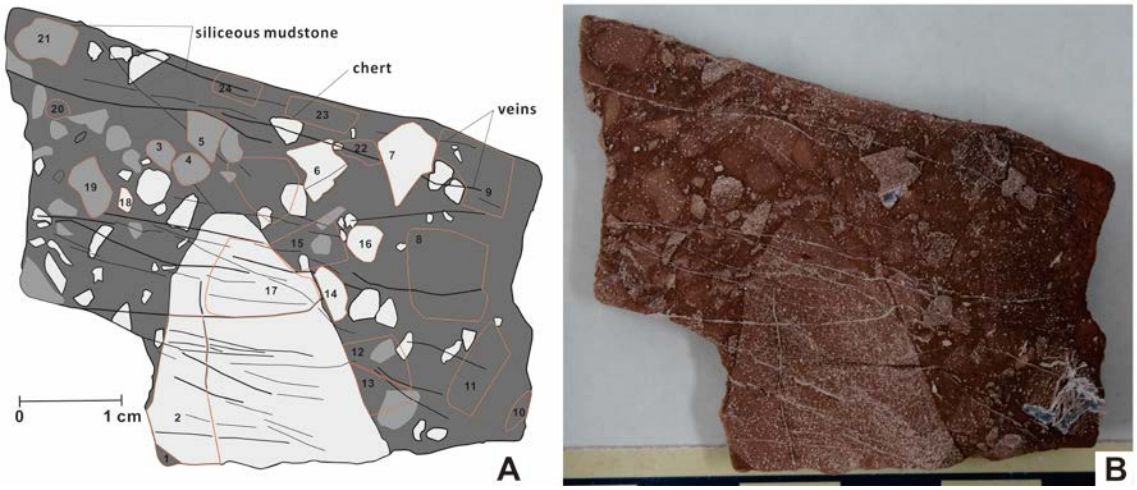

Fig. 5.13 Etched surface of sample 0808-033. **A:** Sketch of the the etched surface. Scanning electron micrographs come from the parts draw by red lines. **B:** Photograph of the etched surface.

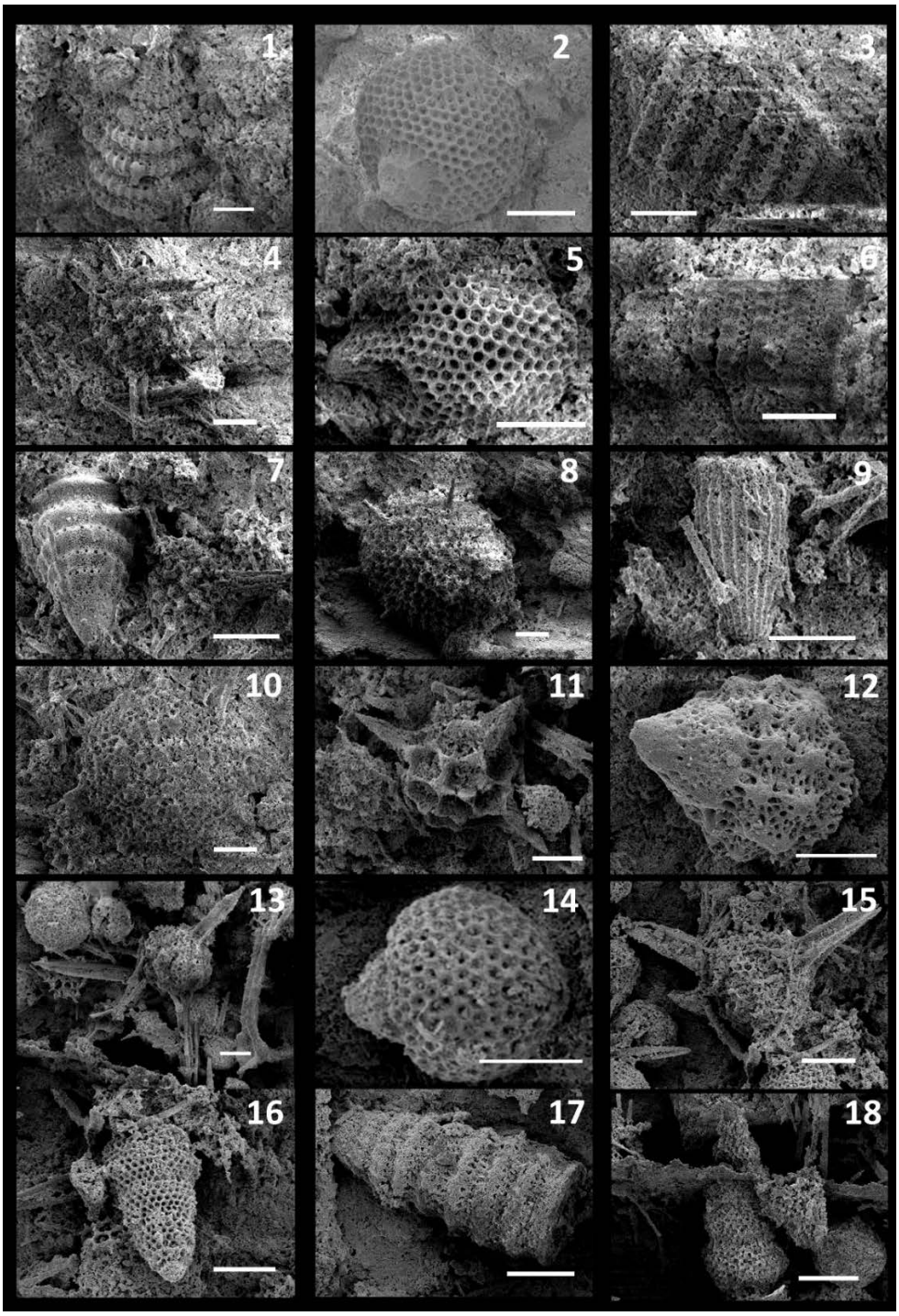

Fig. 5.14 Scanning electron micrographs of radiolarian assemblage from a breccia (sample 0808-033). Part numbers correspond to those in fig. 5.13. 1 from part 1; 2—18 from part 2. **1, 3.** *Svinitzium depressum* (Baumgartner); **2.** *Hemicryptocapsa capita* Tan; **4.** *Becus* sp. **5.** *Hemicryptocapsa* sp. **6, 7, 17.** *Pseudodictyomitra carpatica* (Loziniyak); **9.** *Archaeodictyomitra* sp. **10.** *Dactyliodiscus* sp. **11.** *Cecrops septemporatus* (Parona); **12.** *Xitus* sp. **13, 15.** *Acaeniotyle dentate* Baumgartner; **14.** *Williriedellidue* sp. **16, 18.** *Sticomitra communis* (Squinabol)

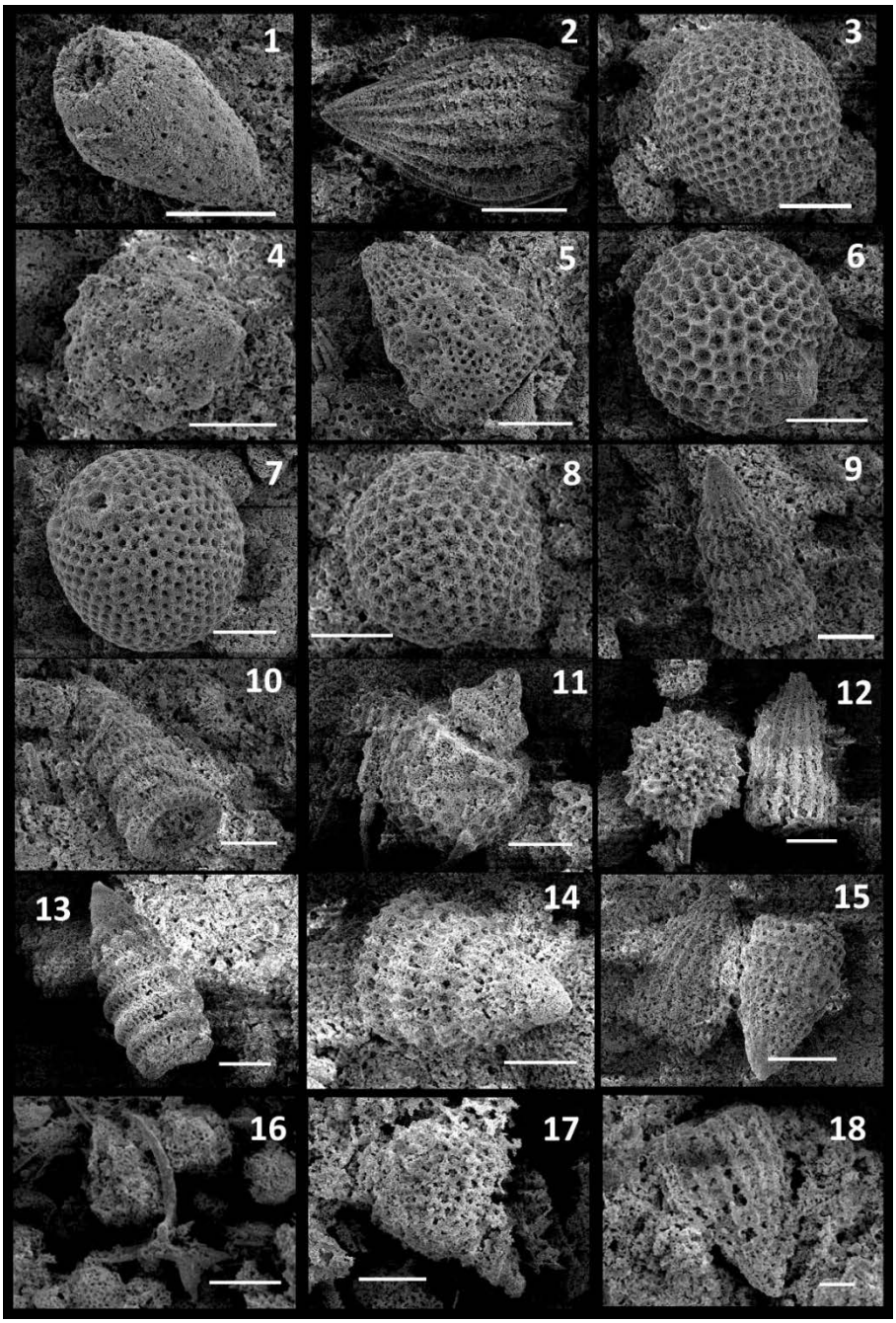

Fig. 5.15 Scanning electron micrographs of radiolarian assemblage from a breccia (sample 0808-033). Part numbers correspond to those in fig. 5.13. 1–7 from part 3; 8–10 from part 4; 11–15 from part 5; 16–18 from part 6. **1.** *Loopus nuda* (Schaaf); **2, 12, 18.** *Archaeodictyomitra* sp. **3, 7.** *Holocryptocanium barbui* Dumitrica; **4.** *Obesacapsula cetia* (Foreman); **5.** *Xitus* sp. **6, 8.** *Cryptamphorella conara* (Foreman); **9, 10, 14, 15.** *Svinitzium depressum* (Baumgartner); **11.** *Hiscocapsa uterculus* (Parona); **12, 18.** *Archaeodictyomitra* sp. **13.** *Pseudodictyomitra carpatica* (Loziniyak); **16.** *Acanthocircus trizonalis dicranacanthos* (Squinabol); **17.** *Hiscocapsa* sp.

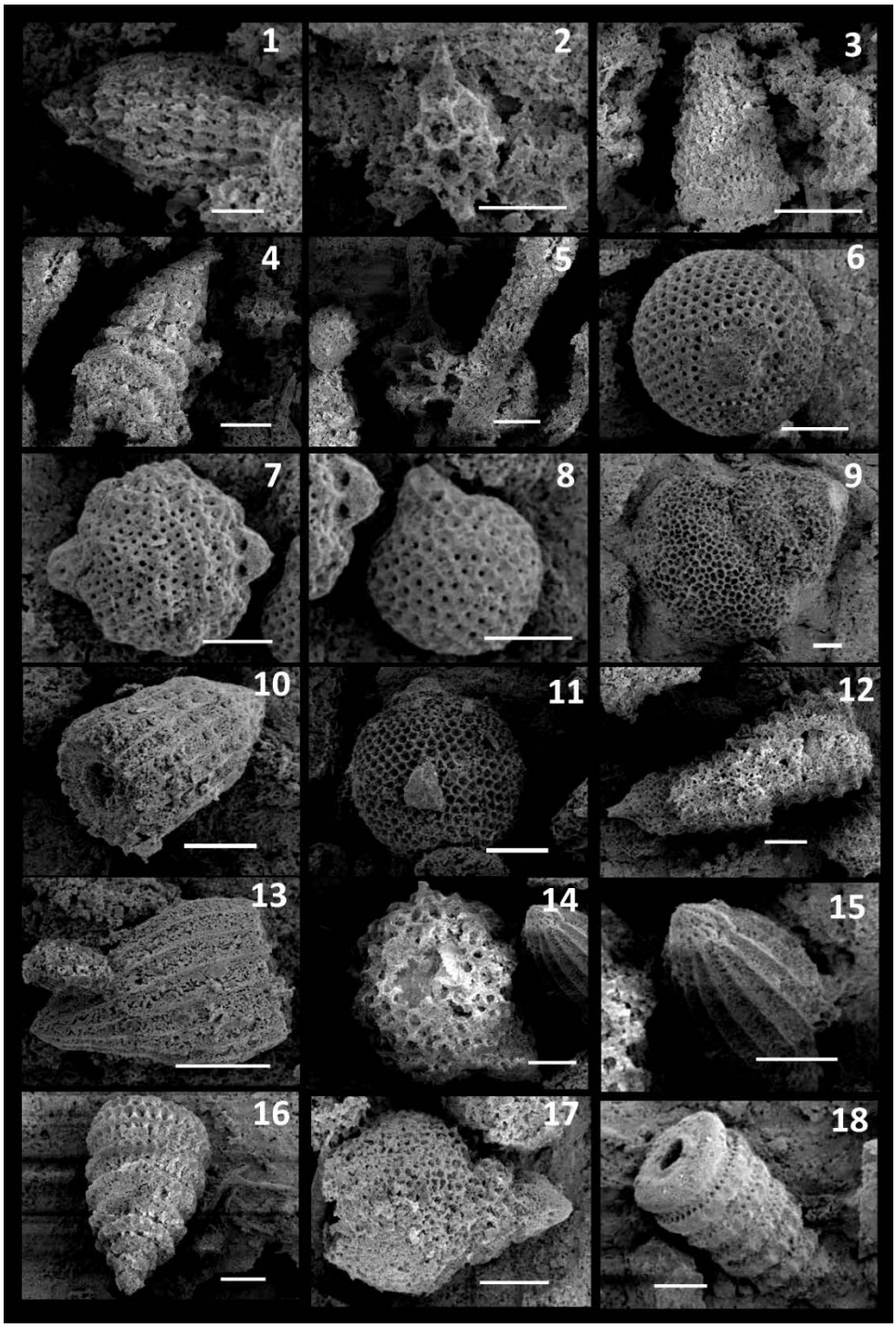

Fig. 5.16 Scanning electron micrographs of radiolarian assemblage from a breccia (sample 0808-033). Part numbers correspond to those in fig. 5.13. 1–2 from part 6; 3–5 from part 7; 6–18 from part 8. **1, 10, 13, 15.** *Archaeodictyomitra* sp. **2, 5.** *Cecrops septemporatus* (Parona); **3, 4, 18.** *Pseudodictyomitra carpatica* (Loziniyak); **6.** *Cryptamphorella conara* (Foreman); **7.** *Hemicryptocapsa tuberose* Dumitrica; **8.** *Zhamoidellum ovum* Dumitrica; **9, 17.** *Obesacapsula* sp. **11.** *Hiscocapsa orca* (Foreman); **12.** *Mirifusus*(?) sp. **16.** *Svinitzium depressum* (Baumgartner)

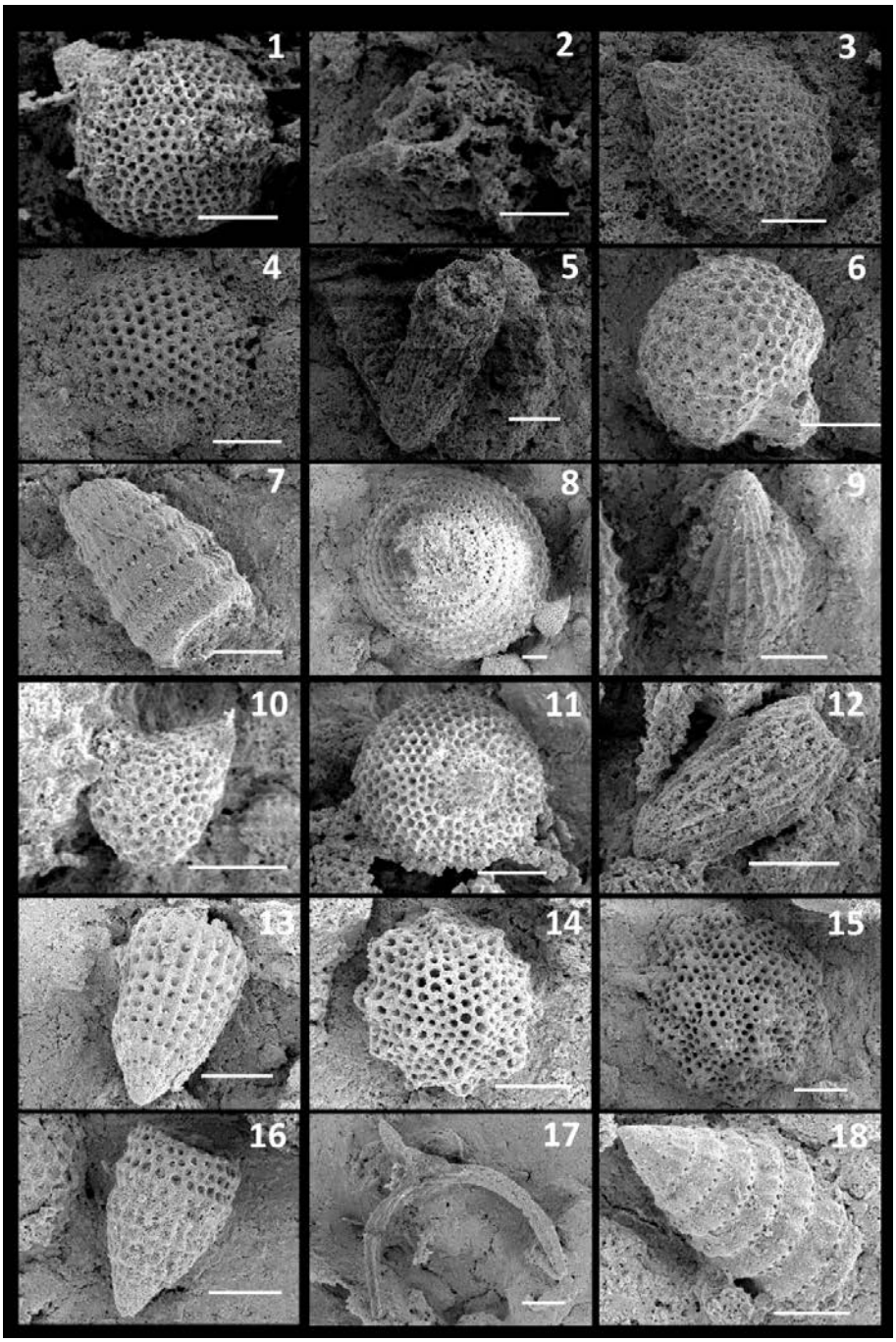

Fig. 5.17 Scanning electron micrographs of radiolarian assemblage from a breccia (sample 0808-033). Part numbers correspond to those in fig. 5.13. 1–5 from part 8; 6–18 from part 9. **1.** *Hiscocapsa* sp. **2.** *Cecrops septemporatus* (Parona); **3.** *Hiscocapsa grutterinki* (Tan); **4, 11.** *Cryptamphorella conara* (Foreman); **5.** *Archaeodictyomitra excellens* (Tan); **6.** *Zhamoidellum ovum* Dumitrica; **7.** *Loopus nuda* (Schaaf); **8.** *Mirifusus* sp. **12, 13.** *Archaeodictyomitra* sp. **14, 15.** *Holocryptocanium tuberculatum* Dumitrica; **17.** *Acanthocircus trizonalis dicranacanthos* (Squinabol); **18.** *Pseudodictyomitra carpatica* (Loziniyak)

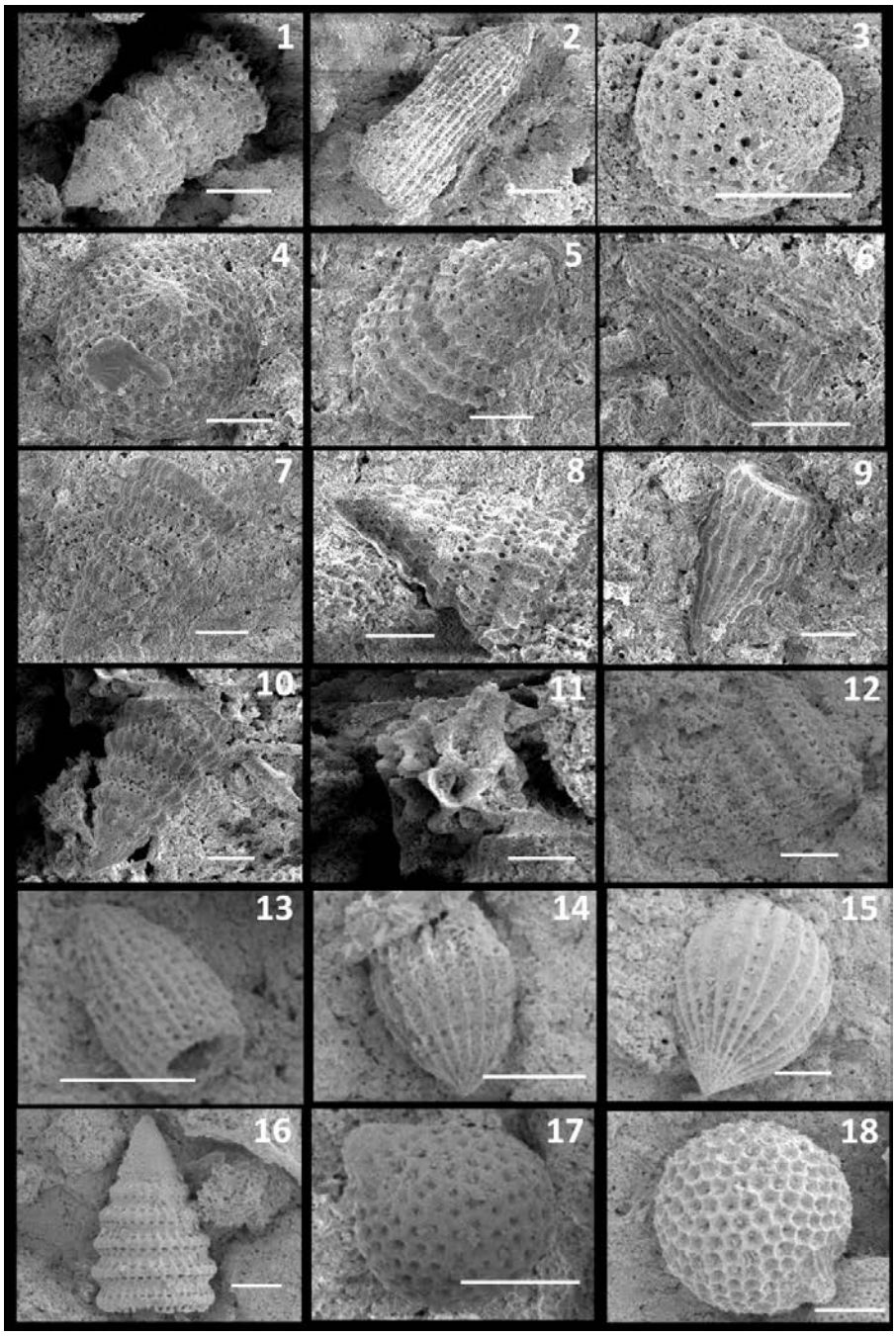

Fig. 5.18 Scanning electron micrographs of radiolarian assemblage from a breccia (sample 0808-033). Part numbers correspond to those in fig. 5.13. 1–3 from part 9; 4–9 from part 10; 10–12 from part 11; 13–17 from part 12; 18 from part 13. **1, 5, 12, 16.** *Svinitzium depressum* (Baumgartner); **2.** *Archaeodictyomitra excellens* (Tan); **3, 17.** *Zhamoidellum* sp. **4, 18.** *Cryptamphorella conara* (Foreman); **6, 13–15.** *Archaeodictyomitra* sp. **7, 8, 10.** *Pseudodictyomitra carpatica* (Loziniyak); **9.** *Archaeodictyomitra pseudoscalaris* (Tan sin Hok); **11.** *Pantanellium lanceola* (Parona)

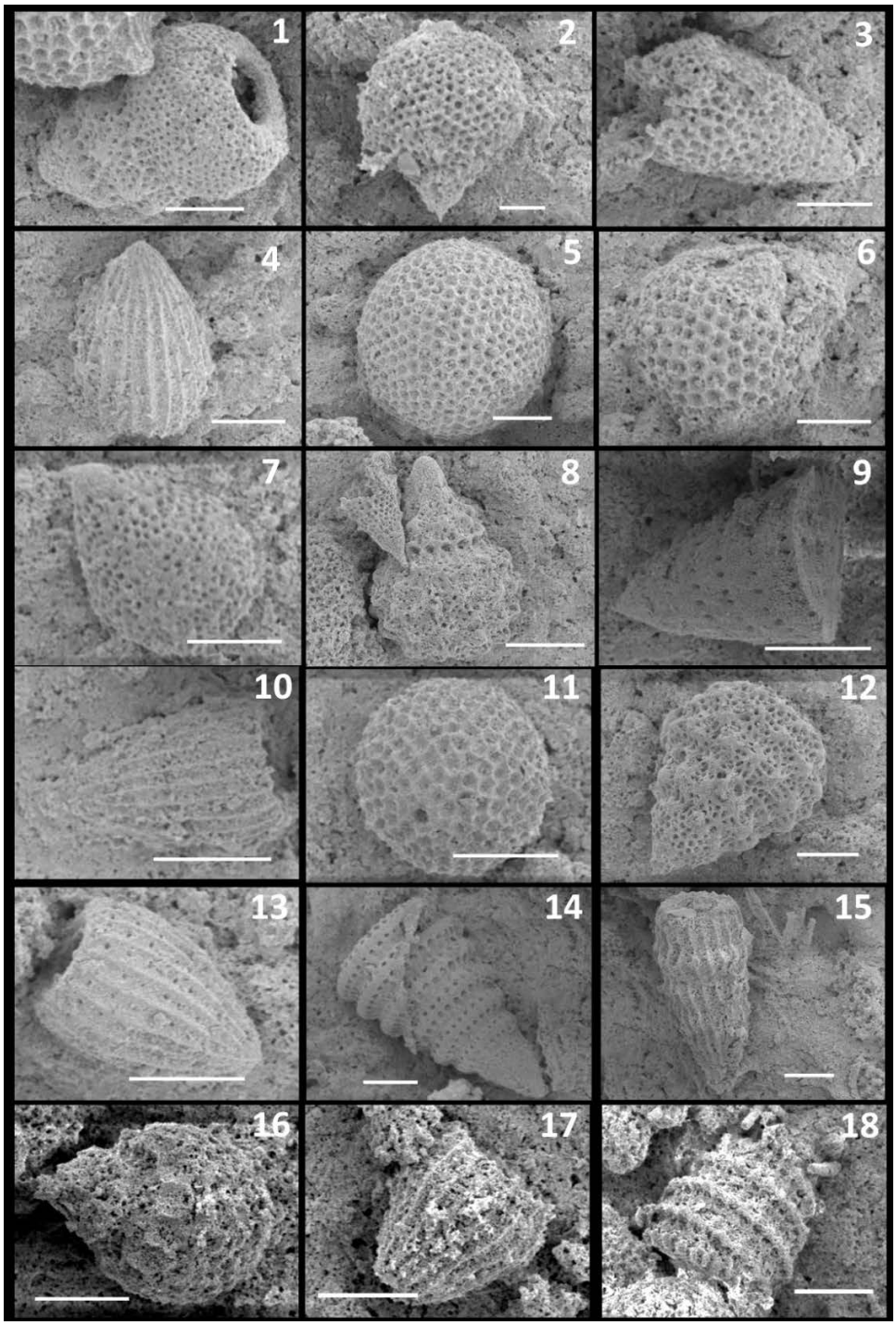

Fig. 5.19 Scanning electron micrographs of radiolarian assemblage from a breccia (sample 0808-033). Part numbers correspond to those in fig. 5.13. 1–15 from part 13; 16–18 from part 15. **1, 3.** *Stichomitra*(?) sp. **2, 7.** *Williriedellum* sp. **4, 10, 13, 17.** *Archaeodictyomitra* sp. **5, 11.** *Holocryptocanium barbui* Dumitrica; **6.** *Zhamoidellum ovum* Dumitrica; **8.** *Hiscocapsa kaminogoensis* (Aita); **9.** *Loopus nuda* (Schaaf); **10, 13, 17.** *Archaeodictyomitra* sp. **12.** *Xitus* sp. **14, 15.** *Archaeodictyomitra pseudoscalaris* (Tan sin Hok); **16.** *Hiscocapsa uterculus* (Parona); **18.** *Svinitzium depressum* (Baumgartner)

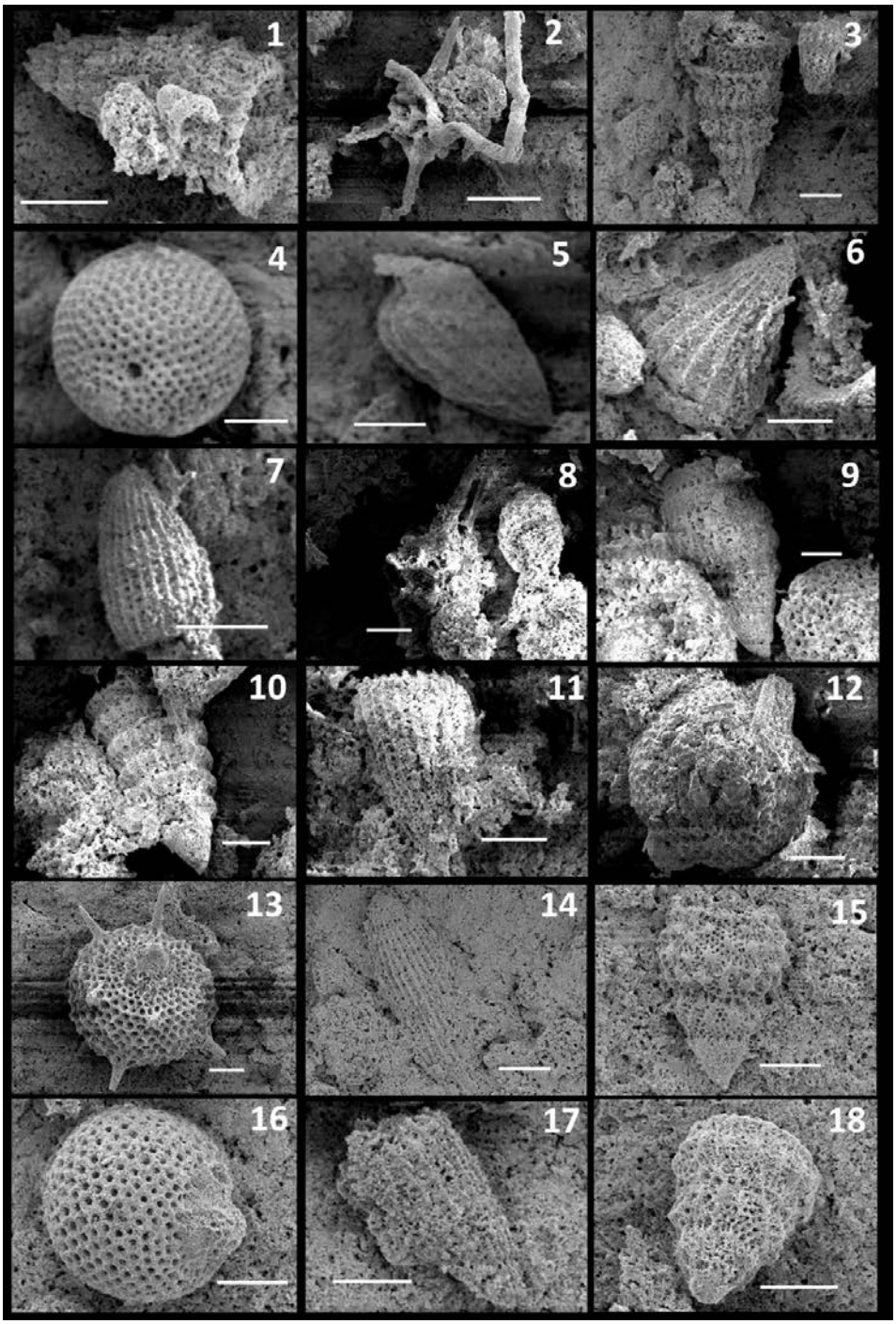

Fig. 5.20 Scanning electron micrographs of radiolarian assemblage from a breccia (sample 0808-033). Part numbers correspond to those in fig. 5.13. 1–5 from part 15; 6–15 from part 16; 16–18 from part 17. **1.** *Pseudodictyomitra carpatica* (Loziniyak); **2.** *Pantanellium* sp. **3.** *Pseudodictyomitra*(?) sp. **4.** *Holocryptocanium barbui* Dumitrica; **5–7, 11, 17.** *Archaeodictyomitra* sp. **8.** *Cecrops septemporatus* (Parona); **9.** *Loopus nuda* (Schaaf); **10.** *Svinitzium depressum* (Baumgartner); **12.** *Hemicryptocapsa capita* Tan; **13.** *Sethocapsa aculeata* Cortese; **14.** *Archaeodictyomitra excellens* (Tan); **15, 18.** *Xitus* sp. **16.** *Cryptamphorella conara* (Foreman)

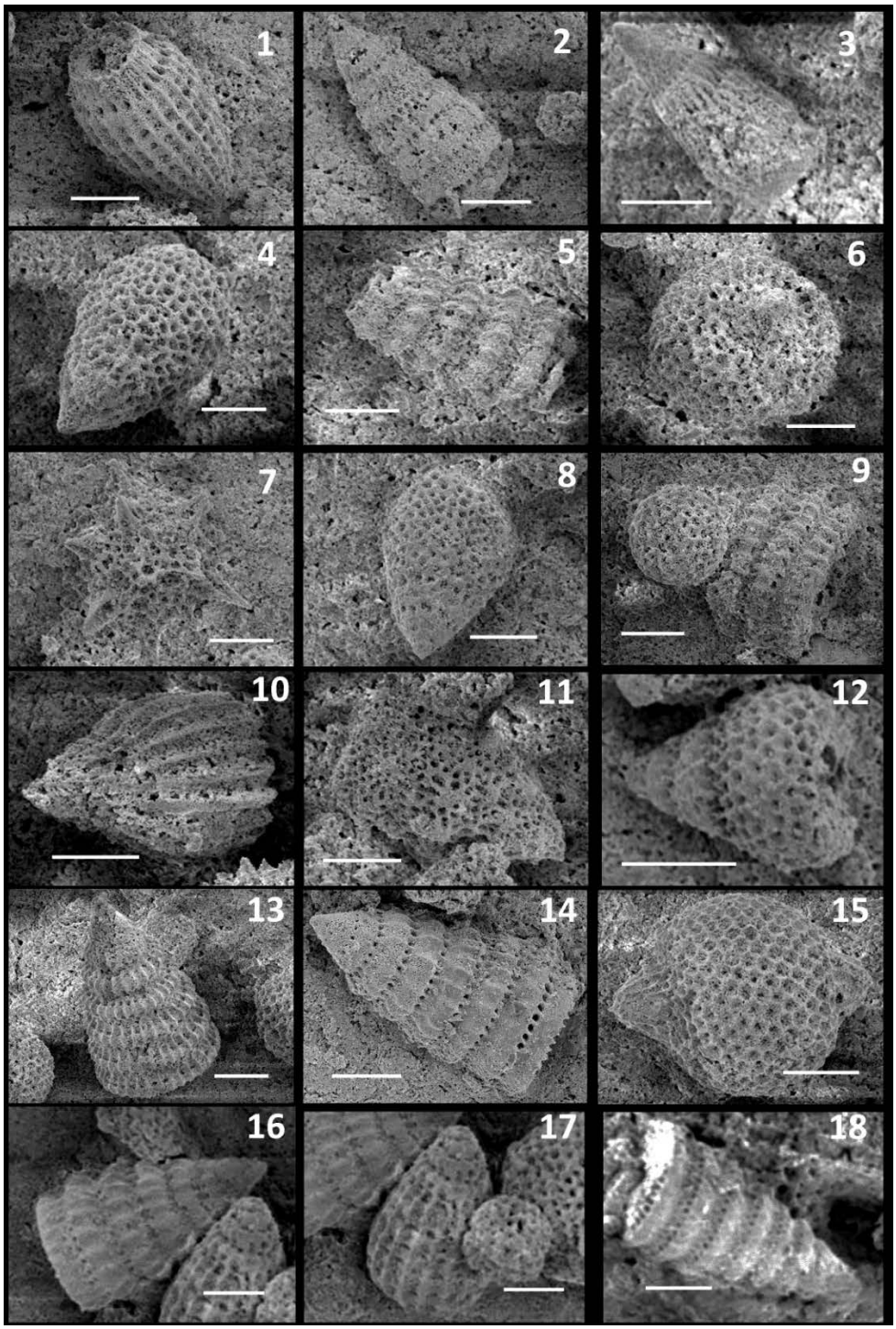

Fig. 5.21 Scanning electron micrographs of radiolarian assemblage from a breccia (sample 0808-033). Part numbers correspond to those in fig. 5.13. 1–2 from part 17; 3–12 from part 19; 13–15 from part 20; 16–18 from part 21. **1, 10, 17.** *Archaeodictyomitra* sp. **2.** *Loopus nuda* (Schaaf); **3.** *Loopus primitivus* (Matsuoka & Yao); **4, 8.** *Stichomitra* sp. **5, 14, 16, 18.** *Pseudodictyomitra carpatica* (Loziniyak); **6.** *Cryptamphorella conara* (Foreman); **9, 13.** *Svinitzium depressum* (Baumgartner); **10.** *Thanarla pulchra* (Squinabol); **15.** *Hemicryptocapsa capita* Tan

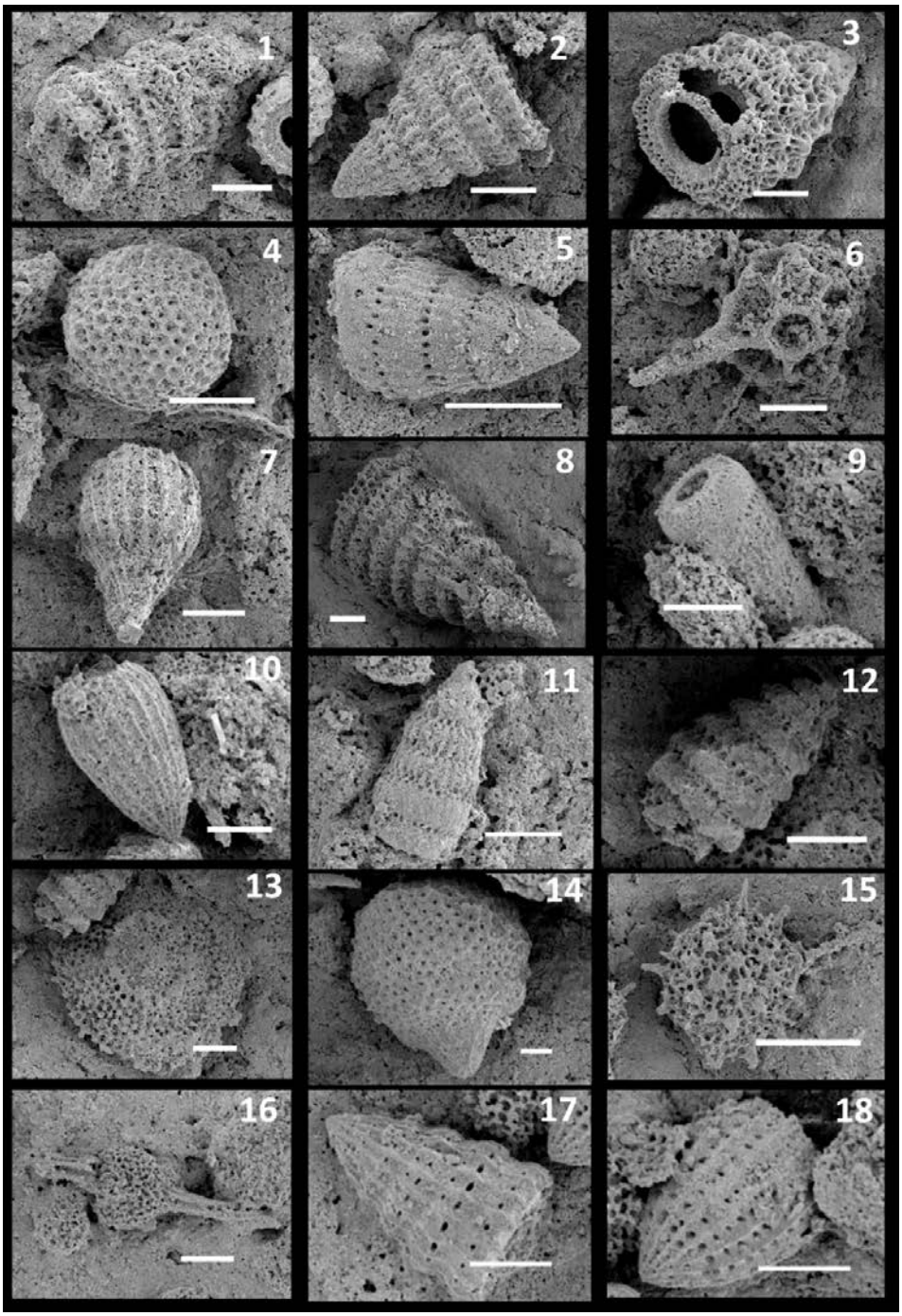

Fig. 5.22 Scanning electron micrographs of radiolarian assemblage from a breccia (sample 0808-033). Part numbers correspond to those in fig. 5.13. 1–18 from part 22. **1, 2, 8.** *Svinitzium depressum* (Baumgartner); **3.** *Xitus* sp. **4.** *Holocryptocanium* sp. **5, 9.** *Loopus nuda* (Schaaf); **6.** *Cecrops septemporatus* (Parona); **7, 10, 18.** *Archaeodictyomitra* sp. **11.** *Loopus primitivus* (Matsuoka & Yao); **12.** *Pseudodictyomitra carpatica* (Loziniyak); **13.** *Pseudoaulophacus* sp. **14.** *Hemicryptocapsa capita* Tan; **15.** *Becus* sp. **16.** *Archaeospongoprunum* sp. **17.** *Archaeodictyomitra pseudoscalaris* (Tan sin Hok)

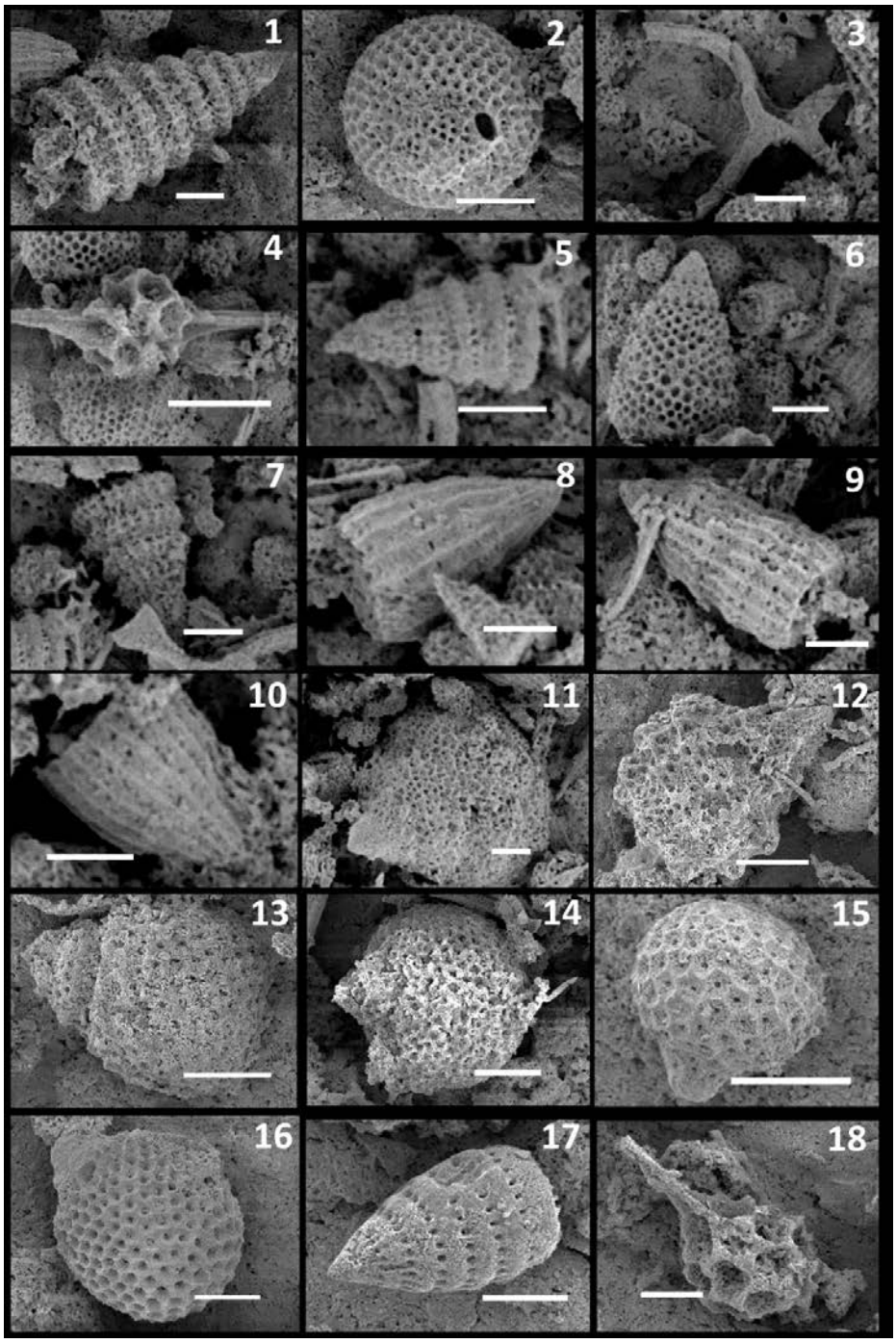

Fig. 5.23 Scanning electron micrographs of radiolarian assemblage from a breccia (sample 0808-033). Part numbers correspond to those in fig. 5.13. 1–2 from part 22; 3–14 from part 23; 15–18 from part 26. **1, 7.** *Svinitzium depressum* (Baumgartner); **2, 16.** *Cryptamphorella conara* (Foreman); **3.** *Acanthocircus trizonalis dicranacanthos* (Squinabol); **4.** *Pantanellium squinaboli* (Tan); **5.** *Pseudodictyomitra carpatica* (Loziniyak); **6.** *Stichomitra* sp. **8–10.** *Archaeodictyomitra* sp. **11.** *Obesacapsula* sp. **12.** *Hiscocapsa grutterinki* (Tan); **13.** *Hiscocapsa uterculus* (Parona); **14.** *Zhamoidellum* sp. **15.** *Gongylothorax verbeeki* (Tan Sin Hok); **16.** *Cryptamphorella conara* (Foreman); **17.** *Loopus nuda* (Schaaf); **18.** *Pantanellium* sp.

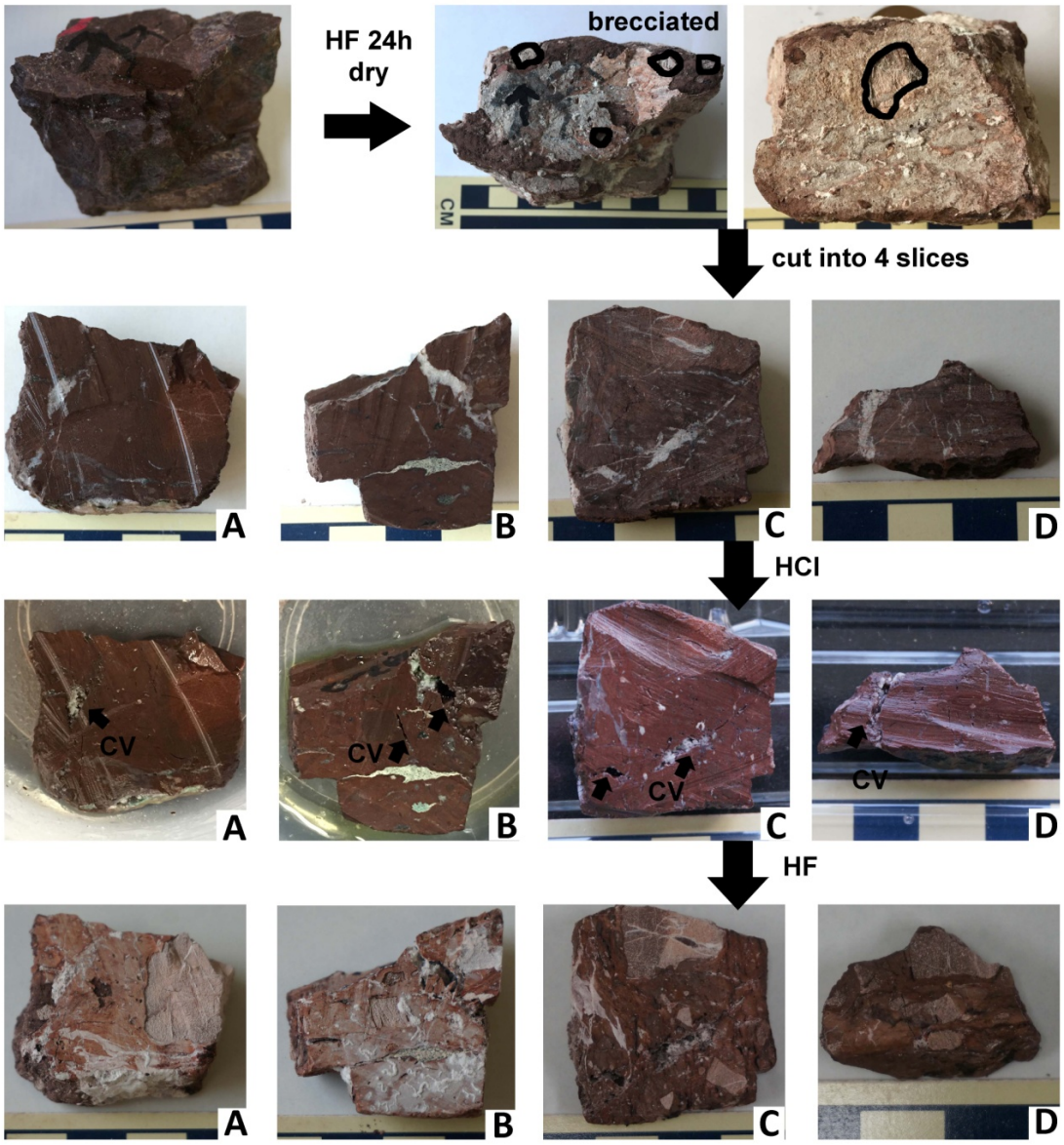

Fig. 5.24 Flowchart using figures of sample SB007 illustrating sample treatment for observing the etched surfaces.

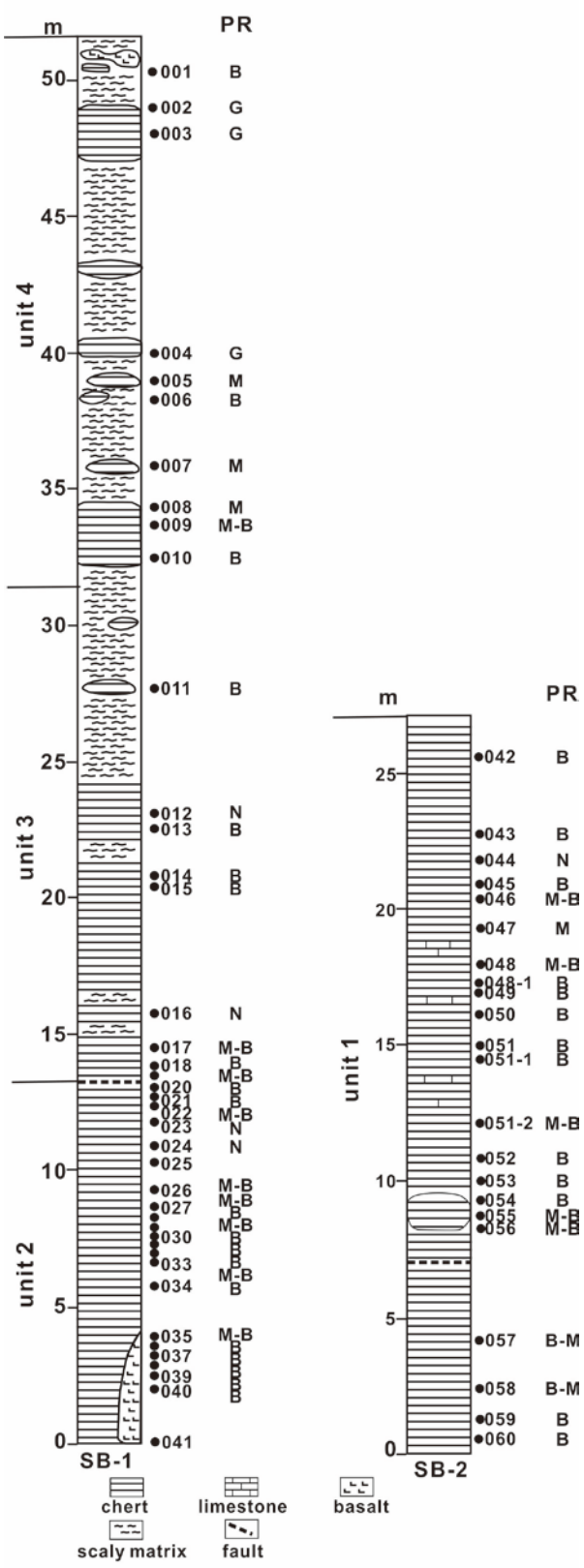

Fig. 5.25 Columnar section showing lithology and subdivision of units

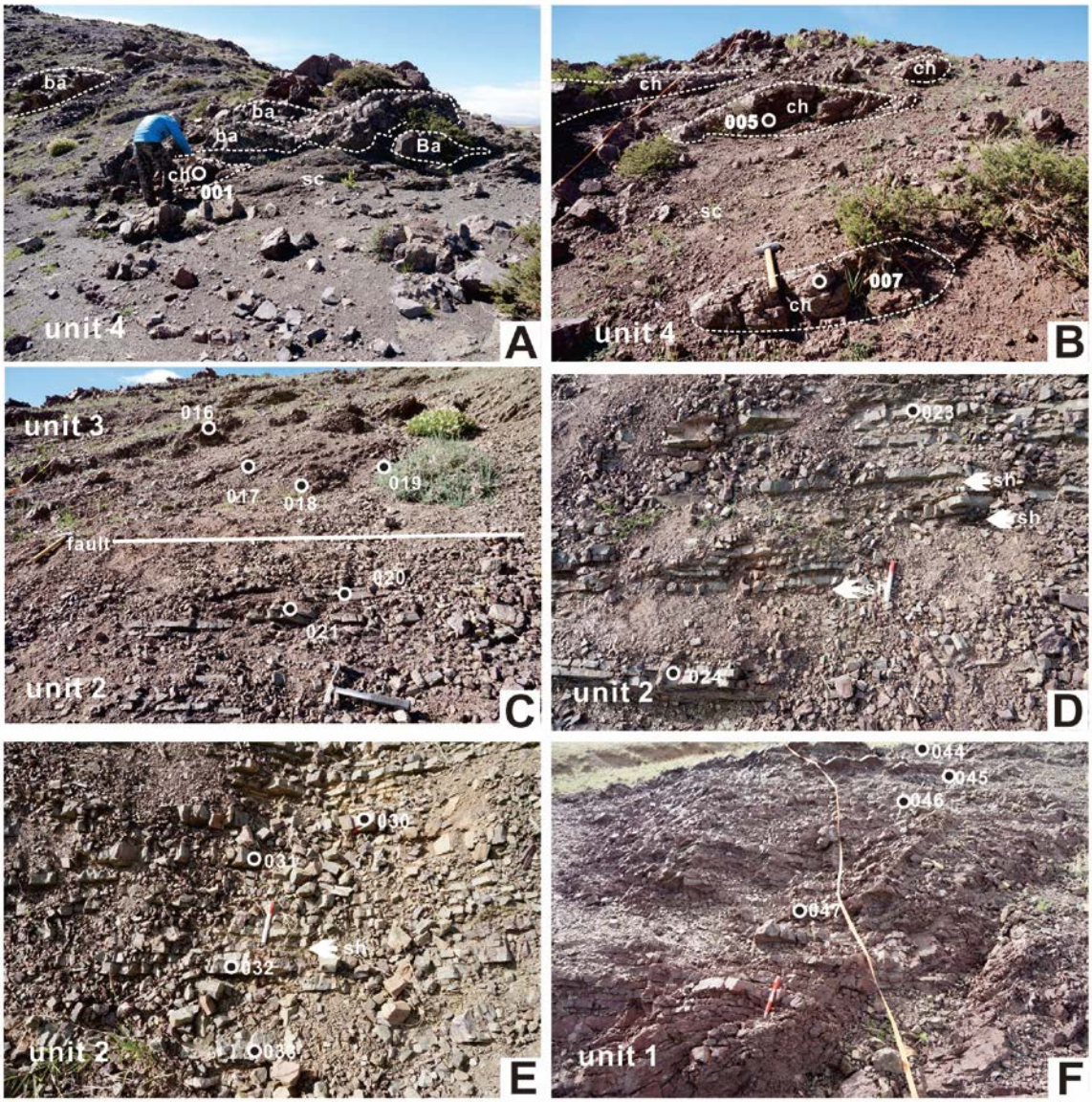

Fig. 5.26 Outcrops showing the lithology and structure in each unit. ba= basalt, ch= chert, sh=shale, sc=scaly shale, number means sampling position. **A**: Pinch-and-swelled structure of basalt and chert in unit 4; **B**: Pinch-and-swelled structure of chert in unit 4; **C**: Grossly layer strata in unit 3, coherent strata in unit 2, and a fault between these two units; **D**: Coherent strata of chert interbedded with shale with a ratio of 1:1; **E**: Coherent strata of chert interbedded with shale with a ratio of 3:1; **F**: Thin bedded red chert in unit 1.

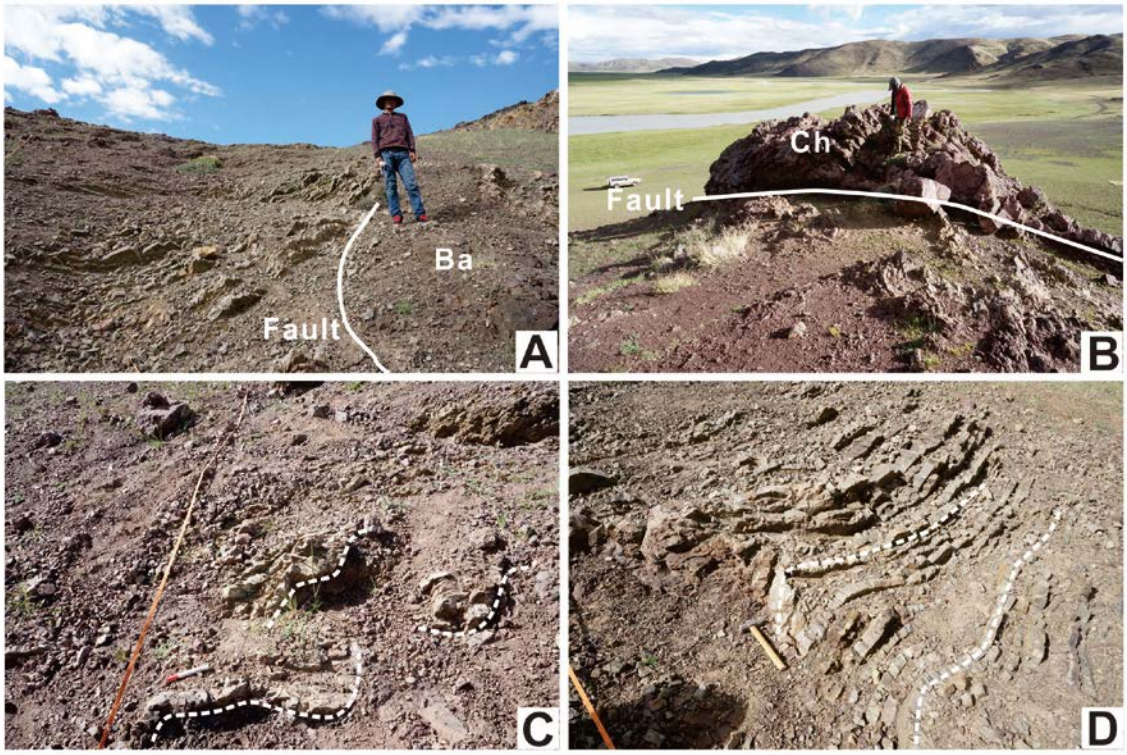

Fig. 5.27 Outcrops showing outcrop-scale structures. ba= basalt, ch= chert. **A:** Fault between basalt block and chert sequence of unit 2; **B:** Fault between chert block and chert sequence of unit 1; **C:** Folds in unit 3; **D:** Folds in unit 2.

Fig. 5.28 Rock samples showing veins and trace fossils. CV=calcite vein, QV=quartz vein. **A:** Sample SB030; **B:** Sample SB033; **C:** Sample SB047.

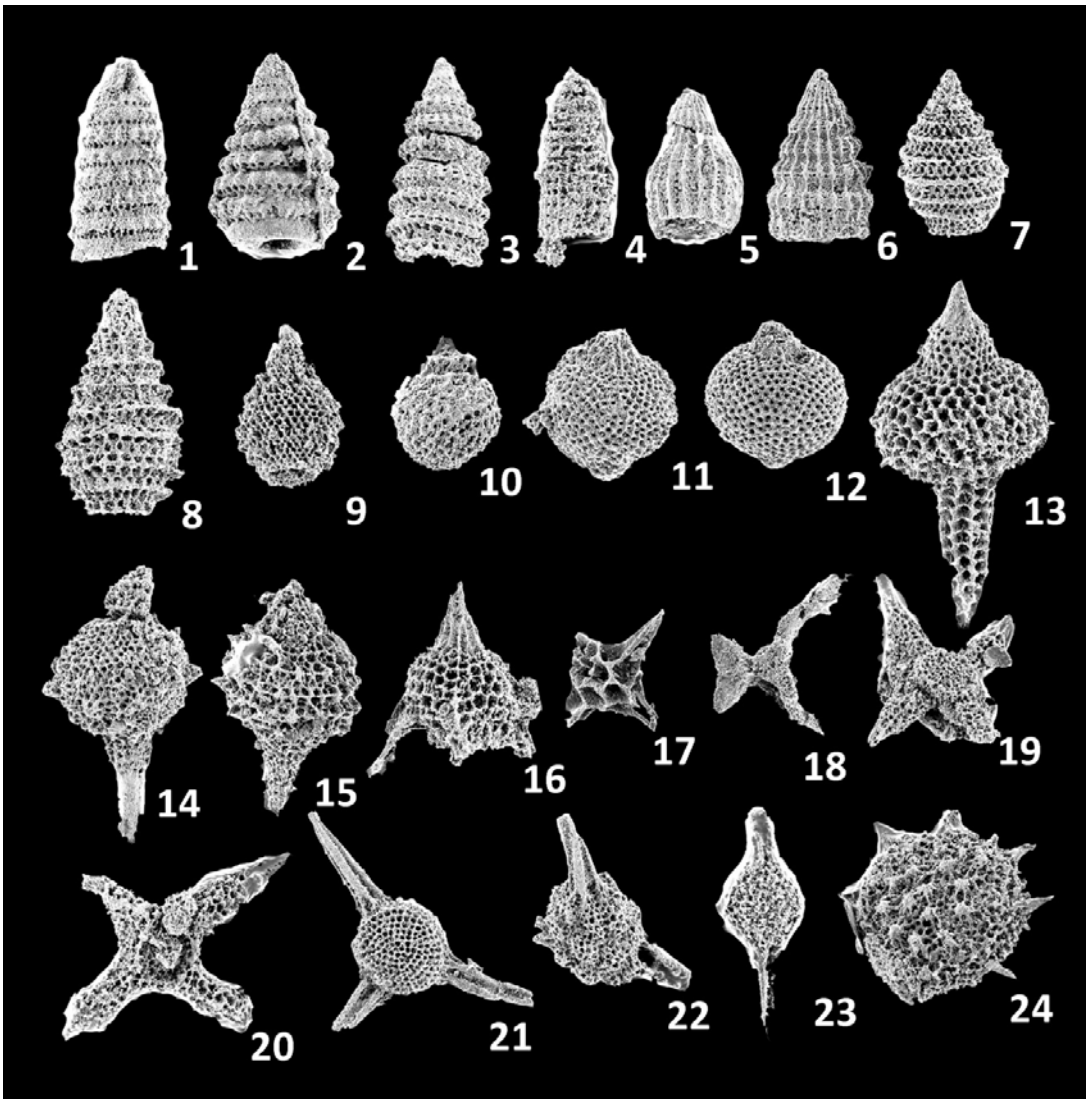

Fig. 5.29 Scanning electron micrographs of radiolarian assemblage from a red chert (sample SB-002). **1, 2.** *Pseudodictyomitra carpatica* (Loziniyak); **3.** *Svinitzium depressum* (Baumgartner); **4, 5.** *Archaeodictyomitra* sp. **6.** *Archaeodictyomitra pseudoscalaris* (Tan sin Hok); **7.** *Tethysetta boessi* (Parona); **8.** *Tethysetta usotanensis* (Tumanda); **9.** *Tethysetta* sp. **10.** *Hiscocapsa uterculus* (Parona); **11, 12.** *Williriedellum carpathicum* Dumitrica; **13–15.** *Podobursa* sp. **16.** *Napora* sp. **17.** *Cecrops septemporatus* (Parona); **18.** *Acanthocircus trizonalis dicranacanthos* (Squinabol); **19.** *Crucella remanei* Jud; **20.** *Crucella bossoensis* Jud; **21.** *Suna echiodes* (Foreman); **22.** *Acastea diaphorognona* (Foreman); **23.** *Archaeospongoprunum* sp. **24.** *Pseudoaulophacus* sp.

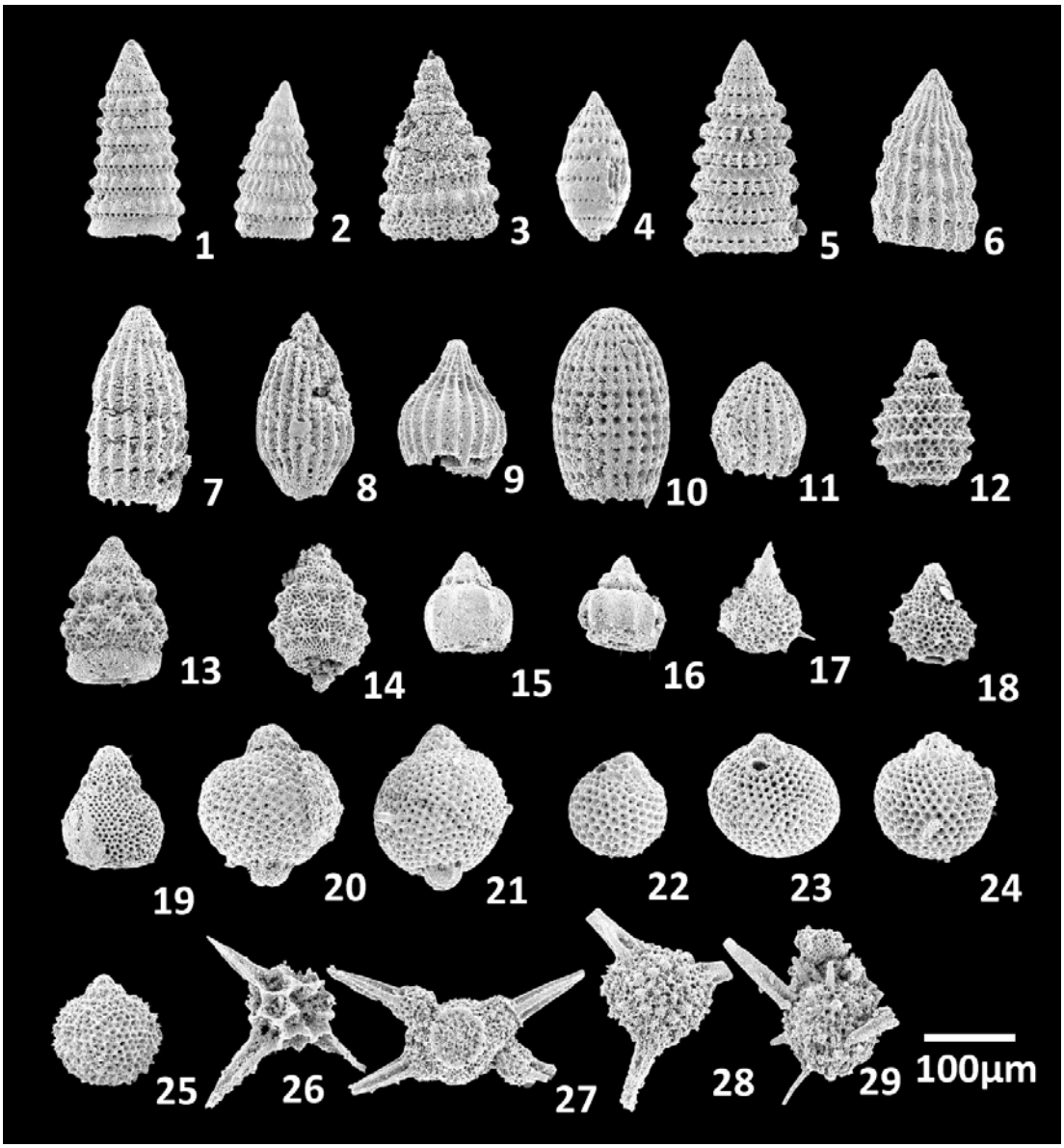

Fig. 5.30 Scanning electron micrographs of radiolarian assemblage from a red chert (sample SB-007). **1, 2.** *Pseudodictyomitra carpatica* (Loziniyak); **3.** *Cinguloturris cylindra* Kemkin et Rudenko; **4.** *Loopus nuda* (Schaaf); **5.** *Svinitzium depressum* (Baumgartner); **6.** *Archaeodictyomitra pseudoscalaris* (Tan sin Hok); **7–9, 11.** *Archaeodictyomitra* sp. **10.** *Archaeodictyomitra apiarium* Rüst; **12.** *Tethysetta usotanensis* (Tumanda); **13, 14.** *Xitus* sp. **15, 16.** *Eucyrtidiellum pyramis* (Aita); **17, 18.** *Sethocapsa* sp. **19.** *Stichmitra doliolum* Aita; **20, 21.** *Hemicryptocapsa capita* Tan; **22–24.** *Cryptamphorella conara* (Foreman); **25.** *Zhamoidellum* sp. **26.** *Cecrops septemporatus* (Parona); **27.** *Crucella* sp. **28, 29.** *Becus triangulocentrum* Dumitrica

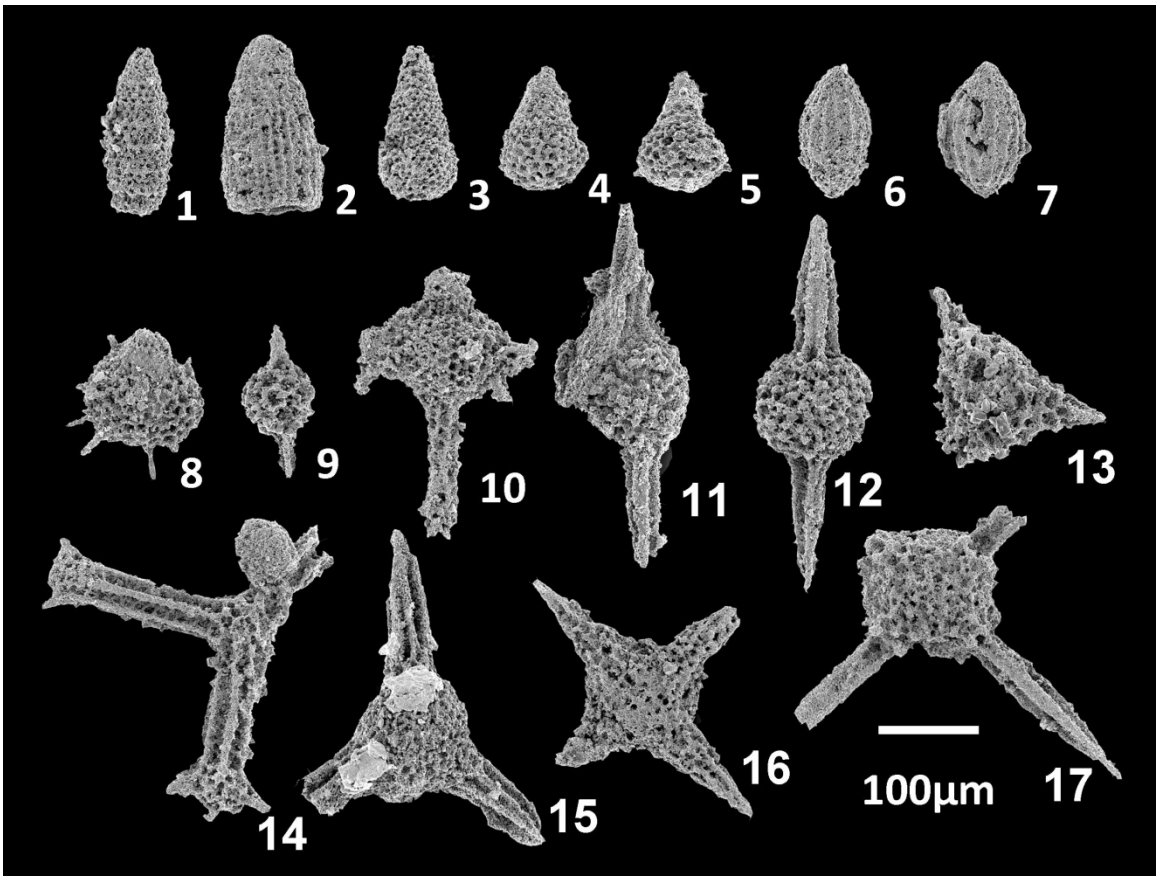

Fig. 5.31 Scanning electron micrographs of radiolarian assemblage from a green chert (sample SB-027). **1.** *Tethysetta dhimeniaensis* (Baumgartner); **2.** *Archaeodictyomitra* sp. **3.** *Amphipyndax tsunoensis* Aita; **4, 5.** *Amphipyndax* sp. **6, 7.** *Protunuma* sp. **8.** *Sethocapsa aculeata* Cortese; **9.** *Pantanellium* sp. **10.** *Podobursa* sp. **11, 12 13.** *Perispyridium ordinarium* (Pessagno); **14.** *Halesium* sp. **15.** *Triactoma jonesi* (Pessagno); **16.** *Crucella* sp. **17.** *Emiluvia* sp.

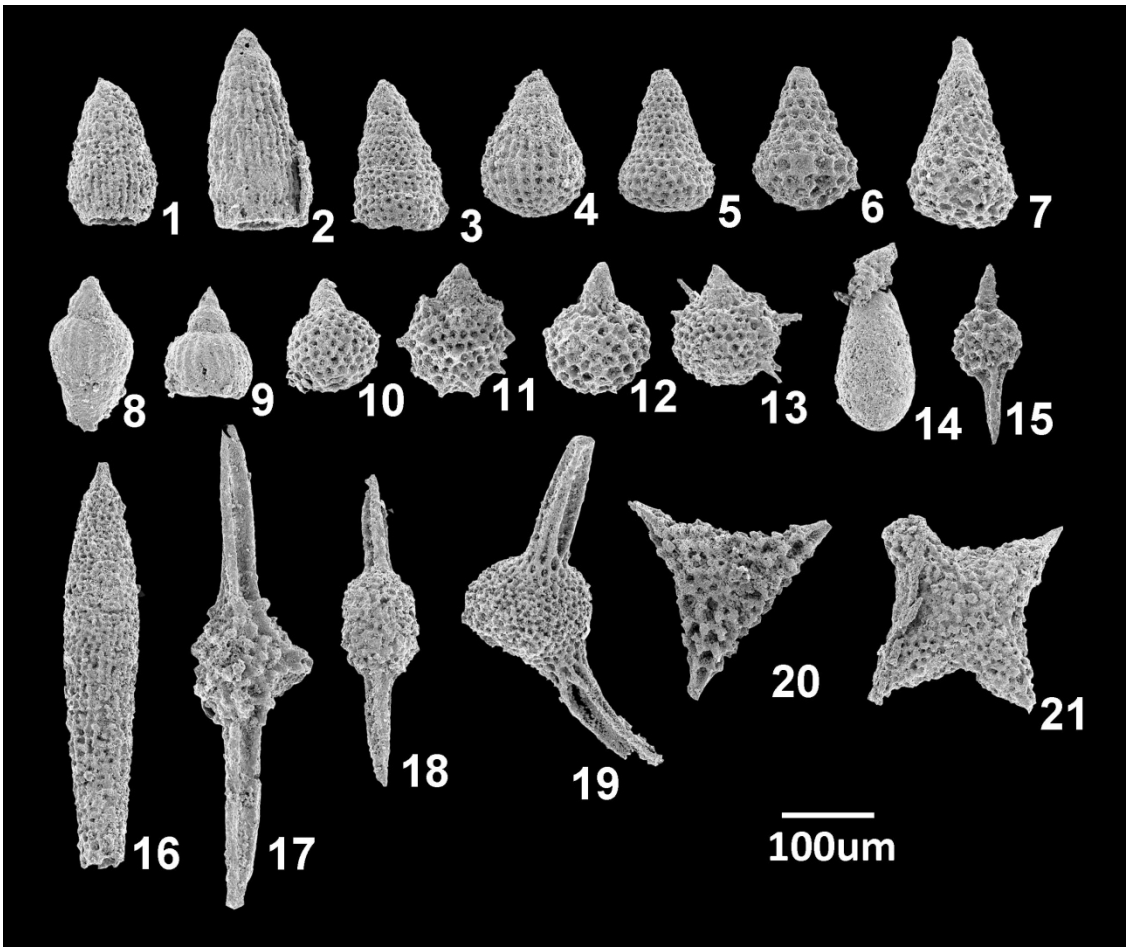

Fig. 5.32 Scanning electron micrographs of radiolarian assemblage from a green chert (sample SB-041). **5–7.** *Amphipyndax tsunoensis* Aita; **8, 9.** *Eucyrtidiellum ptyctum* (Reidel and Sanfilippo); **10, 12.** *Hiscocapsa* sp. **11.** *Sethocapsa trachyostraca* Foreman; **13.** *Sethocapsa aculeata* Cortese; **14.** *Gongylothorax sakawaensis* Matsuoka; **15.** *Pantanellium* sp. **16.** *Pseudoeucyrtis* sp. **17 18.** *Archaeospongoprunum* sp. **19.** *Triactoma* sp. **20.** *Perispyridium ordinarium* (Pessagno); **21.** *Crucella* sp.

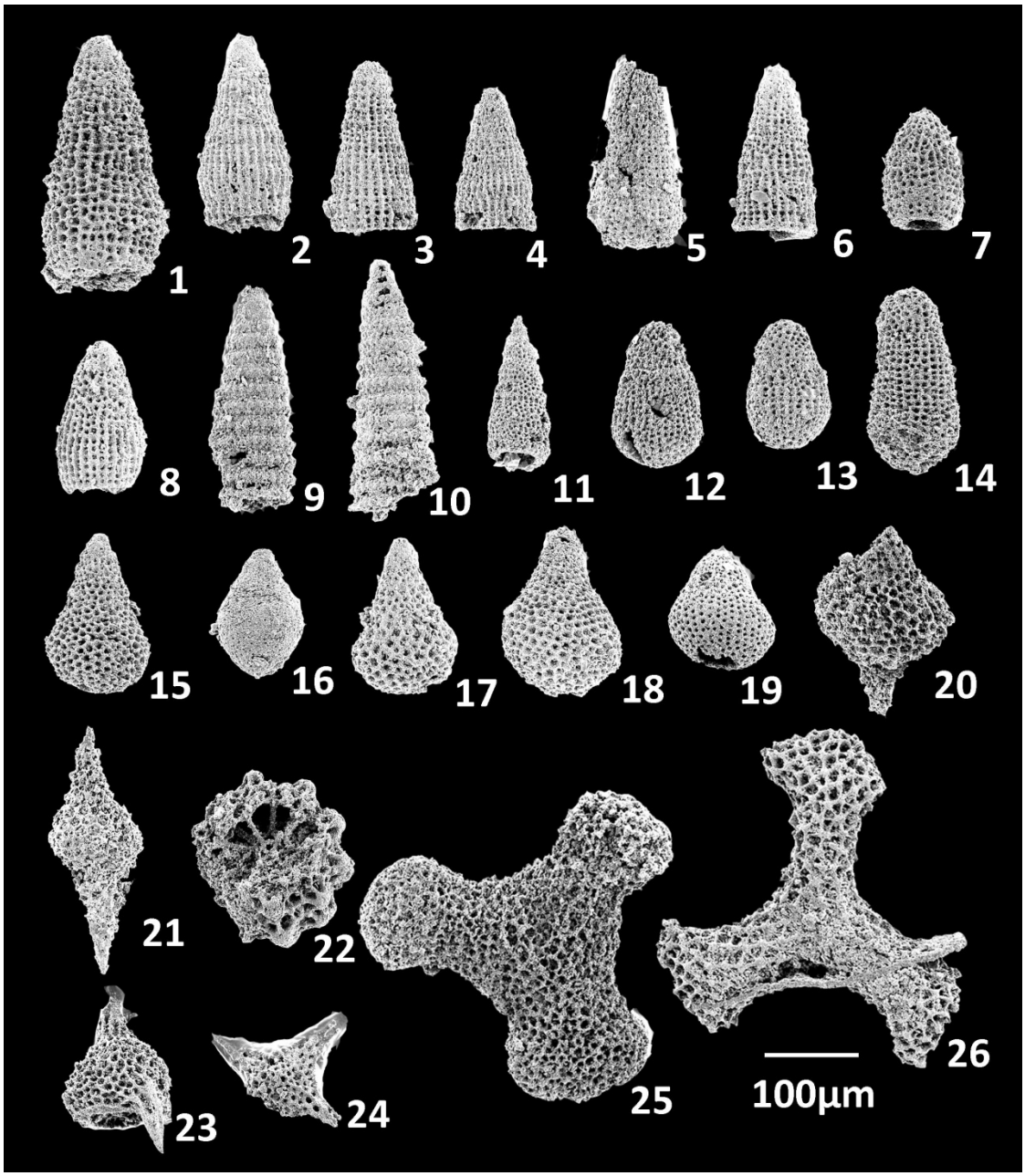

Fig. 5.33 Scanning electron micrographs of radiolarian assemblage from a red chert (sample SB-047). **1–6.** *Parahsuum simplum* Yao; **7, 8.** *Parahsuum* sp. **9, 10.** *Canoptsum anulatum* Passagno & Poisson; **12–14.** *Bagotum* sp. **15, 17, 18.** *Pseudoristola* sp. **16.** *Stichocapsa plicata* Matsuoka; **19.** *Stichocapsa* sp. **20, 21.** *Katroma* sp. **22.** *Holocryptocanium tuberculatum* Dumitrica; **25, 26.** *Paronaella* sp.

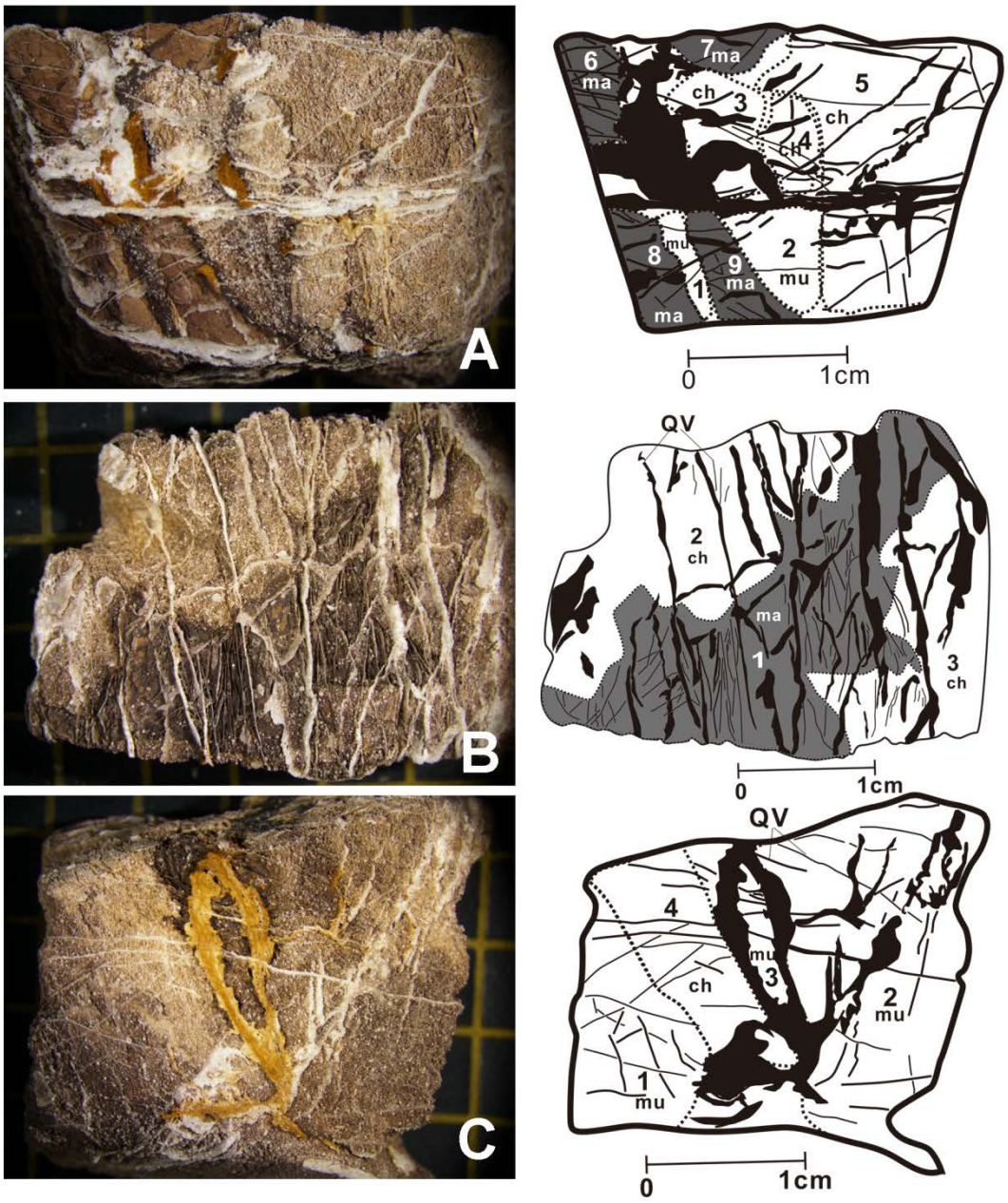

Fig. 5.34 Etched surfaces and sketches of sample SB002. ch=chert, mu=siliceous mudstone, ma=mudstone matrix, QV=quartz vein. **A**: SB002-1; **B**: SB002-2; **C**: SB002-3.

Fig. 5.35 Etched surfaces and sketches of sample SB007. ch= chert, mu=siliceous mudstone, ma=mudstone matrix, CV=calcite vein, QV=quartz vein, SV=siliceous vein. **A**: SB007-1; **B**: SB007-2; **C**: SB007-3; **D**: SB007-4.

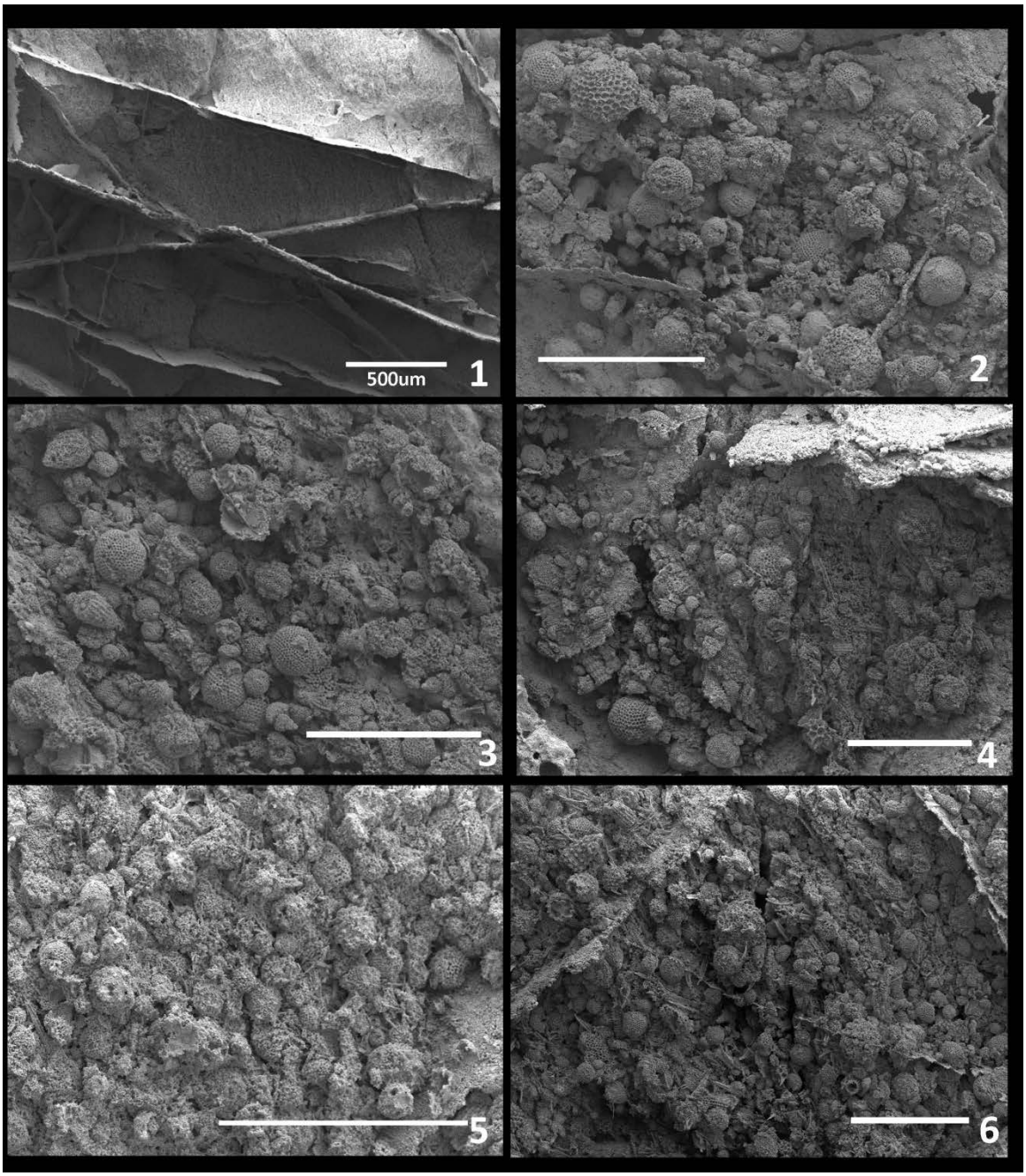

Fig. 5.36 Scanning electron micrographs of the etched surface (sample SB002-1). Figure numbers correspond to those in fig. 5.34A.

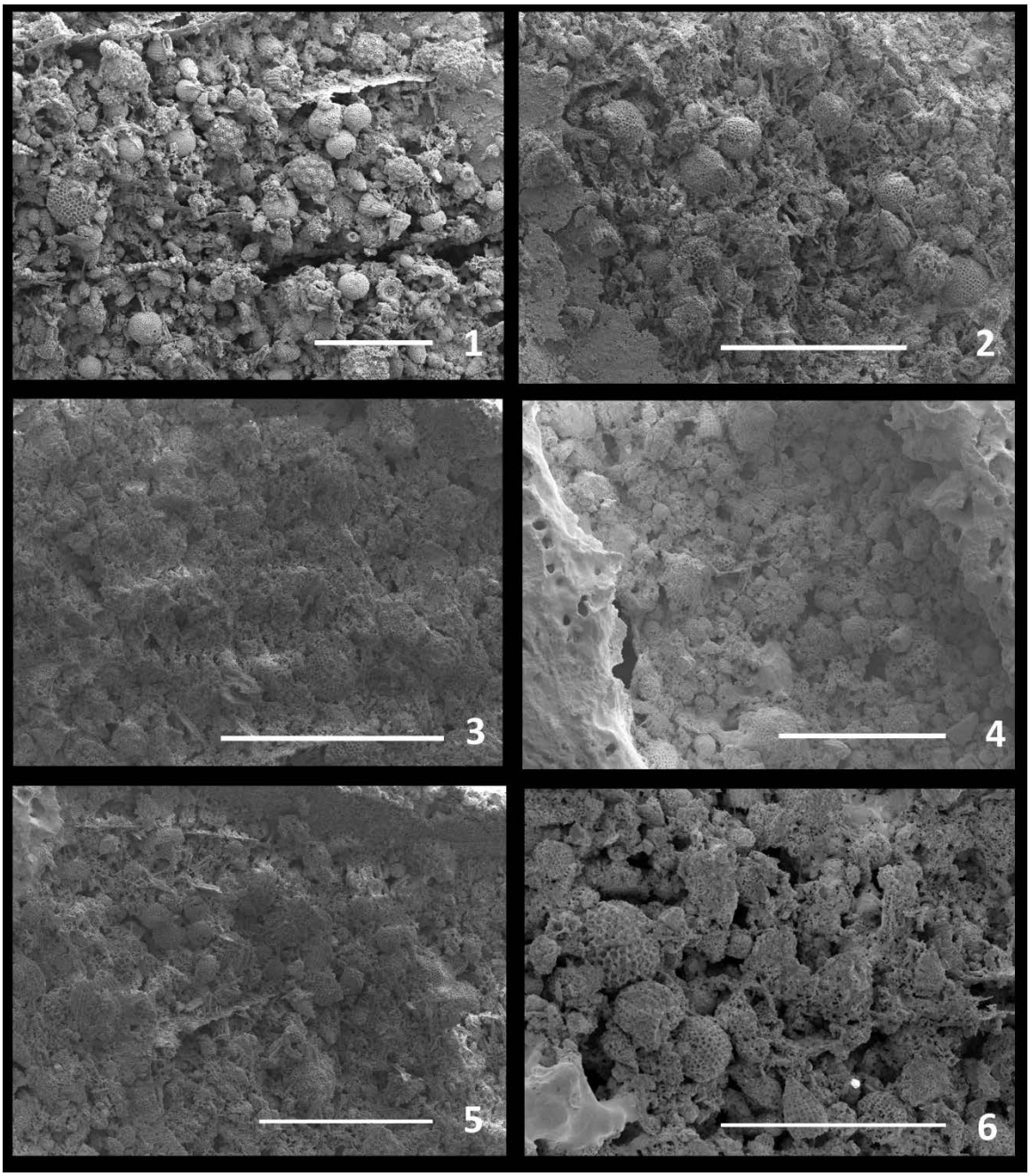

Fig. 5.37 Scanning electron micrographs of the etched surface (sample SB002-3).The scale bars are 500 um. Part numbers correspond to those in fig. 5.34C. 1 from part 1; 2 from part 1, near the boundary between part 1 and part 2; 3 from part 2; 4 from part 3; 5 from part 4 near the boundary between part 3 and part 4; 6 from part 4.

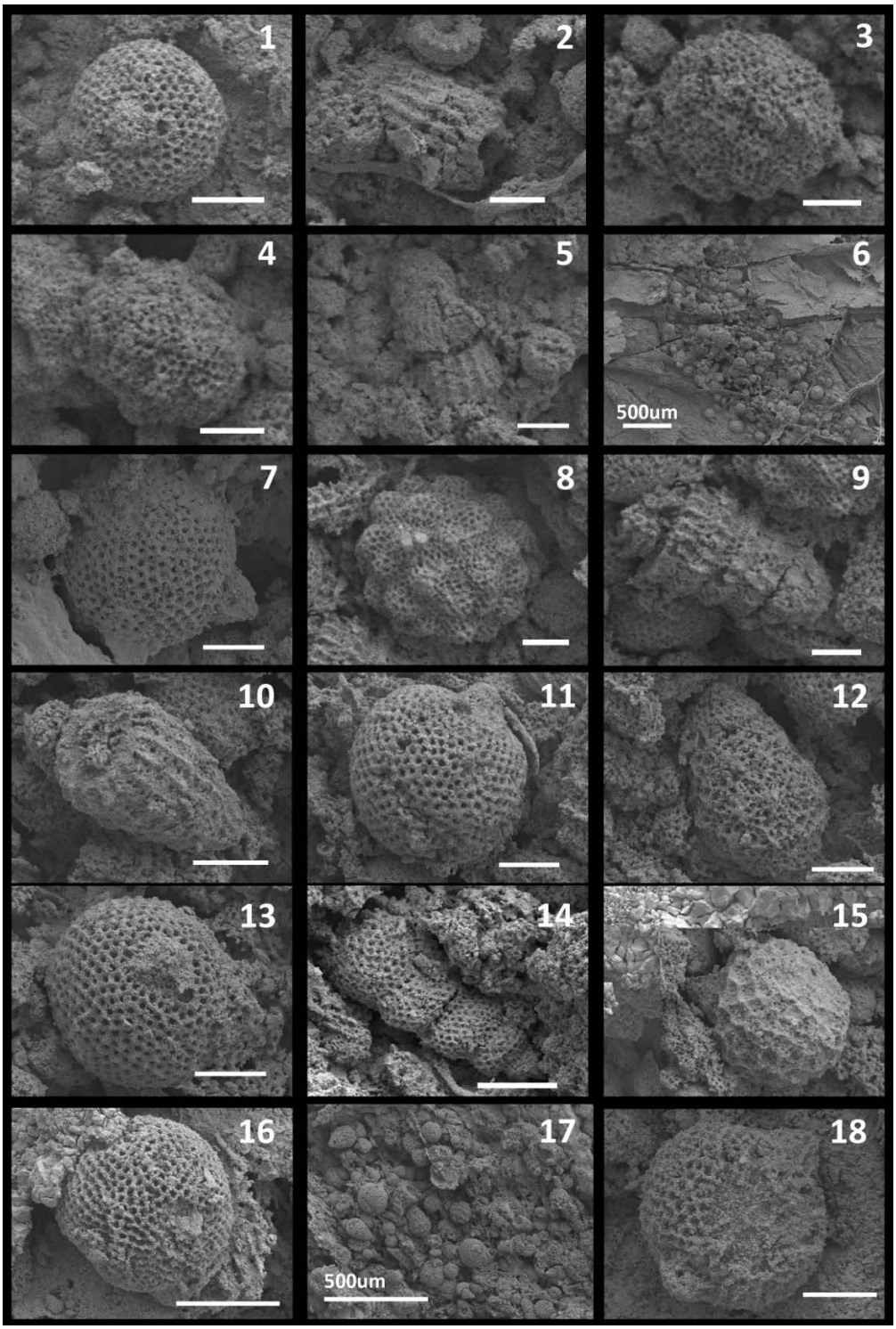

Fig. 5.38 Scanning electron micrographs of radiolarian assemblage from a breccia (sample SB-002-1). The scale bars are 50 um. Part numbers correspond to those in fig. 5.34A. 1–6 from part 2; 3–14 from part 2; 7–17 from part 3; 18 from part 4. **1, 11, 13.** *Cryptamphorella conara* (Foreman); **2, 5, 10.** *Archaeodictyomitra* sp. **3, 4, 8.** *Holocryptocanium tuberculatum* Dumitrica; **7, 16, 18.** *Williriedellum carpathicum* Dumitrica; **9.** *Pseudodictyomitra carpatica* (Loziniyak); **12.** *Xitus* sp. **14.** *Stichomitra communis* Squinabol; **15.** *Sethocapsa trachyostraca* Foreman

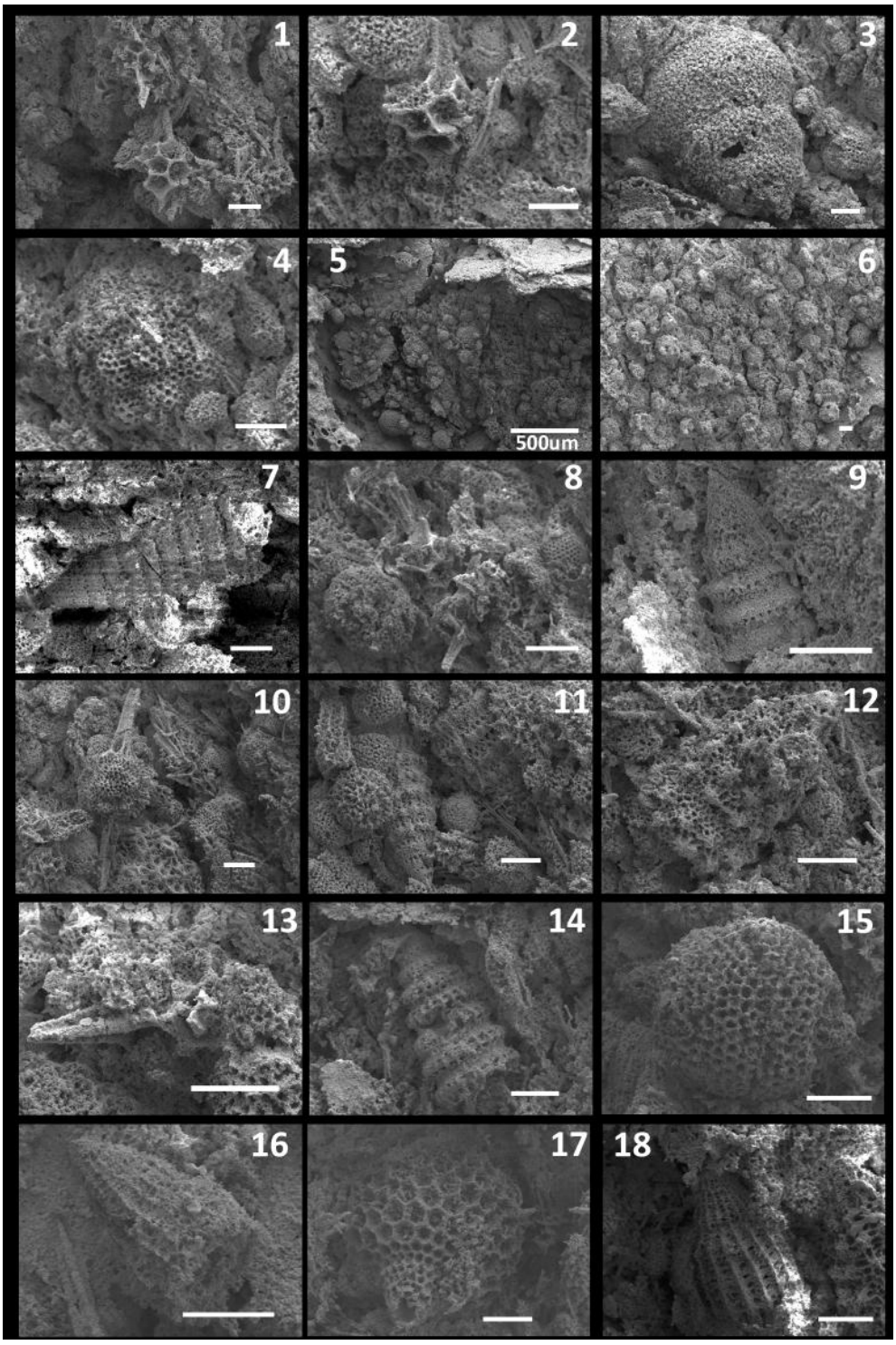

Fig. 5.39 Scanning electron micrographs of radiolarian assemblage from a breccia (sample SB-002-1). The scale bars are 50 um. Part numbers correspond to those in fig. 5.34A. 1–5 from part 4; 6 from part 5; 7–18 from part 6. **1, 2, 8, 13.** *Cecrops septemporatus* (Parona); **4.** *Holocryptocanium tuberculatum* Dumitrica; **7, 9, 11.** *Pseudodictyomitra carpatica* (Loziniyak); **10.** *Acaeniotyle umbilicata* (Rust); **12.** *Xitus* sp. **14.** *Svinitzium depressum* (Baumgartner); **15.** *Williriedellum carpathicum* Dumitrica; **16, 18.** *Archaeodictyomitra* sp. **17.** *Sethocapsa* sp.

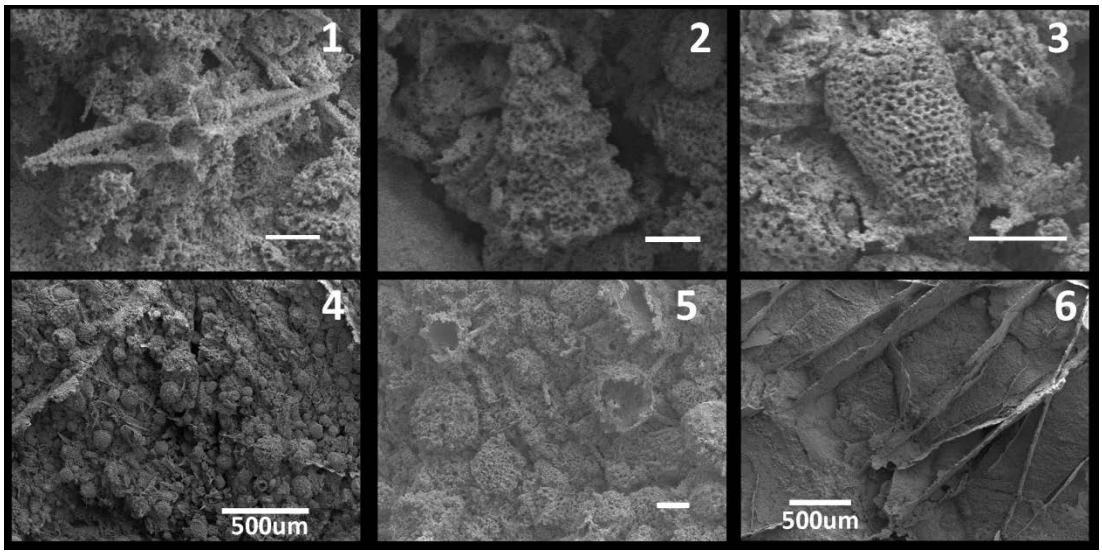

Fig. 5.40 Scanning electron micrographs of radiolarian assemblage from a breccia (sample SB-002-1). The scale bars are 50 um. Part numbers correspond to those in fig. 5.34A. 1–5 from part 6; 6 from part 1. **1.** *Cecrops septemporatus* (Parona); **2.** *Xitus* sp. **3.** *Stichomitra* sp.

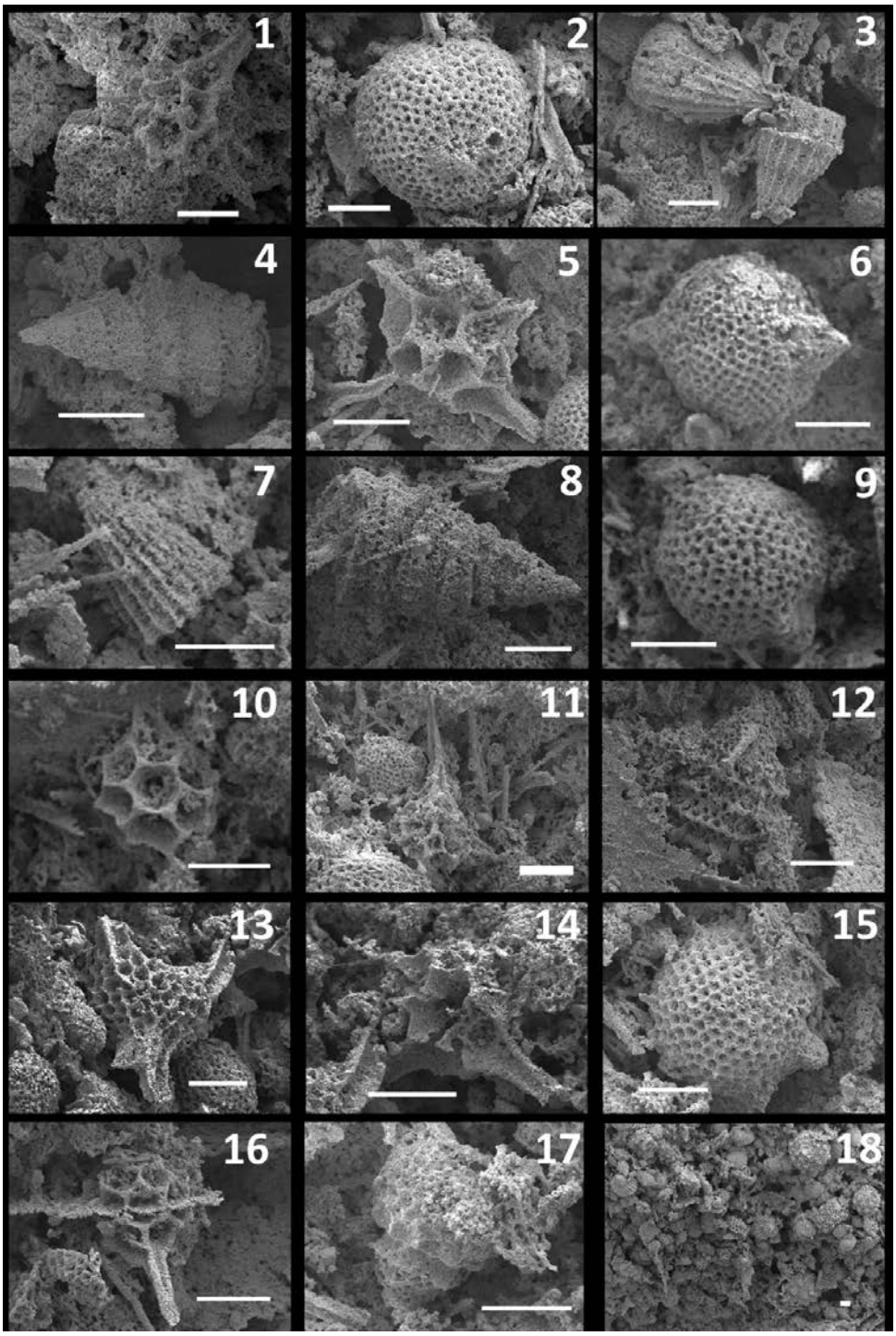

Fig. 5.41 Scanning electron micrographs of radiolarian assemblage from a breccia (sample SB-002-3). The scale bars are 50 um. All the specimens from part 1 in fig. 5.34C. **1, 5, 10, 11, 14, 16.** *Cecrops septemporatus* (Parona); **2.** *Cryptamphorella conara* (Foreman); **3, 7.** *Archaeodictyomitra* sp. **4, 8.** *Pseudodictyomitra carpatica* (Loziniyak); **6.** *Hemicryptocapsa capita* Tan; **9.** *Holocryptocanium barbui* Dumitrica; **12.** *Tethysetta boessi* (Parona); **13.** *Ultranapora* sp. **17.** *Hiscocapsa uterculus* (Parona)

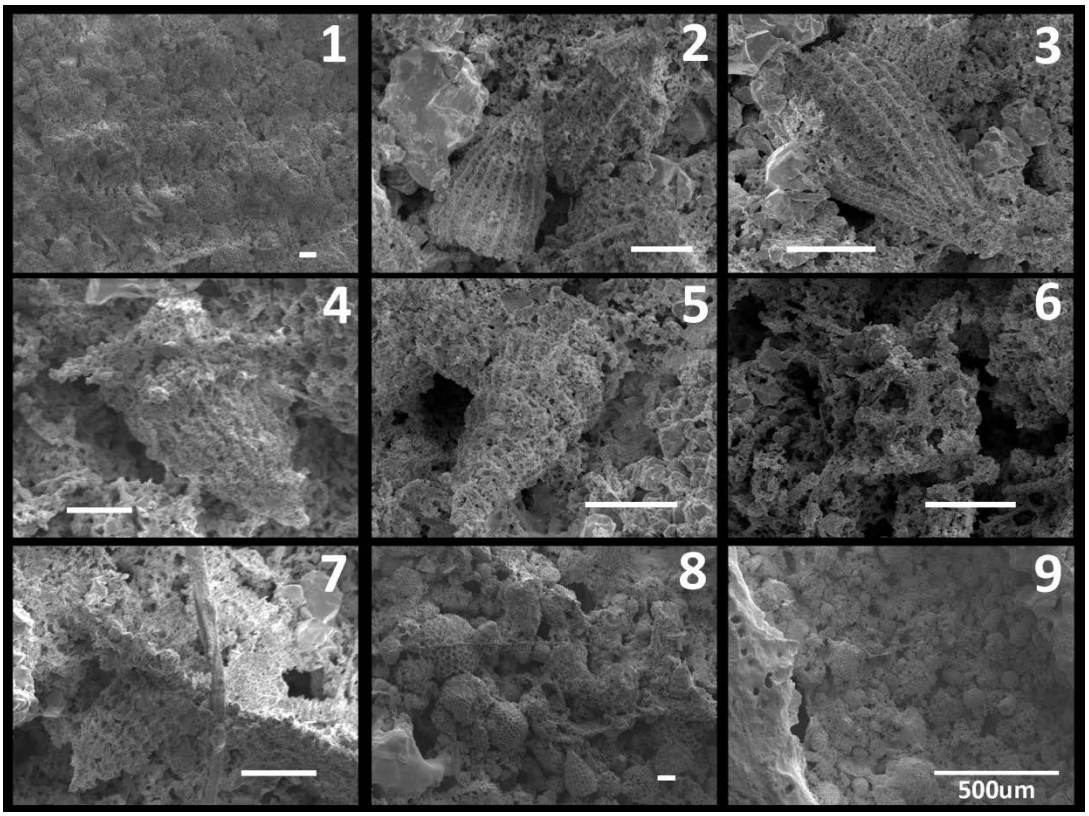

Fig. 5.42 Scanning electron micrographs of radiolarian assemblage from a breccia (sample SB-002-3). The scale bars are 50 um. Part numbers correspond to those in fig. 5.34C. 1–8 from part 4; 9 from part 3. **2, 3.** *Archaeodictyomitra* sp. **5.** *Archaeodictyomitra pseudoscalaris* (Tan sin Hok); **6.** *Cecrops septemporatus* (Parona); **7.** *Archaeodictyomitra excellens* (Tan)

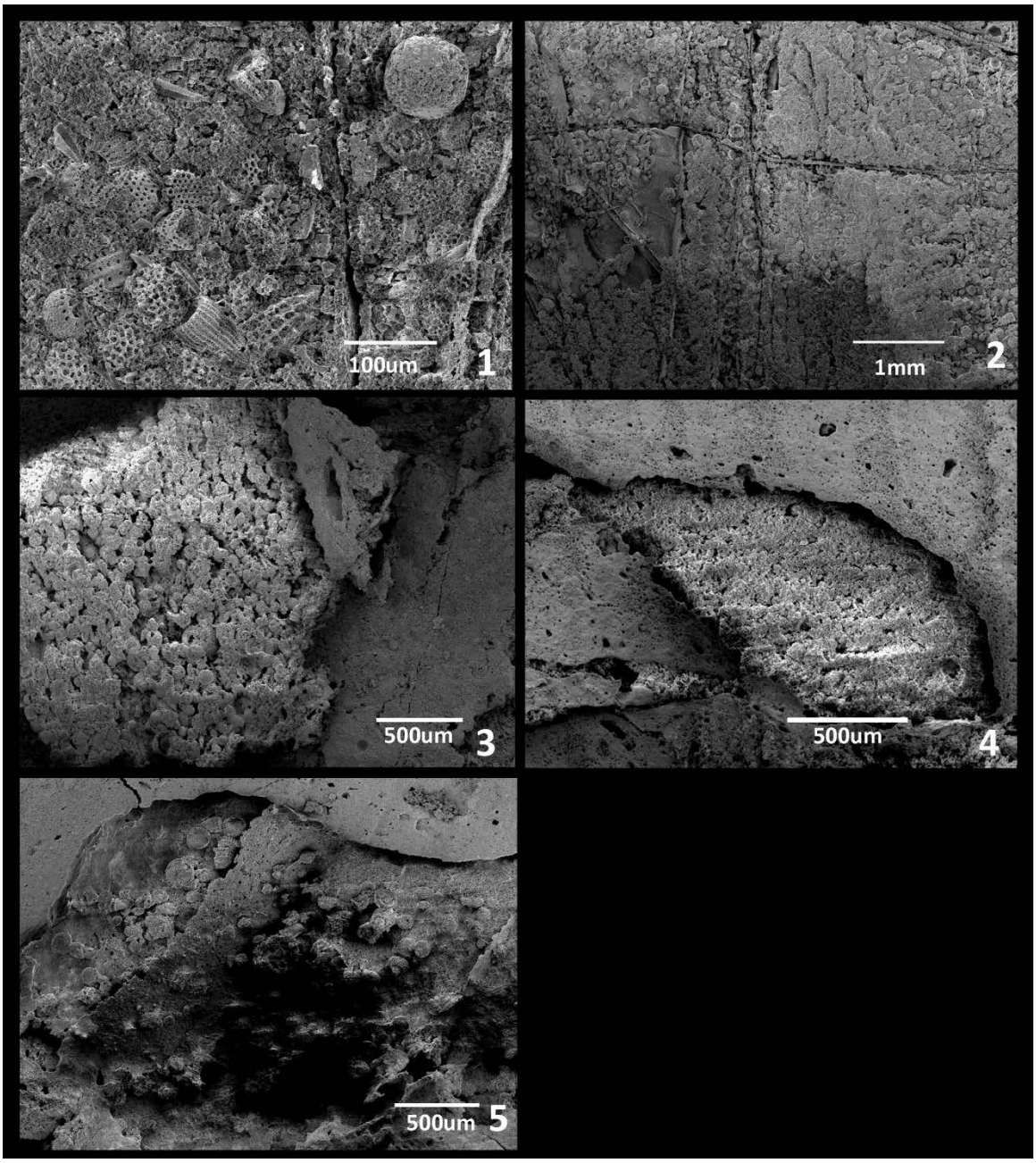

Fig. 5.43 Scanning electron micrographs of the etched surface (samples SB007-1 and SB007-2). Part numbers corresponds to those in fig. 5.35A, B. 1, 2 from part 1 in sample SB007-1; 3 from part 3 in sample SB007-1; 4 from part 4 in sample SB007-1; 5 from part 1 in sample SB007-2.

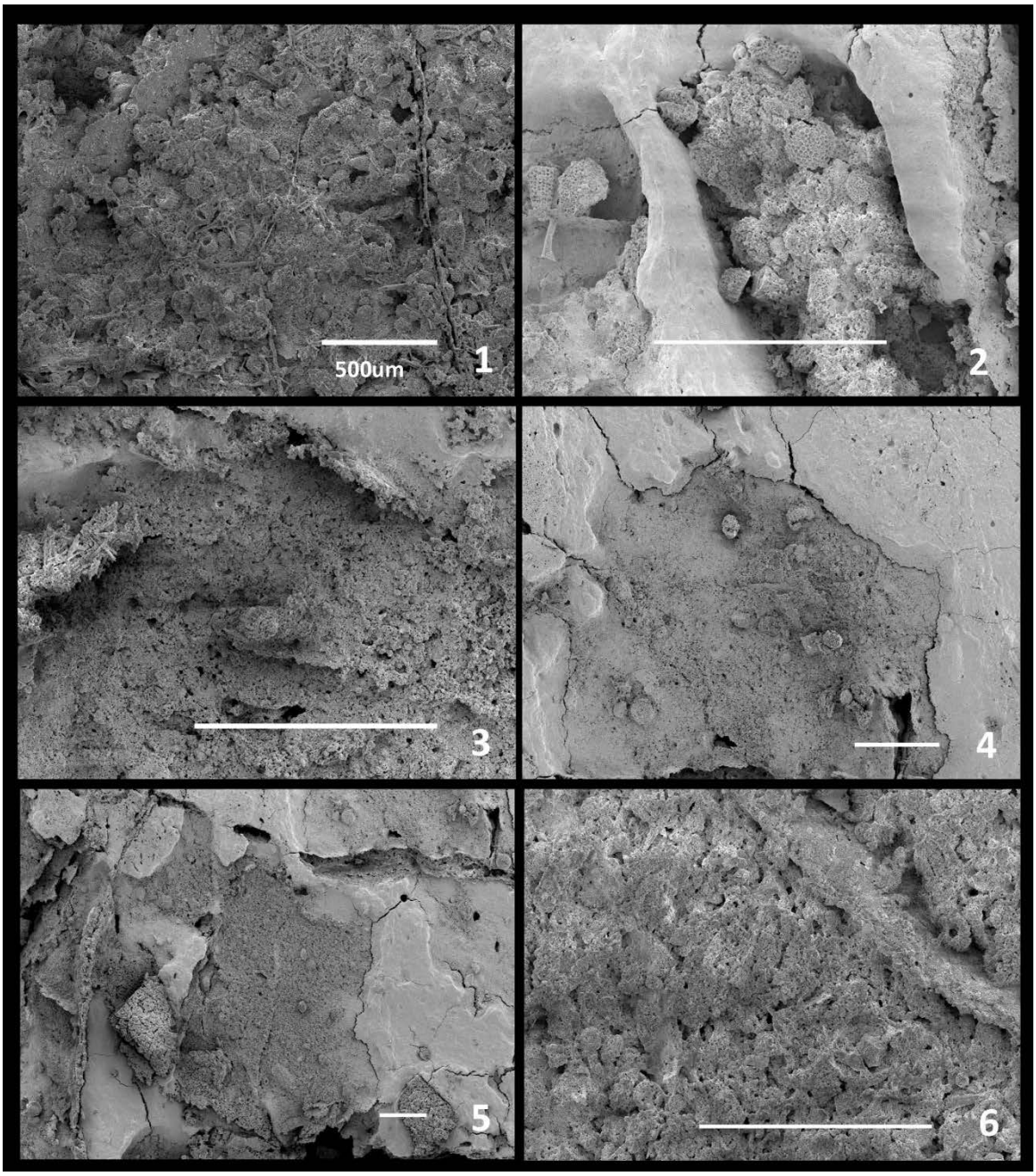

Fig. 5.44 Scanning electron micrographs of the etched surface (samples SB007-3 and SB007-4). The scale bars are 500 um. Part numbers correspond to those in fig. 5.35C, D. 1 from part 1 in sample SB007-3; 2 from part 3 in sample SB007-3; 3 from part 5 in sample SB007-3; 4 from part 6 in sample SB007-3; 5 from part 7 in sample SB007-3; 6 from part 1 in sample SB007-4.

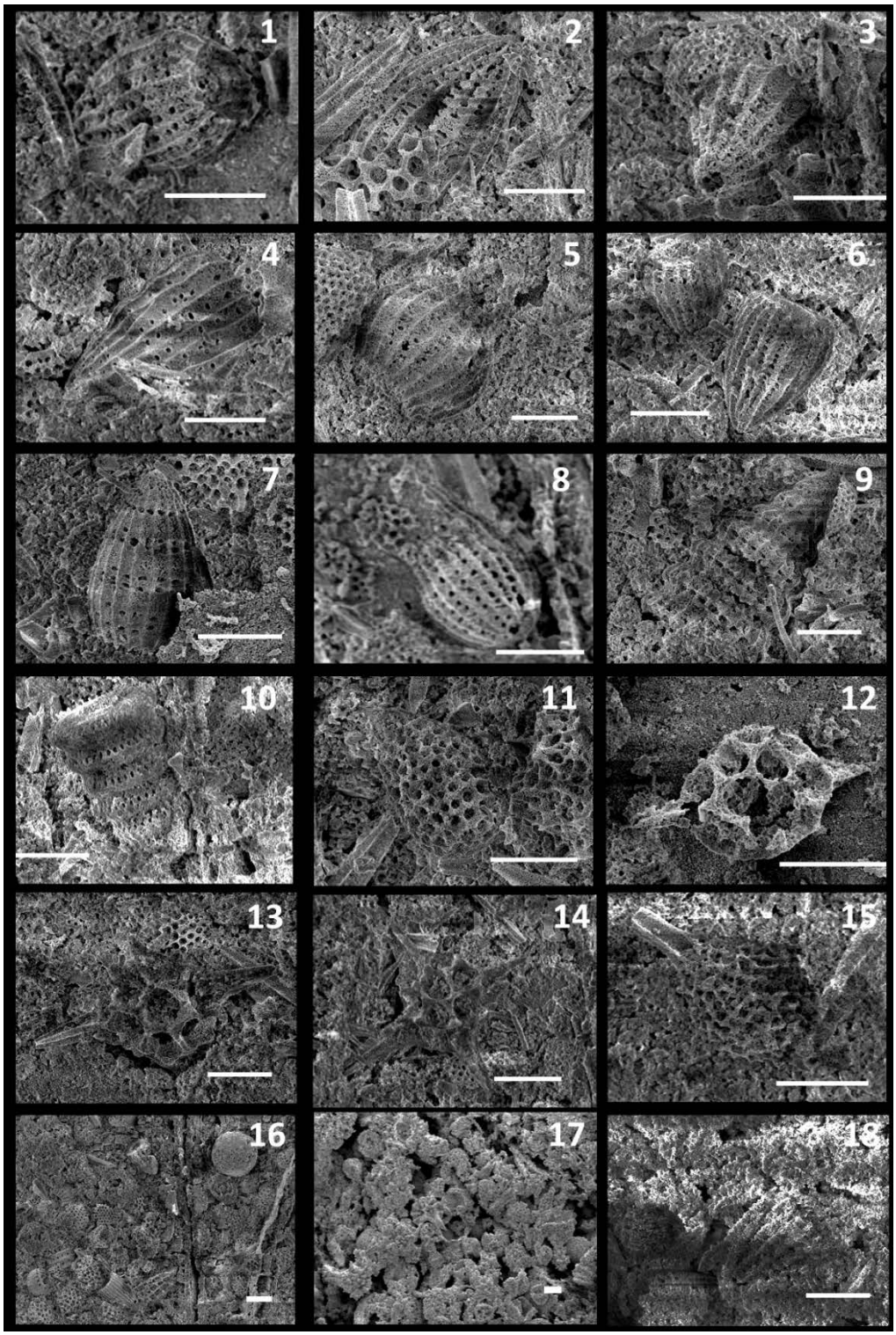

Fig. 5.45 Scanning electron micrographs of radiolarian assemblage from a breccia (sample SB-007-1). The scale bars are 50 um. All the specimens from part 1 in fig. 5.35A. **1–8, 18.** *Archaeodictyomitra* sp. **9.** *Svinitzium depressum* (Baumgartner); **10.** *Pseudodictyomitra carpatica* (Loziniyak); **11.** *Stichomitra* sp. **12.** *Pantanellium* sp. **13, 14.** *Cecrops septemporatus* (Parona); **15.** *Archaeospongoprunum* sp.

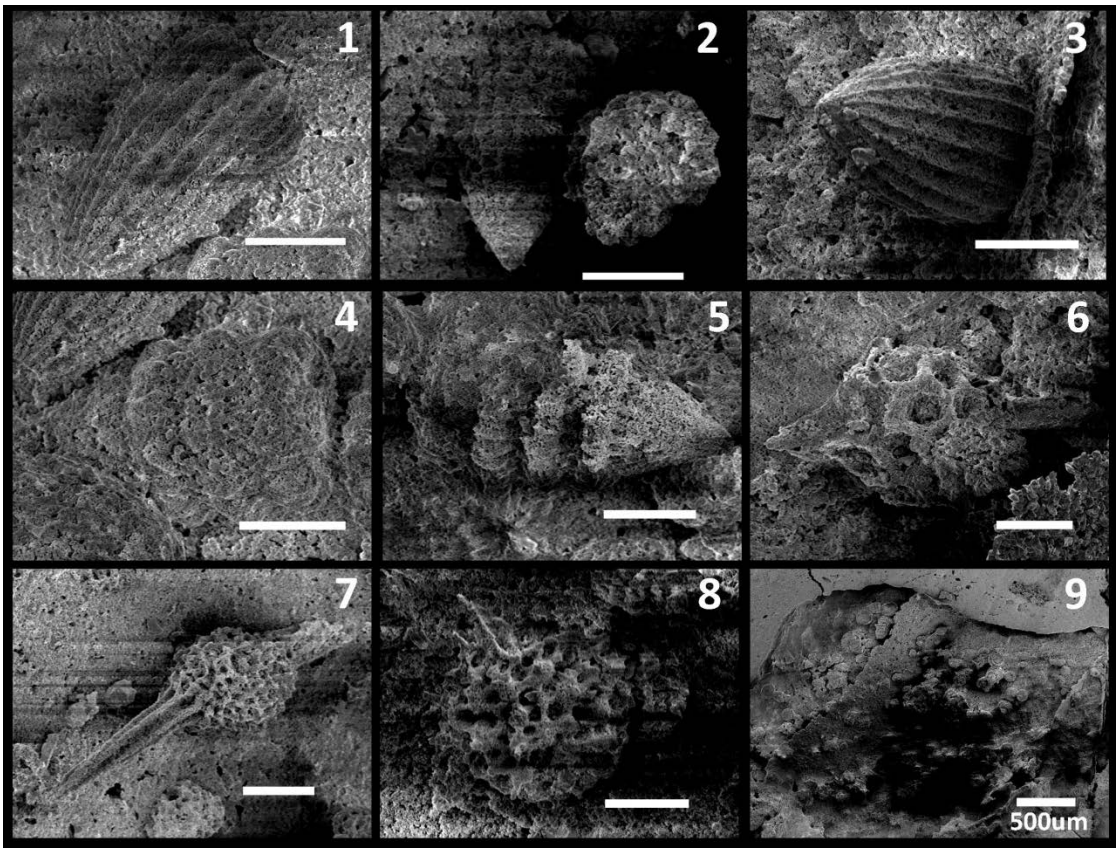

Fig. 5.46 Scanning electron micrographs of radiolarian assemblage from a breccia (sample SB-007-2). The scale bars are 50 um. All the specimens from part 1 in fig. 5.35B. **1–3.** *Archaeodictyomitra* sp. **4.** *Pseudodictyomitra* sp. **5.** *Svinitzium depressum* (Baumgartner); **6.** *Pantanellium* sp. **7.** *Archaeospongoprunum* sp.

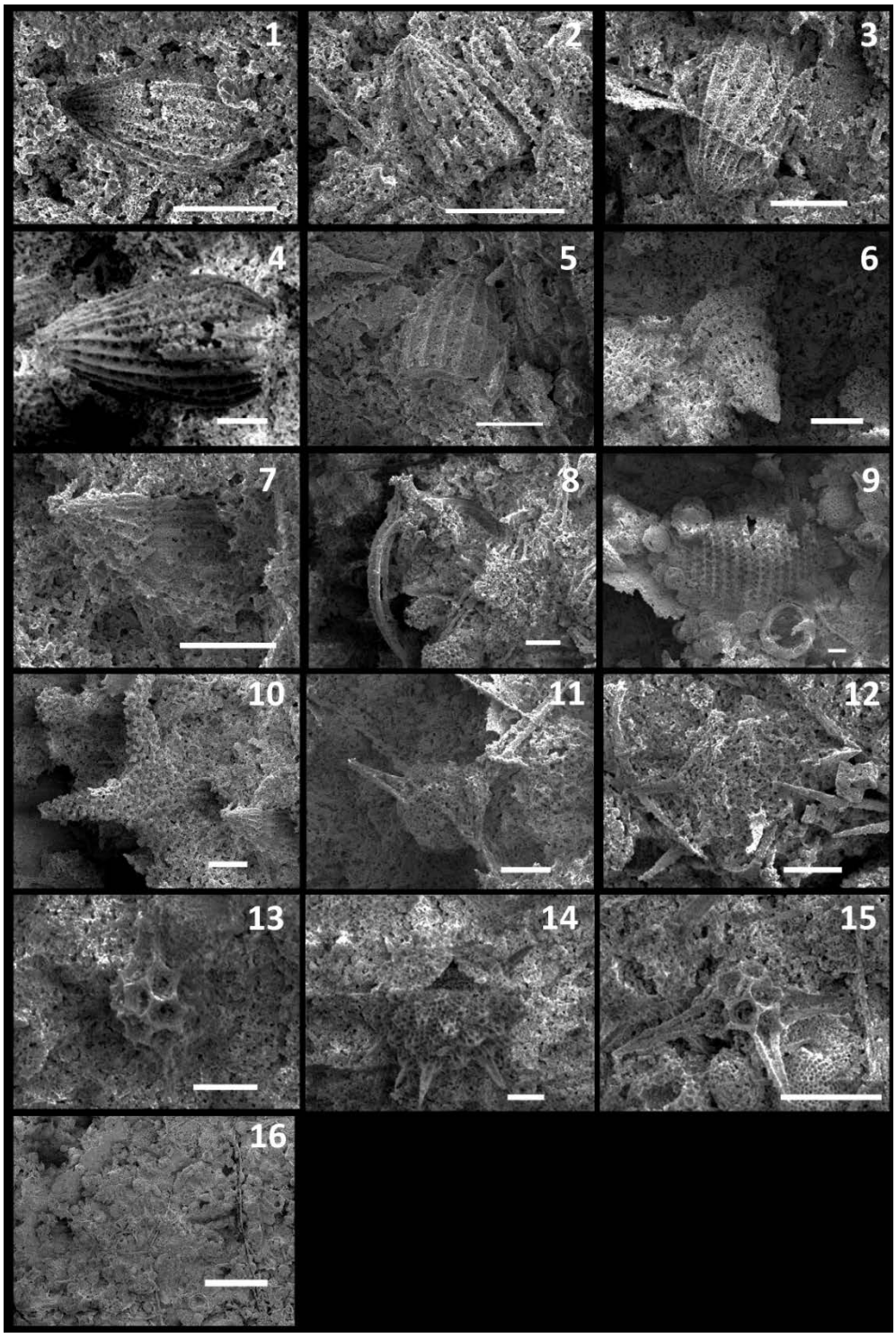

Fig. 5.47 Scanning electron micrographs of radiolarian assemblage from a breccia (sample SB-007-3). The scale bars are 50 um. All the specimens from part 1 in fig. 5.35C. **1–5.** *Archaeodictyomitra* sp. **6.** *Svinitzium* sp. **7.** *Pseudodictyomitra* sp. **8.** *Cecrops septemporatus* (Parona); **9.** *Mirifusus* sp. **10.** *Crucella* sp. **11.** *Suna* sp. **13.** *Pantanellium* sp. **15.** *Cecrops septemporatus* (Parona)

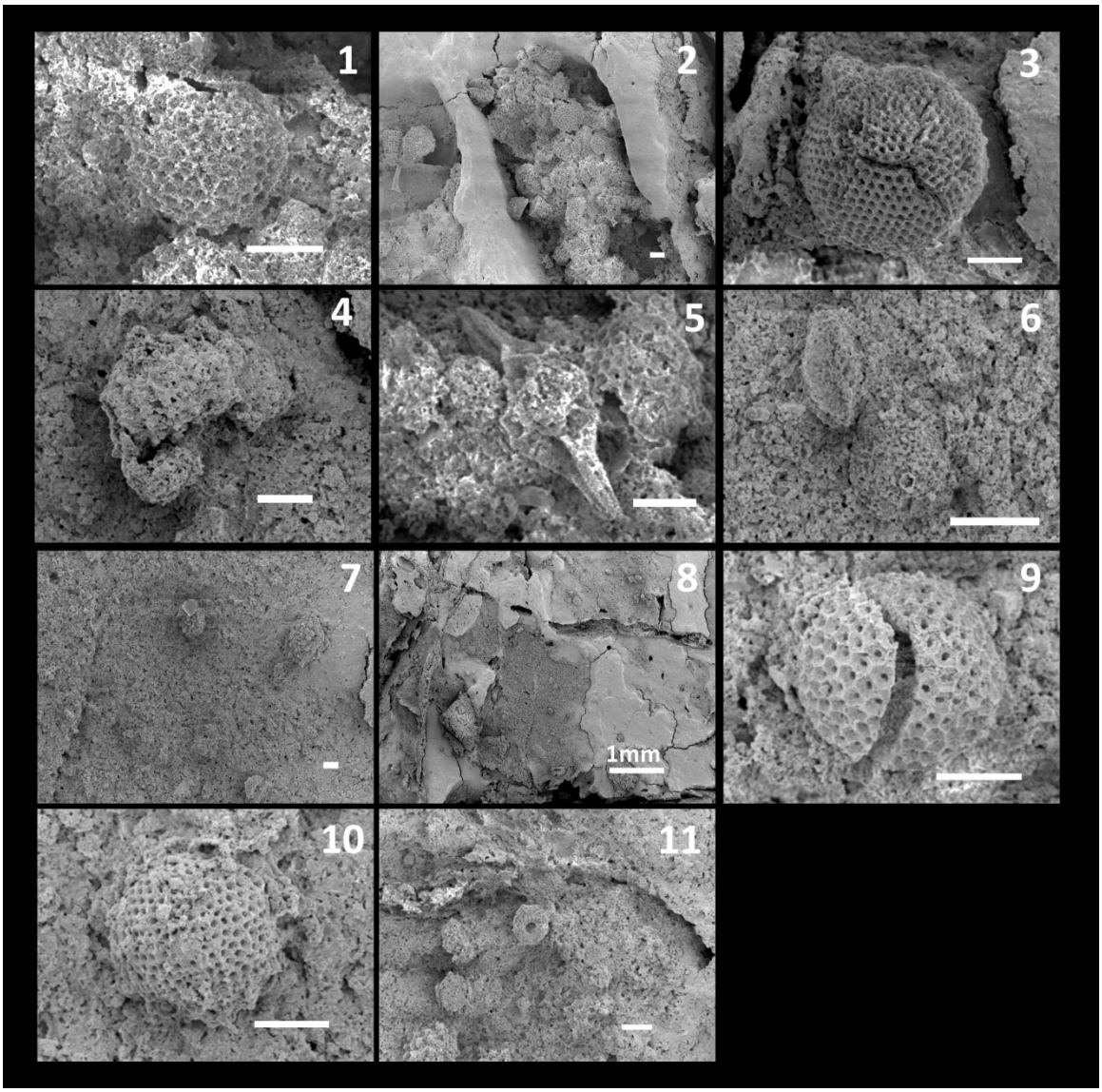

Fig. 5.48 Scanning electron micrographs of radiolarian assemblage from a breccia (sample SB-007-3). The scale bars are 50 um. Parts numbers are corresponding to those in fig. 5.35C. 1, 2 from part 2; 3–7 from part 6; 8–11 from part 7. **1.** *Hiscocapsa uterculus* (Parona); **2.** *Hiscocapsa orca* (Foreman); **5.** *Pantanellium* sp. **9, 10.** *Holocryptocanium* sp.

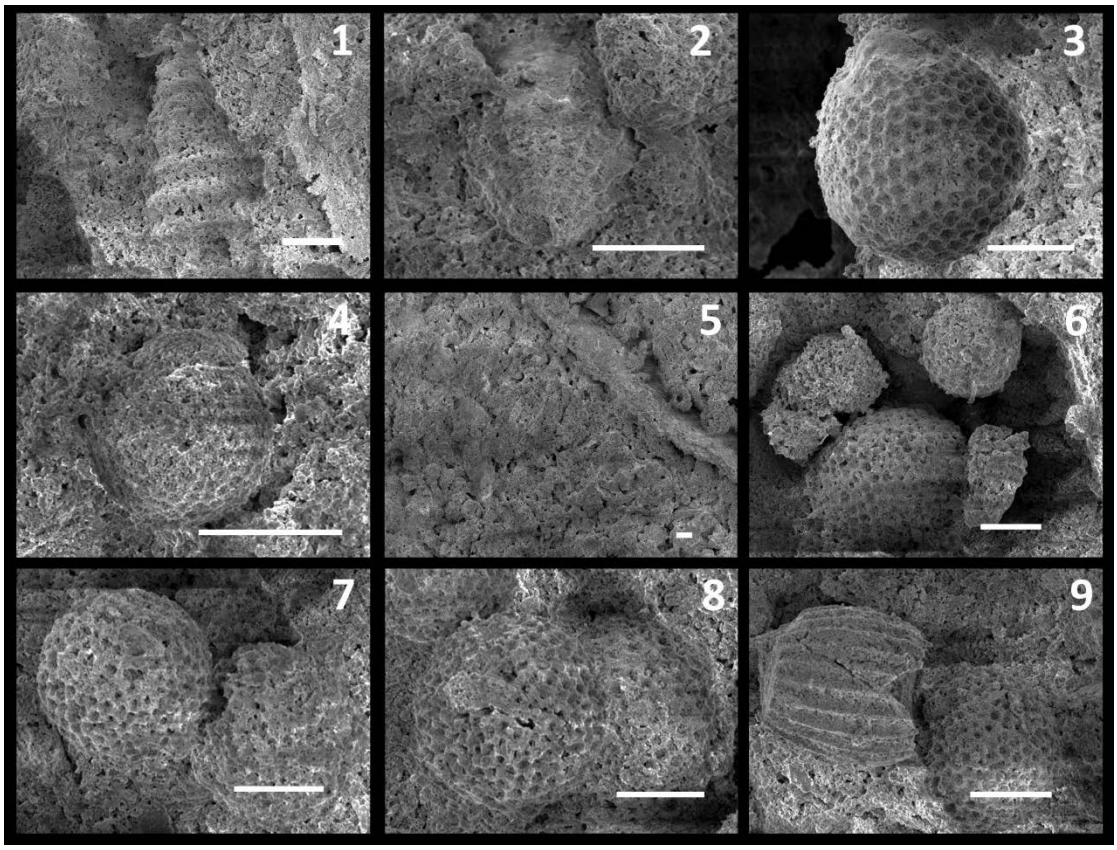

Fig. 5.49 Scanning electron micrographs of radiolarian assemblage from a breccia (sample SB-007-4). The scale bars are 50 um. Part numbers correspond to those in fig. 5.35D. 1–5 from part 1; 6–9 from part 2. **1.** *Pseudodictyomitra carpatica* (Loziniyak); **2, 9.** *Archaeodictyomitra* sp. **3, 8.** *Cryptamphorella conara* (Foreman); **4, 7.** *Holocryptocanium* sp.

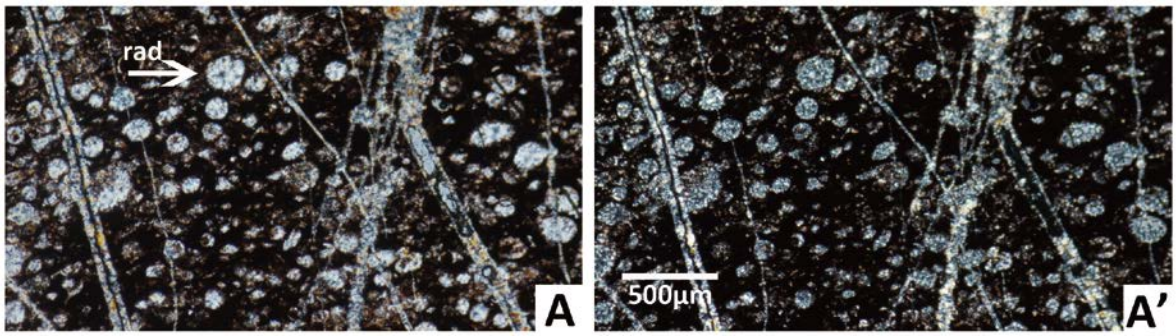

Fig. 5.50 Photographs showing chert with abundant radiolarians (sample 0807-031-1). A is in plane polarized light. A' is in perpendicular polarized light.

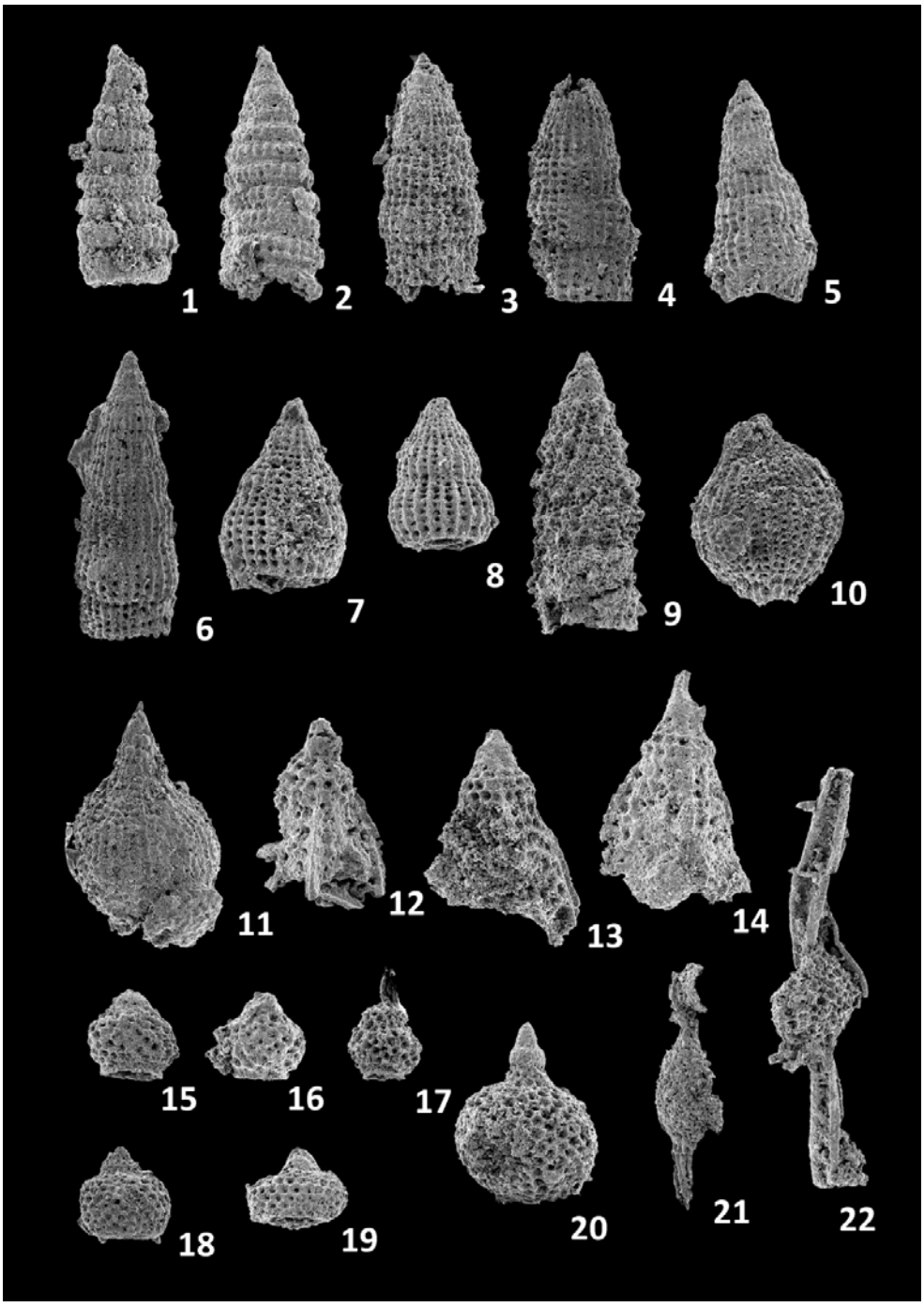

Fig. 5.51 Scanning electron micrographs of radiolarian assemblage from a red chert (sample 0807-032). **1, 2.** *Pseudodictyomitra* sp. **3, 4, 6.** *Dictyomitra montisserei* (Squinabol); **5.** *Dictyomitra gracilis* (Squinabol); **7, 8.** *Thanarla brouweri* (Tan); **9.** *Crolanium* sp. **10.** *Thanarla cucurbita* O'Dogherty; **11.** *Thanarla spoletoensis* O'Dogherty; **12–14.** *Ultranapora praespinifera* Pessagno; **15, 16.** *Rhopalosyringium mosquense* (Smirnova & Aliev); **17.** *Rhopalosyringium* sp. **18, 19.** *Rhopalosyringium* sp. **20.** *Squinabollum fossilis* (Squinabol); **21.** *Archaeospongoprunum cortinaensis* Pessagno; **22.** *Archaeospongoprunum* sp.

Table 5-1 Occurrence of Early Cretaceous radiolarians from clasts in sample 0808-033

Sample	0808—033																			
Clast No.	—1	—2	—3	—4	—5	—7	—8	—9	—10	—11	—13	—15	—16	—17	—19	—20	—22	—23	—26
Abundance	A	A	C	C	C	A	C	C	C	C	C	C	A	C	C	C	C	C	C
Preservation	G	G	G	G	G	M-B	G	G	G	G	G	G	M-B	G	G	G	G	G	G
Radiolarian Zone	—	KR2	—	—	KR1	KR2	KR2	KR1	KR1	KR1	—	KR1	KR2	—	KR1	KR1	KR2	KR1	—
Pseudodictyomitra carpatica (Loziniyak)					●	●		●	●	●		●			●	●	●	●	
Loopus primitivus (Matsuoka & Yao)															●		●		
Loopus nuda (Schaaf)			●					●			●		●	●			●		●
Svinitzium depressum (Baumgartner)	●	●		●	●		●	●	●	●		●	●		●	●	●		
Svinitzium pseudopuga Dumitrica																			
Praeparvicingula cosmoconica (Foreman)																			
Tethysetta boessi (Parona)																			
Tethysetta usotanensis (Tumanda)																			
Cinguloturris cylindra Kemkin et Rudenko																			
Archaeodictyomitra apiarium Rüst																			
Archaeodictyomitra pseudoscalaris (Tan sin Hok)									●		●						●		
Archaeodictyomitra excellens (Tan)							●	●					●						
Archaeodictyomitra minoensis (Mizutani)																			
Thanarla pulchra (Squinabol)															●				
Mictyoditra lacrimula (Foreman)																			
Neorelumbra kiesslingi Dumitrica																			
Neorelumbra buwaydahensis Kiessling																			
Eucyrtidiellum pyramis (Aita)																			
Mirifusus dianae minor Baumgartner																			
Stichomitra sp. aff. *S. euganea* (Squinabol)																			
Stichmitra doliolum Aita																			
Sticomitra communis (Squinabol)		●																	
Hiscocapsa kaminogoensis (Aita)											●								
Hiscocapsa sp. aff. *H. kaminogoensis* (Aita)																			
Hiscocapsa zweilii (Jud)																			
Hiscocapsa uterculus (Parona)					●							●						●	
Hiscocapsa pseudouterculus (Aita)																			
Hiscocapsa orca (Foreman)							●												
Hiscocapsa grutterinki (Tan)							●											●	
Sethocapsa aculeata Cortese													●						
Zhamoidellum ovum Dumitrica							●	●			●								
Hemicryptocapsa capita Tan		●											●			●	●		
Hemicryptocapsa tuberose Dumitrica							●												
Cryptamphorella conara (Foreman)			●	●			●		●	●				●	●		●		●
Williriedellum carpathicum Dumitrica																			
Obesacapsula cetia (Foreman)			●																
Holocryptocanium barbui Dumitrica			●							●	●	●							
Holocryptocanium tuberculatum Dumitrica								●											
Gongylothorax verbeeki (Tan Sin Hok)																			●
Cecrops septemporatus (Parona)		●				●	●						●				●		
Pantanellium squinaboli (Tan)																		●	
Pantanellium lanceola (Parona)									●										
Acanthocircus trizonalis dicranacanthos (Squinabol)								●										●	
Becus triangulocentrum Dumitrica																			
Crucella remanei Jud																			
Crucella bossoensis Jud																			
Suna echiodes (Foreman)																			
castea diaphorognona (Foreman)																			
Acaeniotyle dentate Baumgartner		●																	

The abundance (Ab: A-abundant, C-common, F-few) and preservation (Pr: G-good, M-moderate, P-poor) are shown in the table.

Table 5-2 Lithology and radiolarians in the clasts from SB007

	lithology	shape	internal veins	Ab	Pr	boundary	Zone
SB007-1-1	chert	rectangular	abundant	A	G-M	sharp	KR2
SB007-1-2	chert	angular	rare	A	P	sharp	—
SB007-1-3	chert	rectangular	rare	A	P	sharp	—
SB007-1-4	chert		rare	A	P	sharp	—
SB007-2-1	siliceous mudstone		few	C	M	sharp	—
SB007-2-2	chert	rectangular	few	A	P		—
SB007-2-3	chert	rectangular	rare	A	P		—
SB007-3-1	chert	rectangular	abundant	A	G-M	sharp	KR2
SB007-3-2	siliceous mudstone		rare	C	M-P	vague	—
SB007-3-3	chert	rectangular	none	A	M-P	sharp	—
SB007-3-4	chert	rectangular	few	A	P	sharp	—
SB007-3-5	siliceous mudstone		none	F	M-P	vague	—
SB007-3-6	siliceous mudstone		none	F	M-P	vague	—
SB007-3-7	siliceous mudstone		none	F	M-P	vague	—
SB007-3-8	chert	angular	none	A	P	sharp	—
SB007-3-9	chert	angular	none	A	P	sharp	—
SB007-3-10	chert	rectangular	few	A	P	sharp	—
SB007-4-1	chert	angular	common	A	M-P	sharp	KR1
SB007-4-2	siliceous mudstone	angular	few	C	M-P	sharp	—
SB007-4-3	chert	angular	rare	A	P	sharp	—
SB007-4-4	chert	angular	rare	A	p	sharp	—
SB007-4-5	chert	angular	rare	A	P	sharp	—
SB007-4-6	chert	rectangular	none	A	p	sharp	—
SB007-4-7	chert	rectangular	rare	A	P	sharp	—
SB007-4-8	chert	angular	few	A	P	sharp	—

Clasts numbers correspond to those in fig. 5.35. The abundance (Ab: A-abundant, C-common, F-few) and preservation (Pr: G-good, M-moderate, P-poor) are shown in the table.

Table 5-3 Occurrence of Early Cretaceous radiolarians from clasts in samples SB002 and SB007

Sample	SB002						SB007			
Pieces No.	—1				—2		—1	—2	—3	—4
Clast No.	—2	—3	—4	—6	—1	—4	—1	—1	—1	—1
Abundance	A	A	A	A	A	A	A	C	A	C
Preservation	G	G	G	G	G	M	G-M	M	G-M	M-P
Radiolarian Zone	—	KR1	KR2	KR2	KR2	KR2	KR2	—	KR2	KR1
Pseudodictyomitra carpatica (Loziniyak)		●		●	●		●			●
Loopus primitivus (Matsuoka & Yao)										
Loopus nuda (Schaaf)										
Svinitzium depressum (Baumgartner)				●			●	●		
Svinitzium pseudopuga Dumitrica										
Praeparvicingula cosmoconica (Foreman)										
Tethysetta boessi (Parona)					●					
Tethysetta usotanensis (Tumanda)										
Cinguloturris cylindra Kemkin et Rudenko										
Archaeodictyomitra apiarium Rüst										
Archaeodictyomitra pseudoscalaris (Tan sin Hok)						●				
Archaeodictyomitra excellens (Tan)						●				
Archaeodictyomitra minoensis (Mizutani)										
Thanarla pulchra (Squinabol)										
Mictyoditra lacrimula (Foreman)										
Neorelumbra kiesslingi Dumitrica										
Neorelumbra buwaydahensis Kiessling										
Eucyrtidiellum pyramis (Aita)										
Mirifusus dianae minor Baumgartner										
Stichomitra sp. aff. *S. euganea* (Squinabol)										
Stichmitra doliolum Aita										
Sticomitra communis (Squinabol)		●								
Hiscocapsa kaminogoensis (Aita)										
Hiscocapsa sp. aff. *H. kaminogoensis* (Aita)										
Hiscocapsa zweilii (Jud)										
Hiscocapsa uterculus (Parona)					●					
Hiscocapsa pseudouterculus (Aita)										
Hiscocapsa orca (Foreman)										
Hiscocapsa grutterinki (Tan)										
Sethocapsa aculeata Cortese										
Sethocapsa trachyostraca Foreman		●								
Zhamoidellum ovum Dumitrica										
Hemicryptocapsa capita Tan					●					
Hemicryptocapsa tuberose Dumitrica										
Cryptamphorella conara (Foreman)	●				●					●
Williriedellum carpathicum Dumitrica		●		●						
Obesacapsula cetia (Foreman)										
Holocryptocanium barbui Dumitrica					●					
Holocryptocanium tuberculatum Dumitrica	●		●							
Gongylothorax verbeeki (Tan Sin Hok)										
Cecrops septemporatus (Parona)			●	●	●	●	●		●	
Pantanellium squinaboli (Tan)										
Pantanellium lanceola (Parona)										
Acanthocircus trizonalis dicranacanthos (Squinabol)										
Becus triangulocentrum Dumitrica										
Crucella remanei Jud										
Crucella bossoensis Jud										
Suna echiodes (Foreman)										
castea diaphorognona (Foreman)										
Acaeniotyle dentate Baumgartner										
Acaeniotyle umbilicata (Rust)				●						

The abundance (Ab: A-abundant, C-common, F-few) and preservation (Pr: G-good, M-moderate, P-poor) are shown in the table.

Chapter 6 Discussions

6.1 Deformation style controlled by the original strata

The tectonic melange intrinsically consists of competent blocks in an incompetent matrix: in our studied area, they are chert and basalt blocks in a scaly shale matrix. Melange deformation varies fostering by the relative proportions of competent and incompetent material. With progressive tectonic stress and diagenesis, this siliceous sequence shows four styles of melange deformation.

Where the proportion of chert or basalt to mudstone is low, it occurs as scattered block in a scaly shale matrix. A mixture of competent and incompetent material exhibits continuous competent part bounding by shear parts corresponding to the incompetent material. Where high competence material (chert) is dominant, discontinuities are localized along faults. Folds are well developed. Where low competence material (upper Lower Cretaceous siliceous mudstone) is dominant, scaly shear is well developed.

For the Early Cretaceous blocks, if it is chert dominated, folds are well developed. If it is chert interbedded with claystone, type 2 brecciation is well developed.

6.2 Subduction processes

Tectonic process caused the OPS of the Neo-Tethys to detach from the subducting ocean plate above a decollement. Decollements are surfaces of disharmony separating deformed rocks above from lesser deformed underlying rocks. Decollements are zones of deformation localized by weak rock such as salt or shale, by high fluid pressure, or by some interplay of rock characteristics and fluid pressure. Borehole logs from the northern Barbados accretionary prism show that the plate boundary decollement

initiates in a low-density smectitic radiolarian claystone (Moore et al., 1998). Nevertheless, low density generally indicates high porosity, and porosity inversely correlates to strength or coefficient of friction (Vernik et al., 1993). Due to their open pore framework and low grain densities, radiolarian claystones maintain low densities and high porosities relative to terrigenous or calcareous sediments buried at equivalent depths (Hamilton, 1976).

The oldest strata recorded in the melange near Zhongba are Pliensbachian–Toarcian chert interbeded with limestone. The Early Jurassic and Middle Jurassic siliceous strata preserved in the Erba melange are rare and display as coherent sequences without disruption and mixing. Well developed block-in-matrix fabric of the Late Jurassic to Early Cretaceous strata and rare preservation of strata older than Tithonian indicate a decollement fault formed in a siliceous claystone in the Late Jurassic near Tithonian. Melanges are formed by detachment of the upper part of the OPS on a subducting oceanic plate in the vicinity of the trench.

During the subduction, lithification operated concurrently with deformation. During the early stage, sediment are initially unconsolidated siliceous mudstone, claystone and consolidate or semiconsolidated chert. The siliceous mudstone and claystone contained much water and was deformed by particulate flow, while chert deformed brittlely. With continuously tectonic shearing and fluid overpressure, type 2 breccia was well developed (Fig. 6.1). While the strata were totally consolidated, both the claystone and the chert parts show brittle deformation.

6.3 Intra-oceanic subduction

Early studies argued that the entire Tethyan oceanic crust was subducted along the southern margin of the Lhasa terrane through one subduction system along the continental margin of Tethys. An alternate model proposes the existing of multiple subductions. Recent studies have shown the YTSZ ophiolitic massifs in Yungbwa (Miller et al., 2003; Liu et al., 2010, 2012), Dongbo (Xiong et al., 2011; Liu et al., 2015), Pulan

(Liu et al., 2011), Purang (Guo et al., 2015), Xiugugabu (Xu et al., 2007; Bezard et al., 2011), Saga and Sangsang (Bedard et al., 2009), and Zedong (Aitchison et al.,2000; McDermid et al., 2002) was formed in a intraoceanic suprasubduction zone during the Late Jurassic–Early Cretaceous.

Based on comparable observations of the ophiolitic massifs in the Tanwa melange and other ophiolitic massifs along the whole YZSZ, Dai et al. (2011, 2012) propose that a ca. 2500-km long complex subduction system was active between India and the Lhasa terrane, Burma, and the Karakoram microcontinent within the Neo-Tethys during the Early Cretaceous (120 to 130 Ma), similar to the modern active intra-oceanic subduction systems in the Western Pacific. He et al. (2016) conducted geochemical and Sr–Nd–Pb isotopic analyses for the doleritic samples from the northern belt and the pillow basalt and gabbro samples from the Tanwa melange in the southern belt. They interpreted that the mafic rock associations represent the remnants of a Neo-tethyan oceanic lithosphere, which was developed as part of a plume-proximal seafloor-spreading system, reminiscent of the seamount chains along-across the modern mid-ocean ridges in the Pacific Ocean.

Within the Tanwa melange, type 1 breccia is interpreted as proximal debris flow from the old accretionary complex. No clast of terrestrial material indicates the sources are only pelagic or hemipelagic. From the chert clasts Middle Jurassic and Late Jurassic radiolarian assemblages can be obtained. We did not find younger aged chert clasts. The chert and mafic rock clasts in breccias might come from the accreted pelagic material during the late Jurassic–early Cretaceous intraoceanic suprasubduction. The breccia may testify the existing of the Early Cretaceous intra-oceanic subduction within the Neo-Tethys.

The ophiolitic maffis thrust north to the Tanwa melange as a km-sized nappe, while the type 1 breccia is dominant in some parts of the melange. Type 1 breccia and the ophiolitic massifs, which were formed during the Late Jurassic to Early Cretaceous intra-

oceanic subduction, were envolved in the Tanwa melange accreted during the late Cretaceous.

6.4 Accretion processes

The Aptian to Upper Albian siliceous mudstone is interpreted as sediments near the trench. Because of the lack of terrrigenous trubidites in the Tanwa melange, the Erba melange, and the Maquanhe melange, the age of the youngest siliceous mudstones is the maximum constraint on the timing of accretion. South to the Tanwa melange, the Maquanhe melange consists of upper Albian chert and the North Tethys Himalaya preserved upper Paleocene deep-marine siliceous sediments. A significant temporal gap exists between the Tanwa melange and the Erba melange in the north and Maquanhe melange in the south. This younging polarity of the arrangement of the Tanwa melange, Erba melange, and Maquanhe melange indicate the northward subduction of the Neo-Tethys. The Tanwa melange, which includes the intraoceanic suprasubduction remnants, should be accreted to the south of the Zhada-Zhongba terrane firstly after Albian. Then Maquanhe melange accreted south to the Tanwa melange during Late Cretaceous. Because the Maquanhe melange was deposited proximal to the Indian passive margin compared with Tanwa melange, the strata contain more siliceous mudstone and shallow-water limestone. The strata above Aptian chert in the North Tethys Himalaya are red limestone. From the Aptian, the sediments show apparently southward shallower trend of distribution (Fig. 7.2).

Even isoclinally folds, faults, brecciation, veins, and block-in-matrix fabric are well developed in the melanges. There is no metamorphism and the radiolarian skeletons were not deformed. Therefore, the melanges in this study were formed through subduction-accretion processes in shallow depth.

6.5 The paucity of trench sediments

Melange is lack of terrigenous turbidites in our research area. During the Late Cretaceous, only limited sandstones (this study and Cai et al., 2012) are recorded in the YTSZ. Upper Cretaceous limestones and Upper Paleocene siliceous mudstones are accumulated on the Indian passive margin.

In the Barbados Ridge complex, the offscraped section includes no terrigenous turbidites, the underthrust sedimentary section is principally pelagic in character. The variation in the thickness of sediment entering the subduction zone ranges from more than 5 km in the south to less than 1 km in the north. The lack of terrrigenous trubidites in melanges may caused by increasing distant from the continent and topographic barrier as the Barbados Ridge complex (Moore and Bijuduval, 1984).

North to the melanges in our study, which belongs to the southern belt of the western YTSZ, there are Zhada–Zhongba terrane, northern belt of the YTSZ, and the Xigaze forearc basin. All these entities dispart the trench far away from the Eurasian continent. The existence of the intra-oceanic island arcs north to the Tanwa melange (Dai et al., 2011, 2012; He et al., 2016) and the Zhada–Zhongba terrane were topographic barrier between the trench and the Eurasian continent.

In the erosive margin of Nicoya Penisula in northern Costa Rica, the trench has little amounts of fill, which is generally less than 1 Km. The paucity of sediment in the trench is caused by the efficient sequestration of sediment in the forearc (Tobin, 2014). Clift and Vannucchi (2014) suggested that subduction erosion is controlled by the amount of sediment present in the trench. Erosion is favored if the sediment in the trench are less than 1 km thick.

The Xigaze forearc basin is comprised by flysch-dominant Xigaze Group (consisting of Ngamring, Chongdoi, and Sangzugang Formations) and the shallow marine Cuojiangding Group (Padana, Qubeiya, Quxia, and Gyalaze Formations), with the ages of the Albian–Coniacian and the Santonian–Ypresian respectively (Wang et al., 2012). New

geologic mapping and U-Pb detrital-zircon geochronologic data from the Lhazi region, 340 km south of Lhasa, show that forearc basin sedimentation began ca. 110 Ma conformably atop the Yarlung–Tsangpo ophiolitic melange. Sandstone modal analyses, conglomerate clast compositions, and zircon U-Pb geochronology reveal Asian continental margin, Gangdese magmatic arc, and central to northern Lhasa terrane provenance (Orme and Laskowski, 2016). The sequenstration of sediment in the forearc from Albian may be also one reason of rare coarse terrigenous sediments near the trench.

6.6 A model for Neo-Tethys evolution

Proposed models of India–Asia collision occurred in southern Tibet include single stage collision and multistage collision. The single stage collision models interpreted that the Tethyan oceanic crust was subducted northward beneath the south margin of the Lhasa terrane (Allègre et al., 1984; Chang, 1984; Chang et al.,1986; Searle et al., 1987; Cai et al., 2012). Cai et al. (2011, 2012) noted that the accrecionary complexes were accreted to the Asian margin prior to the India–Asia continental collision through a single subduction zone within the Neo-Tethys Ocean during the Cretaceous. However, this model is difficult to explain the widely distributed ophiolites of intra-oceanic arc and back-arc basin signatures (Hébert et al., 2012). It is also challenged by the enormous amount of subsequent intracontinental shortening required (Van Hinsbergen et al., 2012).

Available data indicate the existence of an intra-oceanic subduction had began from the Early Cretaceous (Hébert et al., 1999, 2003, 2012; Aitchison et al., 2000, 2003; Aitchison and Davis, 2004; Davis et al., 2002, 2004; Guilmette et al., 2007, 2008, 2009). One multistage collision model interpreted that the products of this intra-oceanic subduction system were obducted onto the Indian margin by the end of the Cretaceous and followed by ultimately India–Asia collision at the Eocene/Oligocene boundary (Aitchison et al., 2000, 2007; Ding et al., 2005; Xu et al., 2015). However, there is no

record of the remaining oceanic crust that lay to the north of the intra-oceanic subduction system. Detrital zircon U–Pb geochronology and Paleomagnetic analyses, however, indicate that the Xigaze ophiolite can no longer be viewed as a geological archive of near-equatorial subduction within the Neo-Tethys (Huang et al., 2015). Additional support for this model was previously inferred from the arrival of mafic magmatic debris in the Maastrichtian–Paleocene stratigraphy of the Tibetan Himalaya (e.g., Ding et al., 2005), but recent provenance analysis suggests that this debris was not derived from ophiolites, but from hotspot-related volcanic rocks instead (Garzanti and Hu, 2015).

Based on our study on melanges of the western sector of the YTSZ, an alternative model of the subduction-accretion processes has been proposed (Fig. 6.3).

In its western segment, the YTSZ is divided by the Zhada–Zhongba micro-continent into northern and southern branches.

In the southern belt, both the Erba melange and the Tanwa melange consist of Late Jurassic to Early Cretaceous chert and Aptian to Albian siliceous mudstone.

Dai et al. (2011, 2012) and He et al. (2016) interpreted the phiolitic massif in the Tanwa melange was formed in an intra-oceanic subduction system during the Early Cretaceous (120–130 Ma). Late Jurassic to Early Cretaceous radiolarians can be obtained from the pelagic sediments above the massif. The Tanwa melange was accreted during the Early Cretaceous intra-oceanic subduction (S1).

Type 1 breccia is interpreted to record deposition on slope-aprons that developed between a platform and the basin floor (Stow et al., 1996). The slope-aprons were formed with the growing of the massif and the accreted melange within the Neo-Tethys. The products of the intra-oceanic subduction system provided sources for the breccia.

The Erba melange is the northernmost and structurally highest melange. The Erba melange was interpreted as the product of the subduction of the Neo-Tethys oceanic crust beneath Zhada–Zhongba terrane (S2).

The green felsic tuff yielded the radiolarian fossils of the Aptian to the Albian age. Higher proportion of Aptian to the Albian tuff in the Tanwa melange is herein interpreted that it was sourced from the island arcs formed in the intra-oceanic island arcs.

Type 2 breccia is well developed in the Tanwa melange and the Erba melange. It is interpreted that the type 2 breccia was formed during the subduction. Radiolarian assemblages from the type 2 breccia are assigned to Tithonian to Hauterivian (KR1 and KR2). These two subductions should be initiated after the radiolarian skeletons being deposited. The oldest age of the siliceous mudstone from these two melanges, early Aptian, provide maximum constraint for the subduction. The subduction began from the Barremian when the radiolarian-bearing strata were still unlithified.

He et al. (2016) interpreted that the melt evolution of the mafic rocks from the northern belt and the southern belt are influenced by the same mantle plume within the Neo-Tethyan seaway based on geochemical and Sr–Nd–Pb isotopic analyses. Radiolarian skeletons from the siliceous strata of the north branch are highly deformed and no age data can be obtained.

The northward subduction of the Neo-Tethys oceanic crust beneath the Lhasa Terrane (S3) was initiated in the Barremian. It is constrained by studies of a Tethyan metamorphic sole (Guilmette et al., 2009) and the Early Cretaceous adakite-like Sangri Group (Zhu et al., 2009a, 2011a,b) in the southern Lhasa terrane. Huang et al. (2015) indicate that spreading of the Barremian Xigaze ophiolite occurred in the Gangdese forearc, and formed the basement of the forearc strata based on paleomagnetic, geochronologic and stratigraphical study.

Therefore, there were three subduction systems from the Barremian in the western sector of the YTSZ. The intra-oceanic subduction is responsible for the formation of the Tanwa melange. The subduction of the Neo-Tethys oceanic crust beneath Zhada–Zhongba terrane is responsible for the formation of the Erba melange,

whereas the subduction of the Neo-Tethys oceanic crust beneath the Lhasa terrane is responsible for the formation of the ophiolitic melange in the northern belt.

The collision of the northward-drifting Lhasa block with the Qiangtang block at 140–120Ma (e.g., Kapp et al., 2007; Zhu et al., 2011a) can provide a dynamic force to initiate a new Tethyan subduction cycle in front of the south Lhasa margin. Moreover, the rifting of East Gondwanaland to open the East Indian Ocean and the initial breakup of West Gondwanaland to open the South Atlantic Ocean, both probably were due to the plume activity at 132Ma (e.g., Storey, 1995; Zhu et al., 2009).

The transition from pelagic chert to hemipelagic siliceous mudstone in the Erba melange and the Tanwa melange indicates an early Aptian accretion age for melanges. The S2 subduction persisted to the Albian and obducted to the Zhada–Zhongba terrane. The Tanwa melange including the ophiolitic massif formed in the intra-oceanic subduction system (S1) was emplaced to the south of the Maquanhe melange thereafter.

The near absence of turbidite deposits in the Early Cretaceous may be the result of the Xigaze forearc basin being underfilled until the Campanian (Wan et al., 1997). In this state, sediments from the Lhasa terrane could not bypass the forearc basin and were therefore not deposited in the trenches. The lack of terrrigenous trubidites in melanges may also caused by increasing distant of the trenches located in S1 and S2 subductions from the Eurasian continent and topographic barrier as intra-oceanic island arcs (Dai et al., 2011, 2012; He et al., 2016) and the Zhada-Zhongba terrane.

After the accretion of the Tanwa melange, younger strata (Maquanhe melange) in the south, which contain chert, limestone, and siliceous mudstone, accreted during the continuous S1 subduction. The chert contains radiolarian assemblage late Albian in age.

Latest Cretaceous trench-fill strata are exposed as sandstone accretionary complex or blocks in the mud-matrix melange. The youngest single zircon grain ages in these strata are 71±1 Ma, 71±1 Ma, 73±2 Ma. Detrital zircon age spectra indicate that the

trench filling strata was derived from Lhasa terrane affinity rocks (Cai et al., 2012, An et al., 2015). The Xigaze forearc basin was nearly overfilled and changed from the sloped stage to the ridged stage during this period (Einsele et al., 1994; Wan et al., 1997, Huang et al., 2015). Detrital material from the Lhasa terrane and/or recycled forearc strata would have been transported southward and deposited in the trench. The age of the trech-fill strata constrains a latest Cretaceous emplacing age for the Maquanhe melange.

With the southward accretion of the mélanges, the Neo-Tethys ocean retreat from north to south. Marine deposit existed until the late Paleocene (ca. 56 Ma) in the north Tethyan Himalaya near Zhongba (Liang et al., 2012; our unpublished data), Saga(Li et al., 2007; Ding, 2003, 2005; Wang et al., 2016), and Renbu (Liu and Aitchison, 2002). The latest marine deposit (ca. 34 Ma) was found in the strata of the south Tethyan Himalaya near the middle of the YZSZ (e.g.,Wang et al. 2002; Aitchison et al. 2007; Jiang et al., 2015).

First arrival of Asia-derive detritus on the Indian passive continental margin is ca. 51 Ma in the strata of the south Tethyan Himalaya near Gamba, Tingri (Zhu et al., 2005; Najman et al., 2010; Li et al., 2015; Hu et al., 2014), and the strata of the north Tethyan Himalaya near Saga (Wang et al., 2011). Cr-spinels fromthe Lower Eocene Sangdanlin and Zheya Formations near Saga (52–50 Ma, Wang et al., 2011) and Enba and Zhaguo Formations near Tingri (~50 Ma, Hu et al., 2012; Najman et al., 2010; Zhu et al., 2005) are similar to those in Xigaze forearc strata, but distinct from those in Indus-Yarlung ophiolites (Fig. 5). This indicates provenance of Lower Eocene foreland-basin sediments in southern Tibet from the Lhasa Block, as strongly supported by detrital zircon U–Pb age populations (Hu et al., 2012; Wang et al., 2011). Based on such evidence, we suggest that in the Early Eocene (55–50 Ma) the Indus-Yarlung ophiolites were not yet exposed to erosion (Hu et al., 2014).

In our model, the Tethyan intra-oceanic subduction was developed during the Early Cretaceous. Melanges were obducted onto the Eurasian continent from the Albian to the latest Cretaceous progressively. Deep marine sediments retreated from north to

south and existed until the late Paleocene. The Indian continent collided with the Eurasian continent in the early Eocene (ca. 51 Ma), finally closing the leftover shallow marine Tethyan seaway in the late Eocene (ca. 34 Ma).

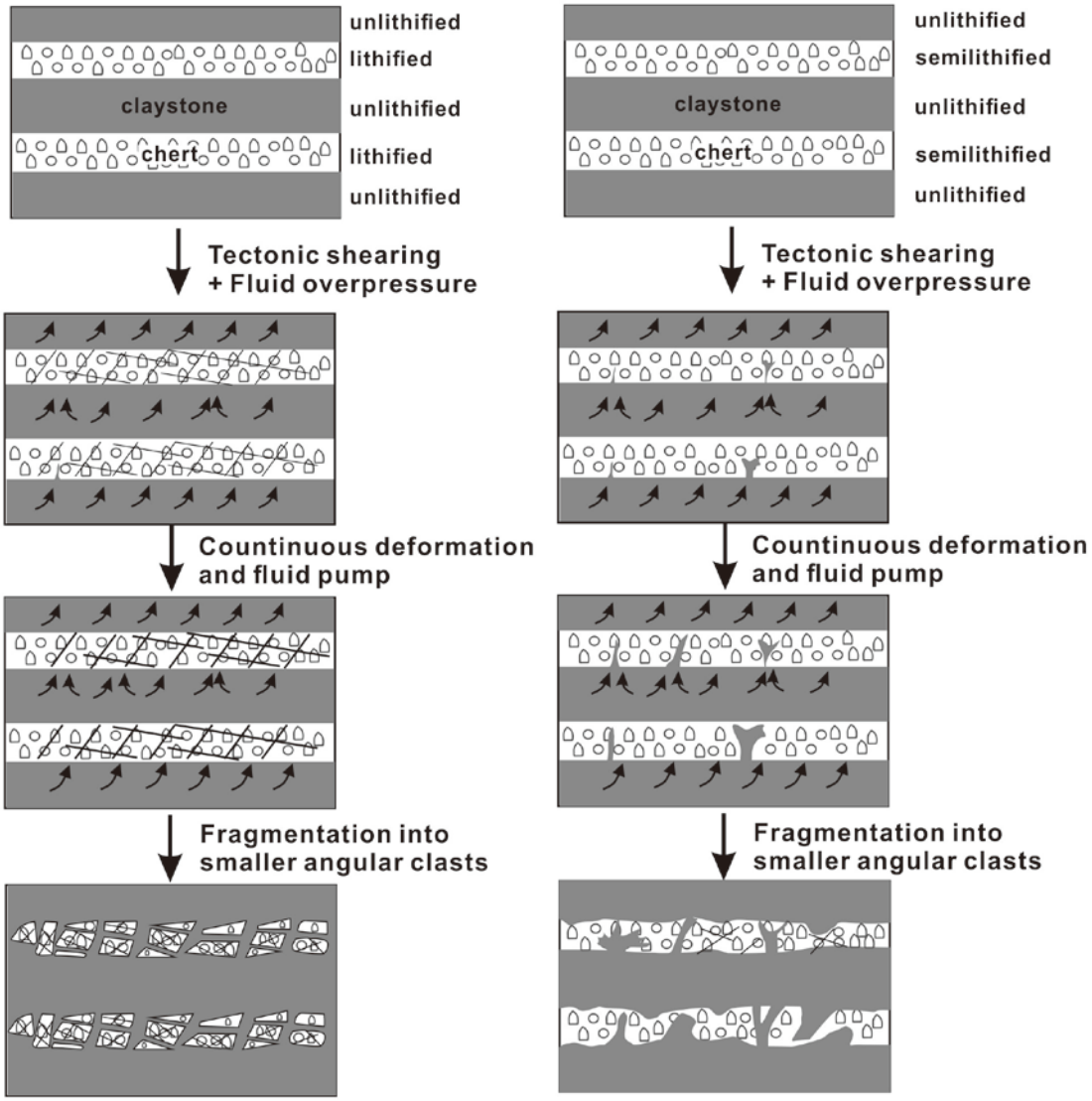

Fig. 6.1 Formations of the breccias

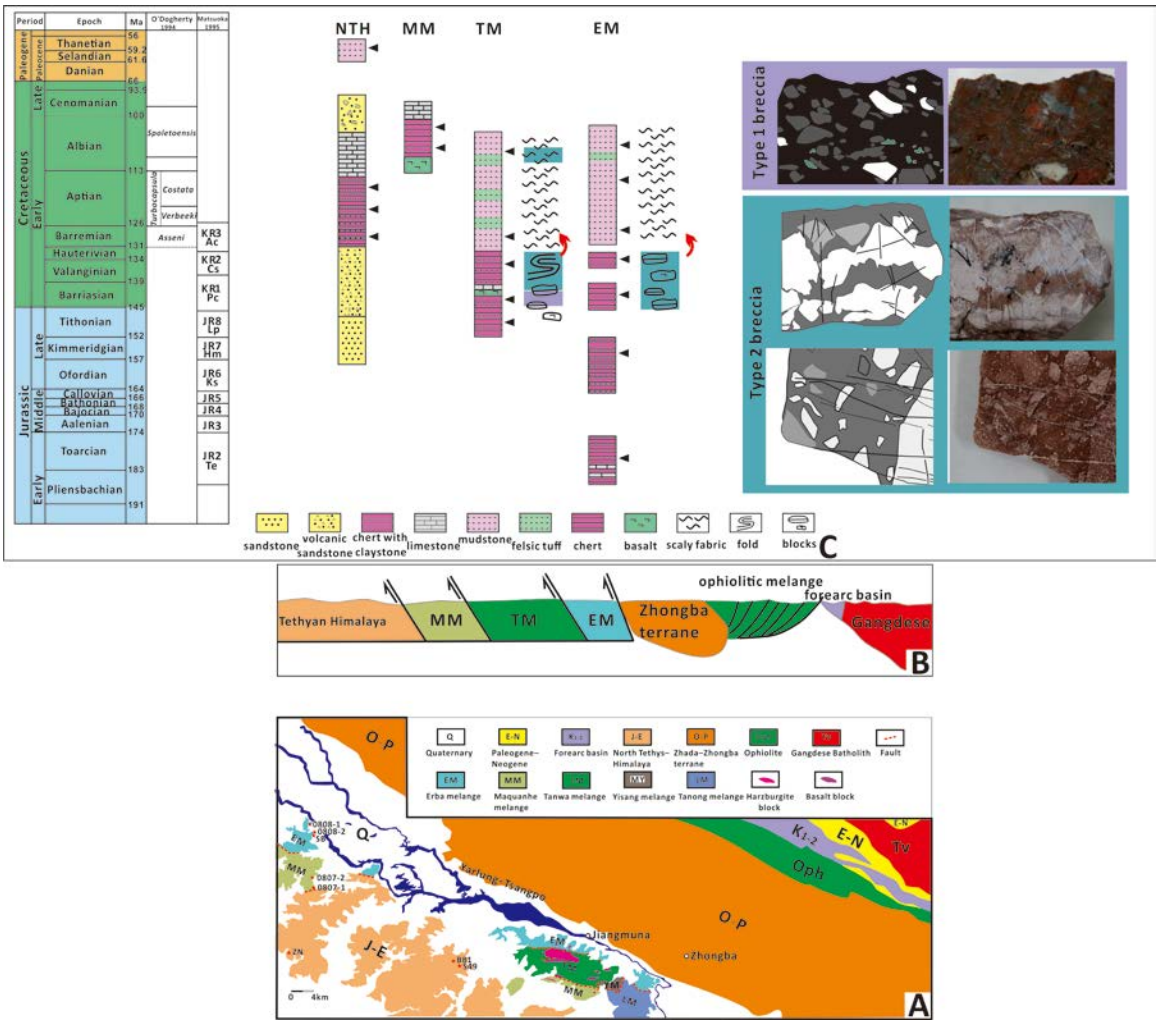

Fig. 6.2 Reconstruction of the oceanic plate stratigraphy and the process of subduction

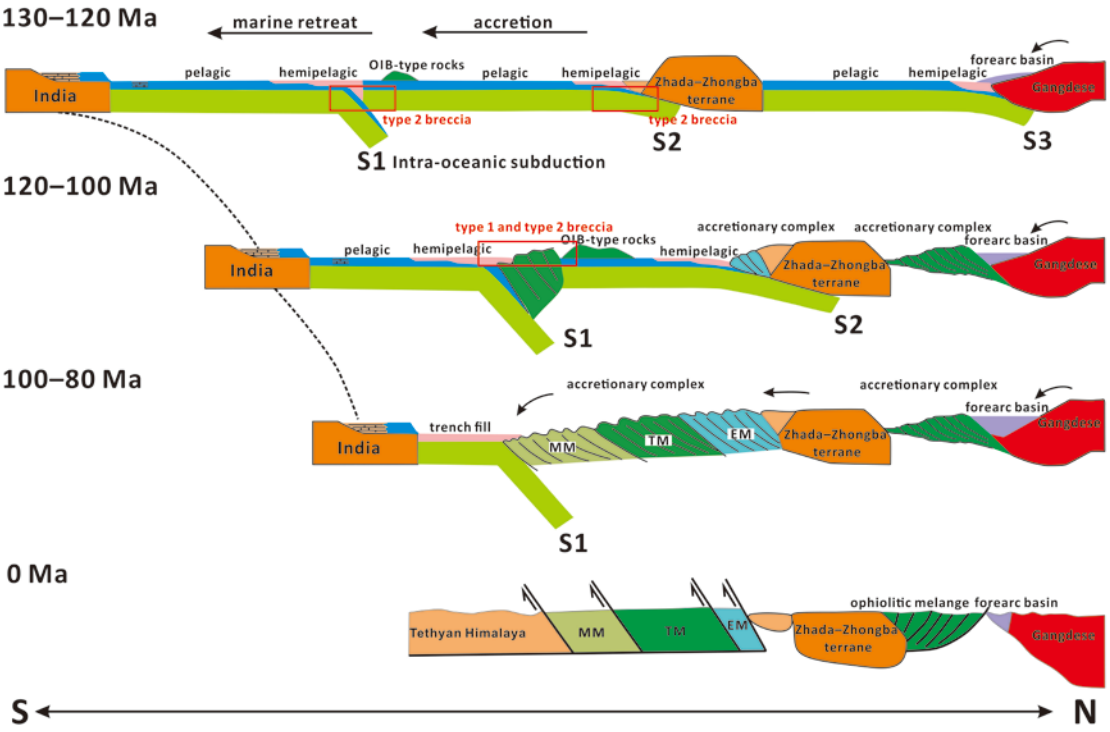

Fig. 6.3 Evolutionary scenario for the subduction and accretion of the Tethys

Chapter 7 Conclusions

1. The southern branch of the western YTSZ contains the ophiolitic melanges (Tanwa melange), the volcanic-sedimentary melanges (Erba melange, Maquanhe melange, Tanong melange) and clastic dominated melange (Yisang melange). Detailed radiolarian analyses are conducted on melanges near Zhongba. Macroscopic-, mesoscopic- and microscopic observations are conducted to elucidate the relationships of age, lithology and structure.

2. The Tanwa melange is characterized by a huge sequence of upper mantle peridotites and mafic rocks thrust north to a siliceous melange sequence. The Erba melange is characterized by highly sheared volcanoclastic or siliceous mudstone matrix including blocks of chert, claystone, basalt, and crystalline limestone. The Maquanhe melange is located south of the Tanwa melange or the Erba melange. They are connected by faults. The melange is characterized by siliceous mudstone, chert, basalt, and limestone. This melange does not display the typical matrix-in-blocks fabric. Strata are grossly continuous.

3. The oceanic plate stratigraphies of the three melanges have been reconstructed based on radiolarian age assignments (Tables 7-1, 7-2, 7-3). During Early Jurassic, bedded red cherts with some layers of limestone were deposited. In the Late Jurassic, thin bedded green cherts interbedded with shales were deposited. Trace fossils were well developed. Above them, red cherts and claystones were accumulated from Late Jurassic to Early Cretaceous. During the Aptian to Albian, siliceous mudstones were accumulated in the northern part (the Tanwa melange and the Erba melange), while chert interbedded with limestone were dominant in the southern part (the Maquanhe melange).

4. Well developed block-in-matrix fabric in the Late Jurassic to Early Cretaceous strata and rare preservation of strata older than Tithonian indicate a decollement fault formed in a siliceous claystone in the Late Jurassic near Tithonian.

5. The melanges become younger southward, which is consistent with the oceanic plate subducting northward under the Lhasa terrane during the Cretaceous.

6. Within the Tanwa melange, type 1 breccia is interpreted as proximal debris flow from the old accretionary complex. No clast of terrestrial material indicates the sources are only pelagic or hemipelagic. This breccia testifies the existing of intra-oceanic subduction within the Neo-Tethys.

7. The Tanwa melange, which includes the intraoceanic suprasubduction remnants, should be accreted to the south of the Zhada-Zhongba terrane firstly after Albian. Then Maquanhe melange accreted south to the Tanwa melange during Late Cretaceous.

8. The lack of terrigenous turbidites in the melanges may caused by increasing distance from the continent, topographic barrier of intraoceanic island arcs and Zhada–Zhongba terrane, and the sequenstration of sediments of the Xigaze forearc basin.

Table 7-1 Occurrence of Early and Late Jurassic radiolarians from samples in section SB in the Erba melange

Section	SB		
Sample	—027	—041	—047
Abundance	A	A	A
Preservation	M	M	G
Radiolarian Zone	JR8	JR6 or JR7	JR2
Tethysetta dhimenaensis (Baumgartner)	●		
Parahsuum simplum Yao			●
Canoptsum anulatum Passagno & Poisson			●
Eucyrtidiellum ptyctum (Reidel and Sanfilippo)		●	
Amphipyndax tsunoensis Aita	●	●	
Stichocapsa plicata Matsuoka			●
Sethocapsa aculeata Cortese	●	●	
Sethocapsa trachyostraca Foreman		●	
Gongylothorax sakawaensis Matsuoka		●	
Perispyridium ordinarium (Pessagno)	●	●	
Triactoma jonesi (Pessagno)	●		
Holocryptocanium tuberculatum Dumitrica			●

The abundance (Ab: A-abundant, C-common, F-few) and preservation (Pr: G-good, M-moderate, P-poor) are shown in the table.

Table 7-2 Occurrence of Early Cretaceous radiolarians from samples in sections 0808 and SB in Erba melange

Section	0808					SB	
Sample	—016	—027	—038	—048	—049	—002	—007
Abundance	A	A	A	A	A	A	A
Preservation	G	G	G	G	G	G	G
Radiolarian Zone	KR1	KR1	KR1	JR8	KR1	KR2	KR2
Pseudodictyomitra carpatica (Loziniyak)	●	●	●	●	●	●	●
Loopus nuda (Schaaf)	●	●	●	●			●
Svinitzium depressum (Baumgartner)	●		●	●		●	●
Svinitzium pseudopuga Dumitrica	●	●	●	●	●		
Praeparvicingula cosmoconica (Foreman)		●					
Tethysetta boessi (Parona)	●	●		●	●	●	
Tethysetta usotanensis (Tumanda)						●	●
Cinguloturris cylindra Kemkin et Rudenko	●		●	●	●		●
Archaeodictyomitra apiarium Rüst	●			●	●		●
Archaeodictyomitra pseudoscalaris (Tan sin Hok)					●	●	●
Archaeodictyomitra excellens (Tan)		●		●	●		
Archaeodictyomitra minoensis (Mizutani)				●			
Mictyoditra lacrimula (Foreman)	●						
Neorelumbra kiesslingi Dumitrica	●			●	●		
Neorelumbra buwaydahensis Kiessling			●				
Eucyrtidiellum pyramis (Aita)				●			●
Mirifusus dianae minor Baumgartner		●					
Stichomitra sp. aff. *S. euganea* (Squinabol)		●					
Stichmitra doliolum Aita							●
Hiscocapsa kaminogoensis (Aita)	●						
Hiscocapsa sp. aff. *H. kaminogoensis* (Aita)			●				
Hiscocapsa zweilii (Jud)				●			
Hiscocapsa uterculus (Parona)					●	●	
Hiscocapsa pseudouterculus (Aita)				●			
Zhamoidellum ovum Dumitrica	●				●		
Hemicryptocapsa capita Tan							●
Cryptamphorella conara (Foreman)	●		●				●
Williriedellum carpathicum Dumitrica						●	
Cecrops septemporatus (Parona)						●	●
Pantanellium squinaboli (Tan)	●	●					
Acanthocircus trizonalis dicranacanthos (Squinabol)		●			●	●	
Becus triangulocentrum Dumitrica						●	●
Crucella remanei Jud						●	
Crucella bossoensis Jud						●	
Suna echiodes (Foreman)						●	
Castea diaphorognona (Foreman)						●	

The abundance (Ab: A-abundant, C-common, F-few) and preservation (Pr: G-good, M-moderate, P-poor) are shown in the table.

Table 7-3 Occurrence of mid-Cretaceous radiolarians from samples in sections 0804 (Tanwa melange), 0808 (Erba melange), and 0807 (Maquanhe melange).

Section	0804				0808			0807
Sample	—015	—055	—080	—134	—045	—051	—062	—032
Abundance	A	A	A	A	C	C	C	A
Preservation	G	G	G	G	G	G	G	G
Radiolarian Zone	*Spoletoensis* Zone				*Turbocapsula costata* Zone	*Spoletoensis* Zone		
Pseudodictyomitra hornatissima (Squinabol)	●				●	●		
Pseudodictyomitra nakasekoi Taketani		●						
Pseudodictyomitra lodogaensis Pessagno			●				●	
Pseudodictyomitra paronai (Aliev)				●		●	●	
Pseudodictyomitra pentacolaensis Pessagno						●	●	
Archaeodictyomitra chalilovi (Aliev)		●						
Dictyomitra communis (Squinabol)			●			●		
Dictyomitra gracilis (Squinabol)								●
Dictyomitra montisserei (Squinabol)				●				●
Thanarla brouweri (Tan)	●	●	●			●		●
Thanarla cucurbita O'Dogherty								●
Thanarla spoletoensis O'Dogherty								●
Xitus spicularius (Aliev)	●	●				●	●	
Xitus elegans (Squinabol)		●	●	●				
Tugurium pagoda (Squinabol)							●	
Sticomitra communis (Squinabol)	●	●				●	●	
Rhopalosyringium (?) sp. C in Musavu & Danelian (2006)	●	●	●				●	
Rhopalosyringium mosquense (Smirnova & Aliev)	●	●	●				●	●
Rhopalosyringium perforaculum O'Dogherty	●		●		●			
Turbocapsula fugitiva O'Dogherty			●					
Turbocapsula costata (Wu)	●				●		●	
Diacanthocapsa betica O'Dogherty			●					
Squinabollum asseni (Tan)	●							
Squinabollum fossilis (Squinabol)								●
Cryptamphorella conara (Foreman)	●							
Archaeospongoprunum cortinaensis Pessagno	●	●						●
Holocryptocanium barbui Dumitrica					●	●		●

The abundance (Ab: A-abundant, C-common, F-few) and preservation (Pr: G-good, M-moderate, P-poor) are shown in the table.

Acknowledgments

I would like to thank Professor Matsuoka Atsushi, my supervisor in Niigata University, for his kindly support and great guidance since I met with him in 2012. I am also grateful for prof. Wang Chengshan and prof. Li Yalin, my supervisor in China University of Geosciences, Beijing, for their inspiring comments and support for the field investigations.

Thanks must be given to Prof. Wei Yushuai, Prof. Chenxi, Li Xiaohan, Zhang Xiaolong, Bi Wenjun, Luo Yipeng, and Zhang Wanyue (China University of Geosciences, Beijing) for their invaluable assistance during the field work. I would like to thank our driver Bazhu very much for his skillful driving and kindly assistance. I would like to express my best regards to our laboratory members (Niigata University) for their assistance in chemical treatment and my daily life in Japan.

This research was financially supported by the National Basic Research Program of China (973 Program, Grant Number 2011CB822001); the National Natural Science Foundation of China (Grant Number 41572188); the Project of Geological Survey of China (Grant Number 1212011086037); and the Japan Society for the Promo on of Science KAKENHI (Grant Numbers 15K05329 and 15H02142E). I would like to thank the China Scholarship Council (CSC) for providing the living expenses in Japan.

I would like to thank my parents and sisters for their patience and supports during my study in Japan.

References

Aitchison, J. C., Davis, A .M., 2004, Evidence for the multiphase nature of the India–Asia collision: the lower Miocene Ganrinboche conglomerates, Yarlung Tsangpo, suture zone, SE Tibet. *In:* Malpas, J., Fletcher, C. J. N., Ali, J., Aitchison, J. C., *Eds*., Aspects of the Tectonic Evolution of China: Geological Society of London Special Publication, 226, pp. 217–233.

Aitchison, J. C., Badengzhu, Davis, A. M., Liu, J., Luo, H., Malpas, J. G., McDermid, I. R. C., Wu, H., Ziabrev, S., Zhou, M. F., 2000, Remnants of a Cretaceous intra-oceanic subduction system within the Yarlung-Zangbo suture zone, southern Tibet. *Earth and Planetary Science Letters*, **183**, 231–244.

Aitchison, J. C., Davis, A. M., Abrajevitch, A. V., Ali, J. R., Badengzhu, Liu, J., Luo, H., McDermid, I. R. C., Ziabrev, S. V., 2003, Stratigraphic and sedimentological constraints on the age and tectonic evolution of the Neotethyan ophiolites along the Yarlung Tsangpo suture zone, Tibet. *In:* Dilek, Y., Robinson, P.T., *Eds.*, Ophiolites in Earth History: Special Publication, The Geological Society of London, London, **218**, pp. 147–164.

Aitchison, J. C., Ali, J. R., Davis, A. M., 2007, When and where did India and Asia collide?. *Journal of Geophysical Research: Solid Earth*, **112(B5)**.

Allègre, C. J., Courtillot, V., Tapponnier, P., 32 others, 1984, Structure and evolution of the Himalaya–Tibet orogenic belt. *Nature*, **307**, 17–22.

An, W., Hu, X., Garzanti, E., 2015, Sandstone provenance and tectonic evolution of the Xiukang Mélange from Neotethyan subduction to India–Asia collision (Yarlung-Zangbo suture, south Tibet). *Gondwana Research*, **41**, 222–234.

An, Z. S., Kutzbach, J., Prell, W., Porter, S., 2001, Evolution of Asian monsoons and phased uplift of the Himalaya-Tibetan plateau since Late Miocene times. *Nature*, **411(6833)**, 62–66.

Audley-Charles, M.G., 1983, Reconstruction of eastern Gondwanaland. *Nature*, **306**, 48–50.

Audley-Charles, M. G., 1988, Evolution of the southern margin of Tethys (North Australian region) from early Permian to late Cretaceous. *Geological Society, London, Special Publications*, **37(1)**, 79–100.

Baumgartner, P. O., O'Dogherty, L., Gorican, S., Urquhart, E., Pillevuit, A., De Wever, P., 1995, Middle Jurassic to Lower Cretaceous Radiolaria of Tethys: Occurrence, Systematics, Biochronology. *Mémoires de Géologie (Lausanne)*, **23**, 1–1172.

Bédard, É., Hébert, R., Guilmette, C., Lesage, G., Wang, C. S., Dostal, J., 2009, Petrology and geochemistry of the Saga and Sangsang ophiolitic massifs, Yarlung Zangbo Suture Zone, Southern Tibet: evidence for an arc–back-arc origin. *Lithos*, **113(1)**, 48–67.

Bezard, R., Hébert, R., Wang, C., Dostal, J., Dai, J., Zhong, H., 2011, Petrology and geochemistry of the Xiugugabu ophiolitic massif, western Yarlung Zangbo suture zone, Tibet. *Lithos*, **125(1)**, 347–367.

Cai, F., Ding, L., Leary, R. J., Wang, H., Xu, Q., Zhang, L., Yue, Y., 2012, Tectonostratigraphy and provenance of an accretionary complex within the Yarlung–Zangpo suture zone, southern Tibet: Insights into subduction–accretion processes in the Neo-Tethys. *Tectonophysics*, **574**, 181–192.

Chang, C. F., Zheng, X. L., 1973, Geological structure of Qomolangma region in southern Tibet and discussions on the origin of EW-trending Mountains in Tibetan Plateau. *Science in China (Series D)*, **2**, 190–210.

Chang, C., 1984. Les caractéristiques tectoniques et l'évolution de la zone de suture du Yarlung–Zangpo. *In:* Mercier, L.J., Li, G.C., *Eds.*, Étude géologique et géophysique de la croûte terrestre et du manteau supérieur du Tibet et de l'Himalaya. CNRS, Paris, pp. 341–350.

Chengfa, C., Nansheng, C., Coward, M. P., 24 others, 1986. Preliminary conclusions of the Royal and Academia Sinica 1985 Geotraverse of Tibet. *Nature*, **323**, 501–507.

Clift, P., Vannucchi, P., 2004, Controls on tectonic accretion versus erosion in subduction zones: Implications for the origin and recycling of the continental crust. *Reviews of Geophysics*, **42(2)**.

Dai, J. G., Wang, C. S., Hébert, R., Santosh, M., Li, Y.L., Xu, J.Y., 2011, Petrology and geochemistry of peridotites in the Zhongba ophiolite, Yarlung Zangbo Suture Zone: implications for the Early Cretaceous intra-oceanic subduction zone within the Neo-Tethys. *Chemical Geology*, **288(3–4)**, 133–148.

Dai, J., Wang, C., Li, Y., 2012, Relicts of the Early Cretaceous seamounts in the central-western Yarlung Zangbo Suture Zone, southern Tibet. *Journal of Asian Earth Sciences*, **53**, 25–37.

Dai, J. G., Wang, C. S., Polat, A., Santosh, M., Li, Y. L., Ge, Y. K., 2013, Rapid forearc spreading between 130 and 120Ma: evidence from geochronology and geochemistry of the Xigaze ophiolite, southern Tibet. *Lithos*, **172**, 1–16.

Davis, A. M., Aitchison, J. C., Badengzhu, Luo, H., Zyabrev, S., 2002, Paleogene island arc collision-related conglomerates, Yarlung-Tsangpo suture zone, Tibet. *Sedimentary Geology*, **150**, 247–273.

Davis, A. M., Aitchison, J. C., Badengzhu, Luo H., 2004, Conglomerates record the tectonic evolution of the Yarlung-Tsangpo suture zone in southern Tibet. *In:* Malpas, J., Fletcher, C. J. N., Ali, J., Aitchison, J. C., *eds.*, Aspects of the Tectonic Evolution of China: Geological Society of London Special Publications, **226**, pp. 157–176.

De Wever, P., Dumitrica, P., Caulet, J. P., Nigrini, C., Caridroit, M., 2001, Radiolarians in the sedimentary record. Gordon & Breach Science Publishers, 1–533.

Ding, L., 2003, Paleocene deep-water sediments and radiolarian faunas: Implications for evolution of Yarlung–Zangbo foreland basin, southern Tibet. *Science in China (Series D)*, **46**, 503–515.

Ding, L., Kapp, P., Wan, X., 2005, Paleocene–Eocene record of ophiolite obduction and initial India–Asia collision, south central Tibet. *Tectonics*, **24(3)**, TC3001.

Einsele, G., Liu, B., Dürr, S., Frisch, W., Liu, G., Luterbacher, H. P., Ratschbacher, L., Ricken, W., Wendt, J., Wetzel, A., Yu, G. and Zheng, H., 1994, The Xigaze forearc basin: Evolution and facies architecture (Cretaceous, Tibet). *Sedimentary Geology*, **90**, 1–32.

Fielding, E. J., 1996, Tibet uplift and erosion. *Tectonophysics*, **260(1–3)**, 55–84.

Garzanti, E., Hu, X., 2015, Latest Cretaceous Himalayan tectonics: Obduction, collision or Deccan-related uplift?. *Gondwana Research*, **28(1)**, 165–178.

Girardeau, J., Mercier, J. C. C., Zao, Y., 1985, Structure of the Xigaze Ophiolite, Yarlung Zangbo suture zone, southern Tibet, China; genetic implications. *Tectonics*, **4**, 267–788.

Guilmette, C., Hébert, R., Bédard, É.,Wang, C. S., Ullrich, T. D., Dostal, J., 2007, Saga ophiolite, Yarlung Zangbo suture Zone, Tibet: field relationships, discovery of garnet-pyroxene amphibolite and Ar/Ar ages. Workshop Abstract Volume, HKTW22 Hong Kong, p. 37.

Guilmette, C., Hébert, R., Dupuis, C., Wang, C. S., Li, Z. J., 2008, Metamorphic petrology of amphibolite from the ophiolitic mélange, Yarlung Zangbo Suture Zone, Tibet. *Journal of Asian Earth Sciences*, **32**, 423–437.

Guilmette, C., Hébert, R., Wang, S. C., Villeneuve, M., 2009, Geochemistry and geochronology of the metamorphic sole underlying the Xigaze ophiolite, Yarlung Zangbo Suturte Zone, Tibet. Lithos, **112**, 149–162.

Guo, G., Yang, J., Liu, X., Xu, X., Liu, Z., Ba, D., 2015, Mid-ocean ridge (MOR) and suprasubduction zone (SSZ) geological events in the Yarlung Zangbo suture zone: Evidence from the mineral record of mantle peridotites. *Journal of Asian Earth Sciences*, **110**, 33–54.

Hamilton, E. L., 1976, Variation of density and porosity with depth in deep-sea sediments. *Journal of Sedimentary Petrology*, **46**, 280–300.

He, J., Li, Y. L., Wang, C. S., Dilek, Y., Wei, Y. S., Chen, X., Hou, Y. L., Zhou, A., 2016, Plume-proximal mid-ocean ridge origin of Zhongba mafic rocks in the western Yarlung Zangbo Suture Zone, Southern Tibet. *Journal of Asian Earth Sciences*, **121**, 34–55.

Hébert, R., Wang, C. S., Liu, Z. F., 1999, Xigaze ophiolites southern Tibet revisited. GACMAC Annual Meeting, Sudbury, Abstract Volume, 24, pp. 52–53.

Hébert, R., Huot, F., Wang, S. C., Liu, Z. F., 2003, Yalung Zangbo ophiolites (Southern Tibet) revisited: geodynamic implications from the mineral record. *In:* Dilek, Y., Robinson, P.T., *eds*., Ophiolites in Earth History: Geological Society of London Special Publication, **218**, 165–190.

Hébert, R., Bezard, R., Guilmette, C., Dostal, J., Wang, C. S., Liu, Z. F., 2012, The Indus–Yarlung Zangbo ophiolites from Nanga Parbat to Namche Barwa syntaxes, southern Tibet: first synthesis of petrology, geochemistry, and geochronology with incidences on geodynamic reconstructions of Neo-Tethys. *Gondwana Research*, **22(2)**, 377–397.

Huang, W. T., Van Hinsbergen, D. J., Maffione, M., Orme, D. A., Dupont-Nivet, G., Guilmette, C., Ding, L., Guo, Z. J., Kapp, P., 2015, Lower Cretaceous Xigaze ophiolites formed in the Gangdese forearc: Evidence from paleomagnetism, sediment provenance, and stratigraphy. *Earth and Planetary Science Letters*, **415**, 142–153.

Hu, X. M., Jansa, L., Wang, C. S., 2008, Upper Jurassic-Lower Cretaceous stratigraphy in south-eastern Tibet: a comparison with the western Himalayas. *Cretaceous Research*, **29**, 301–315.

Jiang, T., Aitchison, J. C., Wan, X., 2016, The youngest marine deposits preserved in southern Tibet and disappearance of the Tethyan Ocean. *Gondwana Research*, **32**, 64–75.

Jud, R., 1994, Biochronology and systematics of Early Cretaceous Radiolarian of the Western Tethys. *Mémoires de Géologie (Lausanne)*, **19**, 1–147.

Kapp, P., DeCelles, P. G., Gehrels, G. E., Heizler, M., Ding, L., 2007, Geological records of the Lhasa-Qiangtang and Indo-Asian collisions in the Nima area of central Tibet. *Geological Society of America Bulletin*, **119(7–8)**, 917–933.

Kojima, S., Ahmad, T., Tanaka, T., Bagati, T. N., Mishra, M., Kumar, R., Islam, R., Khanna, P., 2001, Early cretaceous radiolarians from the Indus suture zone, Ladakh, northern India. *News of Osaka Micropaleontologists*, special volume **12**, 257–270.

Li, H. S. and Wu, H. R., 1985, Radiolaria from the Cretaceous Congdu Formation in southern Xizang (Tibet). *Acta Micropalaeontologica Sinica*, **1**, 61–78 (in Chinese with English abstract).

Li, J., Hu, X. M., Garzanti, E., An, W., Wang, J. G., 2015, Paleogene carbonate microfacies and sandstone provenance (Gamba area, South Tibet): Stratigraphic response to initial India-Asia continental collision. *Journal of Asian Earth Sciences*, **104**, 39–54.

Li, X., Li, Y. L., Wang, C. S. and Matsuoka, A., 2013, Late Jurassic radiolarians from the Zhongba melange in the Yarlung–Tsangpo suture zone, southern Tibet. *Scientific Reports of Niigata University (Geology)*, no. 28, 23–30.

Li, X., Matsuoka A., Li Y. l., Wei, Y. S., Wang, C. S., 2016, Middle Jurassic to Early Cretaceous radiolarian assemblages from the chert blocks in the mélange along the Yarlung–Tsangpo Suture Zone, near Zhongba County, Southern Tibet. N*ews of Osaka Micropaleontologist*, No. 16, 79–94.

Li, X., Matsuoka, A., Li, Y., Wang, C., 2017, Phyletic evolution of the mid-Cretaceous radiolarian genus Turbocapsula from southern Tibet and its applications in zonation. *Marine Micropaleontology*, **130**, 29–42.

Li, X. H., Wang, C. S., Wan, X. Q., Tao, R., 1999, Verification of stratigraphic sequence and classification for the Chuangde crosslocality of Gyangze, southern Tibet. *Journal of Stratigraphy*, **23**, 303–309 (in Chinese with English abstract).

Li, Y. L., Wang, C. S., Hu, X. M., Bak, M., Wang, J. J., Chen, L., 2007, Characteristics of Early Eocene radiolarian assemblages of the Saga area, southern Tibet and their constraint on the closure history of the Tethys. *Chinese Science Bulletin*, **52**, 2108–2114.

Lian, D. Y., Yang, J. S., Robinson, P. T., Liu, F., Xiong, F. H., Zhang, L., Gao, J., Wu, W. W., 2016, Tectonic Evolution of the Western Yarlung Zangbo Ophiolitic Belt, Tibet:

Implications from the Petrology, Mineralogy, and Geochemistry of the Peridotites. *The Journal of Geology*, **124(3)**, 353–376.

Liang, Y. P., Zhang, K. X., Xu, Y. D., He, W. H., An, X. Y., Yang, Y. F., 2012, Late Paleocene radiolarian fauna from Tibet and its geological implications. *Canadian Journal of Earth Sciences*, **49**, 1364–1371.

Liu, C. Z., Wu, F. Y., Wilde, S. A., Yu, L. J., Li, J. L., 2010, Anorthitic plagioclase and pargasitic amphibole in mantle peridotites from the Yungbwa ophiolite (southwestern Tibetan Plateau) formed by hydrous melt metasomatism. *Lithos*, **114(3)**, 413–422.

Liu, C. Z., Wu, F. Y., Chu, Z. Y., Ji, W. Q., Yu, L. J., Li, J. L., 2012, Preservation of ancient Os isotope signatures in the Yungbwa ophiolite (southwestern Tibet) after subduction modification. *Journal of Asian Earth Sciences*, **53**, 38–50.

Liu, F., Yang, J. S., Dilek, Y., Xu, Z. Q., Xu, X. Z., Liang, F. H., Chen, S. Y., Lian, D. Y., 2015, Geochronology and geochemistry of basaltic lavas in the Dongbo and Purang ophiolites of the Yarlung-Zangbo Suture zone: Plume-influenced continental margin-type oceanic lithosphere in southern Tibet. *Gondwana Research*, **27(2)**, 701–718.

Liu, J. B. and Aitchison, J. C., 2002, Upper Paleocene radiolarians from the Yamdrok mélange, south Xizang (Tibet), *China. Micropaleontology*, **48** (suppl. 1), 145–154.

Liu, S. J., Luo, H., Xu, B., Wang, X. H., Chen, D. S., 2016, Late Jurassic–Early Cretaceous radiolarians from Jinlu, Zedong, southern Tibet, China. *Acta Micropalaeontologica Sinica*, **33(3)**, 211–228 (in Chinese).

Liu, Z., Li, Y., Xiong, F. H., Wu, D., Liu, F., 2011, Petrology and geochronology of MOR gabbro in the Purang ophiolite of western Tibet. China. *Acta Petrologica Sinica*, **27(11)**, 3269–3279.

Malpas, J., Zhou, M. F., Robinson, P. T., Reynolds, P. H., 2003, Geochemical and geochronological constraints on the origin and emplacement of the Yarlung Zangbo ophiolites, Southern Tibet. *Geological Society, London, Special Publications*, **218(1)**, 191–206.

Matsuda, T. and Isozaki, Y., 1991. Well-documented travel history of Mesozoic pelagic chert in Japan: from remote ocean to subduction zone. *Tectonics*, **10(2)**, 475–499.

Matsuoka, A., 1995. Middle Jurassic–Lower Cretaceous radiolarian zonation in Japan and the western Pacific, and age assignments based on the Unitary Associations Method. Middle Jurassic to Lower Cretaceous Radiolaria of Tethys: Occurrence, Systematics, Biochronology. *Mémoires de Géologie (Lausanne)*, **(23)**, 1049–1057.

Matsuoka, A., Yao, A., 1990. Southern Chichibu Terrane. In Ichikawa, K., Mizutani, S., Hara, I., Hada, S., Yao, A., eds., Pre-Cretaceous Terranes of Japan. Publication of IGCP Project No. 224: Pre-Jurassic Evolution of Eastern Asia, IGCP Project 224, Osaka, Japan, 203-216.

Matsuoka, A., Kobayashi, K., Nagahashi, T., Yang, Q., Wang, Y. and Zeng, Q., 2001, Early Middle Jurassic (Aalenian) radiolarian fauna from the Xialu chert in the Yarlung Zangbo Suture Zone, southern Tibet. *In:* Metcalfe, I., Smith, J. M. B., Morwood, M. and Davidson, I., *eds.*, Faunal and floral migrations and evolution in SE Asia-Australasia, Balkema Swets Zeitlinger, Lisse, 105–110.

Matsuoka, A., Yang, Q., Kobayashi, K., Takei, M., Nagahashi, T., Zeng, Q. G., Wang, Y. J., 2002, Jurassic–Cretaceous radiolarian biostratigraphy and sedimentary environments of the Ceno-Tethys: records from the Xialu Chert in the Yarlung–Zangbo Suture Zone, southern Tibet. *Journal of Asian Earth Sciences*, **20**, 277–287.

Matsuoka, A., Yang, Q., Takei, M., 2005, Latest Jurassic–earliest Cretaceous radiolarian fauna from the Xialu Chert in the Yarlung Zangbo Suture Zone, Southern Tibet: Comparison with coeval western Pacific radiolarian faunas and paleoceanographic implications. *Island arc*, **14**, 338–345.

McDermid, I. R., Aitchison, J. C., Davis, A. M., Harrison, T. M., Grove, M., 2002, The Zedong terrane: a Late Jurassic intra-oceanic magmatic arc within the Yarlung–Tsangpo suture zone, southeastern Tibet. *Chemical Geology*,**187(3)**, 267–277.

Miller, C., Thöni, M., Frank, W., Schuster, R., Melcher, F., Meisel, T., Zanetti, A., 2003, Geochemistry and tectonomagmatic affinity of the Yungbwa ophiolite, SW Tibet. *Lithos*, **66(3)**, 155–172.

Molnar, P., England, P., Martinod, J., 1993, Mantle dynamics, uplift of the Tibetan Plateau, and the Indian monsoon. *Reviews of Geophysics*, **31(4)**, 357–396.

Moore, J. C., Klaus, A., Bangs, N. L., Bekins, B., Bücker, C. J., Brückmann, W., Erickson, S. N., Hansen, O., Horton, T., Ireland, P., Major, C. O., 1998, Consolidation patterns during initiation and evolution of a plate-boundary decollement zone: Northern Barbados accretionary prism. *Geology*, **26(9)**, 811–814.

Needham, D. T., 1995, Mechanisms of mélange formation: Examples from SW Japan and southern Scotland. *Journal of Structural Geology*, **17(7)**, 971975–973985.

O'Dogherty, L., 1994, Biochronology and Paleontology of Mid-Cretaceous Radiolarians from Northern Apennines (Italy) and Betic Cordillera (Spain). *Mémoires de Géologie (Lausanne)*, **21**, 1–415.

O'Dogherty, L., Carter, E. S., Dumitrica, P., Goriccan, Š., Wever, P. D., Bandini, A. N., Baumgartner, P. O., Matsuoka, A., 2009, Catalogue of Mesozoic radiolarian genera. Part 2: Jurassic–Cretaceous. *Geodiversitas*, **31(2)**, 271–356.

Orme, D. A., Guenthner, W. R., Laskowski, A. K., Reiners, P. W., 2016, Long-term tectonothermal history of Laramide basement from zircon–He age-eU correlations. *Earth and Planetary Science Letters*, **453**, 119–130.

Pan, G. T., Chen, Z. L., Li, X. Z., Yan, Y. J., 1997, Geological-Tectonic Evolution in the Eastern Tethys. Geological Publishing House, Beijing, pp. 1–191 (in Chinese with English summary)

Pan, G. T, Ding, J., Yao, D. S., Wang, L. Q., 2004, Guidebook of 1: 1, 500, 000 geologic map of the Qinghai–Xizang (Tibet) plateau and adjacent areas. Cartographic Publishing House, Chengdu, China, pp.1–148 (in Chinese).

Pessagno Jr, E. A., Newport, R. L., 1972, A technique for extracting Radiolaria from radiolarian cherts. *Micropaleontology*, 231–234.

Ratschbacher, L., Frisch, W., Liu, G., 1994, Distributed deformation in southern and western Tibet during and after the India–Asia collision. *Journal of Geophysical Research*, **99**, 19917–19945.

Raymo,M.E., Ruddiman,W.F., 1992, Tectonic forcing of Late Cenozoic climate. *Nature*, **359**, 117–122.

Robinson, P. T., Bai, W. J., Malpas, J., Yang, J. S., Zhou, M. F., Fang, Q. S., Hu, X. F., Cameron, S., Staudigel, H., 2004, Ultra-high pressure minerals in the Luobusa Ophiolite, Tibet, and their tectonic implications. *In:* Malpas, J., Fletcher, C.J.N., Ali, J., Aitchison, J.C., *eds.*, Aspects of the Tectonic Evolution of China: Geological Society of London Special Publications, **226**, pp. 247–271.

Searle, M. P., Windley, B. F., Coward, M. P., Cooper, D. J. W., Rex, A. J., Rex, D.,Li, T. D., Xiao, X. C., Jan, M. Q., Thakur, V. C., Kumar, S., 1987, The closing of Tethys and the tectonics of the Himalaya. *Geological Society of America Bulletin*, **98(6)**, 678–701.

Stow, D. A. V., Reading, H. G., Collinson, J. D., 1996, Deep seas. *In:* Reading, H.G. *ed.*, Sedimentary environments: processes, facies and stratigraphy. Blackwell Science, Oxford, pp. 395–453.

Storey, B. C., 1995, The role of mantle plumes in continental breakup: case histories from Gondwanaland. *Nature*, **377**, 301–308.

Sun, G. Y., Hu, X. M., 2012, Tectonic affinity of Zhongba terrane: evidences from the detrital zircon geochronology and Hf isotopes. *Acta Petrologica Sinica*, **28 (5)**, 1635–1646 (In Chinese with English abstract).

Tobin, H., Henry, P., Vannucchi, P., Screaton, E., 2014, Subduction Zones: Structure and Deformation History. In: R. Stein et al. *eds.*, Earth and Life Processes Discovered From Subseafloor Environment—A Decade of Science Achieved by the Integrated Ocean Drilling Program (IODP), 599–640.

Van Hinsbergen, D. J., Lippert, P. C., Dupont-Nivet, G., McQuarrie, N., Doubrovine, P. V., Spakman, W., Torsvik, T. H., 2012, Greater India Basin hypothesis and a two-stage Cenozoic collision between India and Asia.*Proceedings of the National Academy of Sciences*, **109(20)**, 7659–7664.

Vernik, L., Bruno, M., Bovberg, C., 1993, Empirical relations between compressive strength and porosity of siliciclastic rocks. *International Journal of Rock Mechanics and Mineral Science*, **30**, 677–680.

Wan, X. Q., Lamolda, M., Wang, C. S., 1997. Upper Cenomanian–Lower Turonian foraminiferal assemblages from southern Tibet: the responses of the biota to oceanic environmental change. *Journal of the Geological Society of the Philippines*, **52**, 183–197.

Wan, X. Q., Zhao, W. J., Li, G. B., 2000, Restudy of the Upper Cretaceous in Gamba, Tibet. *Geoscience*, **14**, p. 281–285.

Wang, J., Hu, X., Jansa, L., Huang, Z., 2011, Provenance of the Upper Cretaceous–Eocene deep-water sandstones in Sangdanlin, southern Tibet: Constraints on the timing of initial India-Asia collision. *The Journal of geology*, **119(3)**, 293–309.

Wang, C. S., Liu, Z. F., Li, X. H., Wan, X. Q., 1999, Xigaze Forearc Basin and Tsangpo Suture Zone, Tibet. Geological Publishing House, Beijing, pp. 1–237 (in Chinese with English abstract).

Wang, C. S., Li, X., Wan, X., Tao, R., 2000, The Cretaceous in Gyangze, southern Tibet. *Acta Geologica Sinica*, **74**, 97–107 (in Chinese English abstract).

Wang, C. S., Li, X. H., Liu, Z. F., Li, Y. L., Jansa, L., Dai, J. G., Wei, Y. S., 2012, Revision of the Cretaceous–Paleogene stratigraphic framework, facies architecture and provenance of the Xigaze forearc basin along the Yarlung Zangbo suture zone. *Gondwana Research*, **22(2)**, 415–433.

Wang, X. H., Luo, H., Xu, B., Zhu, Y. H., Chen, D. S., Liu, S. J., 2016, Upper Paleocene radiolarian fauna from the Sangdanlin section, southern Tibet, China and its geological significance. *Acta Micropalaeontologica Sinica*, **33(2)**, 105–126.

Wang, Y. J., Yang, Q., Matsuoka, A., Kobayashi, K., Nagahashi, T., Zeng, Q., 2002, Triassic radiolarians from the Yarlung Zangbo Suture Zone in the Jinlu area, Zetang County, southern Tibet. *Acta Micropalaeontologica Sinica*, **19**, 215–227.

Wei, Y. S., Li, Y. L., Chen, X., Wang, C. S., Li, X. H., Li, X., Zhong, H. T., 2015, The reconstruction of oceanic plate stratigraphy and its implications: A case study of Zhongba area, southern Tibet. *Geological Bulletin of China*, **34(10)**, 1789–1801.

Wen, S., 1987, Tertiary system, *In*: Xizang Scientific Expedition, Chinese Academy of Sciences *eds.*, Stratigraphy of the Mount Qomolangma Region, Science Press Beijing, 130–159.

Willems, H., Zhou, Z., Zhang, B., Grafe, K. U., 1996, Stratigraphy of the Upper Cretaceous and Lower Tertiary strata in the Tethyan Himalayas of Tibet (Tingri area, China). *Geologische Rundschau*, **85**, 723–754.

Wu, H. R., 1984, The Congdu Formation–Cretaceous deep-sea deposits in southern Xizang (Tibet) and its significance. *Scientia Geologica Sinica*, **1**, 26–33 (in Chinese with English abstract).

Wu, H. R., 1986, Some new genera and species of Cenomanian Radiolaria from southern Xizang (Tibet). *Acta Micropalaeontologica Sinica*, **3**, 347–359 (in Chinese with English abstract).

Wu, H. R., 2000, New data of the Late Jurassic Nassellarian (radiolarian) from the Xialu chert in southern Tibet. *Geoscience*, **14(3)**, 301–306.

Xiong, F. H., Yang, J. S., Liang, F. H., Ba, D. Z., Zhang, J., Xu, X. Z., Li, Y., Liu, Z., 2011, Zircon U-Pb ages of the Dongbo ophiolite in the western Yarlung Zangbo suture zone and their geological significance. *Acta Petrologica Sinica*, **27(11)**, 3223–3238 (in Chinese with English abstract).

Xu, D. M., Huang, G. C., Lei, Y. J., 2007, Origin of the Xiugugabu ophiolite massif, SW Tibet: evidence from petrology and geochemistry. *Geotectonica et Metallogenia*, **31**, 490–501.

Xu, Y., 2000, Early Tertiary calcareous nannofossils from southern Tibet and the closing time of east Tethys in Tibet. *Geoscience*, **14**, 255–262.

Xu, Z. Q., Dilek, Y., Yang, J. S., Liang, F. H., Liu, F., Ba, D. Z.,Cai, Z. H., Li, G. W., Dong, H. W., Ji, S. C., 2015, Crustal structure of the Indus–Tsangpo suture zone and its ophiolites in southern Tibet. *Gondwana Research*, **27(2)**, 507–524.

Yamamoto, S., Komiya, T., Yamamoto, H., Kaneko, Y., Terabayashi, M., Katayama, I., Iizuka, T., Maruyama, S., Yang, J., Kon, Y., Hirata, T., 2013, Recycled crustal zircons from podiform chromitites in the Luobusa ophiolite, southern Tibet. *Island Arc*, **22(1)**, 89–103.

Yang, S., Chen, H., Cheng, X., Xiao, A., He, G., Chen, J., Tian, D., 2007, Deformation characteristics and rules of spatial change for the Northern Qilianshan thrust belt. *Earth Science Frontiers*, **14 (5)**, 211–221.

Yin, A., Harrison, T. M., 2000, Geologic evolution of the Himalayan–Tibetan orogen. *Annual Review of Earth and Planetary Sciences*, **28(1)**, 211–280.

Yin, A., Harrison, T. M., Murphy, M. A., Grove, M., Nie, S., Ryerson, F. J., Feng, W. X., Le, C. Z., 1999, Tertiary deformation history of southeastern and southwestern Tibet during the Indo-Asian collision. *Geological Society of America Bulletin,* **111**, 1644–1664.

Yin, A., Nie, S., 1996, A Phanerozoic palinspastic reconstruction of China and its neighboring regions. *World and Regional Geology*, **1(8)**, 442–485.

Zhong, H. T., Dai, J. G., Wang, C. S., Li, Y. L., Wei, Y. S., 2016, Middle Jurassic–early Cretaceous radiolarian assemblages of the western Yarlung Zangbo Suture Zone: Implications for the evolution of the Neo-Tethys. *Geoscience Frontiers.* http://dx.doi.org/10.1016/j.gsf.2016.09.006

Zhu, D. C., Zhao, Z. D., Niu, Y. L., Mo, X. X., Chung, S. L., Hou, Z. Q., Wang, L. Q., Wu, F. Y., 2011a, The Lhasa Terrane: record of a microcontinent and its histories of drift and growth. *Earth and Planetary Science Letters*, **301(1)**, 241–255.

Zhu, D. C., Zhao, Z. D., Niu, Y., Dilek, Y., Mo, X. X., 2011b, Lhasa terrane in southern Tibet came from Australia. *Geology*, **39**, 727–730.

Zhu, J., Du, Y. S., Liu, Z. X., Feng, Q. L., Tian, W. X., Li, J. P., Wang, C. P., 2005, The origin and tectonic significance of Mesozoic radiolarian chert in the middle of Yarlung–Tsangpo suture zone. Science in China, Ser. D, Earth Sciences, 35, 1131–1139 (in Chinese with English abstract).

Ziabrev, S. V., Aitchison, J. C., Abrajevitch, A., Badengzhu, Davis, A. M. and Luo, H., 2003,Precise radiolarian age constraints on the timing of ophiolite generation and sedimentation in the Dazhuqu terrane, Yarlung–Tsangpo suture zone, Tibet. *Journal of the Geological Society, London*, **160**, 591–599.

Ziabrev, S. V., Aitchison, J. C., Abrajevitch, A. V., Davis, A. M., Luo, H., 2004, Bainang Terrane, Yarlung–Tsangpo suture, southern Tibet (Xizang, China): A record of intra-Neotethyan subduction–accretion processes preserved on the roof of the world. *Journal of the Geological Society, London*, **161**, 523–539.

Zyabrev, S. V., Kojima, S., Ahmad, T., 2008, Radiolarian biostratigraphic constraints on the generation of the Nidar ophiolite and the onset of Dras arc volcanism: Tracing

the evolution of the closing Tethys along the Indus–Yarlung–Tsangpo suture. *Stratigraphy*, **5**, 99–112.